

UNIVERSITY OF READING  
DEPARTMENT OF MATHEMATICS AND STATISTICS

**Modelling a single polymer entanglement**

Timothy Steven Palmer

Thesis submitted for the degree of

Doctor of Philosophy

January 2012

# Abstract

The slip-spring model introduced by Likhtman (Macromolecules **38**, 6128-6139 (2005)) simulates a single chain entangled within a polymer melt. Single-chain models such as the slip-spring model allow the rheology of polymers to be studied without requiring the use of expensive multiple-chain molecular dynamics simulations. This study investigates the slip-spring model in the context of a single entanglement and compares it to a two-chain entanglement model. A better understanding of the mechanisms involved in an entanglement is obtained, through the properties of stress relaxation and mean squared displacement, but also through analysis of the bead positions and bond vectors involved. Flaws are identified within the slip-spring model, for which modifications to the model are suggested, including the addition of a non-isotropic spring-constant and the replacement of the slip-spring by a slip-chain. This examination of the simple case is carried out, so that the knowledge gained may be later applied to the multiple-entanglement slip-spring model.

During the course of this study, the generic polymer simulation (GPS) package was constructed by the Reading Theoretical Polymer Physics Group. GPS provides an object-orientated simulation framework, designed to keep simulations organised and make new simulations faster to create. An overview of the concepts involved is included in this thesis. Another tool encountered within this study is maximum likelihood estimation, a statistical technique that, when applied to polymer models such as the slip-spring model, allows the estimation of model parameters. Such a fitting is not only useful for finding the best parameters, but also prevents the model flaws from being obscured by incorrect parameter fitting.

# Declaration

I confirm that this is my own work and the use of all material from other sources has been properly and fully acknowledged.

Timothy Steven Palmer

# Acknowledgements

I would like to acknowledge my supervisors Alexei Likhtman, Jorge Ramirez and Mark Matsen as well as the rest of the Reading Theoretical Polymer Physics Group, for their knowledge and guidance, which have been invaluable during this study. I would also like to mention by name Jing Cao and Bart Vorselaars who were joint co-developers with myself in the development of the GPS program. Finally, I would like to thank Charlotte and my family for their support and encouragement during my research.

# Contents

<b>1</b>	<b>Introduction</b>	<b>1</b>
1.1	Polymers and the role of entanglements . . . . .	1
1.2	Computer simulation . . . . .	4
1.2.1	Brownian motion . . . . .	5
1.2.2	Molecular dynamics (MD) . . . . .	6
1.2.3	Brownian dynamics (BD) . . . . .	8
1.2.4	Rouse model . . . . .	9
1.2.5	Monte Carlo (MC) . . . . .	13
1.3	Modelling entanglements . . . . .	13
1.3.1	Random Walk . . . . .	14
1.3.2	Tube model . . . . .	14
1.3.3	Slip-link models . . . . .	18
1.3.4	Slip-spring model . . . . .	26
1.4	Motivation for this study . . . . .	30
<b>2</b>	<b>Methods</b>	<b>33</b>
2.1	Observables . . . . .	33
2.1.1	Correlators and time correlation functions . . . . .	33
2.1.2	Stress, $\sigma$ , and the stress relaxation function, $G(t)$ . . . . .	36

2.1.3	Mean and variance of beads and bonds . . . . .	40
2.1.4	Mean squared displacement of beads, $g_{1,i}(t)$ . . . . .	41
2.2	Generic polymer simulation (GPS) . . . . .	44
2.2.1	Model classes . . . . .	48
2.2.2	Observable classes . . . . .	52
2.2.3	Analysis classes . . . . .	55
2.2.4	Comparison to another polymer simulation program . . . . .	57
2.2.5	Usage and future prospects of GPS . . . . .	58
<b>3</b>	<b>Main models</b>	<b>59</b>
3.1	Two-chain simulation . . . . .	59
3.1.1	Entanglement by rejection . . . . .	59
3.1.2	Predictor-corrector method . . . . .	62
3.1.3	Mean and variance of bead positions . . . . .	67
3.1.4	Mean squared displacement, $g_{1,mid}(t)$ . . . . .	71
3.1.5	Stress relaxation functions . . . . .	73
3.1.6	Stress cross-correlation functions . . . . .	75
3.1.7	Alternative: molecular dynamics two-chain simulation . . . . .	82
3.1.8	Stress from interactions between chains . . . . .	88
3.2	Slip-spring model . . . . .	90
3.2.1	Slip . . . . .	91
3.2.2	Analytical calculations . . . . .	92
3.2.3	Parameter finding using $G_{\gamma\gamma}(0)$ and $G_{\gamma\gamma}(\infty)$ . . . . .	101
3.2.4	Simulation results of stress relaxation functions . . . . .	103
3.2.5	Mean bead positions . . . . .	105
3.2.6	Variance of bead positions . . . . .	108
3.2.7	Mean and variance of bond vectors . . . . .	110

---

3.2.8	Mean squared displacement, $g_{1,\text{mid}}(t)$	111
3.2.9	Summary	113
<b>4</b>	<b>Modifications to the slip-spring model</b>	<b>116</b>
4.1	Non-isotropic slip-spring model	116
4.1.1	Analytical calculations	118
4.1.2	Parameter finding	121
4.1.3	Parameters and dependence on entanglement strength	121
4.1.4	Stress relaxation functions	124
4.1.5	Variance of bead and bond vectors	124
4.1.6	Summary	130
4.2	Slip-chain model	130
4.2.1	Mean squared displacement, $g_{1,\text{mid}}(t)$	134
4.2.2	Stress relaxation functions	134
4.2.3	Stress cross-correlation functions	137
4.2.4	Summary	144
4.3	Bulky-slip-chain model	146
4.3.1	Modified two-chain simulation	148
4.3.2	Mean bead positions	150
4.3.3	Variance of bead positions	150
4.3.4	Mean and variance of bond vectors	152
4.3.5	Stress relaxation functions	153
4.3.6	Summary	155
<b>5</b>	<b>Maximum likelihood estimation</b>	<b>157</b>
5.1	Estimation of parameters	157
5.2	Collection of observations, $\{\mathbf{r}_i\}_1, \{\mathbf{r}_i\}_2, \dots, \{\mathbf{r}_i\}_{n_k}$	159
5.3	MLE for the slip-spring models	161

---

5.4	MLE for a multiple entanglement slip-spring model . . . . .	164
5.5	Summary . . . . .	169
<b>6</b>	<b>Discussion and future directions</b>	<b>171</b>
6.1	Dependence on system stretch . . . . .	171
6.2	Slip-spring model for the case of $N_S \rightarrow 0$ , where slip-links are fixed in space . . .	172
6.3	Dual-slip-chain model . . . . .	173
6.4	Computational costs of model modifications and the slip-chain model . . . . .	174
6.5	Expansion to the case of melts . . . . .	174
6.6	Entanglements within a solvent and the bulky-slip-chain model . . . . .	177
<b>7</b>	<b>Conclusions</b>	<b>178</b>
<b>A</b>	<b>Stress correlation functions for a simple four-arm-star model</b>	<b>181</b>
<b>B</b>	<b>List of Gaussian integrals</b>	<b>188</b>

## Notation

$$\delta_{ij} = \begin{cases} 1 & ; \quad i = j \\ 0 & ; \quad i \neq j \end{cases}$$

$k_B$  Boltzmann constant

$T$  temperature

$U$  potential energy

$\xi$  friction coefficient

$m$  mass

$t$  time

$\Delta t$  simulation time step

$\tau_R$  Rouse time

$\tau_d$  disentanglement time

$b$  statistical segment

$N$  number of bonds in a chain

$H$  system height, see Fig.3.1

$D$  system width, see Fig.3.1

$V$  volume

$k$  spring-constant

$k_S$  slip-spring spring-constant

$\hat{k}_S$  tensor slip-spring spring-constant

$\hat{k}_{SC}$  tensor slip-chain spring-constant

## Notation continued...

$h$	slip-spring height, see Fig.3.21
$N_S$	slip-spring strength
$\{N_S\} = N_{S,x}, N_{S,y}, N_{S,z}$	non-isotropic slip-spring strength
$\{n_S\} = n_{S,x}, n_{S,y}, n_{S,z}$	slip-chain spring strength
$N_{SC}$	number of bonds in a slip-chain
$\mathbf{r}_i = (x_i, y_i, z_i)$	position of bead $i$
$\mathbf{R}_{ij} = (X_{ij}, Y_{ij}, Z_{ij})$	bond vector between beads $i$ and $j$
$\mathbf{F}_{ij}$	force on bead $i$ due to bead $j$
$\mathbf{F}_i$	total force on bead $i$
$\sigma$	stress tensor
$G(t)$	stress relaxation/correlation function
$G^A(t)$	stress auto-correlation of lower chain
$G^B(t)$	stress auto-correlation of upper chain
$G^T(t)$	stress auto-correlation for both the lower and upper chain
$G^X(t)$	stress cross-correlation between the lower and upper chain
$g_{1,\text{mid}}(t)$	mean squared displacement of the middle bead
$\text{var}(x)$	variance of $x$

# Chapter 1

## Introduction

### 1.1 Polymers and the role of entanglements

Polymers are long molecules of repeating chemical units, an example being DNA chromosomes, which are  $\sim 10^{-10}$ m wide and can be up to  $\sim 10^{-2}$ m in length. This difference in length scales gives polymers unique dynamics compared to regular small molecules, because the polymer chains become entangled with each other.

#### Polymer melts

A system of unlinked polymers, above melting temperature, is known as a polymer melt. These systems demonstrate an important property known as viscoelasticity, where the polymer has an elastic response for fast deformations, but will demonstrate viscous flow over longer time scales, allowing it to fill a container. Entanglements within the melt restrict the movement of the polymer chains and play a key role in the viscoelasticity. In a dense polymer melt, lateral motion is severely restricted by the presence of the surrounding chains, which means that the polymer mainly moves along its own length. The motion of a polymer only along its length was named reptation by Pierre-Gilles de Gennes in 1971 [1]. An entanglement between two polymers will exist until one of the chains slides out of it by reptation. However, as a polymer slides out

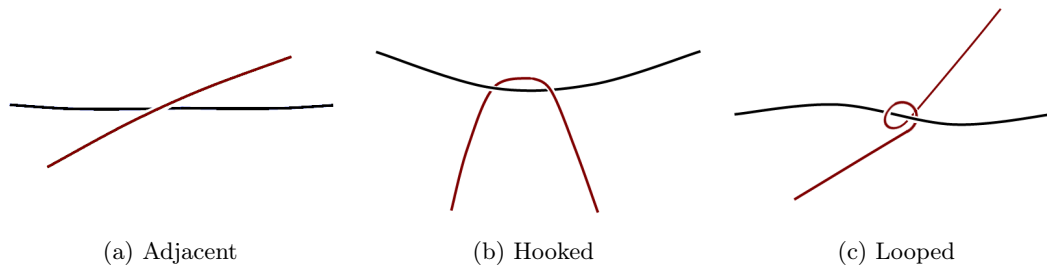


Figure 1.1: Diagram showing examples of entanglements

of entanglements, it will slide into new entanglements. Thus, the polymer is always entangled, but each entanglement has a finite lifetime.

### Polymer networks

A system where the polymers are joined by cross-links is known as a polymer network or elastomer. An example of this is rubber bands made from vulcanised rubber. When the elastomer is relaxed, the chains are slack and thus at their highest state of entropy. When a stretching force is applied, the elastomer stretches significantly, pulling the chains taut and causing the entropy to decrease. When this force is released, the chains become slack again and the elastomer returns to its original shape. The cross-links are crucial to the response of the elastomer to this stretching force. A greater number of cross-links will decrease the length of polymer segments, and therefore increase the restoring force and decrease the relaxation time. Studies have demonstrated that entanglements between cross-links are also vital for explaining the response of the system, because they act as extra cross-links [2]. Hence, the ability to understand the mechanisms of these entanglements is of interest to polymer scientists.

### Entanglements

As depicted in Fig.1.1, different levels of interactions can be labelled as entanglements and there is currently no consensus on what constitutes an entanglement. An entanglement could correspond to one chain completely looped around another (Fig.1.1c), or be as simple as one

polymer adjacent to another (Fig.1.1a). One could suggest that adjacent chains are not an entanglement, but chains hooked around each other are an entanglement (Fig.1.1b). Yet, the difference between these two cases is just the curvature of the chain; if the hooked case had no curvature, it would be equivalent to the adjacent case. Thus, one would have to suggest a point at which the curvature of a chain becomes sufficient enough to constitute an entanglement and not just an interaction. A recent study by Likhtman, Ponmurugan and Cao [3] states that one may characterise entanglements by the duration of contacts and the linking number between two chains, which is related to the curvature of one chain around the other. It was discovered that the longest lived entanglements had the greatest curvature. This thesis shall examine long-lived entanglements where one chain hooks around another.

A polymer network can be considered as consisting of circular polymers [2]. Fig.1.2 demonstrates how a network eventually leads to the creation of circular polymers, which can become entangled. Circular polymers have a number of different possible forms of entanglement. Neighbouring circles may interact with each other (Fig.1.3a), which would result in a temporary entanglement, since the two polymers would eventually separate. A second entanglement type (Fig.1.3b) occurs when two of these circular polymers are entwined together. Such an interaction

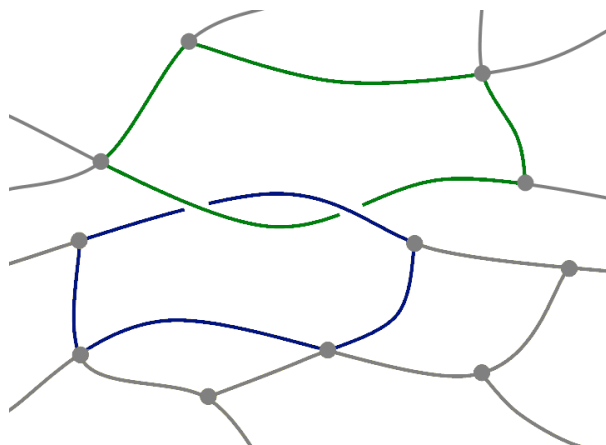


Figure 1.2: Diagram showing a polymer network. Polymers are connected by cross-links, and may also entangle with each other. A sufficiently high density of cross-links will create loops, which prevent the entanglements from being released.

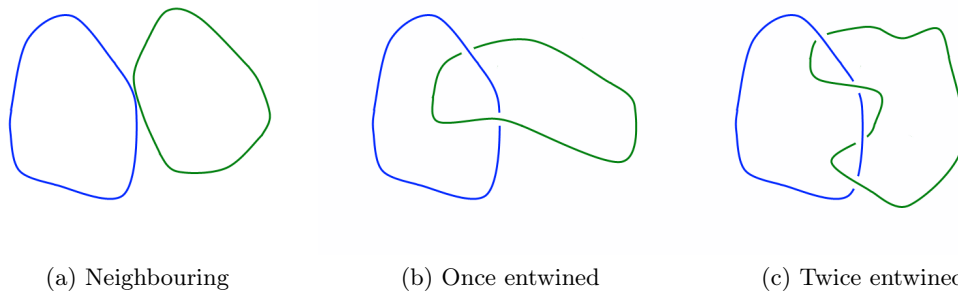


Figure 1.3: Diagram showing three of the possible entanglements between two circle polymers

would lead to permanent entanglements. These circles may also entwine with each other more than once (Fig.1.3c), resulting in twice entwined interactions or greater. This study considers an entanglement in the case of once entwined chains, so that the entanglements in our model are permanent.

## 1.2 Computer simulation

Computer simulation is a vital tool in polymer science. Experiments cannot show exactly what is happening microscopically within a polymer system, but only deduce the mechanisms from observable macroscopic properties. In contrast, a computer simulation can be used to set up a system of polymers with a known configuration and can measure properties on the microscopic scale. Furthermore, with simulations it is possible to easily test how changing details of the system affect these properties. There are a number of different equations of motion that are commonly used for computer simulation. During this study, three of these are used: molecular dynamics (MD), Monte Carlo (MC) and Brownian dynamics (BD), which are described in the following sections.

### 1.2.1 Brownian motion

Before discussing these equations of motion, the concept of Brownian motion shall be introduced. Brownian motion is the seemingly random motion of a particle as a result of unobserved smaller particles. Polymers are often modelled to exist within a solution of smaller particles, so a random force,  $\mathbf{F}_i^{\text{R}}$ , is included in the equation of motion to represent the net effect of collisions between the large particle  $i$  and smaller particles in the solution,

$$\mathbf{F}_i^{\text{R}} = \sum_{j=0}^n \mathbf{f}_{ij}^{\text{R}} \quad (1.1)$$

where  $\mathbf{f}_{ij}^{\text{R}}$  is the force due to a collision, with particle  $j$ . Using central limit theorem, the probability distribution of  $\mathbf{F}_i^{\text{R}}$  is known to be a Gaussian distribution, with  $\langle \mathbf{F}_i^{\text{R}} \rangle = 0$  and variance  $v$ . This may be expressed by a Wiener process as

$$\mathbf{F}_i^{\text{R}} dt = \sqrt{v} d\mathbf{W}_i(t) \quad (1.2)$$

The stochastic Wiener process is defined such that  $d\mathbf{W}_i(t)$  is not correlated between beads,  $i, j$ , not correlated between Cartesian components,  $\alpha, \beta$ , and not correlated between different points in time,  $t, t'$ . Hence,

$$\langle W_i^\alpha(t) W_j^\beta(t') \rangle = \delta_{ij} \delta_{\alpha\beta} \min(t, t') \quad (1.3)$$

The fluctuation-dissipation theorem establishes a relationship between random forces and frictional forces [4]. This is a reasonable relationship, since the faster a particle moves in a particular direction the larger the probability of collisions with other particles occurring on the forward side of the particle. From this, the variance of a particle moving with Brownian motion is known to be

$$v = 2k_B T \xi \quad (1.4)$$

and Eq.(1.2) becomes

$$\mathbf{F}_i^R dt = \sqrt{2k_B T \xi} d\mathbf{W}_i(t) \quad (1.5)$$

where  $k_B$  is the Boltzmann constant,  $T$  the temperature and  $\xi$  the friction coefficient.

### 1.2.2 Molecular dynamics (MD)

MD simulations aim to completely model the forces involved in the system and are typically used to model multi-chain polymer models. MD simulations obey Newtonian mechanics with the equation of motion

$$m\ddot{\mathbf{r}}_i = \mathbf{F}_i^T \quad (1.6)$$

where  $\ddot{\mathbf{r}}_i = \frac{d^2\mathbf{r}_i}{dt^2}$  is the acceleration,  $m$  is the mass, and  $\mathbf{F}_i^T$  is the total force upon bead  $i$ .  $\mathbf{F}_i^T$  is a sum of forces,

$$\mathbf{F}_i^T = \mathbf{F}_i^f + \mathbf{F}_i^B + \mathbf{F}_i^{\text{NB}} + \mathbf{F}_i^R \quad (1.7)$$

combining: the frictional force,  $\mathbf{F}_i^f$ ; the force along bonds,  $\mathbf{F}_i^B$ ; the force between non-bonded beads,  $\mathbf{F}_i^{\text{NB}}$ ; and Brownian motion,  $\mathbf{F}_i^R$  (Eq.(1.5)). The frictional force is given by

$$\mathbf{F}_i^f = -\xi\dot{\mathbf{r}}_i \quad (1.8)$$

where  $\dot{\mathbf{r}}_i$  is the velocity.

#### KGMD model

The simplest MD model of a polymer melt, and the one that we will use later in this study, was created by Kremer and Grest in 1990 [6] and will be referred to as KGMD. This model has a truncated Lennard-Jones (LJ) potential between all beads and finitely extensible nonlinear elastic (FENE) springs for bonds.

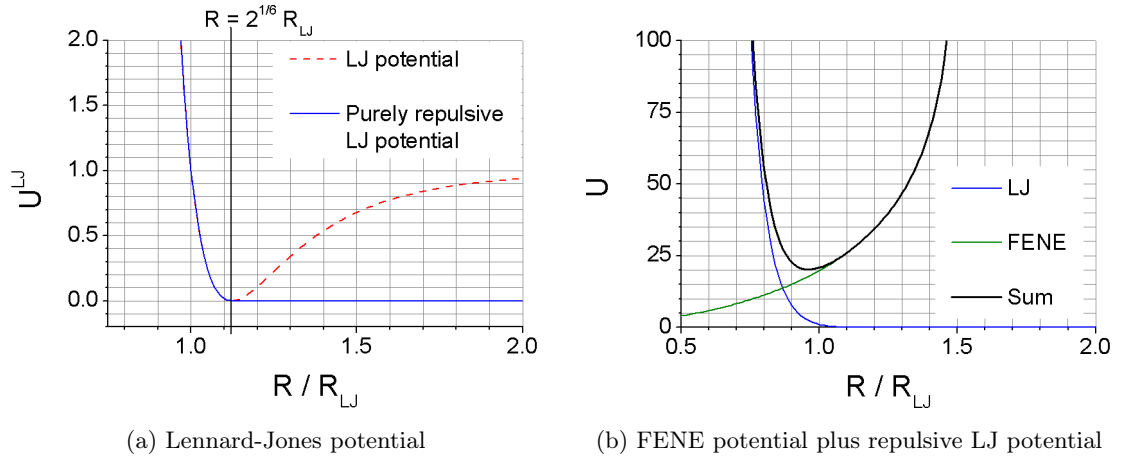


Figure 1.4: KGMD bead interaction potentials.

The repulsive LJ force between all beads is given by

$$\mathbf{F}_i^{\text{NB}} = - \sum_{j=1, j \neq i}^N \frac{\partial U_{ij}^{\text{LJ}}}{\partial \mathbf{R}_{ij}} \quad (1.9)$$

where  $\mathbf{R}_{ij} = \mathbf{r}_i - \mathbf{r}_j$  and  $U_{ij}^{\text{LJ}}$  is the LJ potential,

$$U_{ij}^{\text{LJ}}(\mathbf{R}_{ij}) = \begin{cases} 4\epsilon \left( \left( \frac{R_{LJ}}{R_{ij}} \right)^{12} - \left( \frac{R_{LJ}}{R_{ij}} \right)^6 + \frac{1}{4} \right) & \frac{R_{ij}}{R_{LJ}} < 2^{\frac{1}{6}} \\ 0 & \text{otherwise} \end{cases} \quad (1.10)$$

where  $\epsilon$  is the LJ energy and  $R_{LJ}$  is the LJ radius. In this study, we shall define our units such that  $\epsilon = R_{LJ} = 1$ . The standard LJ potential, demonstrated in Fig.1.4a, is repulsive for  $\frac{R}{R_{LJ}} < 2^{\frac{1}{6}}$  and attractive for  $\frac{R}{R_{LJ}} > 2^{\frac{1}{6}}$ . In the KGMD model only the repulsive potential is required, so a cut-off distance of  $\frac{R}{R_{LJ}} = 2^{\frac{1}{6}}$  is applied. This repulsion becomes very strong as  $R_{ij}$  becomes small and gives beads an excluded volume, which combine in polymer chains to make them uncrossable, provided the springs hold the beads close enough together.

The force,  $\mathbf{F}_i^{\text{B}}$ , between particles connected by bonds with vectors  $\mathbf{R}_{ij}$  is a sum of all attached

bonds. In the case of a bead in the middle of a linear chain, there are two bonded beads and

$$\mathbf{F}_i^{\text{B}} = \mathbf{f}_{i,i-1}^{\text{B}} + \mathbf{f}_{i,i+1}^{\text{B}} \quad (1.11)$$

In the KGMD model

$$\mathbf{f}_{ij}^{\text{B}} = -\frac{\partial U_{ij}^{\text{FENE}}}{\partial \mathbf{R}_{ij}} \quad (1.12)$$

where  $U_{ij}^{\text{FENE}}$  is the potential energy of a FENE spring,

$$U_{ij}^{\text{FENE}}(\mathbf{R}_{ij}) = \begin{cases} -\frac{1}{2}kR_{\text{max}}^2 \ln\left(1 - \left(\frac{R_{ij}}{R_{\text{max}}}\right)^2\right) & R_{ij} < R_{\text{max}} \\ \infty & \text{otherwise} \end{cases} \quad (1.13)$$

where  $k = 30\epsilon/R_{LJ}^2$  and  $R_{\text{max}} = 1.5R_{LJ}$  is the maximum bond length. The FENE potential in Eq.(1.13) increases as the distance between beads increases, such that it becomes infinite when  $R_{ij} \rightarrow R_{\text{max}}$ , and when combined with the LJ force creates a potential well for the bonds, as shown in Fig.1.4b.

### 1.2.3 Brownian dynamics (BD)

The Brownian dynamics equation of motion approximates Eq.(1.6), for the case of large  $\xi$  and small  $m$ , where the inertia becomes relatively unimportant and the  $m\ddot{\mathbf{r}}$  term may be neglected. Thus  $\mathbf{F}_i^{\text{T}} = 0$ , which leads to the equation of motion

$$\xi\dot{\mathbf{r}} = \mathbf{F}^{\text{B}} + \mathbf{F}^{\text{NB}} + \mathbf{F}^{\text{R}} \quad (1.14)$$

By making this approximation the equation of motion has been simplified to a first order stochastic differential equation. The Rouse model is an example of a model that is commonly simulated using the BD equation of motion, and is described below.

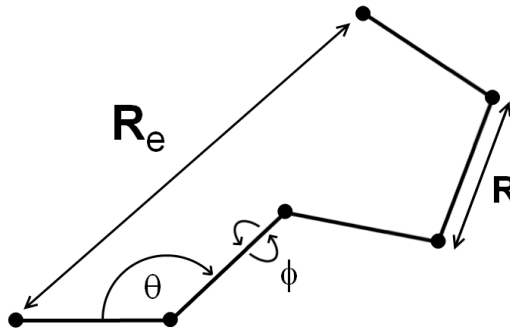


Figure 1.5: Diagram of the monomer scale polymer chain model. Each bond has a length  $R_i$ , the angle between each bond is labelled as  $\theta_i$  and the rotation of bonds is  $\phi_i$ . Each of these degrees of freedom may have any potential,  $U$ , but central limit theorem states that the end-to-end vector  $R_e$  will have a Gaussian distribution when the number of bonds is large.

#### 1.2.4 Rouse model

Proposed by Rouse in 1953 [7], the Rouse model is used extensively in polymer dynamics and during this study. A Rouse chain is composed of massless beads connected by linear springs [4]. To introduce the Rouse chain, a polymer chain is first considered on a scale such that each bead is a monomer. As depicted in Fig.1.5, the chain has three main potentials that can be used to define the model: the bond length potential  $U(R)$ , angle between bonds  $U(\theta)$ , and rotation around bonds  $U(\phi)$ . The statistical segment length of this chain,  $b$ , is defined by the second moment of the end to end vector  $\langle R_e^2 \rangle$  relative to the number of bonds,  $n$ ,

$$b^2 \equiv \frac{\langle R_e^2 \rangle}{n} \quad (1.15)$$

Central limit theorem states that the sum of a random mechanism repeated multiple times will have a Gaussian distribution, independent of the potentials involved (in this case  $U(R)$ ,  $U(\theta)$ )

and  $U(\phi)$ . Thus, the probability distribution of  $\mathbf{R}_e$  takes the form as

$$\begin{aligned} P(\mathbf{R}_e) &= \frac{1}{Q} \exp\left(-\frac{3R_e^2}{2\langle R_e^2 \rangle}\right) \\ &= \frac{1}{Q} \exp\left(-\frac{3R_e^2}{2nb^2}\right) \end{aligned} \quad (1.16)$$

where  $Q$  is such that  $\int P(\mathbf{R}_e) d^3\mathbf{R}_e = 1$ . If one was to model  $\mathbf{R}_e$  as a linear spring between the two end beads, with spring constant  $k$  and energy

$$U = \frac{1}{2}kR_e^2 \quad (1.17)$$

the probability distribution may also be written as a Boltzmann distribution

$$P(\mathbf{R}_e) = \frac{1}{Q} \exp\left(-\frac{kR_e^2}{2k_B T}\right) \quad (1.18)$$

By comparing Eq.(1.16) and Eq.(1.18), the spring constant required for replacing the microscopic chain with a linear spring is found to be

$$k = \frac{3k_B T}{nb^2} \quad (1.19)$$

The Rouse model represents this monomer chain as a chain of coarse-grained blobs, such that one blob represents many beads from the real chain, as depicted by Fig.1.6. Using Eq.(1.19), these coarse-grained blobs are connected by linear springs to form the Rouse chain. By coarse-graining the system, calculations are made simpler and simulations are faster. Once the system has been coarse-grained, the individual monomers are neglected and only the Rouse chain is modelled. The position vectors of the coarse-grained blobs in this new chain are labelled as  $\mathbf{r}_0, \mathbf{r}_1, \dots, \mathbf{r}_N$ . The statistical segment of this coarse-grained chain relative to the statistical segment of the previous monomer chain,  $b_m$  (Eq.1.15), is  $b^2 = nb_m^2$ . Thus from Eq.(1.19), the

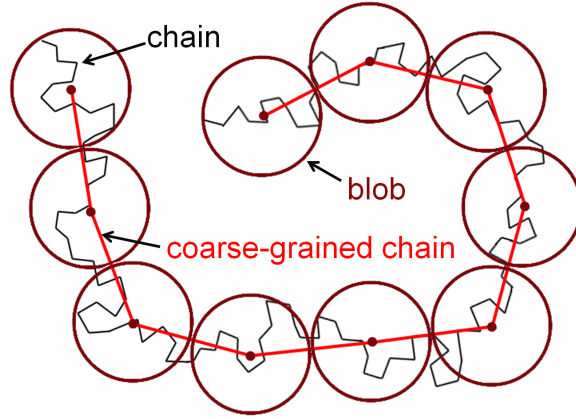


Figure 1.6: Diagram of a coarse-grained chain

spring constant in terms of this new statistical segment is

$$k = \frac{3k_B T}{b^2} \quad (1.20)$$

The energy of a linear spring and thus each Rouse bond is therefore

$$U_{ij} = \frac{1}{2} k (\mathbf{r}_i - \mathbf{r}_j)^2 \quad (1.21)$$

and the energy of the entire Rouse chain with  $N$  bonds is a sum of these bonds,

$$U = \frac{1}{2} k \sum_{i=1}^N (\mathbf{r}_i - \mathbf{r}_{i-1})^2 \quad (1.22)$$

The force of each Rouse bond is

$$\mathbf{f}_{ij}^B = -\frac{\partial U_{ij}}{\partial \mathbf{R}_{ij}} \quad (1.23)$$

where  $\mathbf{R}_{ij} = \mathbf{r}_i - \mathbf{r}_j$ . Using Eq.(1.5), Eq.(1.11), Eq.(1.14), Eq.(1.23) and  $\mathbf{F}_i^{\text{NB}} = 0$ , the equation of motion is obtained,

$$\xi d\mathbf{r}_i = \frac{3k_B T}{b^2} (\mathbf{r}_{i+1} - 2\mathbf{r}_i + \mathbf{r}_{i-1}) dt + \sqrt{2k_B T \xi} d\mathbf{W}_i(t) \quad (1.24)$$

In order to solve this equation of motion, a transformation to normal modes is made such that

$$\mathbf{r}_i = \mathbf{X}_0 + 2 \sum_{p=1}^N \mathbf{X}_p \cos \left( \frac{\pi p (i + \frac{1}{2})}{N + 1} \right) \quad (1.25)$$

One can show that this transformation makes Eq.(1.24) a set of independent Ornstein-Uhlenbeck processes,

$$d\mathbf{X}_p = -\frac{1}{\tau_p} \mathbf{X}_p dt + \sqrt{\frac{2k_B T}{\xi_p}} d\mathbf{W}_p \quad (1.26)$$

with

$$\xi_p = \begin{cases} 2(N+1)\xi & p > 0 \\ (N+1)\xi & p = 0 \end{cases} \quad (1.27)$$

and

$$\tau_p = \frac{\xi b^2}{12k_B T} \sin^{-2} \left( \frac{\pi p}{2(N+1)} \right) \quad (1.28)$$

[4, 7].  $\tau_p$  is the relaxation time of Rouse mode,  $p$ . For the case  $p \ll N$  and  $N \ll 1$ , this may be approximated as

$$\tau_p \approx \frac{\xi b^2 N^2}{3\pi^2 k_B T} \frac{1}{p^2} \quad (1.29)$$

The longest relaxation time is given by  $p = 1$  and is known as the Rouse time,

$$\tau_1 = \tau_R \approx \frac{\xi b^2 N^2}{3\pi^2 k_B T} \quad (1.30)$$

and a unit of time  $\tau_0$  is often defined based on this,

$$\tau_0 \equiv \frac{\tau_R}{N^2} = \frac{\xi b^2}{3\pi^2 k_B T} \quad (1.31)$$

Since this study considers Rouse chains with fixed end bead positions, it should be noted that

for the fixed end case the transformation required is

$$\mathbf{r}_i = 2 \sum_{p=1}^{N-1} \mathbf{X}_p \sin\left(\frac{\pi i p}{N}\right) \quad (1.32)$$

and

$$\xi_p = 2N\xi \quad (1.33)$$

However, for the limit  $p \ll N$ , Eq.(1.29) and Eq.(1.30) are unchanged.

### 1.2.5 Monte Carlo (MC)

The MC method makes extensive use of random numbers. Random changes to the system are made and then accepted or rejected with a probability based on the change in energy, in an algorithm known as Metropolis acceptance. For example, a polymer model will attempt to make a random move of a randomly selected bead from position  $\mathbf{r}_{\text{old}}$  to  $\mathbf{r}_{\text{new}}$ , and have the probability of this move being accepted given by

$$P(\mathbf{r}_{\text{old}} \rightarrow \mathbf{r}_{\text{new}}) = \begin{cases} \exp\left(-\frac{1}{k_B T} (U(\mathbf{r}_{\text{new}}) - U(\mathbf{r}_{\text{old}}))\right) & U(\mathbf{r}_{\text{new}}) - U(\mathbf{r}_{\text{old}}) > 0 \\ 1 & \text{otherwise} \end{cases} \quad (1.34)$$

In a computer simulation, this probability is used with a random number generator that generates a number  $f(t)$  from a uniform distribution  $[0 \dots 1]$ . If  $P(\mathbf{r}_{\text{old}} \rightarrow \mathbf{r}_{\text{new}}) > f(t)$ , then the move is accepted.

## 1.3 Modelling entanglements

Running a multi-chain molecular dynamics simulation takes a lot of processor time to provide useful statistics - often such simulations will have to be run for months. An alternative to a multi-chain model is a single-chain model, which replaces all chains but one in the system with virtual objects that represent the influence of the other chains. As such, single-chain models

are not exact replications of the physical system, but rather an attempt to mimic the motion of a single chain with the use of virtual objects. The core aims of a single-chain model are that it is simple, fast to simulate and able to reproduce experimental results with as few arbitrary parameters as possible. Many single-chain models have been proposed in the attempt to find the best possible model, two of which relate to this project: the tube model and the slip-link model.

### 1.3.1 Random Walk

Before introducing the tube model, it is useful to introduce the random walk. A random walk has steps with vectors,  $\mathbf{R}_i$ , of random length and direction, such that  $\langle \mathbf{R}_i \rangle = 0$  and  $\langle R_i^2 \rangle = b^2$ . These vectors are uncorrelated with each other, such that  $\langle \mathbf{R}_i \cdot \mathbf{R}_j \rangle = \langle \mathbf{R}_i \rangle \cdot \langle \mathbf{R}_j \rangle = 0$  for  $i \neq j$ . A chain composed of  $n$  of these random steps will have an average end-to-end vector

$$\langle \mathbf{R}_e \rangle = \left\langle \sum_{i=1}^n \mathbf{R}_i \right\rangle = \sum_{i=1}^n \langle \mathbf{R}_i \rangle = 0 \quad (1.35)$$

The second moment of the end-to-end vector is

$$\begin{aligned} \langle R_e^2 \rangle &= \left\langle \sum_{i=1}^n \sum_{j=1}^n \mathbf{R}_i \cdot \mathbf{R}_j \right\rangle \\ &= \sum_{i=1}^n \langle R_i^2 \rangle + \sum_{i=1}^n \sum_{j=1, j \neq i}^n \langle \mathbf{R}_i \cdot \mathbf{R}_j \rangle \\ &= \sum_{i=1}^n b^2 + \sum_{i=1}^n \sum_{j=1, j \neq i}^n \langle \mathbf{R}_i \rangle \cdot \langle \mathbf{R}_j \rangle \\ &= nb^2 \end{aligned} \quad (1.36)$$

which is the definition for  $b$ , the statistical segment length, as previously defined in (1.15).

### 1.3.2 Tube model

To calculate the entropy of a chain, the ability to calculate the number of possible chain conformations is required. In a multi-chain model, this cannot be done due to changing topological

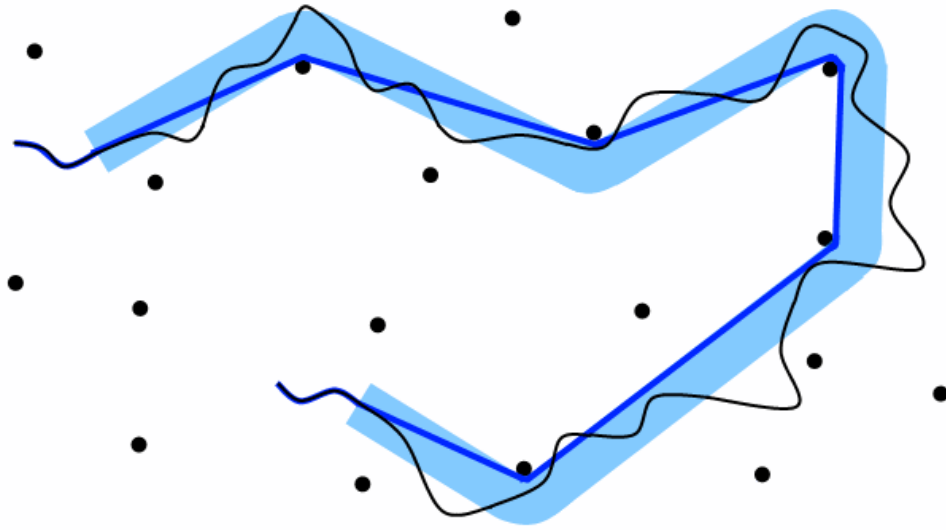


Figure 1.7: Diagram of the tube model. The chain is drawn as a black line with the other polymers in the melt represented perpendicular to the plane the chain is on. The tube is shaded blue and contains a line representing the primitive path.

constraints caused by the other chains. The tube model, introduced by Edwards in 1967 [10], represents a single chain in such a way that the entropy can be calculated. To demonstrate the construction of the tube model, consider the chain in Fig.1.7. It exists on a plane with other chains intersecting the plane, so that they are considered as individual points. The approximation that the other chains do not move is made by assuming that their motion is slower than the reptation of the chain. Constraints nearest to the mean path of the chain are used to construct a tube-like region. The diameter of this tube, labelled  $a$ , depends on the density of the constraining points. The line within the tube-like region is called the primitive chain and is the shortest curve with the same topology as the real chain relative to the entanglements with other chains. The primitive chain is approximately a random walk with  $Z$  sections of length  $a$  and contour length

$$L = Za \tag{1.37}$$

As a random walk, the mean squared end-to-end vector is known to be

$$\begin{aligned}\langle R_e^2 \rangle &= Za^2 \\ &= La\end{aligned}\tag{1.38}$$

However, the primitive chain represents the real chain with mean squared end-to-end vector

$$\langle R_e^2 \rangle = Nb^2\tag{1.39}$$

where  $N$  is the number of bonds and  $b$  the statistical segment length. The end-to-end vector of the real chain must be equal to the end-to-end vector of the primitive chain, so the tube segment length is defined as

$$a \equiv \frac{Nb^2}{L}\tag{1.40}$$

### Equation of motion

The motion of the primitive chain ignores the small fluctuations of the chain, instead focusing upon the more significant reptation motion. This motion is easy to compute because the entire chain either moves forward one step or backward one step. Hence, the position of a bead at time  $t + \Delta t$ , where  $\Delta t$  is the simulation time step, is given by

$$\mathbf{r}_i(t + \Delta t) = \frac{1 + \zeta(t)}{2} \mathbf{r}_{i+1}(t) + \frac{1 - \zeta(t)}{2} \mathbf{r}_{i-1}(t)\tag{1.41}$$

where  $\zeta(t)$  specifies the direction of movement of the chain, either  $+1$  or  $-1$  [8]. At the end of the chain, the beads act differently; there is no tube to move into, so a new tube segment is created with random vector  $\mathbf{v}(t)$  from the last bead, where  $|\mathbf{v}(t)| = a$ . Therefore, the equations

of motion for the end beads are

$$\mathbf{r}_0(t + \Delta t) = \frac{1 + \zeta(t)}{2} \mathbf{r}_1(t) + \frac{1 - \zeta(t)}{2} (\mathbf{r}_0(t) + \mathbf{v}(t)) \quad (1.42)$$

$$\mathbf{r}_N(t + \Delta t) = \frac{1 + \zeta(t)}{2} (\mathbf{r}_N(t) + \mathbf{v}(t)) + \frac{1 - \zeta(t)}{2} \mathbf{r}_{N-1}(t) \quad (1.43)$$

During its motion, the chain will slide out of the end of the tube to create new sections of tube and the old sections of the tube are forgotten. Eventually, the entire original tube orientation will be forgotten and replaced by a new tube. The lifetime of the middle segments is significantly longer than that of the end segments, and the time taken for all of the original segments to be forgotten is known as the disentanglement time,  $\tau_d$ .

The original tube model had only a single relaxation method, reptation. Subsequent to this original incarnation, many amendments have been made to improve comparison to experimental results. As part of these modifications, two additional relaxation mechanisms were introduced: contour length fluctuations and constraint release. One of the tube theory's initial assumptions was that the primitive chain has a fixed length,  $L$ ; contour length fluctuations challenges this assumption. Fluctuations in the real chain cause the length of the primitive chain to vary over time, and were discovered to be important for reproducing the dynamical effects and predicting  $\tau_d$  [11]. Because the length of the primitive chain varies in addition to reptation, the chain has a second mechanism of sliding out of entanglements. Hence,  $\tau_d$  is smaller than the original model predicted, especially when the number of segments is not very large. Another assumption was that all other chains are frozen in time, which is not the case. Constraint release considers the case of existing topological constraints being removed, due to the reptation of other chains. This means that the primitive chain does not only move along its length by reptation, but that the shape of the path also changes. There are different ways of modelling this, one of which is by allowing the primitive chain to move in a slow Rouse like motion [12].

### Criticisms of the tube model

The single chain structure factor,  $S(\mathbf{k}, t)$ , is an experimentally measured property of a material that contains information about the structure of a polymer. In an experiment, photons or neutrons are scattered off a material and the function  $S(\mathbf{k}, t)$  is the intensity of the scattered wave with the vector  $\mathbf{k}$ . Random walk statistics and neutron-spin echo experiments show that this function should be a Debye function, but it has been demonstrated that the function for the tube model is significantly different and has up to a 50% discrepancy [21]. This was acknowledged by Doi and Edwards in their formulation of the model [8]. Mapping the one-dimensional Rouse motion of the primitive chain reptation into three-dimensional space causes this discrepancy.

Other issues include the experimentally observed properties of the storage modulus,  $G'(\omega)$ , and loss modulus,  $G''(\omega)$ . These functions are calculated from the strain of a material given when a stress is applied with frequency  $\omega$ .  $G'(\omega)$  is the elastic component representing the storage of energy, whilst  $G''(\omega)$  represents the loss of energy through heat transfer from the material acting as a viscous liquid. Whilst the tube model is able to model these properties for a monodisperse system, it struggles to reproduce them for bidisperse and branched polymers. Different incarnations and modifications are made to the model to improve the fit in these cases, but these modifications are not consistent with each other and cannot be easily compared. Furthermore there is not a single model that can represent all experimental setups. The slip-link model was created in an attempt to improve upon this situation.

#### 1.3.3 Slip-link models

The concept of the slip-link model has existed for a long time; however, the more recent versions are based upon the slip-link model described by Doi and Edwards [13]. This model is similar to the tube model, where the tube is replaced with a number of virtual slip-link objects fixed in space. The chain is free to move along its length by reptation, but is forced through these slip-links, in order to represent the topological restrictions applied by entanglements. Like the tube model, there have been many subsequent variations of the slip-link model proposed by various

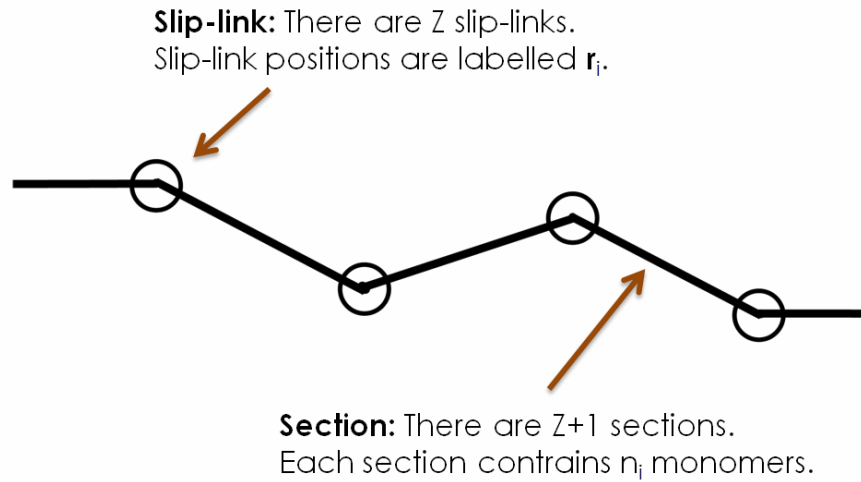


Figure 1.8: Diagram of the Hua-Schieber slip-link model

research groups. Some of the most recent slip-link model variants are presented in the following sections, followed by a critical summary.

### Hua-Schieber slip-link model

The Hua-Schieber (HS) model [14], depicted in Fig.1.8, has a primitive-chain composed of  $Z + 1$  sections joined at  $Z$  slip-links. The position of the  $i^{\text{th}}$  slip-link is specified by  $\mathbf{r}_i$ . The number of monomers in each section,  $i$ , is  $n_i$ , but the positions of these beads are not considered. Instead, the simulation is evolved in respect to the one-dimensional position of each bead along the chain contour length,  $s_j$ , relative to an arbitrarily chosen point along the contour length. The equation of motion for this system is

$$\xi \frac{ds_j}{dt} = F_j^B + F_j^R + F_j^{EV} \quad (1.44)$$

where  $\xi$  is the friction coefficient of the beads.  $F_j^B + F_j^R$  are the forces of a one-dimensional Rouse chain, where  $F_j^B$  is the force due to springs and  $F_j^R$  is a random Brownian force. Finally,  $F_j^{EV}$  is an excluded volume force that prevents beads from passing through each other in the chain.

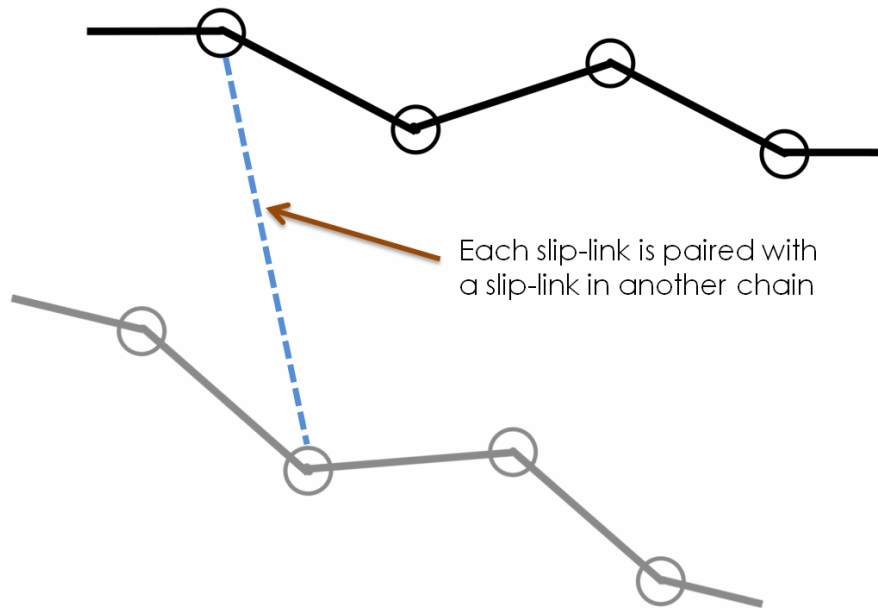


Figure 1.9: Diagram of the Doi-Takimoto slip-link model

If the number of beads in the first or last section becomes zero, then the slip-link for that section is destroyed. Constraint release occurs when this mechanism is triggered. Standard practice is to run multiple independent chains simultaneously, in order to average the results. In this model, whenever a slip-link is destroyed by reptation in one chain, another slip-link from the ensemble of other chains is selected. If this selected link is older than the one that is being destroyed, then the constraint is assumed to have been released and is destroyed also. New slip-links are created when the number of beads in an end section exceeds a critical value. This new slip-link is created at a random vector with a fixed length from the previous slip-link.

### Doi-Takimoto slip-link model - dual slip-link model

The HS model applied constraint release when slip-links were destroyed on other chains. The Doi-Takimoto (DT) model [16], depicted in Fig.1.9, improves upon the HS model by explicitly pairing the slip-links when they are created. When a slip-link is constructed, a counterpart is

added to another random chain in the middle of a random section. Each of these pairs represents an entanglement between two chains. Both of the paired slip-links are destroyed when either of the two chains slide out of one of the slip-links. Hence, the statistical character of the constraint release is directly determined by the other chains.

However, unlike the NS model, the DT model does not store the one-dimensional position of individual beads  $s_j$ ; instead it is assumed that all beads are equally spaced between slip-links, whose positions are fixed in space. This means that the middle sections of the chain can be ignored and only the end sections are considered. Two effects change the length of the end segments. Firstly, reptation is applied randomly with the equation of motion

$$ds = \sqrt{2d_c} dW(t) \quad (1.45)$$

where the diffusion constant is

$$d_c = \frac{a^2}{3\pi^2\tau_0 Z} \quad (1.46)$$

The random movement  $ds$  can be either positive or negative and modifies the length of the end segments  $s_1$  and  $s_2$ , such that  $s_2$  is increased when the length of  $s_1$  decreases and vice versa. The second effect applied to the chain is contour length fluctuations; the total length,  $L$ , fluctuates with the equation

$$dL = -\frac{1}{\tau_R} (L(t) - L_{eq}) dt + \sqrt{2d_L} dW(t) \quad (1.47)$$

which has a restorative term that encourages the chain to return to the equilibrium length  $L_{eq}$  and a random fluctuation with diffusion coefficient  $d_L$ .

### **Masubuchi slip-link model - primitive chain network model**

The DT model recognised that one chain may be used to determine the constraint release dynamics of another by explicitly pairing slip-links. However, there is an ambiguity about the location of the paired slip-link. This is resolved in the more involved Masubuchi model [17]. The

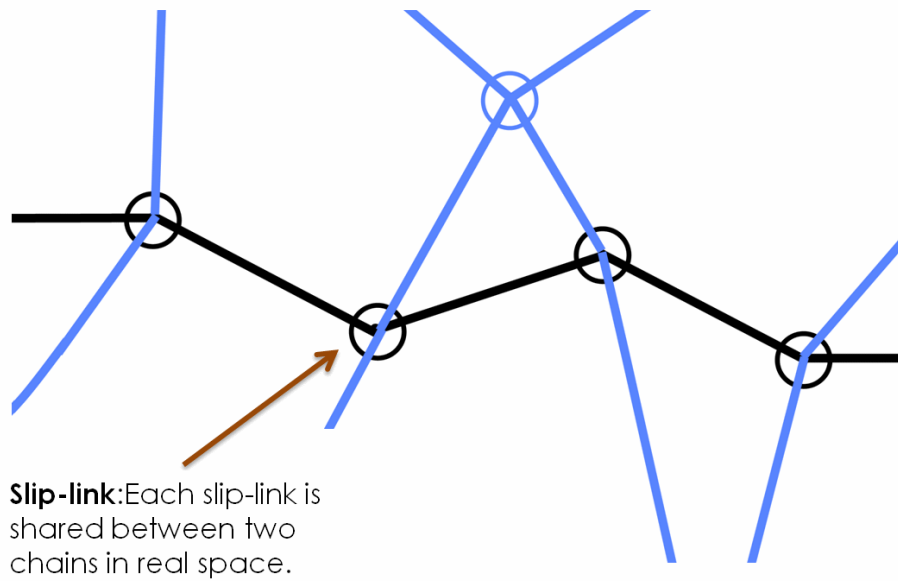


Figure 1.10: Diagram of the Masubuchi slip-link model

slip-link that joins two chains must have the same point in space for both chains, as illustrated in Fig.1.10.

The number of beads in each section is varied with the equation of motion

$$\left( \xi_b \frac{a_0}{n_0} \right) \frac{dn_i}{dt} = F_i^n + F_i^R \tag{1.48}$$

where  $\xi_b$  is the friction coefficient of a bead and  $\frac{n_0}{a_0}$  is the average bead density of the entire chain. This equation represents the one-dimensional reptation, where  $F_i^R$  is a random force and

$$F_i^n = \frac{3k_B T}{b^2} \left( \frac{R_{i+1}}{n_{i+1}} - \frac{R_{i-1}}{n_{i-1}} \right) \tag{1.49}$$

is the force of beads in neighbouring segments, where  $n_i$  is the number of beads and  $R_i$  is the length of section  $i$ . An end section is destroyed if the number of beads within it is less than half the average number of beads in a segment, and a new segment is constructed when the segment

has one and a half times the average number of beads in a segment. When constructing a new slip-link at the end of a chain, a list of all other segments from other chains that are within a certain range of this end segment is generated. One of these segments is chosen and a slip-link is added to both the middle of the selected segment and at the middle of the end segment that was too long.

Another important advance in the Masubuchi model is the addition of thermal motion for slip-links. The equation of motion of these slip-links is

$$\xi_s \frac{d\mathbf{x}_i}{dt} = \mathbf{F}_i^E + \mathbf{F}_i^O + \mathbf{F}_i^R \quad (1.50)$$

where  $\xi_s$  is the friction coefficient of the slip-link and  $\mathbf{F}_i^E$  is the elastic force due to the four chains connected to the slip-link,  $i$ . As such,

$$\mathbf{F}_i^E = \frac{3k_B T}{b^2} \sum_j \frac{\mathbf{R}_j}{n_j} \quad (1.51)$$

where the summation is over the four connected sections, with vectors  $\mathbf{R}_j$  and  $n_j$  beads. The second force  $\mathbf{F}_i^O$  is an osmotic term, such that sections repel the slip-link with a force proportional to the bead density of that section. This results in an approximately constant bead density. The final force,  $\mathbf{F}_i^R$ , is a random motion force. Thermal motion of entanglement points is an important addition to the model, one that is also present in the slip-spring model, described in section 1.3.4.

### **Nair-Schieber slip-link model - consistently unconstrained Brownian slip-link model (CUBS)**

The Nair-Schieber (NS) model [18], illustrated in Fig.1.11, also allows slip-links to move in space, but only due to constraint release, not to represent the fluctuations of the entanglement points in the melt. As such, the NS model has no shared constraint release between chains or destruction

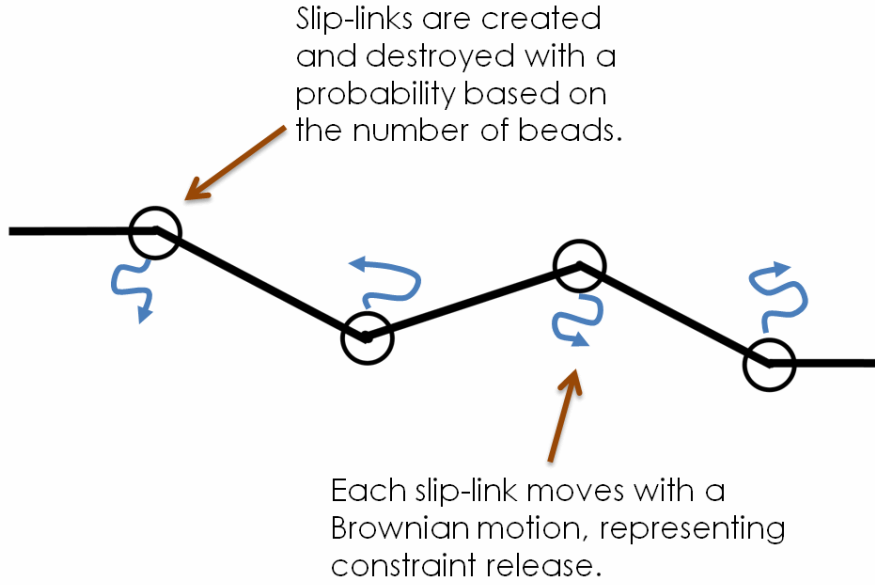


Figure 1.11: Diagram of the Nair-Schieber slip-link model

of middle slip-links. Instead, the slip-links have the equation of motion

$$d\mathbf{r}_i = -\frac{N_e a^2}{12k_B T \tau_i^{\text{CR}}} \left( \frac{\partial \mathcal{F}}{\partial \mathbf{r}_i} \right)_{T, \{n_j\}, \{\mathbf{r}_{j \neq i}\}} dt + \sqrt{\frac{N_e a^2}{6\tau_i^{\text{CR}}}} d\mathbf{W}_i(t) \quad (1.52)$$

where  $a$  is the average bond length of the real chain and  $N_e$  is the number of real chain bonds per entanglement. The free energy,  $\mathcal{F}$ , is the sum of the free energy of each section

$$\mathcal{F} = \mathcal{F}_e(n_1) + \sum_{i=2}^{Z-1} \mathcal{F}_s(n_i) + \mathcal{F}_e(n_Z) \quad (1.53)$$

The free energy of a middle section is given by

$$\mathcal{F}_s(n_i) = \frac{3k_B T \langle n \rangle}{2a^2} \frac{(\mathbf{r}_i - \mathbf{r}_{i+1})^2}{n_i} + \frac{3k_B T}{2} \log \left( \frac{2\pi n_i}{3} \right) \quad (1.54)$$

and the free energy of an end section is given by

$$\mathcal{F}_e(n_i) = -\frac{k_B T}{2} \log(n_i) \quad (1.55)$$

as derived in [19]. The time scale of this constraint release motion is controlled by the parameter  $\tau_i^{\text{CR}}$  for each slip-link.

The equation of motion for the individual beads is the same as for the HS model, but the approach taken towards the construction and destruction of chain ends is a new one. Unlike the previous models, the NS model creates and destroys end segments with a probability, rather than when it reaches a critical value. This probability is derived from a balance condition dependent on the number of beads in the section. The probability of a chain end being destroyed is given by

$$P_d(n_i) = \frac{1}{\langle n \rangle^2 \tau_K} \sqrt{\frac{3 \langle n \rangle}{n_i}} \quad (1.56)$$

and the construction of a new end by

$$P_c(n_i) = \frac{1}{\langle n \rangle^2 \tau_K} \sqrt{\frac{3(n_i - 1)}{n_i \langle n \rangle}} \quad (1.57)$$

where the Kuhn segment time,  $\tau_K = \tau_e / \langle Z \rangle^2$ , is fit from the characteristic time of chain relaxations,  $\tau_e$ , and the number of slip-links,  $Z$ .

## Summary

The modern slip-link model improves upon the tube model, but once again different versions exist, which have focused upon the different methods of constraint release. A study by Masubuchi and Watanabe in 2008 [15] compared the results of these different methods of constraint release, and demonstrated that the NS model's method of constraint release is inferior to the method of pairing slip-links used by the DT and Masubuchi models; since the NS model overestimates the values of  $G'(\omega)$  and  $G''(\omega)$  at intermediate time. This conclusion was confirmed by Schieber in

[20].

Another mechanism that has not been properly resolved is the fluctuation of the entanglement point. Slip-links are assumed to be fixed in space in the HS and DT models, and while the NS model introduced slip-links with motion, this was only applied to reproduce constraint release. Only the Masubuchi model has slip-link positions that fluctuate with forces from the attached segments and Brownian motion. As a result, the NS and DT models have poor agreement with high frequency modes, where  $G'(\omega)$  significantly underestimates experimental values [15]. Compared to these models, the Masubuchi model with fluctuating slip-link positions demonstrates better agreement with experiment.

However, the issues encountered with the structure factor observed with the tube model have not been addressed. The primitive chain's reptation is still a one-dimensional Rouse motion, mapped onto three-dimensional space. The slip-spring model below addresses this problem.

#### 1.3.4 Slip-spring model

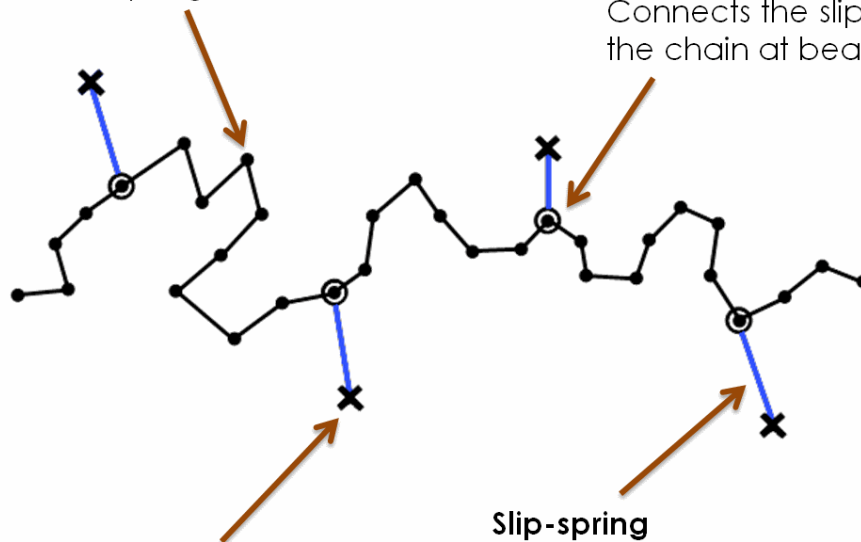
The focus of this study is the slip-spring model, as proposed by Likhtman in 2005 [21], and based upon the slip-tube model of Rubinstein and Panyukov created in 2002 [22]. In the slip-spring model, the slip-links are attached to fixed points in space by linear springs, known as slip-springs, as illustrated in Fig.1.12. Much like the Masubuchi model, the movement of the slip-links represents the motion of the entanglement point, due to the motion of the surrounding chains. Another major difference with the slip-spring model is that beads within the chains are explicitly modelled, whereas previous models focused on the slip-link positions and the number of beads between them. This makes the slip-spring model less coarse-grained than previous models, and allows smaller time scales to be investigated. The explicit knowledge of bead positions also makes all physical observables easily available.

**Polymer chain**

with  $N+1$  beads indexed  $i=0$  to  $N$ .  
 Bead positions are labelled  $\mathbf{r}_i$ .  
 Bonds have spring constant  $k$ .

**Slip-link**

Connects the slip-spring to  
 the chain at bead index  $m_k$ .



**Slip-spring anchor**  
 with position  $\mathbf{a}_k$

**Slip-spring**  
 with spring constant  $k_s = k/N_s$ .  
 There are  $Z$  slip-springs,  
 labelled from  $k=1$  to  $Z$ .

Figure 1.12: Diagram of the slip-spring model

## Parameters

In this model, the positions of beads are labelled as  $\mathbf{r}_i$ , where  $i$  is the bead index, and there are  $N$  bonds connecting  $N + 1$  beads. There are  $Z$  slip-springs per chain, labelled from  $j = 1$  to  $j = Z$ . Their slip-links may only exist on top of chain beads, where  $m_j$  specifies the bead that the  $j^{\text{th}}$  slip-link is currently at. The anchoring point of the  $j^{\text{th}}$  slip-spring is denoted as  $\mathbf{a}_j$ . Furthermore, as demonstrated in Fig.1.12, anchoring points are not chosen to be on the mean path, but rather represent the direction the entanglement is pulling the chain.

## Energy

Since the chain is a Rouse chain (section 1.2.4), it is a series of linear springs with total energy

$$U^{\text{C}} = \frac{1}{2}k \sum_{i=1}^N (\mathbf{r}_i - \mathbf{r}_{i-1})^2 \quad (1.58)$$

where

$$k = \frac{3k_B T}{b^2} \quad (1.59)$$

The strength of the slip-springs is represented by the parameter  $N_S$ , which represents the number of chain bonds that have the same strength as the slip-spring when connected in series. Thus, the energy of a slip-spring is

$$U_j^{\text{S}} = \frac{k}{2N_S} (\mathbf{r}_{m_j} - \mathbf{a}_j)^2 \quad (1.60)$$

and exerts a force

$$\mathbf{F}_j^{\text{S}} = -\frac{k}{N_S} (\mathbf{r}_{m_j} - \mathbf{a}_j) \quad (1.61)$$

on bead  $m_j$ . The energy of the entire system is given by

$$U = \frac{k}{2} \sum_{i=1}^N (\mathbf{r}_i - \mathbf{r}_{i-1})^2 + \frac{k}{2N_S} \sum_{j=1}^Z (\mathbf{r}_{m_j} - \mathbf{a}_j)^2 \quad (1.62)$$

and has equation of motion

$$\xi d\mathbf{r}_i = \frac{3k_B T}{b^2} (\mathbf{r}_{i+1} - 2\mathbf{r}_i + \mathbf{r}_{i-1}) dt + \sqrt{2k_B T \xi} d\mathbf{W}_i(t) + \frac{k}{N_S} \sum_{j=1}^Z \delta_{i,m_j} (\mathbf{a}_j - \mathbf{r}_{m_j}) dt \quad (1.63)$$

The first two terms in Eq.(1.63) are the equation of motion for a Rouse chain (Eq.(1.24)) and the final term applies to beads with a slip-link present.

## Slip

Slip in the model represents the reptation-like motion of the chain past an entanglement. In previous slip-link models, the chain would slide smoothly through the slip-link, because the slip-links were fixed in space and the position of the beads were not modelled. In the slip-spring model, the beads have known positions, which greatly increases the complexity, because one must ensure the chain always passes through the slip-link position. The solution to this problem is to allow the slip-link to move to the beads, instead of applying the topological constraint to the beads. At each time step in the slip-spring simulation, the slip-link has the possibility of slipping along the chain to the next bead in the chain. The direction of the slip is chosen by a random function,  $\zeta_k(t)$ , which is either  $-1$  or  $+1$ . The change in energy due to the proposed slip is therefore given by

$$\begin{aligned} \Delta U_j(\zeta_j(t)) &= U_j^{\text{SS}}(m_j) - U_j^{\text{SS}}(m_j + \zeta_j(t)) \\ &= \frac{k}{2N_S} (\mathbf{a}_j - \mathbf{r}_{m_j})^2 - \frac{k}{2N_S} (\mathbf{a}_j - \mathbf{r}_{m_j + \zeta_j(t)})^2 \end{aligned} \quad (1.64)$$

The change in slip-link index is accepted or rejected by the Metropolis algorithm as described in section 1.2.5. The original model considered the slip-link existing anywhere along the length of the chain, but the method of discrete jumps between beads, first implemented by Müller [24], is equally valid and far simpler.

### Constraint release

Constraint release is added to the slip-spring model using the same mechanism used in the Doi-Takimoto slip-link model. When slip-links are created, they are explicitly paired to other slip-links. When a slip-link reaches an end bead,  $m_k \rightarrow 0$  or  $m_k \rightarrow N$ , the chain is said to have reptated out of the entanglement and that slip-link is destroyed along with the paired slip-link. However, unlike the DT model, new slip-links are not created based upon the length of an end section. To ensure the average density of slip-links is maintained, a new pair of slip-links is created whenever a pair is removed. This new slip-link pair is created with one slip-link on the end section of a random chain and the other on any random location in another chain.

### Results

The slip-spring model has taken the best parts of the previous tube and slip-link models. As such, the intermediate time of  $G'(\omega)$  and  $G''(\omega)$  fits well to experimental data [21], since the DT constraint release is used. The high frequency modes of  $G'(\omega)$  are also in agreement with experimental data [21], because the slip-links may move in space as they do in the Masubuchi model. The slip-spring model improves upon these models further, by considering the position of beads and allowing them to have three-dimensional motion. The previous models had a structure factor that violated random-walk statistics, due to the beads moving with a one-dimensional Rouse motion, and this difference in the slip-spring model fixes this.

## 1.4 Motivation for this study

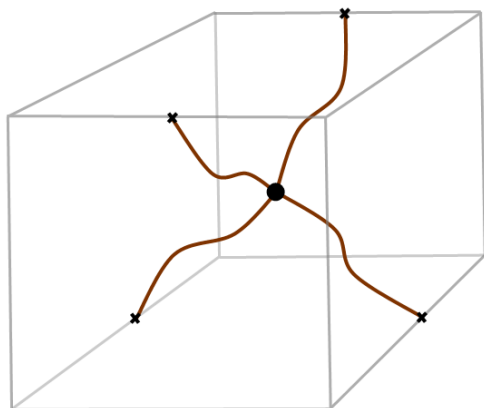
In 1943, Flory and Rehner [25] considered analytically a single cell of a polymer network. This cell consisted of a cross-link connected to four bonded neighbours, as illustrated in Fig.1.13a. The neighbouring cross-links were assumed to be fixed at their average positions, located at the corners of a tetrahedron. In 1977, Graessley and Pearson [2] considered analytically the Flory network cell again, but used a slip-link instead of a central cross-link, in order to compare an

entanglement with a cross-link. The slip-link, as depicted in Fig.1.13b, is an older version of the slip-links that have been discussed in section 1.3.3, where it is a hoop through which both chains have to pass.

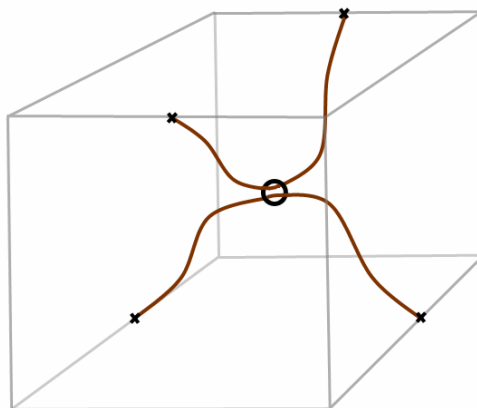
Today, there is a far greater computational power available, which allows this study to run polymer simulations, as described in chapter 2, rather than just analytical models. As such, the two-chain model (Fig.1.13c) is constructed, for which a detailed description is given in section 3.1.7. This is compared to the slip-spring model, where there is only one chain and has a single slip-spring representing the single entanglement (Fig.1.13d). A detailed description of this model is given in section 3.2. By comparing the slip-spring model to the two-chain model, this project aims to demonstrate how well the slip-spring model can reproduce the static and dynamic properties of the single entanglement case, using both macroscopic and microscopic properties. Where discrepancies are discovered, chapter 4 of this project suggests improvements to the slip-spring model that can be made. Whilst this study considers the simplest mapping of the multi-chain system onto a single-chain model, the aim is for the techniques and suggestions proposed to be developed further after this study and applied to the more general case of the full multi-entanglement slip-spring model (section 1.3.4).

Furthermore, this project demonstrates how parameter estimation can be done using the statistical technique of maximum likelihood, as discussed in chapter 5. This method is based purely on the probability distribution of beads, rather than fitting the parameters of a model to particular properties. By having a method that fits the model to the bead positions observed in a multi-chain simulation, the maximum likelihood method finds parameters without bias towards specific properties and does not obscure flaws in the model.

Previous models:

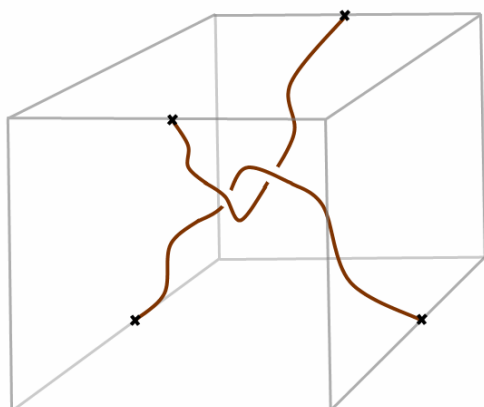


(a) Flory and Rehner

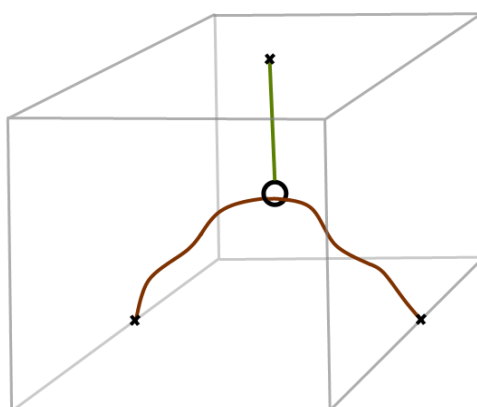


(b) Graessley and Pearson

Models used within this study:



(c) Two-chain single entanglement



(d) Slip-spring

Figure 1.13: Single cell network models

## Chapter 2

# Methods

### 2.1 Observables

#### 2.1.1 Correlators and time correlation functions

Observables are properties of the system that are measured during the simulation. In this study, the majority of observations use time correlation functions, which are the average of the product of a function at two different times,

$$C_{AA}(t) = \langle A(t) A(0) \rangle = \lim_{t_f \rightarrow \infty} \frac{1}{t_f - t} \int_0^{(t_f - t)} A(t + \tau) A(\tau) d\tau \quad (2.1)$$

where  $t_f$  is the final time of simulation [26]. When  $t = 0$  the two values of  $A$  are equal and therefore fully correlated and give the second moment of  $A$ ,

$$C_{AA}(0) = \langle A(0) A(0) \rangle = \langle A^2 \rangle \quad (2.2)$$

In the limit  $t \rightarrow \infty$  the two measurements are completely uncorrelated and produce the first moment of  $A$  squared,

$$C_{AA}(\infty) = \langle A(\infty) A(0) \rangle = \langle A(\infty) \rangle \langle A(0) \rangle = \langle A \rangle^2 \quad (2.3)$$

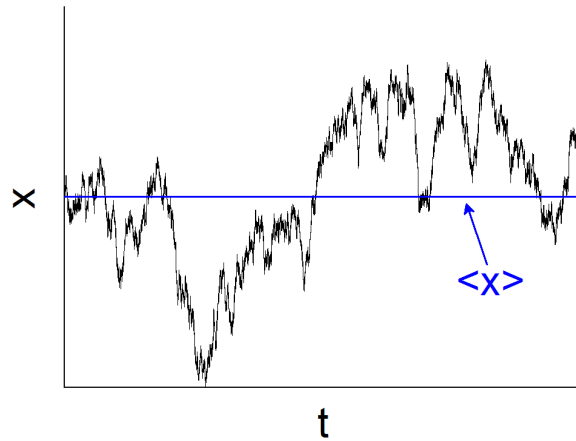


Figure 2.1: Bead position in a random walk

The amplitude of the correlation function and the difference between these is the variance of  $A$

$$C_{AA}(0) - C_{AA}(\infty) = \langle A^2 \rangle - \langle A \rangle^2 = \text{var}(A) \quad (2.4)$$

A stochastic process as a function of time provides very little insight about the dynamics of a system, as demonstrated by Fig.2.1. The time correlation function can be used instead to obtain more information, using the fluctuation-dissipation theorem, which connects the relaxation of a system to correlations between fluctuations occurring at different times [26, 27, 28]. For example, the stress relaxation modulus of an isotropic system can be expressed as correlation function of stress at time  $\tau$  and  $t + \tau$ ,

$$G(t) = \frac{V}{k_B T} \langle \sigma_{\alpha\beta}(t + \tau) \sigma_{\alpha\beta}(\tau) \rangle \quad \begin{array}{l} \alpha, \beta = x, y, z \\ \alpha \neq \beta \end{array} \quad (2.5)$$

where  $V$  is the volume,  $\sigma_{\alpha\beta}$  is a component of the stress tensor and the average  $\langle \rangle$  applies the integral over  $\tau$  in Eq.(2.1) [4]. The stress relaxation may be calculated from measurements of the system relaxing after a deformation, as the name suggests, but the fluctuation-dissipation theorem means that, by measuring the time correlation function of the stress tensor, the stress

relaxation modulus can be calculated from a system without deforming it.

### Correlators in computer simulations

To calculate a time correlation function in a simulation, the integral in Eq.(2.1) is approximated as a summation of  $n_t$  time steps of size  $\Delta t$ ,

$$C_{AA}(t) = \langle A(t) A(0) \rangle \simeq \frac{1}{n_t} \sum_{i=0}^{n_t} A(t + i\Delta t) A(i\Delta t); \quad n_t = \frac{(t_f - t)}{\Delta t} \quad (2.6)$$

A typical simulation would record the function  $A(t)$  during the simulation and write it to file. Only after the simulation is completed, is Eq.(2.6) calculated. The major drawback of this is the amount of storage memory required for the output file, which limits the number of observations that may be recorded. The University of Reading Polymer Physics Group has its own programming objects called correlators, which improves upon this situation greatly [29]. Rather than calculating the correlation function after the simulation, the correlation function is calculated as the data is obtained. Thus, when a new value is observed, it is compared with all previous observations to calculate  $A(t) A(0)$ , where the latest observation is  $A(0)$  and  $A(t)$  is the observation a time  $t$  ago. When this is done for every observation and averaged, Eq.(2.6) is obtained. However, this would have greatly increased the amount of run-time memory required to impossible levels. This is where the correlators become clever.

Time correlation functions are normally plotted on a logarithmic scale. This means that the correlator object does not need to calculate  $C_{AA}(t)$  for all available  $t$ . Instead the correlator uses an array of queue objects to create a non-linear scale. Illustrated in Fig.2.2, these queues shift all values one place every time a new value is added, such that the final value is forgotten, but every two values added are averaged and passed to the next queue object in the array. Because of this, the  $n^{\text{th}}$  queue is only given 1 value for every  $2^{n-1}$  values added to the 1<sup>st</sup> queue. Thus, a non-linear storage of past observations is created, with increased averaging as  $t$  increases, so no past observations are completely forgotten.

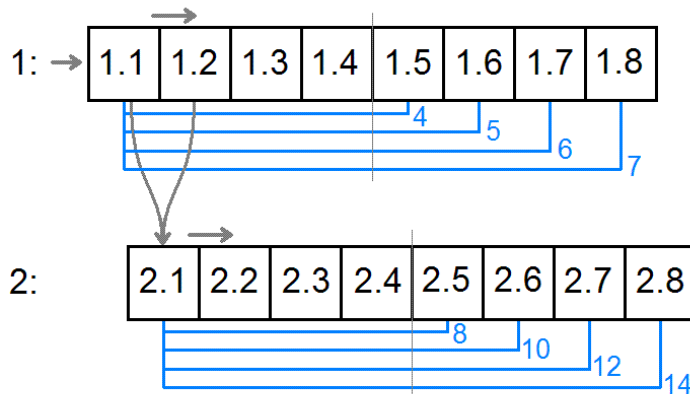


Figure 2.2: Diagram of the correlator object, indicating insertion, shifting and averaging of values (grey). Also shown are the combinations of elements used for calculation of the correlation function (blue). Only two queue structures are depicted in this diagram, but many more are used within simulations. Each queue structure repeats the operations demonstrated here, such that the  $n^{\text{th}}$  correlator obtains new a value every  $2^{(n-1)}$  values added to the 1<sup>st</sup> correlator.

The correlation function,  $C_{AA}(t)$ , is calculated from this structure with the same non-linear scale. Using Fig.2.2 for reference, a new value in the 1<sup>st</sup> queue is compared with the values in cell 1.5, 1.6, 1.7, 1.8 to obtain the correlation function at  $t = 4\Delta t, 5\Delta t, 6\Delta t, 7\Delta t$ ; a new value in the 2<sup>nd</sup> queue is compared with 2.5, 2.6, 2.7, 2.8 to obtain  $t = 8\Delta t, 10\Delta t, 12\Delta t, 14\Delta t$ ; and continuing for later queues. These are averaged with the results calculated when previous values were added to the correlator object to obtain the correlation function,  $C_{AA}(t)$ . This method is more efficient on memory and provides a more accurate correlation function, than the standard method, for the same simulation time.

### 2.1.2 Stress, $\sigma$ , and the stress relaxation function, $G(t)$

The stress property shall be considered in relation to a single Rouse chain, consisting of  $N$  bonds connecting  $N + 1$  beads. Beads in this chain are labelled with the position vectors  $\mathbf{r}_0, \mathbf{r}_1, \dots, \mathbf{r}_N$ , where the end beads  $\mathbf{r}_0$  and  $\mathbf{r}_N$  are fixed in space. For this chain, the microscopic expression for

the stress tensor is

$$\sigma_{\alpha\beta} = -\frac{1}{V} \sum_{i=1}^N R_{i,i-1}^{\alpha} F_{i,i-1}^{\beta} \quad (2.7)$$

where  $V$  is the volume of the system,  $\mathbf{R}_{i,i-1}$  is a bond vector and  $\mathbf{F}_{i,i-1}$  is the force along the bond,

$$\mathbf{R}_{i,i-1} = \mathbf{r}_i - \mathbf{r}_{i-1} \quad (2.8)$$

$$\mathbf{F}_{i,i-1} = \frac{\partial U_{i,i-1}}{\partial R_{i,i-1}} = -k\mathbf{R}_{i,i-1} \quad (2.9)$$

where  $U_{i,i-1}$  is given by Eq.(1.21). Thus, the diagonal components of the stress tensor, which are of most interest to this study, are given by

$$\sigma_{\gamma\gamma} = \frac{k}{V} \sum_{i=1}^N (r_i^{\gamma} - r_{i-1}^{\gamma})^2 \quad (2.10)$$

where  $\gamma = x, y, z$  and  $k$  is given by Eq.(1.20).

The first moment of stress for a Rouse chain with fixed end beads is given by

$$\langle \sigma_{\gamma\gamma} \rangle = \frac{\int \sigma_{\gamma\gamma} \exp\left(-\frac{U}{k_B T}\right) d^3\mathbf{r}_1 \dots d^3\mathbf{r}_{N-1}}{\int \exp\left(-\frac{U}{k_B T}\right) d^3\mathbf{r}_1 \dots d^3\mathbf{r}_{N-1}} \quad (2.11)$$

which averages over all bead positions, where  $d^3\mathbf{r}_i = dr_i^x dr_i^y dr_i^z$  and  $U$  is given by (1.22) to produce

$$\langle \sigma_{\gamma\gamma} \rangle = \frac{\int k \sum_{i=1}^N (r_i^{\gamma} - r_{i-1}^{\gamma})^2 \exp\left(-\frac{k}{2k_B T} \sum_{i=1}^N (\mathbf{r}_i - \mathbf{r}_{i-1})^2\right) d^3\mathbf{r}_1 \dots d^3\mathbf{r}_{N-1}}{\int \exp\left(-\frac{k}{2k_B T} \sum_{i=1}^N (\mathbf{r}_i - \mathbf{r}_{i-1})^2\right) d^3\mathbf{r}_1 \dots d^3\mathbf{r}_{N-1}} \quad (2.12)$$

To integrate this, the three-dimensional integral

$$\int_{-\infty}^{\infty} (\tilde{r}^\gamma)^p e^{-a\tilde{r}^2} d^3\tilde{\mathbf{r}} = \begin{cases} \frac{(2q-1)!!}{(2a)^q} \left(\frac{\pi}{a}\right)^{\frac{3}{2}} & ; \quad p = 2q \\ 0 & ; \quad p = 2q + 1 \end{cases} \quad (2.13)$$

is used, where  $p, q$  are integers and  $!!$  is the double factorial defined as

$$(2q-1)!! = \prod_{i=1}^q (2i-1) \quad (2.14)$$

In order to use Eq.(2.13) the exponential in Eq.(2.12) must be first transformed to have the form  $e^{-a\tilde{r}^2}$ . To do this the transformation  $\mathbf{r} \rightarrow \tilde{\mathbf{r}}$  is applied, such that

$$\begin{aligned} ar^2 - \mathbf{b} \cdot \mathbf{r} + c &= a \left( \mathbf{r} - \frac{\mathbf{b}}{2a} \right)^2 - \frac{b^2}{4a} + c \\ &= a\tilde{r}^2 - C \end{aligned} \quad (2.15)$$

where  $\tilde{\mathbf{r}} = \mathbf{r} - \frac{\mathbf{b}}{2a}$ . When Eq.(2.12) is integrated the result

$$\langle \sigma_{\gamma\gamma} \rangle = \frac{k_B T}{V} (N-1) + \frac{k}{V} \frac{(r_N^\gamma - r_0^\gamma)^2}{N} \quad (2.16)$$

is obtained. The first term is stress from thermal fluctuations, where each vibrating bead contributes  $\frac{k_B T}{V}$  in accordance with equipartition theorem, and the second term is due to the stretch between the fixed beads.

The second moment of stress can be found in a similar way

$$\langle (\sigma_{\gamma\gamma})^2 \rangle = \frac{\int (\sigma_{\gamma\gamma})^2 \exp\left(-\frac{U}{k_B T}\right) d^3\mathbf{r}_1 \dots d^3\mathbf{r}_{N-1}}{\int \exp\left(-\frac{U}{k_B T}\right) d^3\mathbf{r}_1 \dots d^3\mathbf{r}_{N-1}} \quad (2.17)$$

This integral is more complicated because the stress is squared and therefore generates cross

terms, but the results in

$$\langle (\sigma_{\gamma\gamma})^2 \rangle = \frac{k_B^2 T^2}{V^2} (N-1)(N+1) + \frac{2}{V^2} k_B T (N-1) k \frac{(r_N^\gamma - r_0^\gamma)^2}{N} + \frac{k^2}{V^2} \frac{(r_N^\gamma - r_0^\gamma)^4}{N^2} \quad (2.18)$$

### Stress relaxation function, $G_{\alpha\beta}(t)$

The stress relaxation function for the anisotropic system is given by

$$G_{\alpha\beta}(t) = \frac{V}{k_B T} \langle \sigma_{\alpha\beta}(t) \sigma_{\alpha\beta}(0) \rangle \quad (2.19)$$

where  $\alpha, \beta = x, y, z$  and  $V$  is the volume, which is defined in this study as

$$V = \frac{N-1}{c} \quad (2.20)$$

where  $c$  is the number of non-fixed beads per unit volume. Thus, the relaxation of a diagonal component of the stress tensor is given by

$$G_{\gamma\gamma}(t) = \frac{(N-1)}{c k_B T} \langle \sigma_{\gamma\gamma}(t) \sigma_{\gamma\gamma}(0) \rangle \quad (2.21)$$

For the limit  $t \rightarrow 0$ , Eq.(2.2) and Eq.(2.18) give

$$\begin{aligned} G_{\gamma\gamma}(0) &= \frac{(N-1)}{c k_B T} \langle \sigma_{\gamma\gamma}^2 \rangle \\ &= c k_B T (N+1) + 2ck \frac{(x_N - x_0)^2}{N} + \frac{ck^2}{k_B T (N-1)} \frac{(x_N - x_0)^4}{N^2} \end{aligned} \quad (2.22)$$

Similarly for the limit  $t \rightarrow \infty$ , Eq.(2.3) and Eq.(2.16) lead to

$$\begin{aligned} G_{\gamma\gamma}(\infty) &= \frac{(N-1)}{c k_B T} \langle \sigma_{\gamma\gamma} \rangle^2 \\ &= c k_B T (N-1) + 2ck \frac{(x_N - x_0)^2}{N} + \frac{ck^2}{k_B T (N-1)} \frac{(x_N - x_0)^4}{N^2} \end{aligned} \quad (2.23)$$

The amplitude of the stress relaxation function is therefore simply

$$G_{\gamma\gamma}(0) - G_{\gamma\gamma}(\infty) = 2ck_B T \quad (2.24)$$

### In simulations

During a simulation,  $\sigma_{\alpha\beta}$  is measured using Eq.(2.7) every time step and submitted to the correlator object, previously described, to calculate  $G_{\alpha\beta}(t)$ . The stress is also split into contributions from different objects in the system, such that, in the two-chain simulation (Fig.1.13c), the stress contribution from the lower chain can be analysed separately from the stress contribution from the upper chain. This allows the system to be investigated in greater detail.

### 2.1.3 Mean and variance of beads and bonds

The mean and variance of beads and bonds are vital in understanding the mechanisms of the system that result in the macroscopic properties, such as stress. When comparing with experimental data these properties can rarely be used, because most experiments only observe macroscopic properties. However, when comparing different simulations these properties are easily obtained and provide the best indication of where the simulations differ.

The mean vector position of beads,  $\langle \mathbf{r}_i \rangle$  and the mean vector of bonds  $\langle \mathbf{R}_i \rangle$ , where bond vectors are given by  $\mathbf{R}_{i,i-1} = \mathbf{r}_i - \mathbf{r}_{i-1}$ , are easily understood properties. The covariance tensor of the vector  $\mathbf{r}_i$  is given by

$$c_{\alpha\beta}(\mathbf{r}_i) = \left\langle \left( r_i^\alpha - \langle r_i^\alpha \rangle \right) \left( r_i^\beta - \langle r_i^\beta \rangle \right) \right\rangle \quad (2.25)$$

[30]. During this study, the variances of individual components of  $\mathbf{r}_i$  and  $\mathbf{R}_i$  are considered separately and are given by

$$\text{var}(r_i^\gamma) = c_{\gamma\gamma}(\mathbf{r}_i) \quad (2.26)$$

such that

$$\text{var}(r_i^\gamma) = \langle (r_i^\gamma - \langle r_i^\gamma \rangle)^2 \rangle = \langle (r_i^\gamma)^2 \rangle - \langle r_i^\gamma \rangle^2 \quad (2.27)$$

$$\text{var}(R_i^\gamma) = \langle (R_i^\gamma - \langle R_i^\gamma \rangle)^2 \rangle = \langle (R_i^\gamma)^2 \rangle - \langle R_i^\gamma \rangle^2 \quad (2.28)$$

### Relation to the average stress, $\langle \sigma_{\gamma\gamma} \rangle$

The average stress of the diagonal components is given by Eq.(2.10). This can be expressed in terms of bonds and expanded by Eq.(2.28) to produce

$$\begin{aligned} \langle \sigma_{\gamma\gamma} \rangle &= \frac{k}{V} \sum_{i=1}^N \langle (R_{i,i-1}^\gamma)^2 \rangle \\ &= \frac{k}{V} \sum_{i=1}^N \langle R_{i,i-1}^\gamma \rangle^2 + \frac{k}{V} \sum_{i=1}^N \text{var}(R_{i,i-1}^\gamma) \end{aligned} \quad (2.29)$$

Hence, by studying the mean positions and variances of the bonds, one is able to assess why the stress in one model is not equal to the stress in another.

#### 2.1.4 Mean squared displacement of beads, $g_{1,i}(t)$

The bead mean squared displacement function,

$$g_{1,i}(t) = \langle (\mathbf{r}_i(t) - \mathbf{r}_i(0))^2 \rangle \quad (2.30)$$

expresses the second moment of the distance the bead  $i$  moved during time  $t$  [4]. If we consider  $g_{1,i}(t)$  for  $t \rightarrow \infty$ , expand and apply Eq.(2.2) and Eq.(2.3),

$$\begin{aligned} g_{1,i}(\infty) &= \langle (\mathbf{r}(0))^2 \rangle + \langle (\mathbf{r}(\infty))^2 \rangle - 2 \langle \mathbf{r}(\infty) \cdot \mathbf{r}(0) \rangle \\ &= 2 \langle \mathbf{r}^2 \rangle - 2 \langle \mathbf{r} \rangle^2 \\ &= 2 \sum_{\gamma=x,y,z} c_{\gamma\gamma}(\mathbf{r}) \end{aligned} \quad (2.31)$$

the trace of the covariance is obtained. Thus, the static values of  $g_{1,i}(\infty)$  and  $g_{1,i}(0) = 0$  do not provide any new information; instead it is the dynamics between these limits which are of most interest, as is now demonstrated for the single Rouse chain.

### Single Rouse chain

In this study the displacement of the middle bead is used,

$$g_{1,\text{mid}}(t) \equiv g_{1,\frac{N}{2}}(t) \quad (2.32)$$

as plotted for a single Rouse chain with fixed end beads in Fig.2.3. It is an interesting plot for polymers because three regimes are observed. Initially, (a) the motion of the individual beads is observed. Because beads move as a random walk, it is observed that  $g_{1,i}(t) = \langle (\mathbf{r}_i(t) - \mathbf{r}_i(0))^2 \rangle \sim t$  in this regime. After  $\tau_0 = \tau_R/N^2$  (b), the beads feel the influence of the rest of the chain and  $g_{1,i}(t) \sim t^{0.5}$ . This motion is known as Rouse motion. It is this regime that is of most interest to this study as it is dependent on the interactions within the polymer and will differ for different models. To emphasise the detail  $g_{1,\text{mid}}(t)/t^{0.5}$  is also plotted, such that Rouse motion appears as a constant value. The final regime (c) occurs after  $\tau_R$  and represents the chain moving as a whole. If the chain did not have fixed beads, the motion would be proportional to  $t$ , as the entire polymer would move like a single coarse-grained blob. Since the two end beads of this Rouse chain are fixed, a constant value is observed instead, which indicates the point where the middle bead starts to realise that it is connected to the fixed bead points.

### In simulations

Similar to a correlation function, the mean squared displacement averages over two different points in time. As such, the correlator objects in our simulations are applicable to  $g_{1,\text{mid}}(t)$ , and at each time step, the position of the middle monomer is given to the mean squared displacement correlator object.

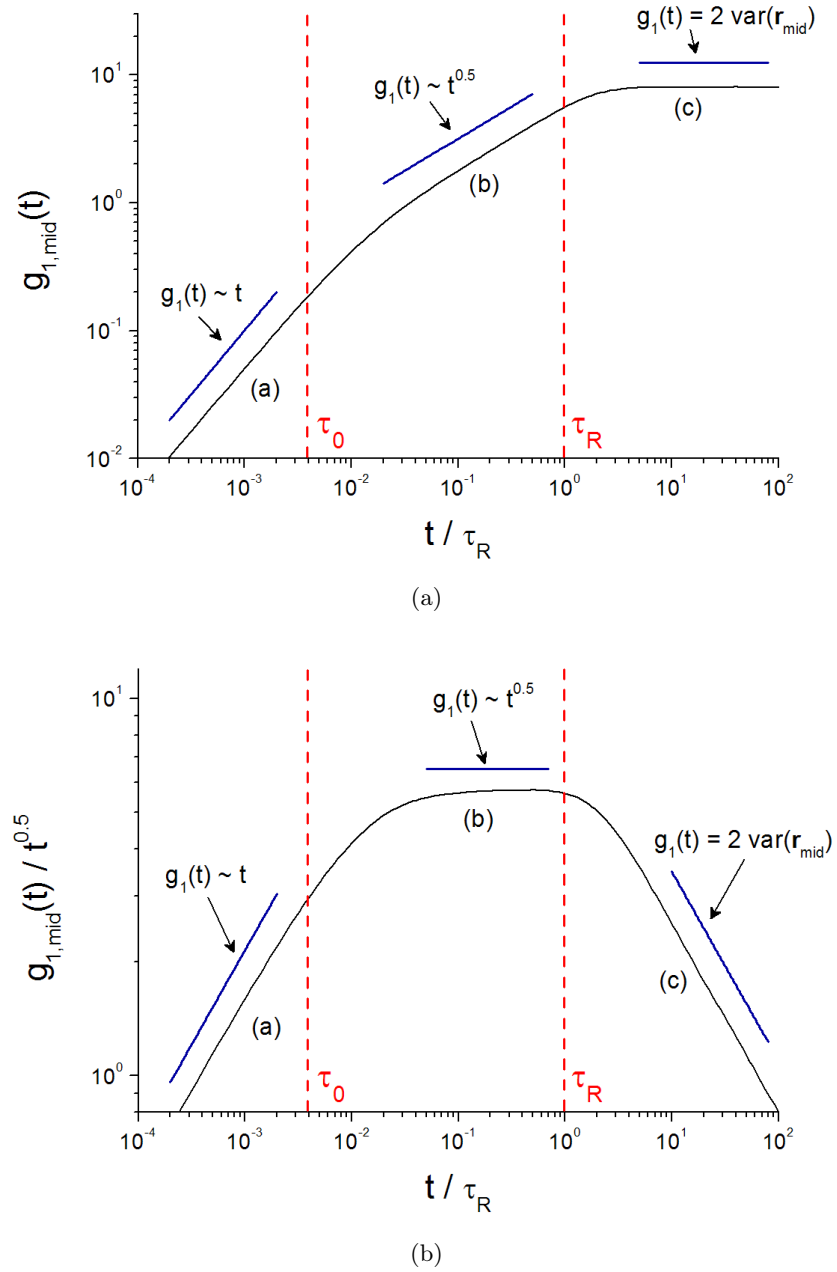


Figure 2.3: Mean squared displacement for the middle bead in a single Rouse chain with fixed ends. Single chain parameters are  $N = 16$  and  $(\mathbf{r}_N - \mathbf{r}_0) = (10, 0, 0)$ .

## 2.2 Generic polymer simulation (GPS)

Within the Reading Theoretical Polymer Physics Group, there were multiple research projects with each member running their own simulation program. These programs were developed separately, so taking components from one project to another was far more time consuming than necessary. Furthermore, because the simulations were written independently, the observable outputs were incompatible. This meant that, whilst the same properties were often produced by multiple programs, each program would name and normalise it differently, which made comparison between programs awkward. GPS was developed as a solution to these issues.

Developed by Likhtman, Palmer, Cao and Vorselaars, the main aim of GPS is to be a programming environment that allows common code to be reused by many projects. This should create a situation where a common set of observables can be activated for any project, independent of the particular model. Having this common set of observables should allow the comparison of data from different models directly. In GPS, creating new models is easier, since there is common code already available for the common models and equations of motion. This also reduces the amount of programming knowledge required by a new user starting their first model. Another design consideration, was that GPS must be fast to run. Many simulations take weeks or months, so even a 10% increase in efficiency is important. To create GPS the programming language C++ was used, because of its familiarity to most users, but also its speed at performing numerical calculations and the general availability of compilers on many systems.

### Overview

Fig.2.4 is an overview of the GPS program; boxes are classes and arrows show the direction that information flows. To prevent circular referencing, these arrows should only flow in a single direction. A key feature of the design is that the model unit does not know anything about the analysis unit and vice versa. This means that the model and analysis classes are independent and different models may use the same analysis objects, or the same model may be run with

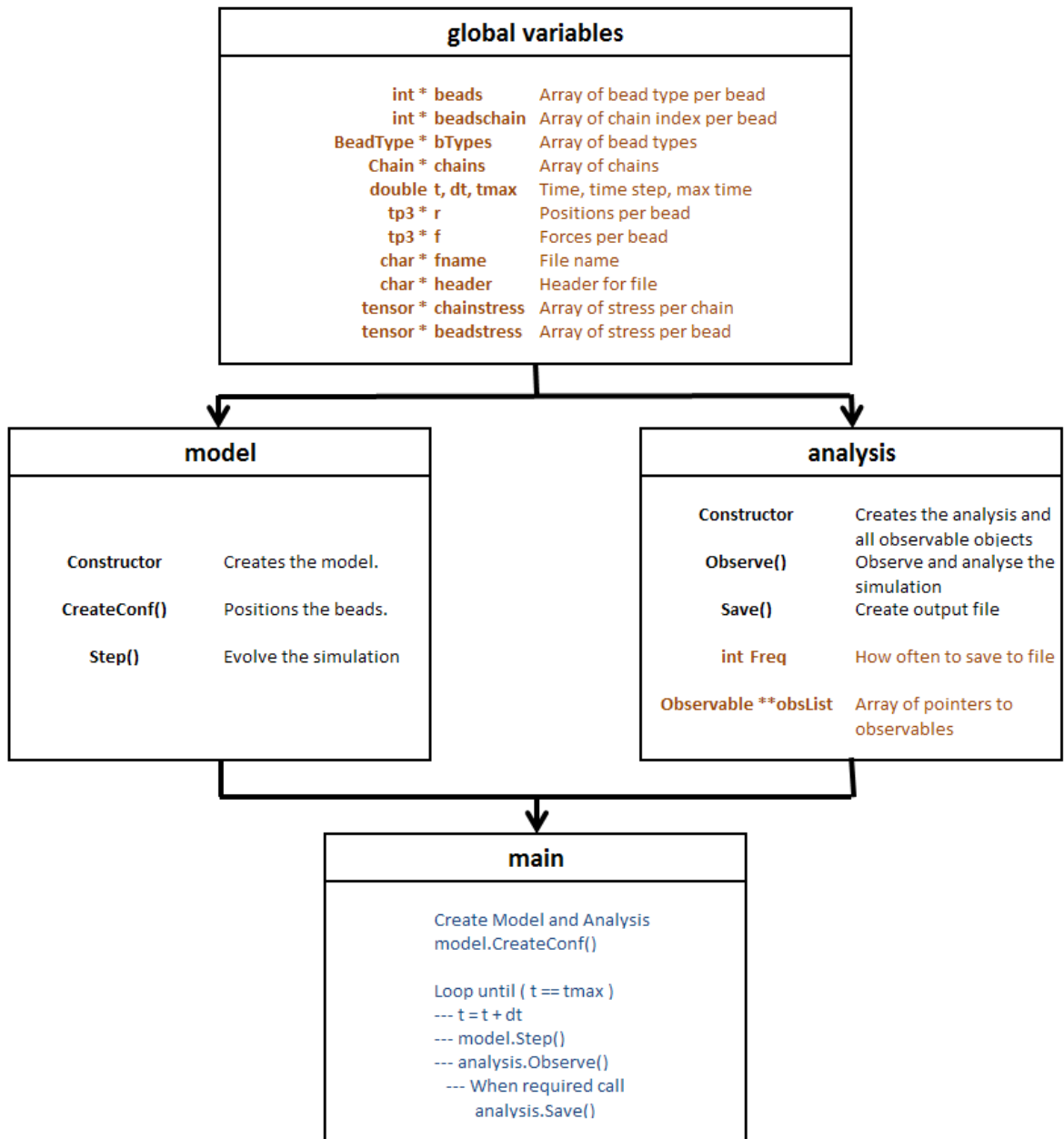


Figure 2.4: Overview of the GPS program design, including the public interfaces of each unit. Arrows indicate the flow of information.

different analysis objects.

The global variables unit acts as the method of communication between the model and the analysis classes. The variables stored here are common to many models, including the simulation clock with the time parameter,  $t$ . The most important variables stored here are the position of beads  $r$  and the latest force applied to them  $f$ . These values are stored as arrays of a vector type, known as  $tp3$ , which stores the x, y, z vector components, but also has an associated set of appropriate operators. Access to these arrays can be done in the form of a loop over all beads, but it is often the case that a loop over all beads in a single chain is preferred within a loop over all chains. For this purpose, the array *chains* exists. Each *chain* object stores the starting index and number of beads in that chain, which can be used to construct a loop over the beads. The array *beadschain* is the inverse of this array, where each bead index provides a chain index to which the bead belongs. In addition to this, there are bead types. Types allow polymers to be distinguished from each other, but also allow each type to have a different chain length and force potential parameters. The types have parameters that allow the looping of beads by type. The array of these types is *bTypes*, and the array *beads* is the inverse of this, linking each bead to a particular type. The stress values of the system are also stored within this class. The model calculates the stress values, which are then stored in the arrays *chainstress* and *beadstress* so that the analysis object may access the data.

The main unit of the program contains the code that controls the simulation loop. When the program is run, the system parameters are parsed from an input file, which are then used to populate global variables and construct the model and analysis objects. The input file is simple to construct and an example can be found in Fig.2.5. An additional method of supplying parameters is also available on the command line, as demonstrated in Fig.2.6, which is commonly used when calling batch jobs, where a user requires each job in the batch to have a different parameter value. Once the units have been constructed using the input parameters, the model's *CreateConf()* function is used to position all the beads in the system. After which *main()* starts the simulation loop. Each loop calls the *Step()* function of the model, which evolves the simulation by moving

```
;; model and analysis modules
mname=twochain
aname=twochain

;; two chain model parameters
H=5
d=10

;; number of types
;; number of beads per chain per type
;; number of chains per type
nBeadTypes=2
n0=16
n1=16
nc0=3
nc1=3

;; initial time
;; time step
t0=-2560
dt=0.0001
```

Figure 2.5: Example input file for GPS.

```
gps myModel.ini -dt 0.012 -xi 2
```

Figure 2.6: Example command line instruction for GPS.

the beads and calculating the stress in the system. Following this the *Observe()* function of the analysis object is called to analyse the new system state. The simulation analysis is saved to a file during the simulation, but infrequently, as it is an expensive operation. The frequency that the output file should be written is controlled by the parameter *freq* in the analysis class. The program will repeat this loop, increasing the simulation time, *t*, by the time step, *dt*, until the maximum time, *tmax*, is reached.

### 2.2.1 Model classes

The model classes in the program contain the code to control how the simulation evolves at each time step. Models are modular, which means that at run-time the user specifies which model to use. The design concept of the model classes that the models should inherit from each other, as demonstrated in Fig.2.7 where double lines indicate the inheritance of classes. A base model class contains the interface and common functions that all models inherit. Having a shared interface between all models is important, because it allows the main code to treat all models in exactly the same way, no matter how much they might differ internally. The three functions to be called by the main code are the constructor, *CreateConf()* and *Step()*. The constructor is a function called when an object is created; typically its role is to create any arrays required and to initialise all variables. *CreateConf()* stands for “create conformation” and is used to give the initial positions to beads before the main loop is started. *Step()* is the heart of the model and is called every time step. This function depends upon the model, but will generally calculate new bead positions and stress values. Normally in this process, forces are calculated to determine how the beads should move. Since calculating forces is a common function to most models, the *CalculateBondedForces()* and *CalculateNonBondedForces()* functions are defined in the base class, making them available to all models. The bonded forces function loops over just the bonded particles and the non-bonded forces function performs a loop over all pairs of beads. These functions take a force function as a parameter, so they can be applied to most situations by changing the force function without having to edit the base functions. The force functions are declared in the force and

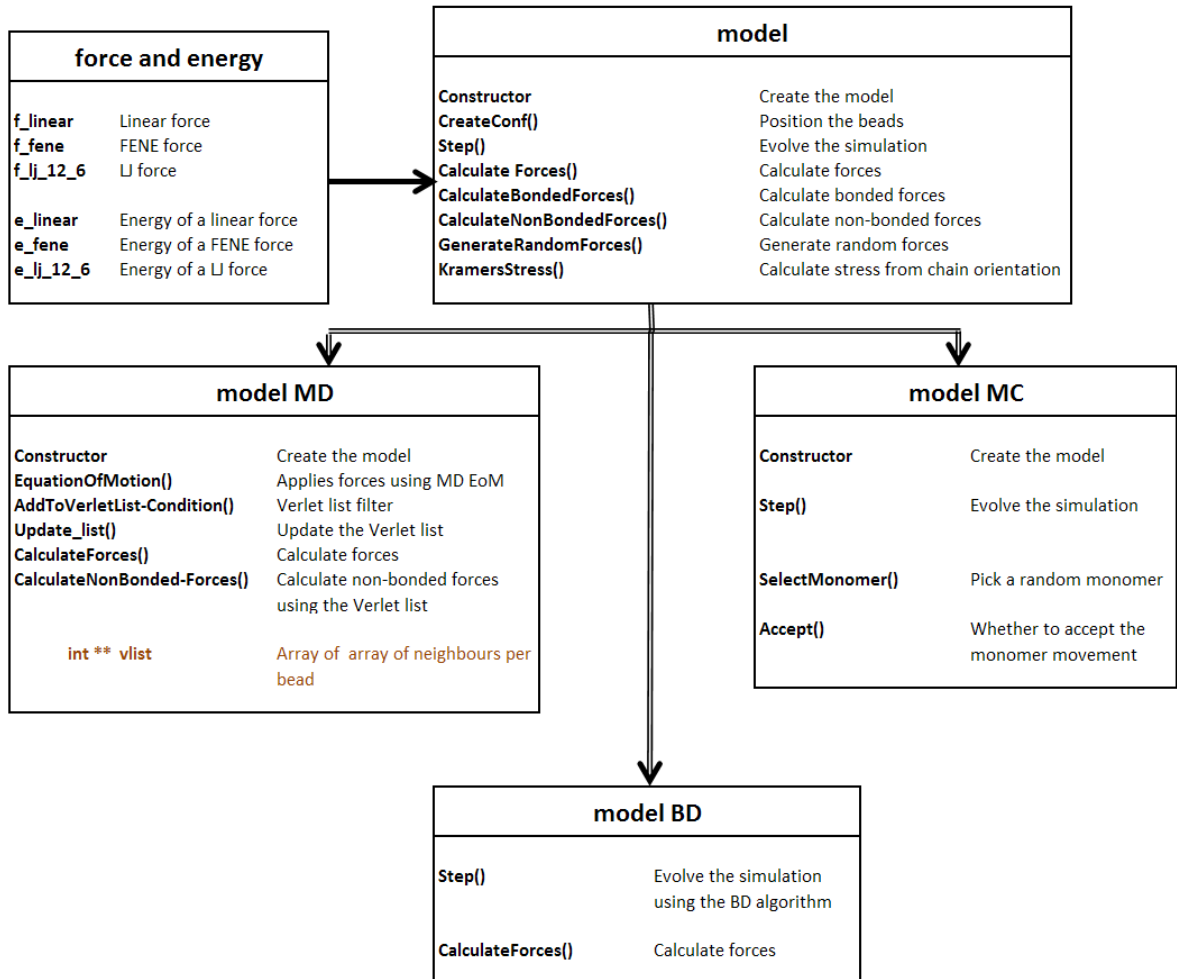


Figure 2.7: Diagram of the relationship between the files comprising the model unit. Single lines indicate one class being used by another and double lines indicate inheritance from another class.

energy unit, a sample of which can be seen in Fig.2.7. The function *CalculateForces()* collects any *CalculateBondedForces()* and *CalculateNonBondedForces()* function calls, such that a model may have more than one type of force in action. A new model that wants to change the default force calculations can override just the *CalculateForces()* function, so that it does not need to know how the more complex *CalculateBondedForces()* and *CalculateNonBondedForces()* work internally. An example is shown in Fig.2.8, where the *CalculateForces()* function has been overridden to apply a linear spring force along bonds and a Lennard-Jones force between all beads. These lines of code are simple but powerful.

The next tier of models inheriting from the base model are the different equations of motion (EoM) and were implemented by Likhtman and Cao. Three examples of these are shown in Fig.2.7: molecular dynamics, Monte Carlo and Brownian dynamics. These EoM base models define the crucial functions that the models in their family require. This involves creating code for the *Step()* function, which may be split into multiple model specific functions, allowing a user inheriting from the model to modify individual sub-functions without having to rewrite the entire *Step()*. As an example, the Monte Carlo EoM works by generating random movements and then testing to see whether this movement will be accepted by a Metropolis algorithm, as discussed in section 1.2.5. This family's *Step()* function has a sub-function *Accept()*, which is used to determine whether or not to keep this movement. *Accept()* calculates the change in energy and applies the Metropolis algorithm. Descendants of this family base model will typically override the *Accept()* function to change the potentials applied between beads, but will not touch the rest of the *Step()* function.

The most complicated EoM model is molecular dynamics (MD), as described in section 1.2.2. This model implements a Verlet list, which is a tool used to ignore negligible non-bonded interactions [5]. The code to construct and maintain this list is not something the user wants to repeat every time they make a new model, so instead the code for the Verlet list is in the family base model that other MD models inherit from. If a new model wants to change which beads are added to the Verlet list and are allowed to interact with each other, only the function

```

// Model inherits from the MD family base
class Model_rousemd : public Model_md
{
public:
    Model_rousemd(void){};
    virtual ~Model_rousemd(void){};

    // Position the initial position of all beads
    virtual void CreateConf(void);
    {
        for(int j=0;j<nc;j++) // loop over all chains
        {
            int si = chains[j].startIndex;
            r[si]=oo;
            for(int i=1;i<=chains[j].n;i++) // loop over all beads
            {
                // Position a random vector away from the previous bead
                r[si+i] = r[si+i-1] + gau_v(sqrt(1./3.));
            }
        }
    }

protected:

    virtual bool AddToVerletListCondition(int i,int j)
    {
        // Add to Verlet list only only beads in the same chain.
        // i<j so that we don't double count interactions.
        if ((i<j) && (beadchain[i]==beadchain[j]))
            return true;
        else
            return false;
    }

    virtual void CalculateForces(tp3 *r,tp3 *f)
    {
        // Reset the force for all beads
        for(int i=0;i<np;i++) _f[i]=oo;

        // Bonded beads interact by linear forces.
        int nParam; double param[maxParam];
        nParam = 1; param[0]=3.;
        CalculateBondedForces(_r,_f,&f_linear,nParam,param);

        // Lennard-Jones repulsion is applied between beads.
        nParam = 2; param[0] = 1; param[1] = 1;
        CalculateNonBondedForces(_r,_f,&f_lj_12_6,nParam,param);
    }
};

```

Figure 2.8: Example code for a model in GPS, inheriting from the MD family. The functions *CreateConf()*, *AddToVerletListCondition()* and *CalculateForces()* have been overridden from the MD model family base.

*AddToVerletListCondition()* needs to be overridden, not the entire Verlet code. An example is shown in Fig.2.8, where the function has been overridden to only allow beads within the same chain to interact.

To add a virtual object, such as a slip-spring, into a model, the user should create a slip-spring object within their own model and then override the *CalculateForces()* function to add code that applies forces produced by the slip-spring object. Furthermore, a more complex slip-spring model can inherit from this slip-spring model, allowing the slip-spring code to be reused. Reusing common code for models keeps them short and easier to read.

### 2.2.2 Observable classes

A simulation may have many observables as discussed in section 2.1. These observables are separate objects, which can be added to analysis objects as required. The analysis and observable classes were developed by Palmer and Likhtman. As depicted in Fig.2.9, there are a number of observable base classes, which define the interfaces and establishes the common functions and variables. These base classes create the complex storage locations and key functions that a user-created observable can inherit from. The base class function *init()* is used for initialising the observable, providing the crucial parameters such as its name, output frequency and normalisation; the function *calc()* uses the variables found in the global variables unit to perform a calculation and add the result to the appropriate data structure; and the output functions *output(i,\*s)* and *output2header(\*s)* are used to report the results back to analysis object.

An observable, such as mean squared displacement, inherits from the base class most suitable for storing its data. The *Observable* class can store a single value, whilst the *ObservableArray* class stores data in a multiple columned table; the *ObservableCorr* class is the most complicated, as it uses the correlator class described in section 2.1.1. Mean squared displacement uses the *ObservableCorr* class, as shown in Fig.2.10. The complicated correlator code is hidden and only a few lines of code are required. The first line of the class specifies the correlator type, in this case a diffusion correlator. The *init()* statement names the observable “g1mid”, specifies “nc”

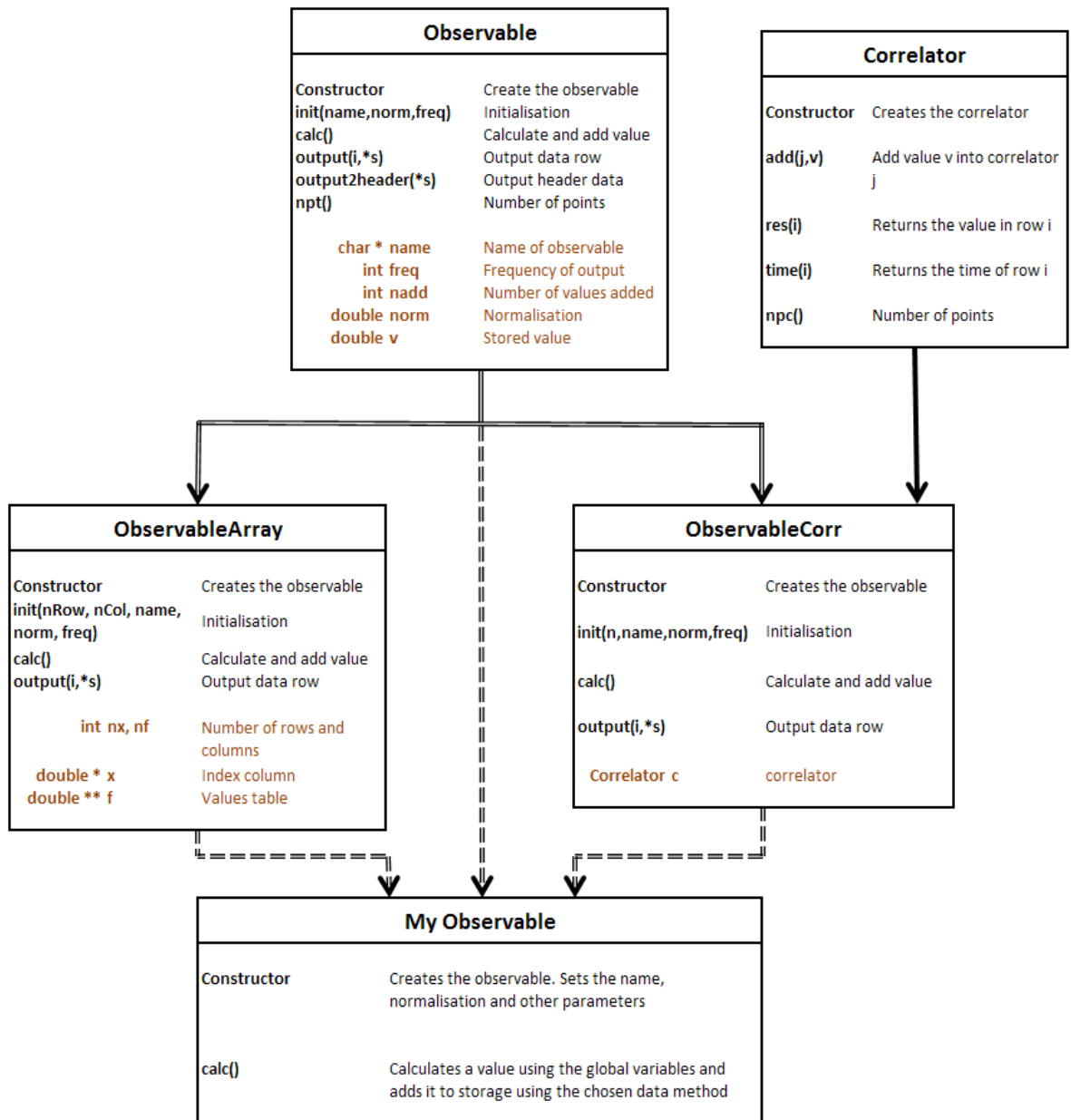


Figure 2.9: Diagram of the relationship between the objects comprising the observable unit. Single lines indicate one class being used by another and double lines indicate inheritance from another class. The dashed double lines indicate that *MyObservable* could inherit from any one of the observable objects.

```
// -- Mean squared displacement of the middle monomer --
// Correlator type : Diffusion correlator
class Observable_glmid: public ObservableCorr<CorrelatorArray<DiffusionCorrelatorT<tp3> > >
{
public:
Observable_glmid(int freqin=1, int typein=-1)
{
// Set the:
// - number of independant correlators to average
// - name of observable
// - normalisation
// - frequency of calc
init(nc,"glmid",1.,freqin);
}

void calc()
{
// For every chain
for(int j=0;j<nc;j++)
{
// Get the first monomer of chain j
int i = j*(n+1);
// Add to the correlator with index j the middle monomers position.
c.add(j,r[i+n/2]);
}
}
};
```

Figure 2.10: Example code of an observable in GPS. This example calculates the mean squared displacement of the middle monomer.

correlator objects (one for each chain), sets the normalisation to “1.”, and specifies the frequency that the observable is calculated. The *calc()* function obtains the position of the middle bead and then is added to the correlator by the function *c.add()*, which calls the complicated correlator calculation and storage.

The other important functions *output(i, \*s)* and *output2header(\*s)* are not normally overwritten by the user. The *output2header(\*s)* function is used for single value outputs such as found in the *Observable* class; while *output(i, \*s)* is used for passing data intended for row *i* to the analysis class. When the *Observable* or *ObservableArray* classes calculate a new value, it is added to the existing values and the integer *nadd* is increased. When outputting, the sum of values is divided by *nadd* in order to produce the average value. With the *ObservableCorr* class, multiple correlators are created. These are chosen dependent on the property; for mean squared displacement there is one correlator created per chain. When outputting, the results of the separate correlators are averaged together. All of these observables also use the *norm* parameter to normalise the results before output.

### 2.2.3 Analysis classes

The analysis class is used for collecting and managing the observables in the simulation. The class controls on which time steps observables perform their calculations and then collates the results of all the observables to create a single output file. A number of interface functions are available, including *AddObservable()*, *Observe()* and *Save()*, as depicted in Fig.2.11. The analysis class contains an array of pointers to observable objects, and the *AddObservable()* function is used to create and collect these observables. The *Observe()* function is called every time step by the main code and loops over all observables that have been added to the analysis object, calling the *Calc()* function for each. The *Save()* function saves the results of the observables to a single output file, by calling each of the observables in turn requesting their component of each row of the file. Having written the results to file, the analysis object will also write to the screen using the function *screen\_print()*, which shows the current simulation time and a

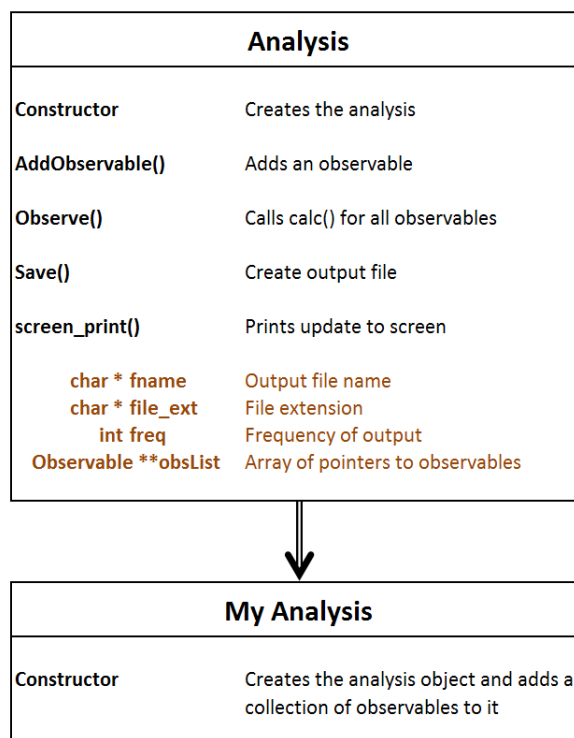


Figure 2.11: Diagram of the relationship between the objects comprising the analysis unit.

```
class Analysis_min : public Analysis
{
public:
    Analysis_min(void)
    {
        // Set the file extension
        sprintf(file_ext,"steady");

        // Add observables
        AddObservable( new ObservablePhi(10));
        AddObservable( new Observable_glend(10));
        AddObservable( new Observable_g3(10));
        AddObservable( new ObservableR2ij(10000));
        AddObservable( new Observable_bl(10000));
    }

    virtual ~Analysis_min(void){};
};
```

Figure 2.12: Example code of an analysis object in GPS. The *AddObservable()* function is used to add observables to the list of observables to be executed by the analysis object.

measure of the number of cycles per millisecond that the simulation is performing, so the user may judge the progress of the program. None of this analysis code is expected to be modified by the user. Instead, the user is expected to either use an existing analysis class, or create a new one that inherits from the base analysis class. This descendant analysis object defines a constructor, as demonstrated in Fig.2.12, which consists of a number of *AddObservable()* statements, each adding a new observable to the analysis. By doing this, the user can create a set of observables to apply to their project and can reuse this set of observables for multiple models.

#### 2.2.4 Comparison to another polymer simulation program

A commonly used polymer simulation package is LAMMPS, Large-scale Atomic/Molecular Massively Parallel Simulator [31, 32], which is also written in C++ and designed to be usable for many different simulations, but is restricted to MD models. To run LAMMPS, the user must provide an input file of parameters and second input file for the polymer initial positions and bonds. The first input file has an extensive number of options, allowing the MD simulation to be

configured massively. However, the number of options is so large that it is difficult to know what is available and how to apply it. In contrast, GPS has a simpler input file and provides the user with the tools to create their own model in the code that defines the specifics of the simulation. This allows a GPS user much greater flexibility than LAMMPS. The second input file of bead positions, has to be generated prior to a LAMMPS simulation, whilst the model classes within the GPS program specify how they will generate the bead positions at the start of the simulation. LAMMPS and GPS have been designed to fulfill different requirements. LAMMPS has a large number of existing models and options, using the MD equation of motion; while GPS is designed to run a wider range equations of motion and allows the user to create and modify models by adding new code to the program. LAMMPS does provide the possibility of adding new code, but incorporating our correlator objects into the code was not possible without major modifications, because correlators are an evolving observable rather than an instantaneous calculation that can be output. The design of GPS means that the user has the control and flexibility to add new models and observables that require extra variables and code to be added to the simulation, such as slip-springs and correlators.

### **2.2.5 Usage and future prospects of GPS**

GPS is currently in use by the majority of the members of the Theoretical Polymer Physics Group at the University of Reading. Development of the model and observable library has continued with the input of the whole group, which means that GPS has a large collection of pre-made content. Within this project, the modular characteristics of GPS were especially useful for studying the different two-chain models in section 3.1.7. By inheriting from existing models, new two-chain models were created with a minimal amount of new code. In addition, the analysis used by the models was shared by all of the two-chain and slip-spring models, which made the all results directly comparable.

## Chapter 3

# Main models

### 3.1 Two-chain simulation

In order to study the slip-spring model reproducing a single entanglement, an appropriate entanglement model is required, for which the two-chain model is used, as illustrated in Fig.3.1. This model consists of two Rouse chains with the ends fixed in space to represent cross-links in a polymer network, as discussed in section 1.4. The parameters of the model are: the number of bonds,  $N$ ; the horizontal separation of anchor beads in the same chain,  $D$ ; and the vertical separation of anchor beads in different chains,  $H$ . The beads are given initial positions as shown in Fig.3.1 and the simulation is run for  $10\tau_R$  before taking any observations, so that the two chains relax to equilibrium state. The equation of motion for the chains are given by Eq.(1.24) plus a rejection condition to prevent the chains from being able to cross.

#### 3.1.1 Entanglement by rejection

The rejection routine for detecting chain crossing is called every time a new bead position is generated and tests each bond that is affected by the move. Using Fig.3.2 for reference, the bond vector  $\mathbf{BA}$  becomes  $\mathbf{BC}$  as the bead at position  $\mathbf{A}$  moves to  $\mathbf{C}$  in the simulation time step, such that the bond must sweep across the area of the triangle  $\mathbf{ABC}$ . The rejection routine tests for a

crossing of this triangle by each bond  $\mathbf{LM}$  in the other chain. The routine begins by determining the point  $\mathbf{P}$  where vector  $\mathbf{LM}$  intersects the plane defined by the three points  $\mathbf{ABC}$ , as depicted in Fig.3.2a. Hence,

$$\mathbf{P} = \mathbf{L} + \alpha\mathbf{LM} \quad (3.1)$$

where  $\alpha$  is the fractional distance along the vector  $\mathbf{LM}$  where the plane intersects. This can be calculated as

$$\alpha = \frac{\mathbf{n} \cdot \mathbf{LB}}{\mathbf{n} \cdot \mathbf{LM}} \quad (3.2)$$

where  $\mathbf{n}$  is the normal to the plane  $\mathbf{ABC}$ . Only if  $0 < \alpha < 1$  does the vector  $\mathbf{LM}$  intersect the plane defined by  $\mathbf{ABC}$  and the routine moves onto the next stage. Otherwise, the bond cannot intersect the triangle and the routine moves onto the next bond. The next stage finds

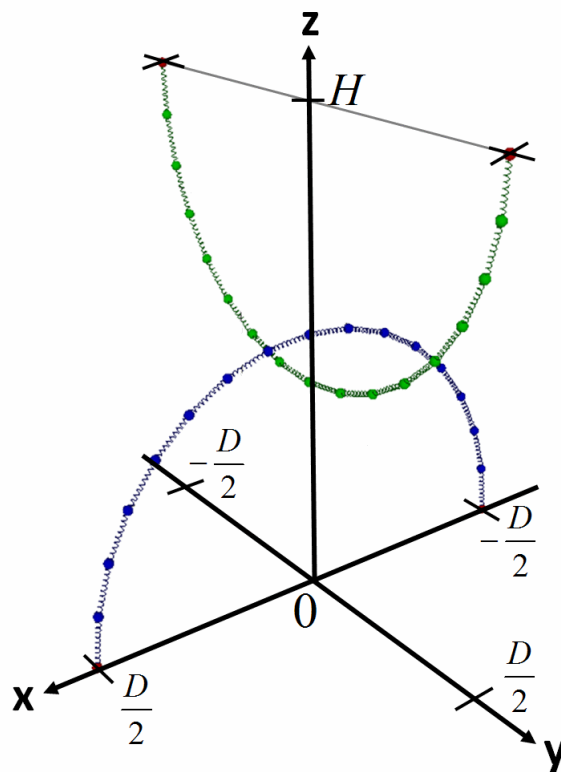


Figure 3.1: Diagram of the two-chain model

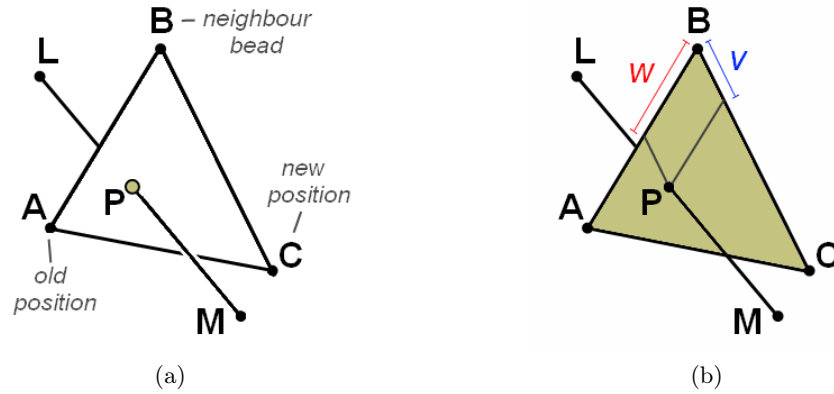


Figure 3.2: Diagrams of the rejection routine. Six points are labelled: old bead position, **A**; neighbouring bead position, **B**; new bead position, **C**; intersection bond vector, **LM**; intersection point, **P**.

the position of the intersection point **P**, expressed as a sum of the vectors **BA** and **BC** using the weightings  $w$  and  $v$ , such that

$$\mathbf{BP} = w\mathbf{BA} + v\mathbf{BC} \quad (3.3)$$

as demonstrated in Fig.3.2b. These weightings can be found as

$$w = \frac{(\mathbf{BP} \times \mathbf{BA})_z}{n_z} \quad (3.4)$$

$$v = \frac{(\mathbf{BP} \times \mathbf{BC})_z}{n_z} \quad (3.5)$$

If the conditions  $w > 0$ ,  $v > 0$  and  $w + v < 1$  are true, then the intersection point is within the triangle and chains must have crossed, therefore the move  $\mathbf{A} \rightarrow \mathbf{C}$  is rejected.

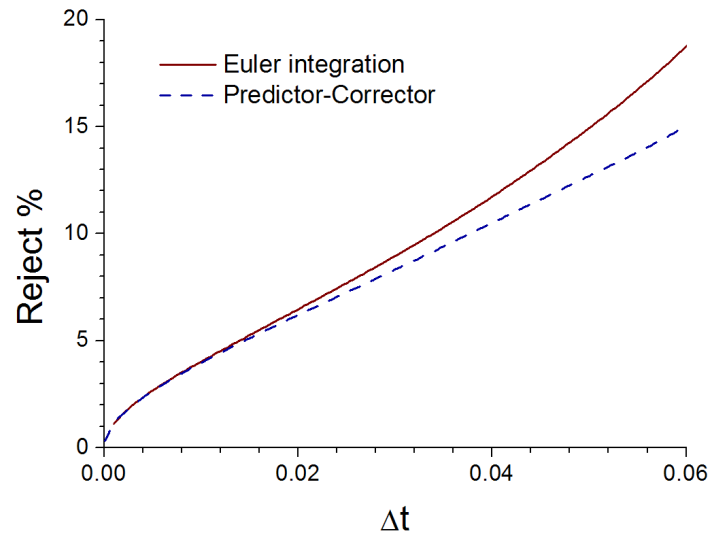
When a bead movement is rejected, a new bead movement is generated using the equation of motion with a different random Brownian force, which is also tested for intersections. This is repeated until a movement is generated that does not cause the chains to cross. When using this rejection method, the beads should be moved in a random order, which is generated by creating an array of all the bead indices and then shuffling it every time step. Whilst all beads are moved

within the same time step, the rejection algorithm can only be applied to one bead at a time and must respond to the new position of beads that have previously passed the rejection test. This means that the first bead to be moved in the chain may do so using the current positions of the other beads in the same chain, but the last bead in the chain will be using all the new positions. There is a bias introduced by always moving the beads in the same order. For example, if the upper chain moves away from the lower chain, the first bead in the lower chain is most able to take advantage of that new space available. Performing the bead movements in a random order, ensures that such artefacts are not present when averaged over many loops.

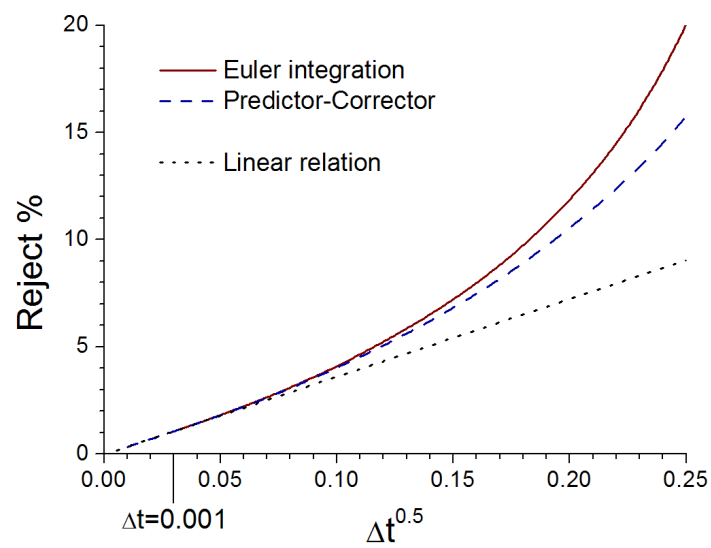
With a small time step,  $\Delta t$ , the Brownian motion dominates the equation of motion and the average distance moved by each bond is proportional to  $\sqrt{\Delta t}$ . The number of bead movement attempts rejected during the simulation should therefore also be proportional to  $\sqrt{\Delta t}$ . Plotted in Fig.3.3 is the percentage of bead movements that were rejected during two-chain simulations as a function of  $\Delta t$ , where it is indeed observed that this relationship is true for small  $\Delta t$ . However, it is observed that for  $\Delta t \gtrsim 0.001$  the relationship changes and the number of rejections increases due to other effects. In order to prevent these effects creating artefacts in the simulation, we will use  $\Delta t = 0.001$  in our simulations.

### 3.1.2 Predictor-corrector method

When a computer simulation computes the equations of motion, it cannot use an infinitely small time step. Instead an acceptable error tolerance is selected and a time step,  $\Delta t$ , is chosen to provide the appropriate degree of accuracy. Fig.3.4a demonstrates how the error in a property, such as the second moment of stress,  $\langle \sigma^2 \rangle$ , will decrease with smaller values  $\Delta t$  in a standard Brownian dynamics simulation. However, while a smaller  $\Delta t$  will reduce the error in the simulation, it also restricts the maximum simulation time that can be reached within the duration of the simulation, so there is a desire to increase the degree of accuracy of the simulation without having to reduce  $\Delta t$ . The simplest form of integration is the Euler method, where the equation



(a)



(b)

Figure 3.3: Percentage of bead movements that were rejected by the entanglement routine for simulation with time step,  $\Delta t$ . Model parameters are  $N = 16$ ,  $H = 10$  and  $D = 10$ . (Predictor corrector integration for the two-chain model is described in section 3.1.2).

of motion

$$\xi d\mathbf{r}_i = \frac{3k_B T}{b^2} (\mathbf{r}_{i+1} - 2\mathbf{r}_i + \mathbf{r}_{i-1}) dt + \sqrt{2k_B T \xi} d\mathbf{W}_i(t) \quad (3.6)$$

is discretised as

$$\xi (\mathbf{r}_i(t + \Delta t) - \mathbf{r}_i(t)) = \frac{3k_B T}{b^2} (\mathbf{r}_{i+1}(t) - 2\mathbf{r}_i(t) + \mathbf{r}_{i-1}(t)) \Delta t + \sqrt{2k_B T \xi \Delta t} \mathbf{g}_i(t) \quad (3.7)$$

where  $\mathbf{g}_i(t)$  is a random vector with each component obeying Gaussian distribution with zero average and variance 1. A better method of integration is the predictor-corrector method (PC), which takes the force at time  $t$

$$\mathbf{F}_i(t) = \frac{3k_B T}{b^2} (\mathbf{r}_{i+1}(t) - 2\mathbf{r}_i(t) + \mathbf{r}_{i-1}(t)) \quad (3.8)$$

to calculate a predicted position for time  $t + \Delta t$

$$\mathbf{r}_i^P(t + \Delta t) = \mathbf{r}_i(t) + \frac{1}{\xi} \mathbf{F}_i(t) \Delta t + \sqrt{2k_B T \xi \Delta t} \mathbf{g}_i(t) \quad (3.9)$$

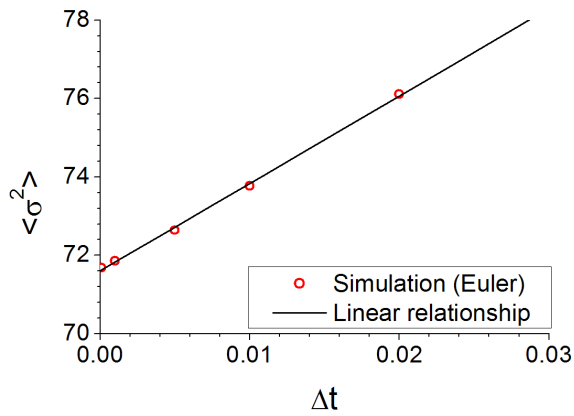
for all beads,  $i$ . Then using this, calculates the force at  $t + \Delta t$

$$\mathbf{F}_i(t + \Delta t) = \frac{3k_B T}{b^2} (\mathbf{r}_{i+1}^P(t + \Delta t) - 2\mathbf{r}_i^P(t + \Delta t) + \mathbf{r}_{i-1}^P(t + \Delta t)) \quad (3.10)$$

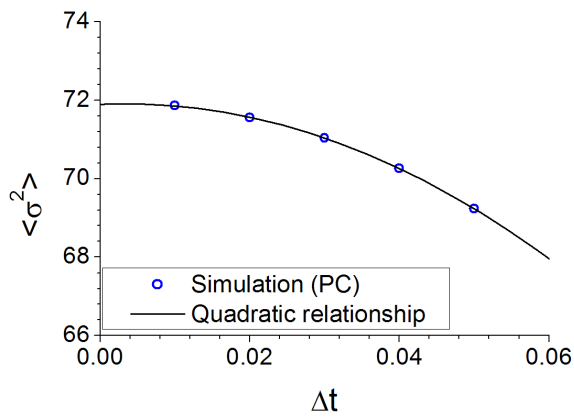
which is known as the corrector. By using the average force between  $t$  and  $t + \Delta t$ , the PC method is able to get a better estimate of  $\mathbf{r}_i(t + \Delta t)$ . This is calculated from  $\mathbf{r}_i^P(t + \Delta t)$  by

$$\mathbf{r}_i(t + \Delta t) = \mathbf{r}_i^P(t + \Delta t) + \frac{1}{2\xi} (\mathbf{F}_i(t + \Delta t) - \mathbf{F}_i(t)) \Delta t \quad (3.11)$$

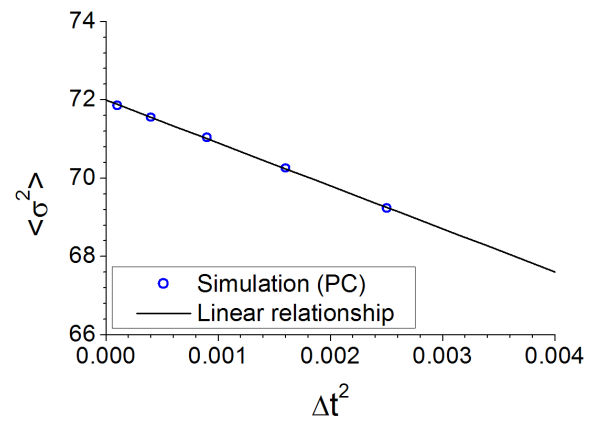
The error of a simulation using a PC method is demonstrated in Fig.3.4, where it is observed that the PC method has a quadratic convergence towards the true value, such that the error  $\epsilon \sim \Delta t^2$ .



(a) Euler integration



(b) Predictor-corrector integration



(c) Predictor-corrector integration

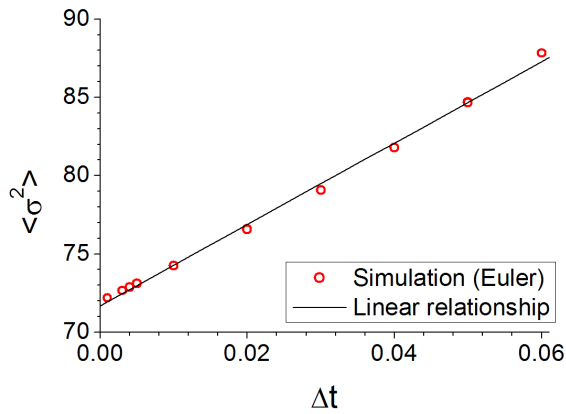
Figure 3.4: Convergence for a Brownian dynamics simulation

1. For each bead:
  - (a) Calculate bond forces based on old positions
  - (b) Generate random force
  - (c) Calculate predicted position
2. For each bead in a random order:
  - (a) Calculate bond forces based on predicted positions
  - (b) Calculate corrected positions
  - (c) If movement caused chains to cross:
    - i. Generate new random force
    - ii. Calculate new predicted position using original bond forces from 1(a) and new random force
    - iii. Go to 2(a)
3. Make observations
4. Go to 1

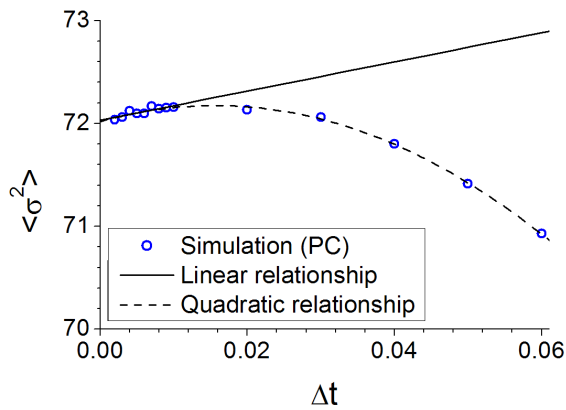
Figure 3.5: Algorithm of a predictor-corrector Brownian dynamics model with rejection routine

When using PC integration, the rejection method must be handled slightly differently than with the Euler integration. The pseudo-code algorithm for this simulation time step is written in Fig.3.5. First, predicted positions are calculated for every bead. Then, in a random order, the corrector force and new position is calculated for each bead, at which point the rejection algorithm is called to check the new position for topological violations. If the rejection algorithm rejects the new position, then the predicted position is recalculated with a new random force before the corrector force and new position are recalculated and retested. This is repeated until a new bead position is accepted. When the predicted position of a bead is changed to reflect a new random force, a problem occurs; any beads calculating their corrector force after this bead, use the new predicted position, but any beads calculated prior to this bead will have used the old predicted position. This introduces a small error in the PC method, but the recalculation of all previous beads would be less efficient than using Euler integration.

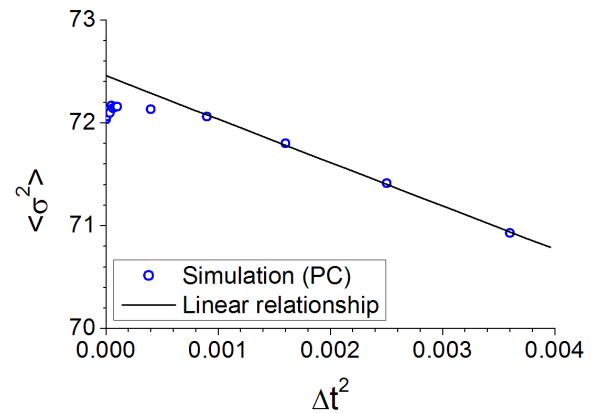
In Fig.3.6 the convergence of  $\langle \sigma^2 \rangle$  for the two-chain model is shown and it may be observed that the rejection algorithm has had a derogatory effect on the PC method. As before, there is a



(a) Euler integration



(b) Predictor-Corrector integration



(c) Predictor-Corrector integration

Figure 3.6: Convergence for the two-chain model

linear convergence with  $\Delta t$  for the Euler integration, but the PC method no longer demonstrates a convergence simply proportional to  $\Delta t^2$ , because the rejections produce a linear convergence, which dominates for small  $\Delta t$ . Despite this, the accuracy of the PC method remains much better than the Euler integration and is used within this study.

### 3.1.3 Mean and variance of bead positions

The properties of the two-chain model will now be examined with reference to two other models, as depicted in Fig.3.7. One is a single non-interacting chain with fixed ends, identical to the

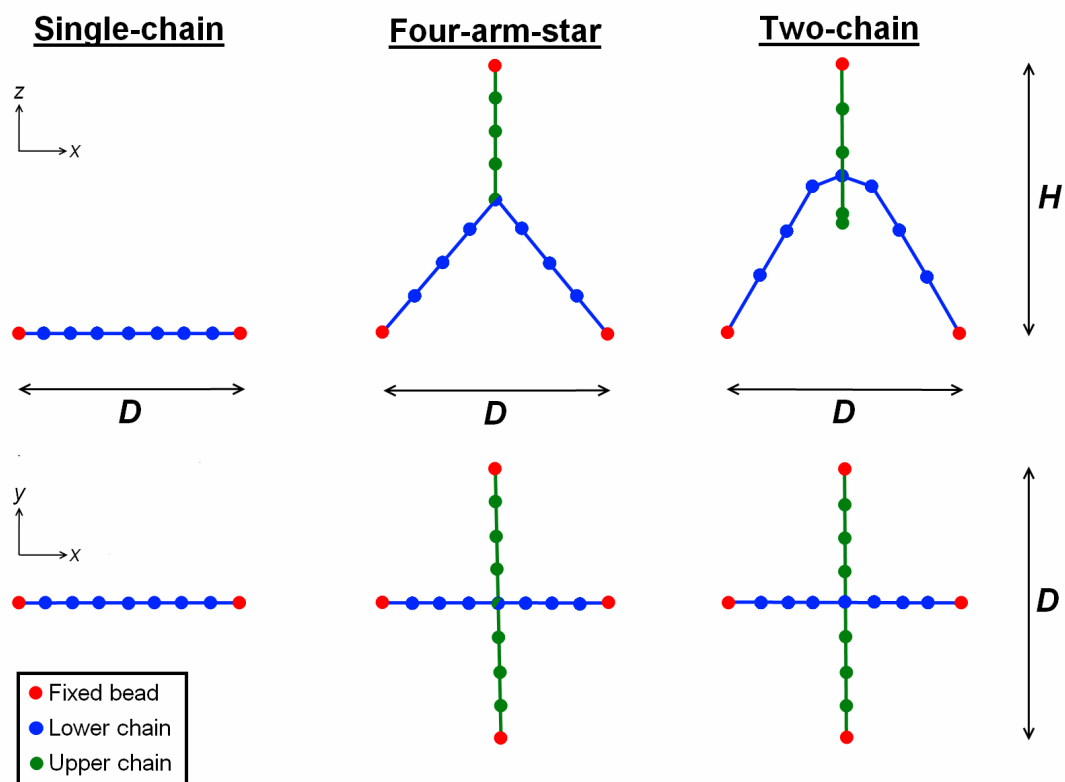


Figure 3.7: Diagram of the two-chain model and two other reference models: the single chain and the four-arm-star. Side views are depicted in the top row and overhead views are shown in the bottom row.

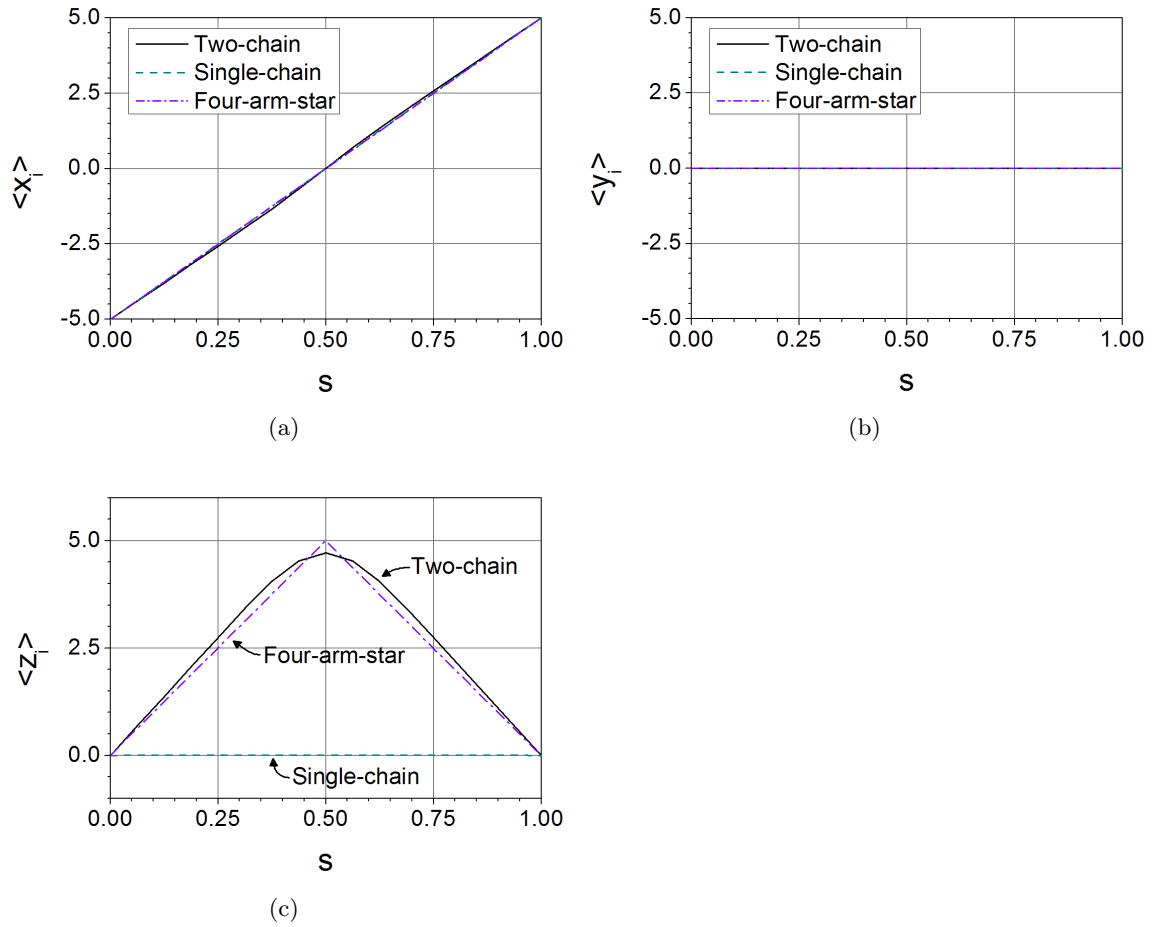


Figure 3.8: Mean position of each bead, where the bead number is expressed as a fraction along the chain,  $s = \frac{i}{N}$ . Parameters are  $N = 16$ ,  $H = 10$  and  $D = 10$ .

lower chain from the two-chain model with  $N$  bonds; the other is a four-arm-star polymer model where each arm has  $\frac{1}{2}N$  bonds. The four ends of the star are fixed in space at identical positions to those of the two-chain model. The middle bead of the four-arm-star model, can be regarded as a join between the middle bead of the lower chain and the middle bead of the upper chain.

The mean bead positions are plotted in Fig.3.8. In the single-chain model, the beads are only stretched in the x-direction and are equally distributed between the two fixed beads. In the four-arm-star polymer, the beads are also equally distributed, but have additional stretch in the z-direction towards the middle bead. The two-chain model displays important differences

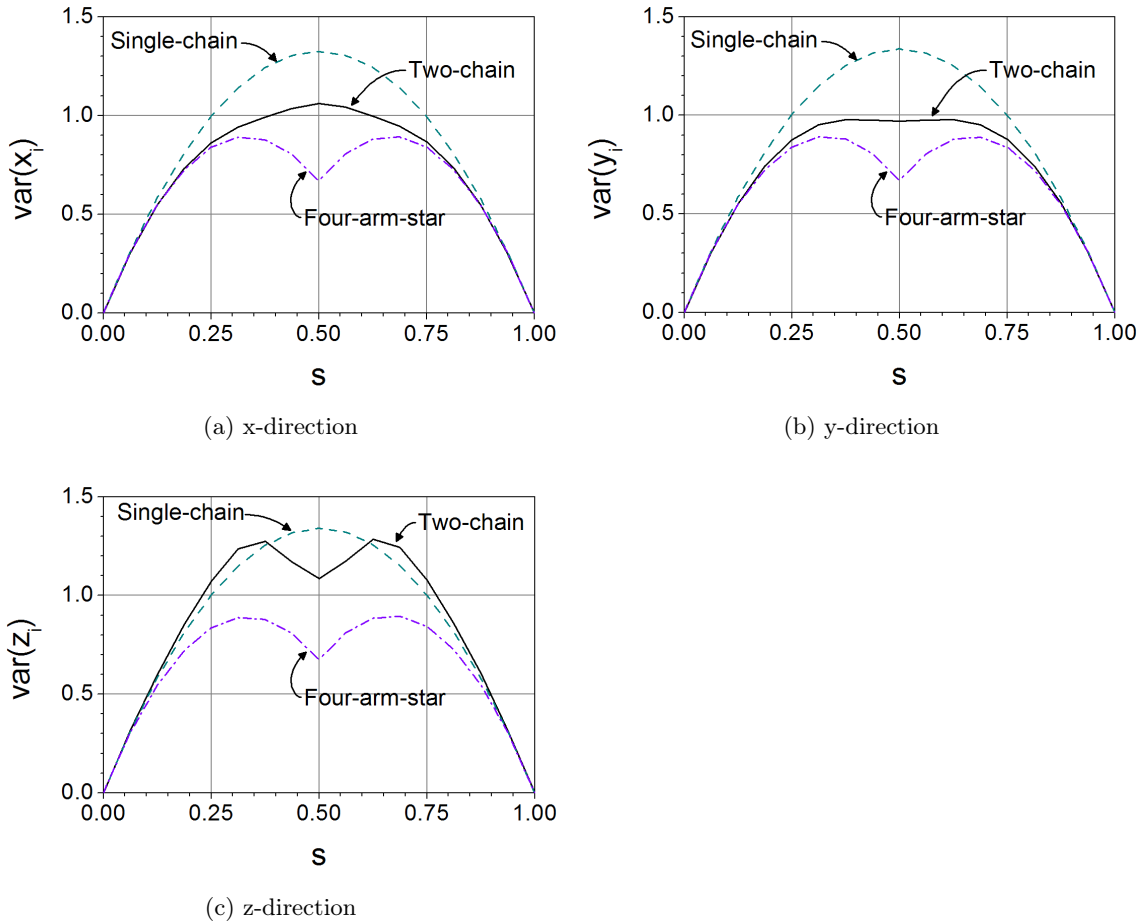


Figure 3.9: Variance of each bead position, where the bead number is expressed as a fraction along the chain,  $s = \frac{i}{N}$ . Parameters are  $N = 16$ ,  $H = 10$  and  $D = 10$ .

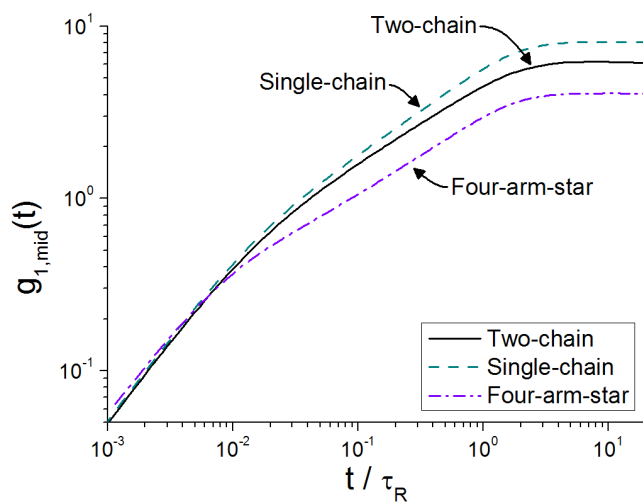
from these two models. In the x-direction, the beads are nearly equally distributed between the two fixed beads, but it is observed that the entanglement slightly repels beads, causing a greater separation of beads near the centre of the chain. The z-direction has a stretch similar to the four-armed-star model. However, the force stretching the chain in the z-direction is not only applied to the middle bead, but also neighbouring beads as the entanglement slides along the chain. Each of the beads directly affected by the entanglement form a dome shape in Fig.3.8c, while beads near the edge of the chain are not affected by the entanglement and form straight lines with an equal average spacing.

In Fig.3.9 it is observed that the variance of each bead is dependent on the neighbouring beads. The outer-most beads have fixed positions and as such have zero variance. The further beads get away from these fixed beads, the higher the variance becomes. In the single-chain model, the middle bead has the greatest variance, while in the four-arm-star model, the middle bead is bonded to four neighbours and has a lower variance for the middle bead, which leads to a lower variance in neighbouring beads.

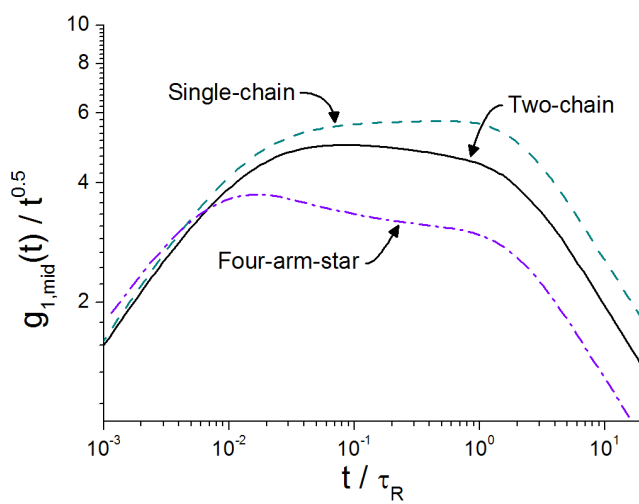
Due to the entanglement in the two-chain model, different Cartesian components are coupled and the variances are different. In the x-direction, the shape resembles the single-chain model, but the magnitude of the variance is lower, similar to the four-arm-star model. The same is observed in the y-direction. The entanglement restricts the motion of beads, by limiting the distance beads may move in certain directions, but the entanglement slides easily along the chain in these directions sharing the restriction with a range of beads. In the z-direction, the presence of the entanglement has a restrictive effect on the middle bead much like that observed in the four-arm-star model and the slide of the entanglement does not act in a way that minimises the energy of the chain in this direction, as it did in the x- and y-directions. However, it is observed that the amplitude for some beads is greater than that of the single-chain model. Since the single chain model has no restrictions at the centre of the chain, the variance in the two-chain model must have been increased by the entanglement. This can be explained by the entanglement sliding along the chain. When the entanglement is acting on one section of the chain, the beads experience a force in the z-direction. When the entanglement slides away that force is removed and the beads relax to having an equal bead spacing between neighbouring sections. It is this pull and release by the entanglement that results in a variance higher than even the single-chain model.

#### 3.1.4 Mean squared displacement, $g_{1,mid}(t)$

The mean squared displacement of the middle bead,  $g_{1,mid}(t)$ , plotted in Fig.3.10, describes how far the middle bead moves on average over a time,  $t$ . As discussed in section 2.1.4, the value of



(a)



(b)

Figure 3.10: Mean squared displacement of the middle bead  $g_{1,mid}(t)$ . Parameters are  $N = 16$ ,  $H = 10$  and  $D = 10$ .

$g_{1,mid}(\infty)$  reproduces the results for variance, and therefore the single-chain model has a higher value than the four-arm-star. It is observed that the middle bead in the four-arm-star model moves slower than the middle bead in the single-chain model, because in the four-arm-star model it is bonded to twice as many beads; the two-chain model is intermediate to these two cases.

### 3.1.5 Stress relaxation functions

The simulation results for the diagonal components of the stress relaxation function are plotted in Fig.3.11, along with the function  $(G_{\gamma\gamma}(t) - G_{\gamma\gamma}(\infty))$ . This function provides an extra insight into the dynamics of the system especially when  $\langle\sigma\rangle$  is different for each model. At  $t = 0$ , it is observed that  $(G_{xx}(0) - G_{xx}(\infty))$  and  $(G_{yy}(0) - G_{yy}(\infty))$  are the same for all three models, but relax at a different rates. It is observed in Fig.3.11b and Fig.3.11d that the four-arm-star model demonstrates faster relaxation than the single-chain model. In the single-chain model, the slowest relaxation time is  $\tau_S \sim N^2$  (Eq.(1.30)). In the four-arm-star model the arms have  $\frac{1}{2}N$  beads each and therefore a relaxation time of  $\frac{1}{4}\tau_S$ , while the connecting bead at the centre of the star is bonded to four beads and therefore has a relaxation time of  $\frac{1}{2}\tau_S$ , which produces the relaxation time observed that is faster than the single-chain model. In the two-chain model,  $G_{xx}(t)$  acts initially as a four-armed-star model, but later demonstrates a relaxation speed similar to the single-chain, as the chain may slide past the entanglement point.  $G_{yy}(t)$  acts more like the four-arm-star model at all times, because the other chain in the entanglement hooks around the chain.

In Fig.3.11f it is found that the two-chain and the four-arm-star models have a larger value of  $(G_{zz}(t) - G_{zz}(\infty))$  at  $t = 0$ , than the single-chain model, and take noticeably longer to relax. This is due to a second, slower relaxation that can also be observed in Fig.3.11e. The source of this second relaxation is explained during the analytical calculations for the cross-correlations below.

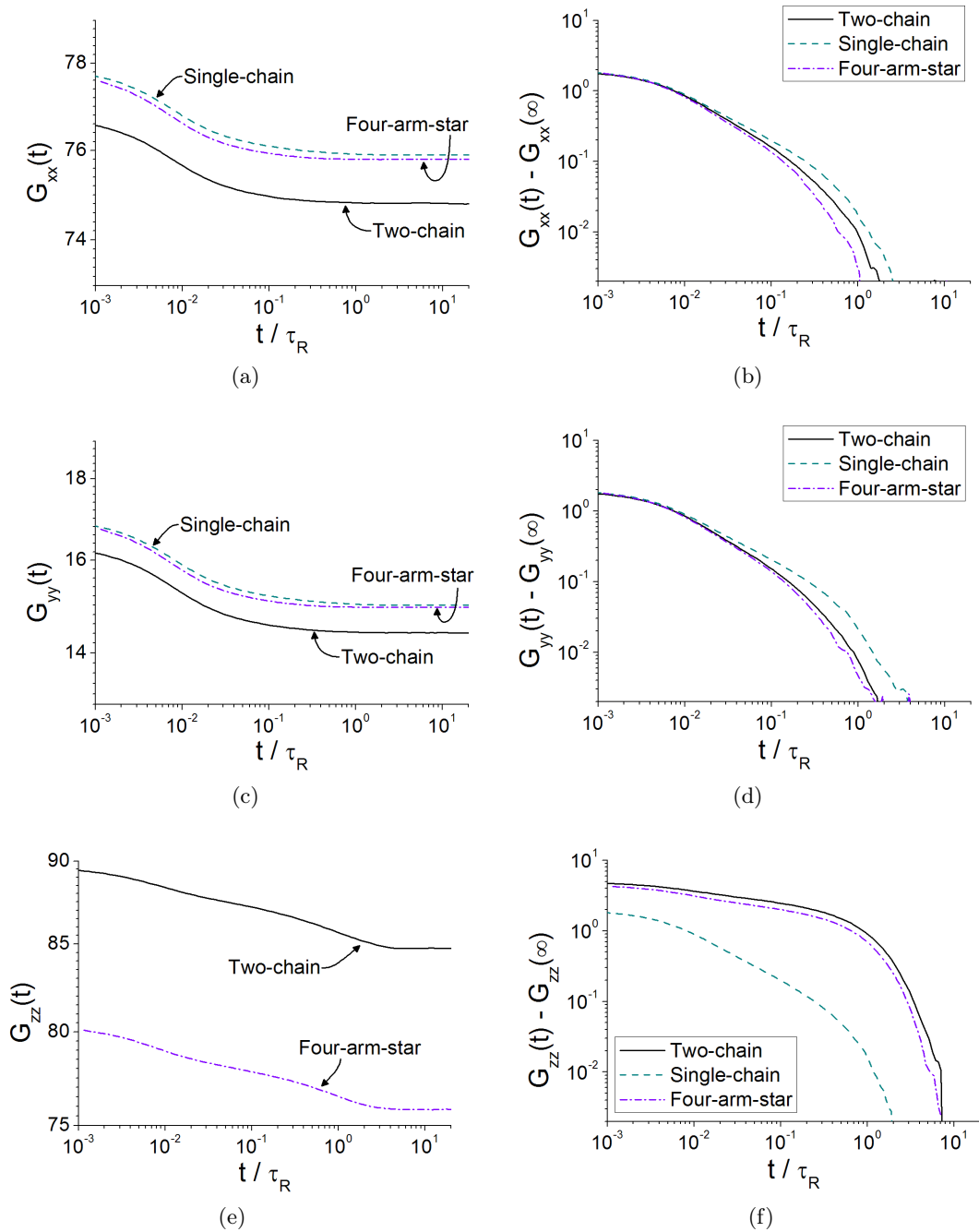


Figure 3.11: Diagonal components of the stress relaxation tensor. Parameters are  $N = 16$ ,  $H = 10$  and  $D = 10$ .

### 3.1.6 Stress cross-correlation functions

The total stress of the system is a sum of the lower half of the system ( $A$ ) and the upper half of the system ( $B$ ), such that

$$\sigma^T(t) = \sigma^A(t) + \sigma^B(t) \quad (3.12)$$

In Fig.3.7 the  $N$  bonds that constitute the lower half of the system are coloured blue and the upper half green. The correlation function of the total stress is

$$\begin{aligned} G^T(t) &= \langle (\sigma^A(t) + \sigma^B(t)) (\sigma^A(0) + \sigma^B(0)) \rangle \\ &= \langle \sigma^A(t) \sigma^A(0) \rangle + 2 \langle \sigma^A(t) \sigma^B(0) \rangle + \langle \sigma^B(t) \sigma^B(0) \rangle \\ &= G^A(t) + 2G^X(t) + G^B(t) \end{aligned} \quad (3.13)$$

where  $G^X(t) = \langle \sigma^A(t) \sigma^B(0) \rangle = \langle \sigma^B(t) \sigma^A(0) \rangle$  is the cross-correlation function between the lower and upper chains. The cross-correlation describes how the value of stress in one chain is affected by the stress in the other chain at a time  $t$  previously. From this point on, the correlation of a function with itself shall be known as the auto-correlation, where  $G^A(t)$  is the auto-correlation of  $\sigma^A(t)$  and  $G^T(t)$  is the auto-correlation of  $\sigma^T(t)$ .

In Fig.3.12, the auto-correlation functions of the lower chain and the total stress are considered. For the four-armed-star model,  $G_{\gamma\gamma}^T(t)$  demonstrates an equal relaxation time for all components, which is equal to that of  $G_{xx}^A(t)$  and  $G_{yy}^A(t)$ , but a slower relaxation time is observed for  $G_{zz}^A(t)$ . A similar effect is observed with the two-chain model, although the coupling of components means that  $G_{\gamma\gamma}^T(t)$  and  $G_{\gamma\gamma}^A(t)$  are not exactly equal for  $\gamma = x, y, z$ . It is curious that  $G_{zz}^T(t)$  relaxes faster than  $G_{zz}^A(t)$ . Eq.(3.13) implies that the relaxation of  $G_{zz}^X(t)$  must cancel out with the relaxation in  $G_{zz}^A(t)$  for this to happen. To demonstrate that this is the case Fig.3.13 plots  $\frac{1}{4}G_{zz}^T(t)$ ,  $G_{zz}^A(t) = G_{zz}^B(t)$  and  $G_{zz}^X(t)$ , where it is observed that the slowest relaxation of  $G_{zz}^A(t)$  and  $G_{zz}^X(t)$  are equal and opposite.

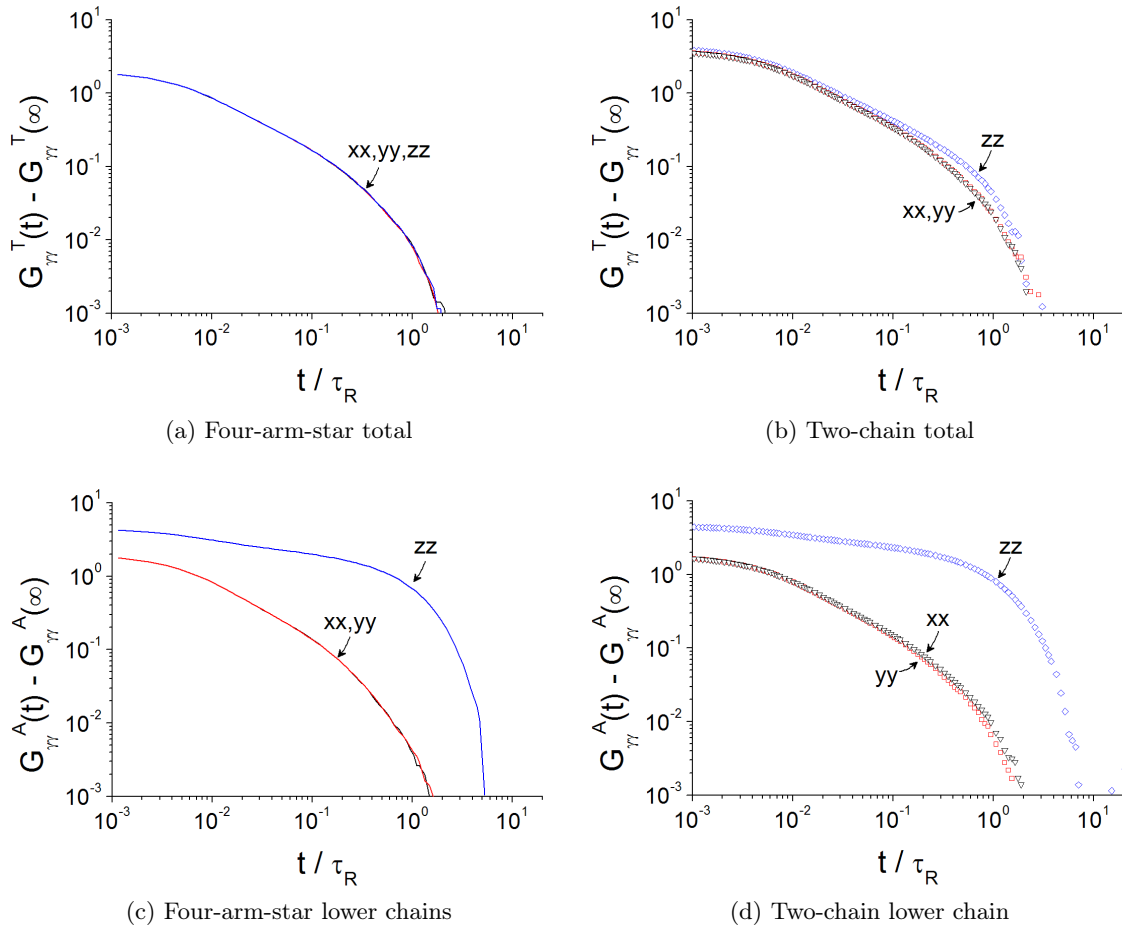
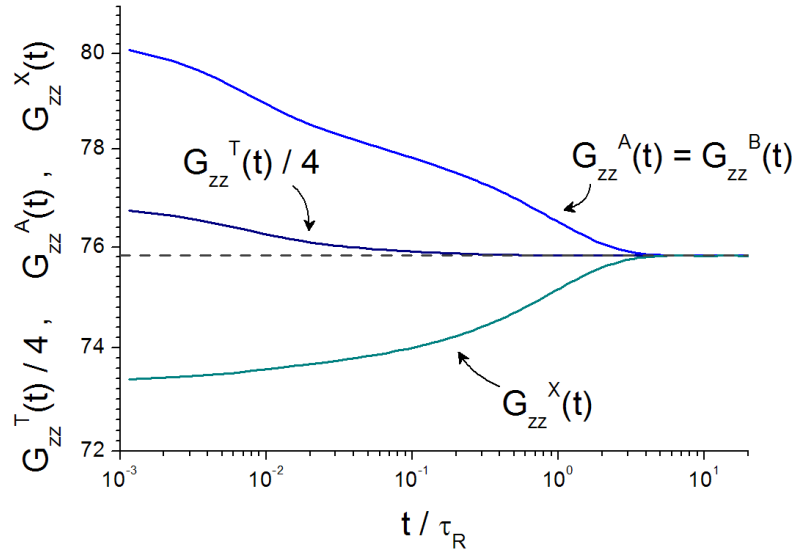
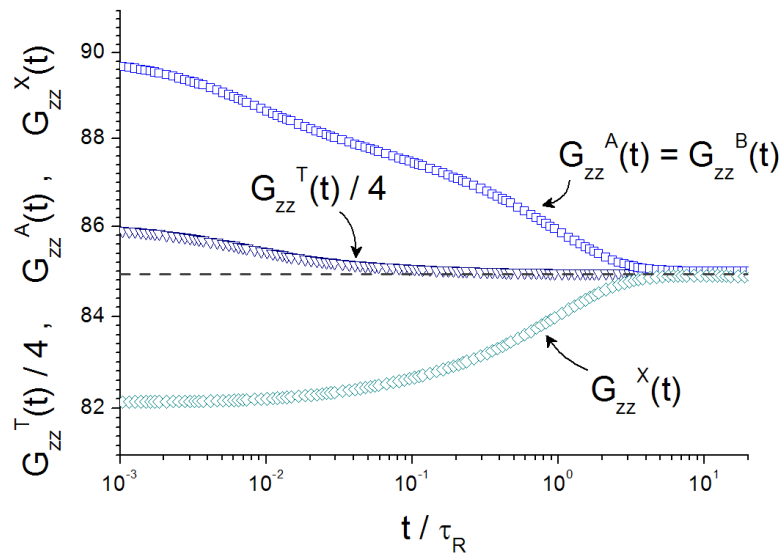


Figure 3.12: Auto-correlation of the four-arm-star and the two-chain models, for the lower half of the system,  $G_{\gamma\gamma}^A(t)$ , and the sum of all components,  $G_{\gamma\gamma}^T(t)$ . Parameters are  $N = 16$ ,  $H = 10$ ,  $D = 10$ .



(a) Four-arm-star



(b) Two-chain

Figure 3.13: Exploration of the function  $G_{zz}^T(t) = 2G_{zz}^A(t) + 2G_{zz}^X(t)$ , where the final relaxation of  $G_{zz}^A(t)$  cancels out with the relaxation of  $G_{zz}^X(t)$ . Parameters are  $N = 16$ ,  $H = 10$ ,  $D = 10$ .

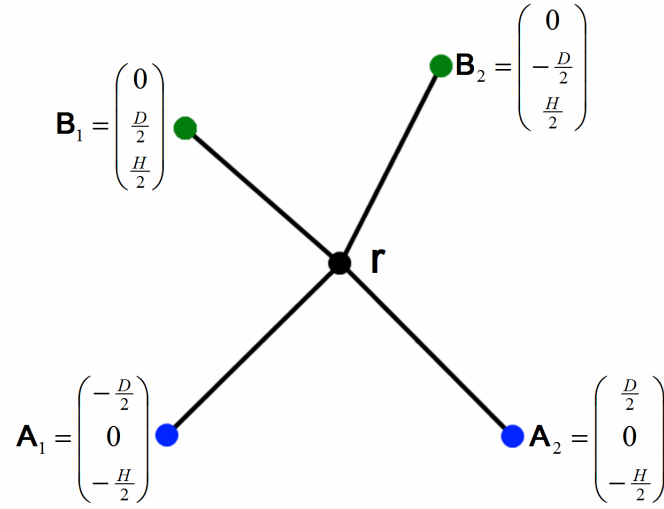


Figure 3.14: Diagram of the single bead four-arm-star model

### Analytical calculations

To illustrate how this occurs, a simplified four-arm-star model is considered analytically, where each arm only has only a single bond with spring-constant  $k$ . There is a single moving bead in this system, which has position vector  $\mathbf{r}$ , as depicted in Fig.3.14. The equation of motion for this bead is given by

$$d\mathbf{r} = \frac{k}{\xi} (\mathbf{A}_1 + \mathbf{A}_2 + \mathbf{B}_1 + \mathbf{B}_2 - 4\mathbf{r}) dt + \sqrt{\frac{2k_B T}{\xi}} d\mathbf{W}(t)$$

This is an Ornstein-Uhlenbeck process,

$$d\mathbf{r} = -\frac{1}{\tau} \mathbf{r} dt + \sqrt{2d_c} d\mathbf{W}(t) \quad (3.14)$$

where the diffusion constant is  $d_c = \frac{k_B T}{\xi}$  and the characteristic time is  $\tau = \frac{\xi}{4k}$ . As an Ornstein-Uhlenbeck process, the first two moments of the bead position at a time,  $t$ , after a deformation are known to be

$$\langle \mathbf{r}(t) \rangle = \langle \mathbf{r} \rangle e^{-\frac{t}{\tau}} \quad (3.15)$$

and

$$\langle \mathbf{r}(t) \cdot \mathbf{r}(s) \rangle = \text{var}(\mathbf{r}_0) e^{-\frac{t+s}{\tau}} + d_c \tau \left( e^{\frac{s-t}{\tau}} - e^{-\frac{s+t}{\tau}} \right) \quad (3.16)$$

The lower half of this system is defined as bonds  $\mathbf{A}_1$  to  $\mathbf{r}$  and  $\mathbf{r}$  to  $\mathbf{A}_2$ , and the upper half as the bonds  $\mathbf{B}_1$  to  $\mathbf{r}$  and  $\mathbf{r}$  to  $\mathbf{B}_2$ . The stresses of these are given by

$$\sigma_{\gamma\gamma}^A(t) = k (r^\gamma(t) - A_1^\gamma)^2 + k (r^\gamma(t) - A_2^\gamma)^2 \quad (3.17)$$

$$\sigma_{\gamma\gamma}^B(t) = k (r^\gamma(t) - B_1^\gamma)^2 + k (r^\gamma(t) - B_2^\gamma)^2 \quad (3.18)$$

from which it is possible to find the auto- and cross-correlations of the system as a function of time,  $t$ . The details can be found in appendix A, while just the results are presented here.

The xx-components of the stress correlation functions are given by

$$G_{xx}^A(t) = \frac{1}{2} \frac{k_B T}{V} e^{-\frac{2t}{\tau}} + \frac{1}{4} \frac{k_B T}{V} + \frac{1}{2} \frac{k}{V} D^2 + \frac{1}{4} \frac{k^2}{k_B T V} D^4 \quad (3.19)$$

$$G_{xx}^B(t) = \frac{1}{2} \frac{k_B T}{V} e^{-\frac{2t}{\tau}} + \frac{1}{4} \frac{k_B T}{V} \quad (3.20)$$

$$G_{xx}^X(t) = \frac{1}{2} \frac{k_B T}{V} e^{-\frac{2t}{\tau}} + \frac{1}{4} \frac{k_B T}{V} + \frac{1}{4} \frac{k}{V} D^2 \quad (3.21)$$

$$G_{xx}^T(t) = 2 \frac{k_B T}{V} e^{-\frac{2t}{\tau}} + \frac{k_B T}{V} + \frac{k}{V} D^2 + \frac{1}{4} \frac{k^2}{k_B T V} D^4 \quad (3.22)$$

Only the first terms of these correlation functions depends on  $t$  and have the form  $c_1 \exp(-\frac{t}{\tau'})$ , where  $\tau'$  is the relaxation time. In terms of the Ornstein-Uhlenbeck characteristic time,  $\tau$ , this relaxation time is  $\tau'_{xx} = \frac{1}{2}\tau$ . The zz-components of the stress correlation functions are

$$G_{zz}^A(t) = \frac{1}{2} \frac{k_B T}{V} e^{-\frac{2t}{\tau}} + \frac{k}{V} H^2 e^{-\frac{t}{\tau}} + \frac{1}{4} \frac{k_B T}{V} + \frac{1}{2} \frac{k}{V} H^2 + \frac{1}{4} \frac{k^2}{k_B T V} H^4 \quad (3.23)$$

$$G_{zz}^B(t) = G_{zz}^A(t) \quad (3.24)$$

$$G_{zz}^X(t) = \frac{1}{2} \frac{k_B T}{V} e^{-\frac{2t}{\tau}} - \frac{k}{V} H^2 e^{-\frac{t}{\tau}} + \frac{1}{4} \frac{k_B T}{V} + \frac{1}{2} \frac{k}{V} H^2 + \frac{1}{4} \frac{k^2}{k_B T V} H^4 \quad (3.25)$$

$$G_{zz}^T(t) = 2 \frac{k_B T}{V} e^{-\frac{2t}{\tau}} + \frac{k_B T}{V} + 2 \frac{k}{V} H^2 + \frac{k^2}{k_B T V} H^4 \quad (3.26)$$

While these functions are similar to their xx-component counterparts,  $G_{zz}^A(t)$  in Eq.(3.23) and  $G_{zz}^X(t)$  in Eq.(3.25) contain a previously unseen term,  $\pm k H^2 e^{-\frac{t}{\tau}}$ . This term has the longest relaxation time of the entire system, and is equal to the Ornstein-Uhlenbeck characteristic time  $\tau'_{zz} = \tau$ , which is twice that of the xx-component counterparts. This accounts for the delay in stress relaxation observed in both the four-arm-star model and the two-chain model. This occurs, because the zz-component functions have 2<sup>nd</sup> order terms  $\langle z(t) z(0) \rangle$ , whilst other directions only have 4<sup>th</sup> order terms  $\langle x^2(t) x^2(0) \rangle$ . As can be seen in appendix A, these 2<sup>nd</sup> order terms come from Eq.(A.23), the expansion of

$$\langle \sigma_{zz}^A(t) \sigma_{zz}^A(0) \rangle = \frac{k^2}{V^2} \left\langle \left( 2 \left( z(t) - \frac{H}{2} \right)^2 \right) \left( 2 \left( z(0) - \frac{H}{2} \right)^2 \right) \right\rangle \quad (3.27)$$

which cancels out in the xx-component, Eq.(A.23),

$$\langle \sigma_{xx}^A(t) \sigma_{xx}^A(0) \rangle = \frac{k^2}{V^2} \left\langle \left( \left( x(t) - \frac{D}{2} \right)^2 + \left( x(t) + \frac{D}{2} \right)^2 \right) \left( \left( x(0) - \frac{D}{2} \right)^2 + \left( x(0) + \frac{D}{2} \right)^2 \right) \right\rangle \quad (3.28)$$

### Stress cross-correlation functions from simulations

Simulation results for the stress cross-correlation functions are plotted in Fig.3.15 for the four-arm-star model and the two-chain model, where we once again use the original four-arm-star model with arms of length  $\frac{N}{2}$ . The amplitudes of cross-correlations observed in  $G_{xx}^X(t)$  and  $G_{yy}^X(t)$  are very small, indicating there is little correlation between the lower chain and the upper chain in the two-chain model. The little correlation observed could possibly be a systematic error, but is more likely to be the cross-correlation predicted by Eq.(3.21) in the case of one bond per arm. It is expected for the case of  $\frac{1}{2}N$  bonds per arm that the amplitude of the correlation

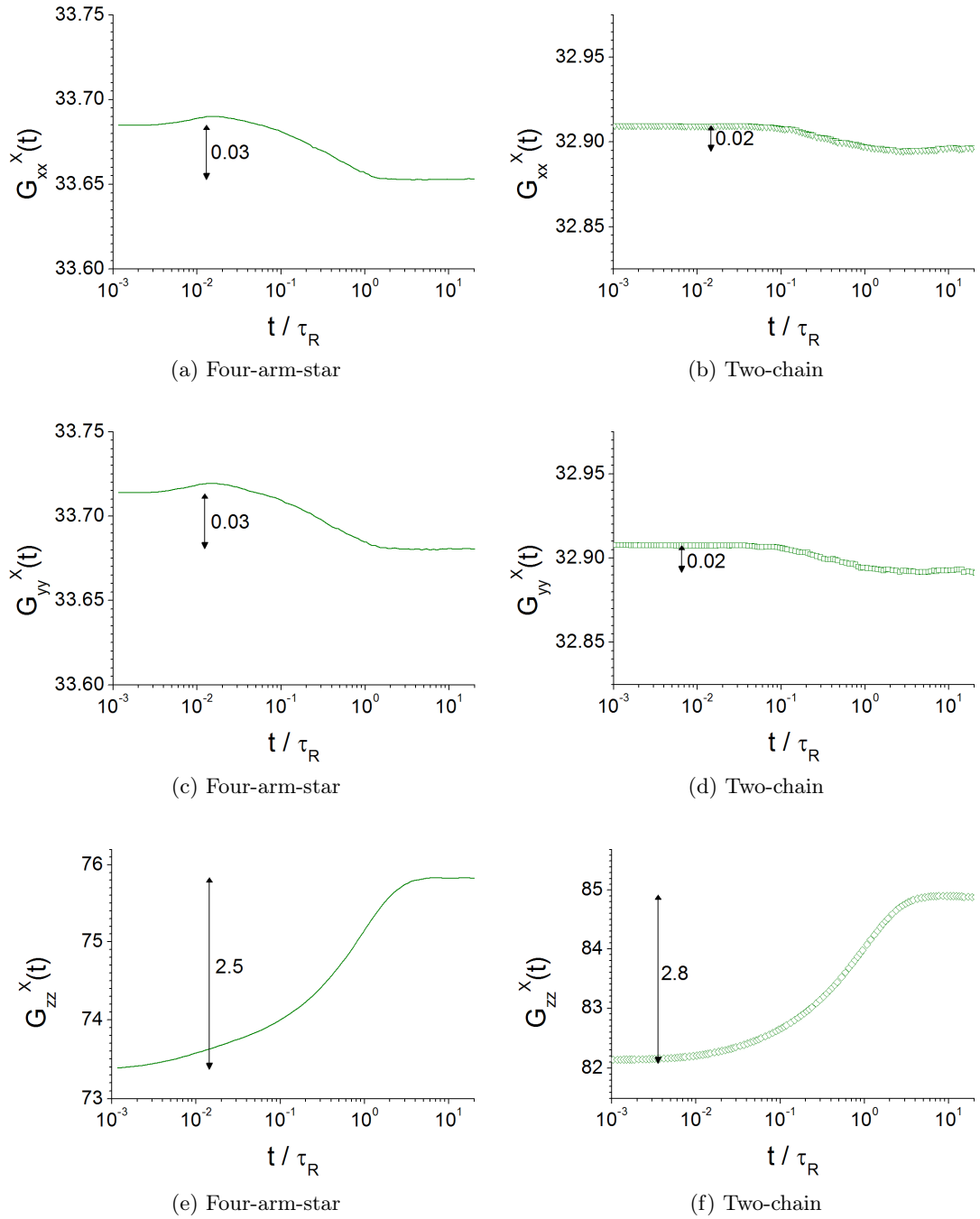


Figure 3.15: Stress cross-correlation functions,  $G_{\gamma\gamma}^X(t)$ , of the four-arm-star model and the two-chain model. Parameters are  $N = 16$ ,  $H = 10$ ,  $D = 10$ .

is smaller, but it is unknown why the amplitude is the exact value observed in Fig.3.15a and Fig.3.15c. There is much greater cross-correlation in  $G_{zz}^X(t)$ , where the function increases with  $t$  via the second term in Eq.(3.25), indicating anti-correlation.

### 3.1.7 Alternative: molecular dynamics two-chain simulation

Applying repulsive forces between chains is an alternative to using the rejection algorithm to prevent chains from crossing in the two-chain simulation. Here we investigate whether the rejection method produces the same results as the repulsion method, which is the more realistic model of the entanglement. In order to create a repulsion model, the potentials from the Kremer-Grest molecular dynamics model (KGMD) are used, because they are specifically designed to enforce uncrossability between chains (section 1.2.2). Hence, the new MD two-chain simulation has FENE springs and LJ potentials for bonds and a purely repulsive LJ potential between beads in opposing chains. The BD simulation allowed chains to pass through themselves, so this new MD simulation also allows chains to pass through themselves by not applying the LJ potential between beads of the same chain, except along bonds where it is required to balance the strong attractive FENE force. Fig.3.16, shows the two-chain simulations used within this study: the original BD two-chain simulation is (a) and this new simulation is (b).

The repulsive MD simulation was created so that the method of rejection could be compared to a method of repulsion. In order to test this properly, a qualitatively similar model is required for rejection; one that uses the same potential along bonds, but uses rejection rather than repulsion between chains. The ideal type simulation to do this is a Monte Carlo (MC) simulation, as described in section 1.2.5, because the rejection routine can be incorporated seamlessly. Movement each time step is generated as a random vector per bead and accepted with a probability based upon the change in energy, so any move that causes the two chains to cross can be treated as an infinite increase in energy. This MC simulation is (c) on Fig.3.16. A final simulation, (d), was also created for comparison, using the MC equation of motion, but incorporating the repulsive LJ force from the MD simulation.

		Equation of motion			
		<i>Brownian Dynamics</i>	<i>Molecular Dynamics</i>	<i>Monte-Carlo</i>	
Potential	Linear springs	Rejection Algorithm	a		
		Lennard-Jones Repulsion			
	FENE + LJ springs	Rejection Algorithm			c
		Lennard-Jones Repulsion		b	d

Figure 3.16: Simulations used within this section.

a) *BD: Linear bonds + rejection*b) *MD: FENE + LJ bonds + LJ repulsion*c) *MC: FENE + LJ bonds + rejection*d) *MC: FENE + LJ bonds + LJ repulsion*

### Mean bead positions

Since the potentials of simulations (b) and (d) are equal (Fig.3.16), the static properties we shall now examine are also equal. Therefore, only simulations (b) and (c) shall be compared; a MD repulsion simulation and a MC rejection simulation. The mean positions of the beads are plotted in Fig.3.17 for multiple values of  $H$ , the vertical stretch of the system. These range from  $H = -4$  to  $H = 15$ , where  $H = -4$  corresponds to chains that are barely in contact with each other and  $H = 15$  corresponds to the chains that are strongly entangled. In the z-direction, the repulsion model has a higher middle bead than the rejection model, which indicates that the two chains in the rejection model are closer to each other at the point of entanglement. This is to be expected, since repulsion creates an excluded volume around each chain, leading to a higher average position. This may be corrected in the rejection simulation by adjusting the parameter  $H$  to make  $\langle z_{N/2} \rangle$  equal in both simulations. In the x-direction, it is observed that the beads are not equally spaced. The entanglement has pushed the central beads outwards towards their anchoring beads, but the repulsion model has pushed its beads significantly further out than

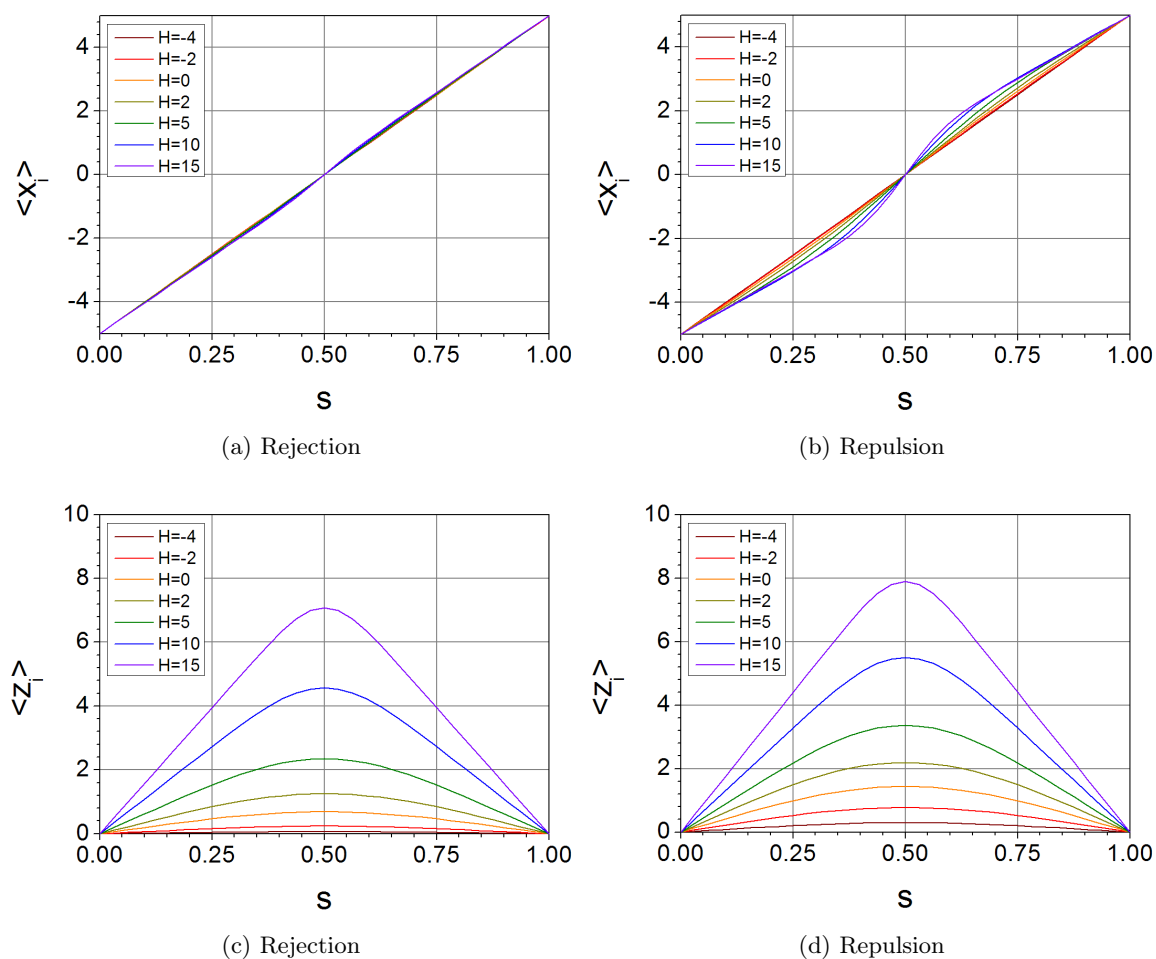


Figure 3.17: Mean bead positions for a repulsive molecular dynamics simulation and a Monte Carlo simulation with entanglement by rejection. Each is plot for a range of vertical stretch,  $H$ . Other parameters are  $N = 16$  and  $D = 10$ .

the rejection model. This, similar to the z-direction, is because of the excluded volume effect. However, unlike the excluded volume in the z-direction, this effect cannot be overcome with a slight shift in parameters.

### Variance of bead positions

The variance of the bead positions is plotted in Fig.3.18. The difference between rejection and repulsion appears to have little effect on the y- and z-direction variance, but a qualitative difference is clearly evident in the x-direction, particularly for large system heights,  $H$ . Increasing  $H$  stretches the system in the z-direction, making the entanglement stronger and more localised around the middle bead. In the MC rejection simulation, this reduces the variance and creates a dip in  $\text{var}(x_i)$  around the central beads. This is also observed in the repulsion simulation, but a second more striking effect occurs. The central-most beads have increased bead variance that rises out of the previous dip. The method of entanglement by rejection is passive and only effects the chain when an illegal move is attempted, whilst the repulsion method actively repels the chain. It appears that when the entanglement slides along the chain, applying and removing the force to different sections of the chain, causes an increase in variance, similar to that observed in section 3.1.3. This means that entanglement by rejection is missing certain effects in the x-direction.

### Stress relaxation functions

In Fig.3.19, the stress relaxation functions of the MC rejection simulation (Fig.3.16(b)) and the MC repulsion simulation (Fig.3.16(d)) are compared. This plot does not include the MD simulation, because it demonstrates ballistic motion at early time that is not captured by the MC or BD simulations. Therefore, it is easier to compare the two MC simulations, than to compare MD with MC. In order to provide the fairest possible comparison between the rejection and repulsion MC simulations, the rejection simulation has a larger system stretch,  $H$ , such that  $\langle z_{N/2} \rangle$  is equal for both models. In Fig.3.19a and Fig.3.19c, it is observed that the static values

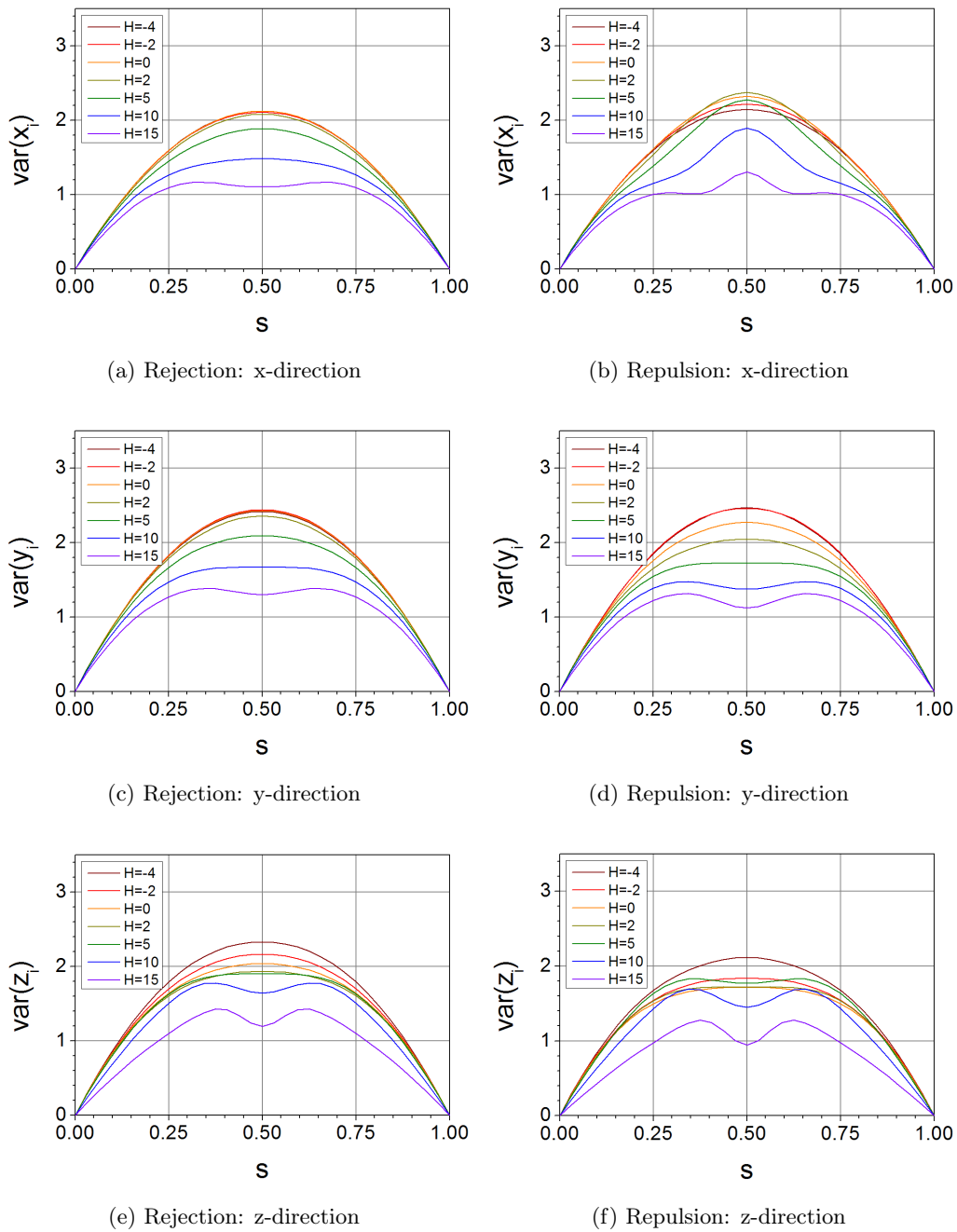


Figure 3.18: Variance of bead positions for a repulsive molecular dynamics simulation and a Monte Carlo simulation with entanglement by rejection. Each is plot for a range of vertical stretch,  $H$ . Other parameters are  $N = 16$  and  $D = 10$ .

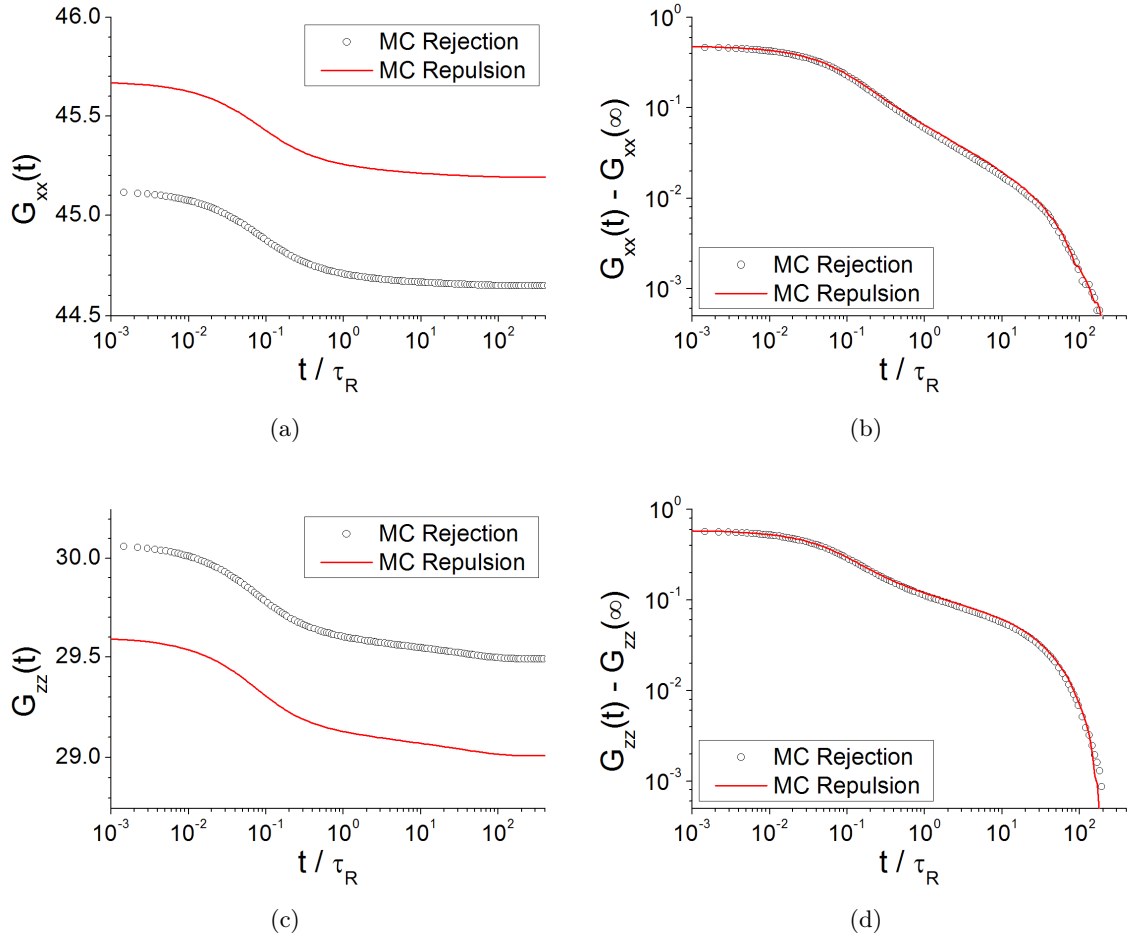


Figure 3.19: Cross-correlation functions of two MC simulations. One with entanglement by rejection and another with a repulsive potential between chains. Parameters are  $N = 32$ ,  $H = 7$ ,  $D = 14$ .

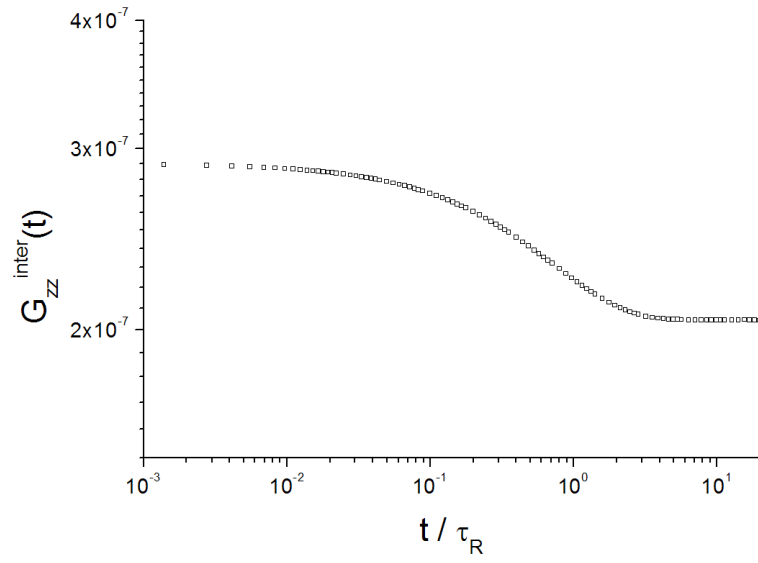
disagree between the the rejection and repulsion simulations, but such a issues can be overcome by a shift in parameters. Importantly, the dynamics of the two simulations in Fig.3.19b and Fig.3.19d are the same and no extra artefacts have been generated by the rejection method.

### Molecular dynamics two-chain simulation summary

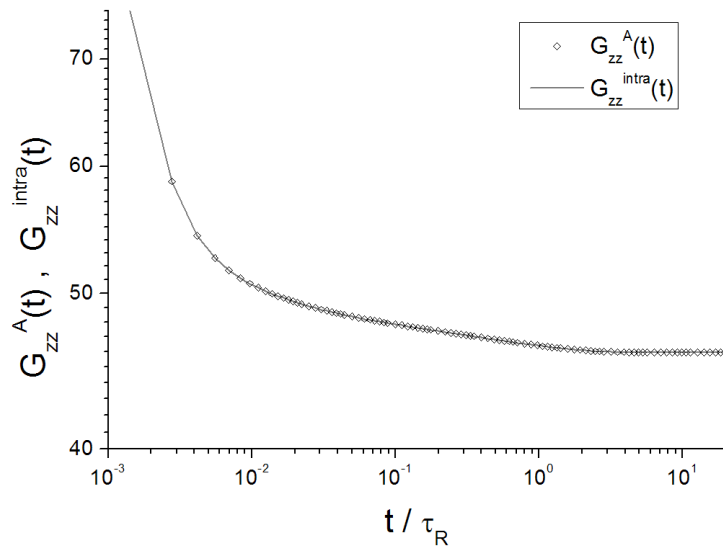
Despite the rejection method having flaws, it is still used extensively in this study, because the largest time step that can be used in the repulsive two-chain simulation is 100 times smaller than that of the rejection two-chain simulation due to the of strong repulsive forces. Consequently, simulating the repulsive model requires orders of magnitude more time to achieve the same final simulation time. The differences in static properties between rejection and repulsion can be mostly compensated for by system parameters which take excluded volume into account, and most importantly, the dynamics are the same for both of the entanglement methods.

#### 3.1.8 Stress from interactions between chains

Using the molecular dynamics two-chain simulation, it is possible to measure the stress contribution from interactions between chains; the auto-correlation of which is shown in Fig.3.20a. The auto-correlation function of stress due to the interactions between chains,  $G_{zz}^{\text{inter}}(t)$ , is negligible compared to the stress contributions from bonds in the same chain,  $G_{zz}^{\text{intra}}(t)$  (Fig.3.20b); for our parameters  $G_{zz}^{\text{inter}}(t) \sim 10^{-7}G_{zz}^{\text{intra}}(t)$ . Furthermore, the auto-correlation function of stress from all contributions involving the lower chain,  $G_{zz}^A(t)$ , displays no noticeable difference from  $G_{zz}^{\text{intra}}(t)$ . Hence, it is concluded that contribution to stress due to interactions between chains is negligible for this study. A similar conclusion was obtained in [33] from observations of a many chain MD simulation. The benefit of this is two-fold. Firstly, it allows the use of the rejection simulation, which is significantly faster to simulate. Secondly, it removes the need to calculate the cross-correlations of  $\sigma_{\gamma\gamma}^{\text{inter}}(t)$  with  $\sigma_{\gamma\gamma}^{\text{intra}}(t)$  in order to obtain  $G_{\gamma\gamma}^A(t)$ . Such cross-correlations would be challenging to reproduce in the slip-spring model, which has no measurement of  $\sigma_{\gamma\gamma}^{\text{inter}}(t)$ .



(a)



(b)

Figure 3.20: Auto-correlation functions of stress due to interactions between chains,  $G_{zz}^{\text{inter}}(t)$ ; compared to stress contribution from the forces along bonds alone,  $G_{zz}^{\text{intra}}(t)$  and due to all stress contributions involving the chain including forces between chains,  $G_{zz}^A(t)$ . Parameters are  $N = 16$ ,  $H = 10$ ,  $D = 10$ .

### 3.2 Slip-spring model

The slip-spring model used in this study retains the lower chain of the two-chain model, but replaces the upper chain and rejection routine with a slip-spring anchored at  $\mathbf{r}_A$ , as illustrated in Fig.3.21. The bead positions in the chain are denoted by  $\mathbf{r}_i$  and the fixed beads of the chain are referred to as  $\mathbf{r}_B = \mathbf{r}_0$  and  $\mathbf{r}_C = \mathbf{r}_N$ . The slip-spring is a single linear spring, one end of which has a fixed position,  $\mathbf{r}_A$ , while the other end shares the position of bead  $j$  in the Rouse chain. The slip-spring's fixed anchor position,  $\mathbf{r}_A$ , is known to be central in the x- and y-axes due to symmetry, and is a height,  $h$ , above the lower chain's fixed beads, such that

$$\mathbf{r}_A = \frac{\mathbf{r}_B + \mathbf{r}_C}{2} + \hat{\mathbf{k}}h \quad (3.29)$$

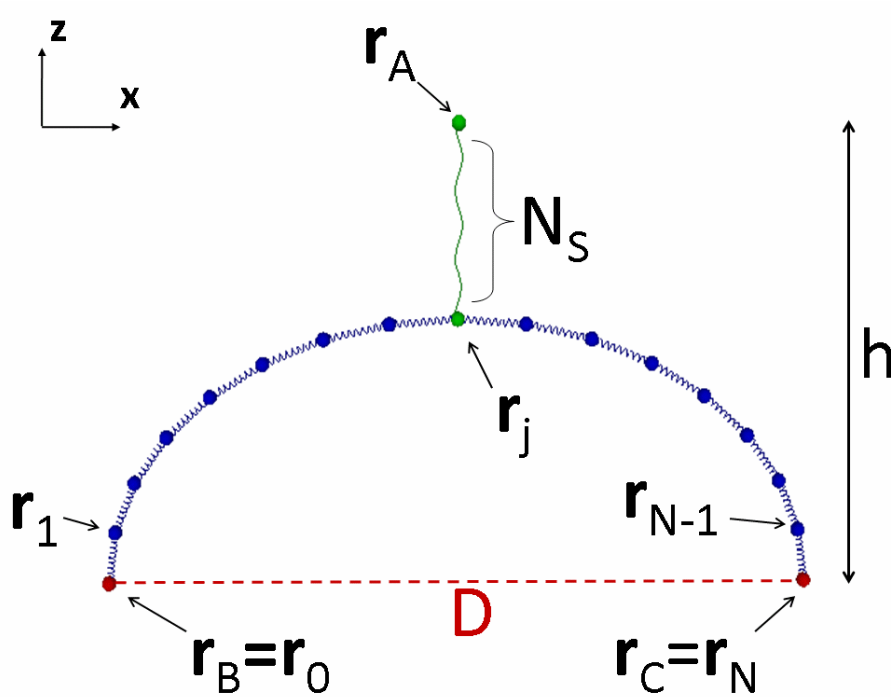


Figure 3.21: Diagram of the slip-spring model. The polymer chain has two fixed beads at  $(-\frac{D}{2}, 0, 0)$  and  $(\frac{D}{2}, 0, 0)$ . A slip-spring anchored at the point  $(0, 0, h)$  applies a force to bead  $j$  equal to that of a chain with  $N_S$  bonds.

where  $\hat{\mathbf{k}} = (0, 0, 1)$ . The slip-spring acts upon bead  $\mathbf{r}_j$  as a linear spring with a slip-spring strength equivalent to a chain of  $N_S$  bonds. The spring-constant for bonds in the Rouse chain is given by

$$k = \frac{3k_B T}{b^2} \quad (3.30)$$

therefore the spring-constant of the slip-spring is

$$k_S = \frac{k}{N_S} = \frac{3k_B T}{b^2 N_S} \quad (3.31)$$

The slip-spring model is a single slip-spring version of the multiple-slip-spring model described in section 1.3.4, so the energy of the system is given by

$$U = \sum_{i=1}^N \frac{3k_B T}{2b^2} (\mathbf{r}_i - \mathbf{r}_{i-1})^2 + \frac{3k_B T}{2b^2 N_S} (\mathbf{r}_A - \mathbf{r}_j)^2 \quad (3.32)$$

and the equation of motion for bead  $i$  in the chain is

$$\xi d\mathbf{r}_i = \frac{3k_B T}{b^2} (\mathbf{r}_{i+1} - 2\mathbf{r}_i + \mathbf{r}_{i-1}) dt + \sqrt{2k_B T \xi} d\mathbf{W}_i(t) + \delta_{ij} \frac{3k_B T}{b^2 N_S} (\mathbf{r}_A - \mathbf{r}_j) dt \quad (3.33)$$

where the slip-link acts on bead  $j$  and thus the last term is the force applied by the slip-spring to the bead at index  $i = j$ .

### 3.2.1 Slip

Slip is a vital part of the model. As described for the multiple entanglement slip-spring model (section 1.3.4), the slip-link will attempt to move one position along the chain in either direction on every simulation time step. In order to ensure that the slip-link is not lost in this single chain model, the slip-link is forbidden from being on the fixed end beads, such that  $0 < j < N$ . However, the Monte Carlo mechanism for slip is in contrast to the Brownian Dynamics equation of motion of the Rouse chain. An alternative method of slip would have the slip-link obeying

one-dimensional Brownian Dynamics along the chain and allowing the slip-link to exist on the bonds between beads, but a previous investigation found that the Monte Carlo method produces the same results and is simpler and faster to compute.

To validate the slip method used in the slip-spring model, Fig.3.22 compares the position of the entanglement in the two-chain simulation to the slip-link position in the slip-spring model. In the two-chain simulation, the position of the entanglement is sampled every time a bead position is rejected. Since the actual rejection occurred because of a bond crossing another bond, the rejection is attributed to whichever bond caused the rejection to occur. For the slip-spring, the position of the slip-link is stored every time step, during a simulation with parameters chosen to approximately reproduce the statics and dynamics of the two-chain simulation. It is observed in Fig.3.22 that the slip-link samples the chain with the same probability density as the two-chain entanglement, both of which are Gaussian. This validates the use of the slip mechanism.

### 3.2.2 Analytical calculations

#### Probability density function

The probability density of the bead positions in a slip-spring model with fixed slip-link position,  $j$ , is given by

$$P_j(\{\mathbf{r}_i\}, \mathbf{r}_A, N_S) = \frac{1}{Q_j(\mathbf{r}_A, N_S)} \exp\left(-\frac{3}{2b^2} \left(\sum_{i=1}^N (\mathbf{r}_i - \mathbf{r}_{i-1})^2 + \frac{(\mathbf{r}_A - \mathbf{r}_j)^2}{N_S}\right)\right) \quad (3.34)$$

where  $Q_j(\mathbf{r}_A, N_S)$  is the partition function,

$$Q_j(\mathbf{r}_A, N_S) = \int \exp\left(-\frac{3}{2b^2} \left(\sum_{i=1}^N (\mathbf{r}_i - \mathbf{r}_{i-1})^2 + \frac{(\mathbf{r}_A - \mathbf{r}_j)^2}{N_S}\right)\right) d^3\mathbf{r}_1 \dots d^3\mathbf{r}_{N-1} \quad (3.35)$$

where  $d^3\mathbf{r} = dx dy dz$ . In order to integrate  $Q_j(\mathbf{r}_A, N_S)$ , the slip-spring model can be broken down into three Rouse chains joined at the slip-link bead as illustrated in Fig.3.23. The partition

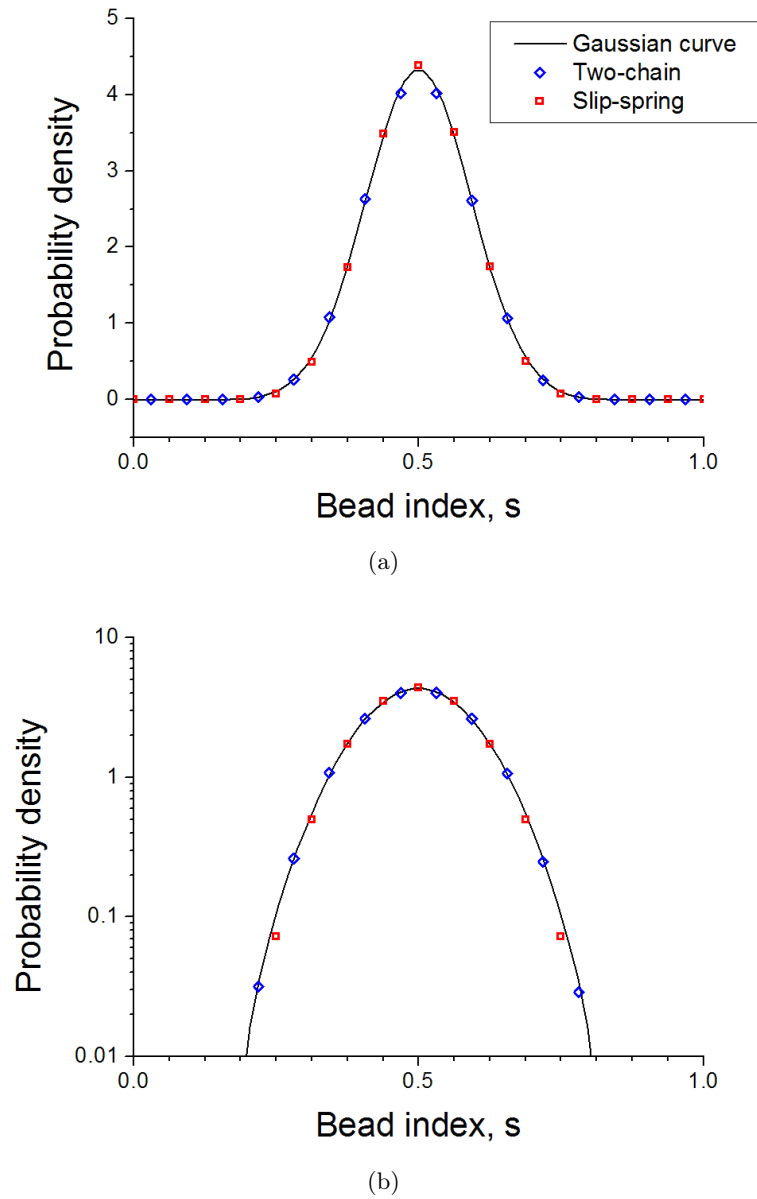


Figure 3.22: Comparing the probability density of entanglement position observed in the two-chain simulation to the probability density of slip-link positions in the slip-spring model simulation. The slip-spring model uses values of  $N_S$  and  $h$  that give the best fit to stress relaxation as discussed in section 3.2.3. Both models use the parameters  $N = 16$ ,  $H = 10$ ,  $D = 10$ . The bead number is expressed as a fraction along the chain,  $s = \frac{i}{N}$ . The probability density is plotted against a Gaussian distribution.

function of each Rouse chain with fixed ends is known to be

$$\begin{aligned}
 Z(\mathbf{r}_0, \mathbf{r}_n, n) &= \int \exp\left(-\frac{k}{2k_B T} \sum_{i=1}^n (\mathbf{r}_i - \mathbf{r}_{i-1})^2\right) d^3\mathbf{r}_1 \dots d^3\mathbf{r}_{n-1} \\
 &= \left(\frac{1}{n}\right)^{\frac{3}{2}} \left(\frac{2\pi k_B T}{k}\right)^{\frac{3}{2}(n-1)} \exp\left(-\frac{k}{2k_B T} \frac{(\mathbf{r}_n - \mathbf{r}_0)^2}{n}\right) \\
 &= \left(\frac{1}{n}\right)^{\frac{3}{2}} \left(\frac{2\pi b^2}{3}\right)^{\frac{3}{2}(n-1)} \exp\left(-\frac{3}{2b^2} \frac{(\mathbf{r}_n - \mathbf{r}_0)^2}{n}\right) \quad (3.36)
 \end{aligned}$$

(appendix B), where  $k = \frac{3k_B T}{b^2}$ . By setting  $n = 1$  and  $k = k_S$  (Eq.(3.31)), the slip-spring's partition function is

$$Z_S(\mathbf{r}_A, \mathbf{r}_j, N_S) = \exp\left(-\frac{3}{2b^2} \frac{(\mathbf{r}_A - \mathbf{r}_j)^2}{N_S}\right) \quad (3.37)$$

It can also be shown that the partition function for two chains joined end-to-end is

$$Z(\mathbf{r}_B, \mathbf{r}_C, N_1 + N_2) = \int Z(\mathbf{r}_B, \mathbf{r}_j, N_1) Z(\mathbf{r}_C, \mathbf{r}_j, N_2) d^3\mathbf{r}_j \quad (3.38)$$

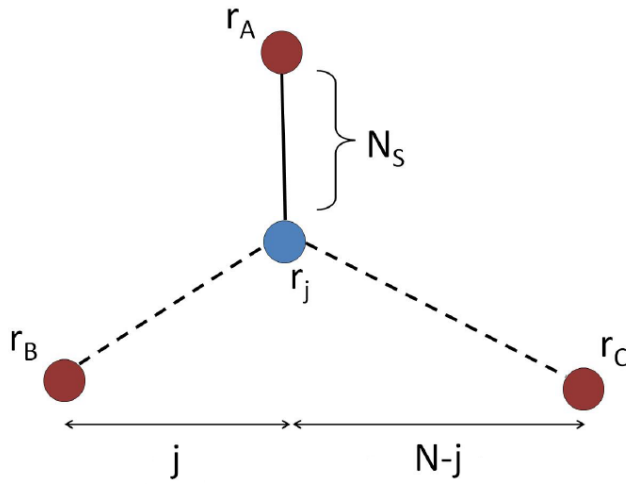


Figure 3.23: The slip-link model with a fixed slip-link position can be considered as three chains joined at bead  $j$ . Two Rouse chains span from  $\mathbf{r}_B$  to  $\mathbf{r}_j$  with with  $j$  bonds, and from  $\mathbf{r}_j$  to  $\mathbf{r}_C$  with  $N - j$  bonds. The slip-spring spans from  $\mathbf{r}_A$  to  $\mathbf{r}_j$  as a single bond, but with strength  $N_S$ .

where the connecting bead  $\mathbf{r}_j$  is mobile. Using these equations, the partition function is found to be

$$\begin{aligned}
Q_j(\mathbf{r}_A, N_S) &= \int Z_S(\mathbf{r}_A, \mathbf{r}_j, N_S) Z(\mathbf{r}_B, \mathbf{r}_j, j) Z(\mathbf{r}_C, \mathbf{r}_j, N-j) d^3\mathbf{r}_j \\
&= \left(\frac{2\pi b^2}{3}\right)^{\frac{3}{2}(N-2)} \left(\frac{1}{j(N-j)}\right)^{\frac{3}{2}} \\
&\quad \int \exp\left(-\frac{3}{2b^2} \left(\frac{(\mathbf{r}_A - \mathbf{r}_j)^2}{N_S} + \frac{(\mathbf{r}_B - \mathbf{r}_j)^2}{j} + \frac{(\mathbf{r}_C - \mathbf{r}_j)^2}{N-j}\right)\right) d^3\mathbf{r}_j \\
&= \left(\frac{2\pi b^2}{3}\right)^{\frac{3}{2}(N-1)} \left(\frac{1}{j(N-j)}\right)^{\frac{3}{2}} \left(\frac{1}{N_S} + \frac{1}{j} + \frac{1}{N-j}\right)^{-\frac{3}{2}} \\
&\quad \exp\left(\frac{-\frac{3}{2b^2} \left(\frac{(\mathbf{r}_A - \mathbf{r}_B)^2}{N_S j} + \frac{(\mathbf{r}_A - \mathbf{r}_C)^2}{N_S(N-j)} + \frac{(\mathbf{r}_B - \mathbf{r}_C)^2}{j(N-j)}\right)}{\frac{1}{N_S} + \frac{1}{j} + \frac{1}{N-j}}\right) \tag{3.39}
\end{aligned}$$

where the integral

$$\int \exp(-a r^2 + \mathbf{b} \cdot \mathbf{r}) d^3\mathbf{r} = \left(\frac{\pi}{a}\right)^{\frac{3}{2}} \exp\left(\frac{b^2}{4a}\right)$$

has been used. (This integral and similar Gaussian integrals can be found in appendix B).

### Probability density of slip-link bead position

Using the partition function, Eq.3.39, it is possible to calculate the average position of the middle bead,

$$\begin{aligned}
\langle \mathbf{r}_j \rangle &= \frac{\int \mathbf{r}_j Z_S(\mathbf{r}_A, \mathbf{r}_j) Z(\mathbf{r}_B, \mathbf{r}_j, j) Z(\mathbf{r}_C, \mathbf{r}_j, N-j) d^3\mathbf{r}_j}{Q_j(\mathbf{r}_A, N_S)} \\
&= \frac{\frac{\mathbf{r}_A}{N_S} + \frac{\mathbf{r}_B}{j} + \frac{\mathbf{r}_C}{N-j}}{\frac{1}{N_S} + \frac{1}{j} + \frac{1}{N-j}} \tag{3.40}
\end{aligned}$$

The variance of this bead is  $\frac{b^2}{3} \left(\frac{1}{N_S} + \frac{1}{j} + \frac{1}{N-j}\right)^{-1}$ , because bead  $j$  is attached to chains with effective spring-constant  $\frac{k}{j}$  and  $\frac{k}{N-j}$ , and a slip-spring with spring-constant  $\frac{k}{N_S}$ . Using the mean

and variance, the Gaussian probability density of  $\mathbf{r}_j$  is

$$P_j(\mathbf{r}_j, \mathbf{r}_A, N_S) = \frac{1}{\mathcal{N}} \exp\left(-\frac{3}{2b^2} \left(\frac{1}{N_S} + \frac{1}{j} + \frac{1}{N-j}\right) (\mathbf{r}_j - \langle \mathbf{r}_j \rangle)^2\right) \quad (3.41)$$

where

$$\begin{aligned} \mathcal{N} &= \int \exp\left(-\frac{3}{2b^2} \left(\frac{1}{N_S} + \frac{1}{j} + \frac{1}{N-j}\right) (\mathbf{r}_j - \langle \mathbf{r}_j \rangle)^2\right) d^3\mathbf{r}_j \\ &= \left(\frac{2\pi b^2}{3}\right)^{\frac{3}{2}} \left(\frac{1}{N_S} + \frac{1}{j} + \frac{1}{N-j}\right)^{-\frac{3}{2}} \end{aligned} \quad (3.42)$$

is the normalisation such that

$$\int P_j(\mathbf{r}_j, \mathbf{r}_A, N_S) d^3\mathbf{r}_j = 1 \quad (3.43)$$

### Average stress, $\langle \sigma_{j,\gamma\gamma} \rangle$ , for the slip-spring model with fixed slip-link position

Using Fig.3.23 to consider the slip-spring model as three Rouse chains, it is possible to use the stress of a single Rouse chain, Eq.(2.16), to calculate the stress contribution from the entire chain in the slip-spring model. Only the contribution from the chain and not the slip-spring is considered, because including the slip-spring would add additional stress to the system that is not observed in the entanglement model; it has previously been demonstrated that the stress contribution due to the entanglement is negligible in the two-chain model (section 3.1.8). To obtain  $\langle \sigma_{j,\gamma\gamma} \rangle$ , the stress of a Rouse chain with  $j$  bonds between fixed beads  $\mathbf{r}_B$  and  $\mathbf{r}_j$  is added to the stress of a Rouse chain with  $N-j$  bonds between  $\mathbf{r}_j$  and  $\mathbf{r}_C$ . In order to account for the movement of the slip-link bead, this is then integrated over the probability density of  $\mathbf{r}_j$ , Eq.(3.41). Hence,

$$\langle \sigma_{j,\gamma\gamma} \rangle = \frac{1}{V} \int P_j(\mathbf{r}_j, \mathbf{r}_A, N_S) \left( k_B T (N-2) + k \frac{(r_B^\gamma - r_j^\gamma)^2}{j} + k \frac{(r_C^\gamma - r_j^\gamma)^2}{N-j} \right) d^3\mathbf{r}_j \quad (3.44)$$

This is integrated using the integral Eq.(2.13) to obtain

$$\begin{aligned} \langle \sigma_{j,\gamma\gamma} \rangle &= \frac{k_B T}{V} (N-2) + \frac{k_B T}{V} \left( \frac{1}{j} + \frac{1}{N-j} \right) \left( \frac{1}{N_S} + \frac{1}{j} + \frac{1}{N-j} \right)^{-1} \\ &\quad + \frac{k}{V} \frac{(r_B^\gamma - \langle r_j^\gamma \rangle)^2}{j} + \frac{k}{V} \frac{(r_C^\gamma - \langle r_j^\gamma \rangle)^2}{N-j} \end{aligned} \quad (3.45)$$

The same technique may also be used to find the average stress from the slip-spring object,

$$\langle \sigma_{j,\gamma\gamma}^S \rangle = \frac{k_B T}{V} \frac{1}{N_S} \left( \frac{1}{N_S} + \frac{1}{j} + \frac{1}{N-j} \right)^{-1} + \frac{k}{V} \frac{1}{N_S} (r_A^\gamma - \langle r_j^\gamma \rangle)^2 \quad (3.46)$$

Similarly  $\langle \sigma_{\gamma\gamma}^2 \rangle$  can be calculated, but this requires the calculation of cross terms between  $\sigma_{B,\gamma\gamma}$  and  $\sigma_{C,\gamma\gamma}$ , where  $\sigma_B$  is the stress of the chain from bead  $\mathbf{r}_B$  to  $\mathbf{r}_j$ , and  $\sigma_C$  from bead  $\mathbf{r}_C$  to  $\mathbf{r}_j$ .  $\sigma_{B,\gamma\gamma}$  and  $\sigma_{C,\gamma\gamma}$  are for Rouse chains with fixed  $\mathbf{r}_j$  and therefore are uncorrelated, such that we may write

$$\begin{aligned} \langle \sigma_{j,\gamma\gamma}^2 \rangle &= \int P_j(\mathbf{r}_j, \mathbf{r}_A, N_S) \langle (\sigma_{B,\gamma\gamma} + \sigma_{C,\gamma\gamma})^2 \rangle d^3\mathbf{r}_j \\ &= \int P_j(\mathbf{r}_j, \mathbf{r}_A, N_S) (\langle \sigma_{B,\gamma\gamma}^2 \rangle \\ &\quad + 2 \langle \sigma_{B,\gamma\gamma} \rangle \langle \sigma_{C,\gamma\gamma} \rangle + \langle \sigma_{C,\gamma\gamma}^2 \rangle) d^3\mathbf{r}_j \end{aligned} \quad (3.47)$$

Using Eq.(2.16) and Eq.(2.18), the average stress squared for a slip-spring system, where the slip-link is fixed to bead number  $j$ , is given by

$$\begin{aligned}
\langle \sigma_{j,\gamma\gamma}^2 \rangle &= \frac{k_B^2 T^2}{V^2} \left( N(N-2) + 2(N-2) \frac{\frac{1}{j} + \frac{1}{N-j}}{\frac{1}{N_s} + \frac{1}{j} + \frac{1}{N-j}} + 3 \left( \frac{\frac{1}{j} + \frac{1}{N-j}}{\frac{1}{N_s} + \frac{1}{j} + \frac{1}{N-j}} \right)^2 \right) \\
&+ 2 \frac{1}{V^2} k_B T (N-2) k \left( \frac{(r_B^\gamma - \langle r_j^\gamma \rangle)^2}{j} + \frac{(r_C^\gamma - \langle r_j^\gamma \rangle)^2}{N-j} \right) \\
&+ 2 \frac{1}{V^2} k_B T \frac{k}{\frac{1}{N_s} + \frac{1}{j} + \frac{1}{N-j}} \left( \frac{(r_B^\gamma - r_C^\gamma)^2}{j(N-j)} + 3 \left( \frac{\langle r_j^\gamma \rangle - r_B^\gamma}{j} + \frac{\langle r_j^\gamma \rangle - r_C^\gamma}{N-j} \right)^2 \right) \\
&+ \frac{k^2}{V^2} \left( \frac{(r_B^\gamma - \langle r_j^\gamma \rangle)^2}{j} + \frac{(r_C^\gamma - \langle r_j^\gamma \rangle)^2}{N-j} \right)^2 \tag{3.48}
\end{aligned}$$

### Probability distribution of slip

Using the partitions function of each slip-link position for the fixed case, Eq.(3.39), it is possible to express the probability of the slip-link being on bead  $j$ , given the slip-spring parameters  $\mathbf{r}_A$  and  $N_S$ ,

$$P(j, \mathbf{r}_A, N_S) = \frac{Q_j(\mathbf{r}_A, N_S)}{\sum_{j'=1}^{N-1} Q_{j'}(\mathbf{r}_A, N_S)} \tag{3.49}$$

To add slip to a property calculated for a fixed slip-spring position, the property should be summed over all  $j$ , with each  $j$  weighted by  $P(j, \mathbf{r}_A, N_S)$ . For example, the probability density of bead positions  $\{\mathbf{r}_i\}$  with the slip-link fixed at  $j$ , Eq.(3.34), can be used in conjunction with

Eq.(3.49) to obtain the probability density of  $\{\mathbf{r}_i\}$  with slip,

$$\begin{aligned}
P(\{\mathbf{r}_i\}, \mathbf{r}_A, N_S) &= \sum_{j=1}^{N-1} P(j, \mathbf{r}_A, N_S) P_j(\{\mathbf{r}_i\}, \mathbf{r}_A, N_S) \\
&= \sum_{j=1}^{N-1} \frac{Q_j(\mathbf{r}_A, N_S)}{\sum_{j'=0}^N Q_{j'}(\mathbf{r}_A, N_S)} \frac{\exp\left(-\frac{3}{2b^2} \left(\sum_{i=1}^N (\mathbf{r}_i - \mathbf{r}_{i-1})^2 + \frac{(\mathbf{r}_A - \mathbf{r}_j)^2}{N_S}\right)\right)}{Q_j(\mathbf{r}_A, N_S)} \\
&= \frac{\sum_{j=0}^N \exp\left(-\frac{3}{2b^2} \left(\sum_{i=1}^N (\mathbf{r}_i - \mathbf{r}_{i-1})^2 + \frac{(\mathbf{r}_A - \mathbf{r}_j)^2}{N_S}\right)\right)}{\sum_{j'=0}^N Q_{j'}(\mathbf{r}_A, N_S)} \tag{3.50}
\end{aligned}$$

### Average stress, $\langle\sigma_{\gamma\gamma}\rangle$ , for the slip-spring model with the slip mechanism

Using Eq.(3.49), the average stress of the slip-spring model is

$$\langle\sigma_{\gamma\gamma}\rangle = \sum_{j=1}^{N-1} P_j(\mathbf{r}_A, N_S) \langle\sigma_{j,\gamma\gamma}\rangle \tag{3.51}$$

which is plotted in Fig.3.24 as a function of slip-spring strength,  $N_S$ , for a number of different slip-spring lengths,  $h$ . Fig.3.24d splits  $\langle\sigma_{xx}\rangle$  into the thermal fluctuation contribution to stress and the stress due to stretch. The stress due to fluctuations is given by the first two terms of Eq.(3.45). In the limit  $N_S \rightarrow \infty$ , the slip-spring becomes infinitely weak and the chain has a contribution of  $\frac{k_B T}{V}$  from the slip-link bead's thermal fluctuations, such that it is equivalent to an unentangled Rouse chain. In the limit  $N_S \rightarrow 0$ , the slip-spring becomes infinitely strong and the position of the slip-link bead is fixed at  $\mathbf{r}_j = \mathbf{r}_A$ . In this case, the second term of Eq.(3.45) becomes zero, and the stress is equal to two separate Rouse chains with bead  $j$  not contributing to the thermal fluctuations. If Eq.(3.46) is considered, it can be seen that the virtual slip-spring object acquires the stress contribution belonging to the slip-spring bead as  $N_S$  increases, such that bead  $j$  contributes  $\frac{k_B T}{V}$  to the total stress independent of  $N_S$  in accordance with the equipartition theorem.

The stretch term is also interesting. In  $\langle\sigma_{zz}\rangle$ , the stress due to stretch increases with slip-spring strength and  $h$ , simply because the chain is being stretched towards the slip-spring anchor

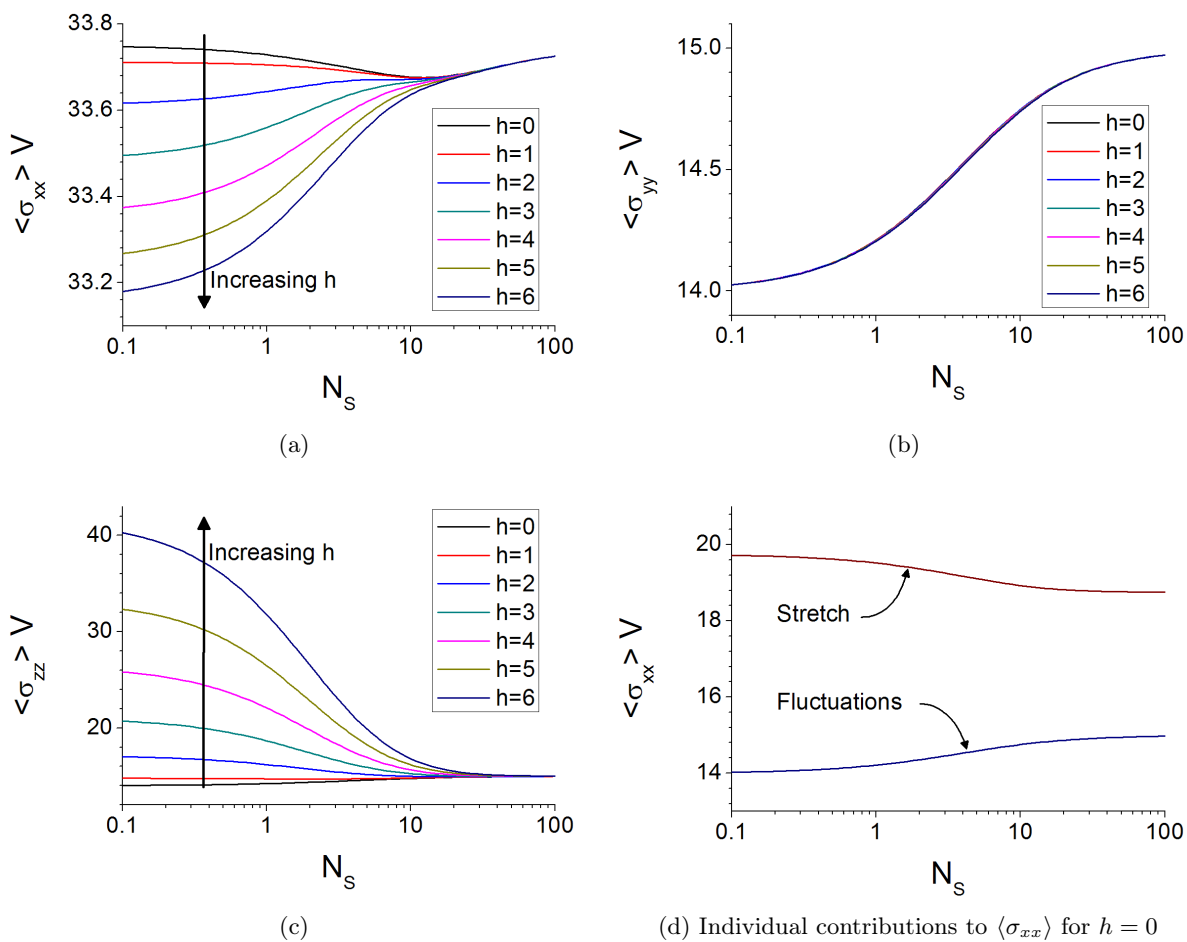


Figure 3.24: Average stress contribution from the chain in the slip-spring model as a function of  $N_s$  for multiple  $h$  values. Parameters are  $N = 16$ ,  $H = 10$  and  $D = 10$ .

at  $\mathbf{r}_A$ . This is not the case for  $\langle \sigma_{xx} \rangle$ , which decreases with  $h$ . This effect can be explained by slip. Stress is added to the chain by the slip-spring deforming the distribution of beads away from their unentangled positions,

$$\langle \mathbf{r}_i^{\text{Single}} \rangle = \mathbf{r}_B + \frac{i}{N} (\mathbf{r}_C - \mathbf{r}_B) \quad (3.52)$$

Since  $\langle x_i \rangle - \langle x_i^{\text{Single}} \rangle = 0$ , the stress due to stretch is at a minimum. The probability distribution of slip,  $P(j, \mathbf{r}_A, N_S)$ , is dependent on the vector position of the anchoring point,  $\mathbf{r}_A = (0, 0, h)$ , such that increasing  $h$  causes the probability distribution to narrow. Therefore, the position of beads further from the middle bead are less likely to be sampled by the slip-link and deform less. In the x-direction, the average position of the middle bead is equal to the anchoring point of the slip-spring,  $\langle x_{N/2} \rangle = x_A$ , which means a very strong slip-spring does not affect  $\langle x_{N/2} \rangle$  as it did in the z-direction. Thus, the effects of  $P(j, \mathbf{r}_A, N_S)$  dominate and  $\langle \sigma_{xx} \rangle$  decreases with increasing  $h$ .

### 3.2.3 Parameter finding using $G_{\gamma\gamma}(0)$ and $G_{\gamma\gamma}(\infty)$

Using results from a two-chain simulation in conjunction with these analytical calculations, it is possible to find the point in parameter space where the slip-spring model reproduces the stress relaxation properties of the two-chain simulation. Plotted in Fig.3.25 are the best  $N_S$  and  $h$  combinations to fit

$$G_{\gamma\gamma}(0) = \frac{V}{k_B T} \langle \sigma_{\gamma\gamma} \rangle^2 \quad (3.53)$$

and

$$G_{\gamma\gamma}(\infty) = \frac{V}{k_B T} \langle \sigma_{\gamma\gamma}^2 \rangle \quad (3.54)$$

for  $\gamma = x, y, z$ , where  $V = \frac{N-1}{c}$ . The shaded areas indicate where the value is within 1% of the amplitude,  $(G_{\gamma\gamma}(0) - G_{\gamma\gamma}(\infty))$ , from the target value of  $G_{\gamma\gamma}(t)$ .  $t = 0$  is shown by backward slashes and  $t = \infty$  by forward slashes. These two shaded areas always overlap for  $G_{xx}(t)$  and

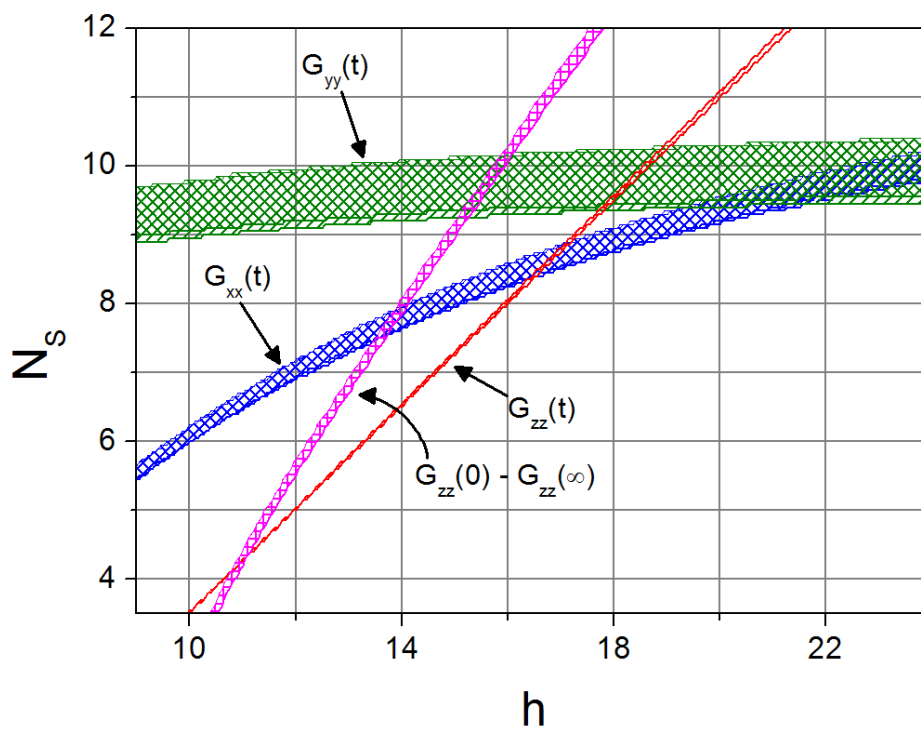


Figure 3.25: Best  $N_S$  values as a function of  $h$  for multiple stress relaxation properties. Shaded areas indicate the best  $N_S$  to within 1% of the amplitude.  $G_{\gamma\gamma}(0)$  is shown as backward slashes and  $G_{\gamma\gamma}(\infty)$  by forward slashes. For  $G_{xx}(t)$  and  $G_{yy}(t)$  these areas overlap. Parameters are  $N = 16$ ,  $H = 10$  and  $D = 10$ .

$G_{yy}(t)$ , which means that when the value for  $t = 0$  is fit to the two-chain simulation,  $t = \infty$  will also fit the two-chain results. The widths of the shaded areas indicate the dependence upon  $N_S$ , which controls the spring strength.  $G_{yy}(t)$  has a wide area, because it has the least dependence on  $N_S$ , while  $G_{zz}(t)$  has very little shaded area, because it is strongly affected by  $N_S$ . The width of  $G_{zz}(0)$  and  $G_{zz}(\infty)$  are so thin in Fig.3.25 that they appear simply as single lines.

It is observed that, at  $h \approx 23$ , it is possible to find a point where there is a good fit between the models for both  $G_{xx}(t)$  and  $G_{yy}(t)$ , but not  $G_{zz}(t)$ . There are no points found where all three diagonal components agree with each other. Furthermore, the values of  $G_{zz}(0)$  and  $G_{zz}(\infty)$  do not always overlap with each other; instead they diverge as  $h$  increases. To investigate this further,  $(G_{zz}(0) - G_{zz}(\infty))$ , is included on the graph. Unlike  $G_{xx}(t)$  and  $G_{yy}(t)$ , the amplitude of  $G_{zz}(t)$  is strongly affected by  $N_S$ . In the slip-spring model, the direction in which the entanglement is distorting the chain is most important, therefore the parameters that result in the best fit of  $G_{zz}(t)$  are preferred. This occurs where the shaded areas for  $G_{zz}(0)$ ,  $G_{zz}(\infty)$  and  $(G_{zz}(0) - G_{zz}(\infty))$  overlap. In Fig.3.25, where  $N = 16$ ,  $H = 10$  and  $D = 10$ , the optimum parameters are  $h = 10.89$  and  $N_S = 4.20$ .

### 3.2.4 Simulation results of stress relaxation functions

Using parameters obtained in the previous section,  $G_{\gamma\gamma}(t)$  is plotted for the simulation of the slip-spring model in Fig.3.26 against the results from a two-chain simulation. The models differ for the static values of  $G_{xx}(t)$  and  $G_{yy}(t)$ , as predicted by the parameter fitting method, but nevertheless their amplitudes are equal. From equations Eq.(3.45) and Eq.(3.48), we know that

$$\begin{aligned} G_{yy}(0) - G_{yy}(\infty) &= \frac{N-1}{c k_B T} \left( \langle \sigma_{j,yy} \rangle^2 - \langle \sigma_{j,yy}^2 \rangle \right) \\ &= \frac{2ck_B T}{N-1} \left( N - 2 + \left( \frac{\frac{1}{j} + \frac{1}{N-j}}{\frac{1}{N_s} + \frac{1}{j} + \frac{1}{N-j}} \right)^2 \right) \end{aligned} \quad (3.55)$$

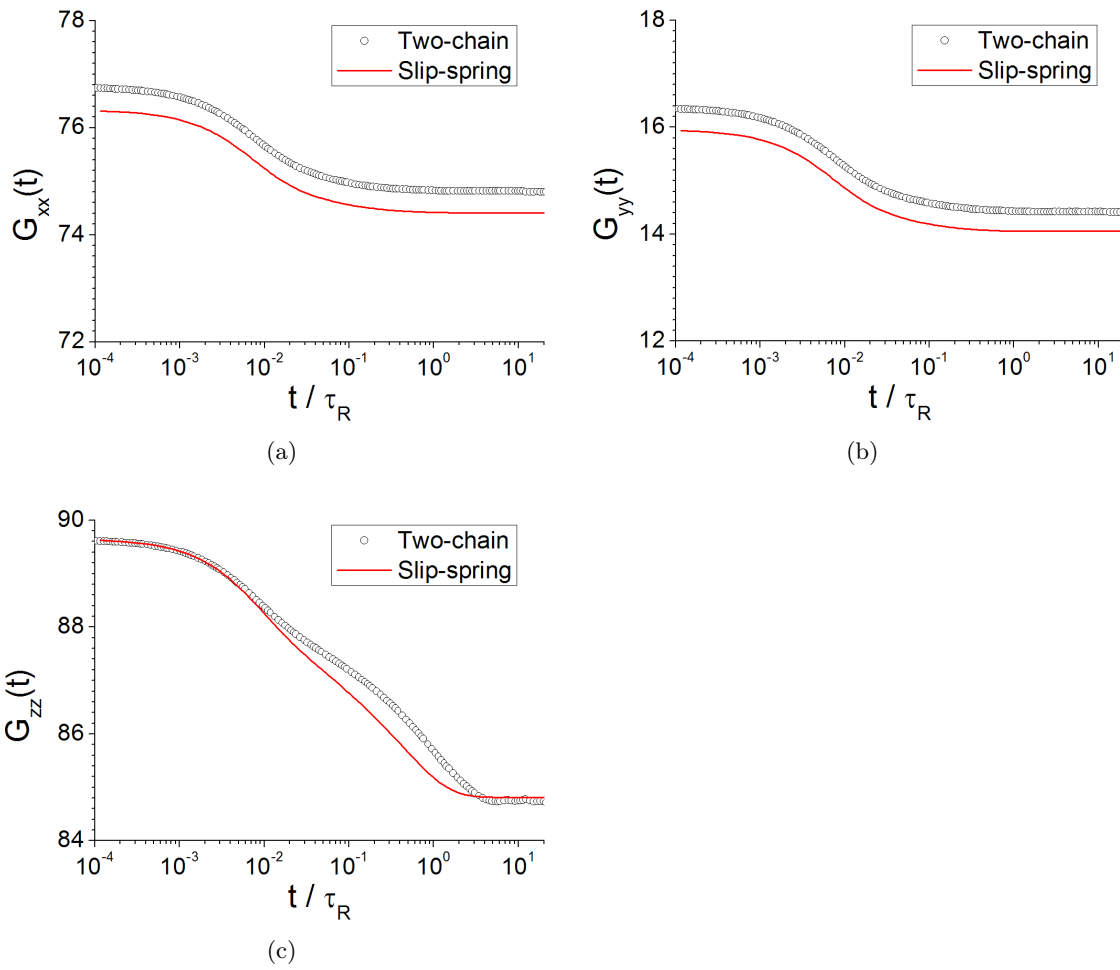


Figure 3.26: Comparison of two-chain model with the slip-spring model simulation for  $G_{\gamma\gamma}(t)$ . Parameters are  $N = 16$ ,  $H = 10$ ,  $D = 10$ ,  $h = 10.89$  and  $N_S = 4.20$ .

where  $y_0 = y_N = \langle y_j \rangle$  and there is no slip mechanism. In the limit of  $N \rightarrow \infty$ , this amplitude reduces to

$$\lim_{N \rightarrow \infty} (G_{yy}(0) - G_{yy}(\infty)) = 2ck_B T \quad (3.56)$$

as observed in the graph. For  $G_{xx}(t)$ , the stretch does play a role, but as Fig.3.26a demonstrates, this does not have a significant effect on the amplitude.  $G_{zz}(t)$  is more interesting; the slip-spring model has a secondary relaxation similar to the two-chain simulation, but the relaxation time is significantly shorter in the slip-spring model. After testing a range of other parameters, it appears that it is impossible to fully reproduce the dynamics of  $G_{zz}(t)$  with the current slip-spring model. The off-diagonal stress components are considered in Fig.3.27. These also indicate faster relaxation with the slip-spring model than the two-chain simulation. Any solution that corrects the delay in the relaxation of  $G_{zz}(t)$  will probably rectify the relaxation of the off-diagonal components as well. Such a solution is presented in section 4.2.

### 3.2.5 Mean bead positions

As described in section 2.1.3, the mean and variance of beads and bonds can explain the effects observed in properties such as  $G_{\gamma\gamma}(t)$ . For the best fit of the model to the two-chain model, the mean and variances should be as closely matched as possible. The mean position of the beads in the system are plotted in Fig.3.28. The domed shape of  $\langle z_i \rangle$  is produced by the slip of the slip-spring model, since without slip the model would be a three-armed-star, which has straight mean paths between the anchors and  $\mathbf{r}_j$ . The domed shape is the same for both the slip-spring and two-chain models, which indicates that the slip-spring strength and slip probability distribution in the slip-spring model are well matched to the force and dynamics of the entanglement in the two-chain model.

When the mean positions in the x-direction are examined closely, a discrepancy is observed

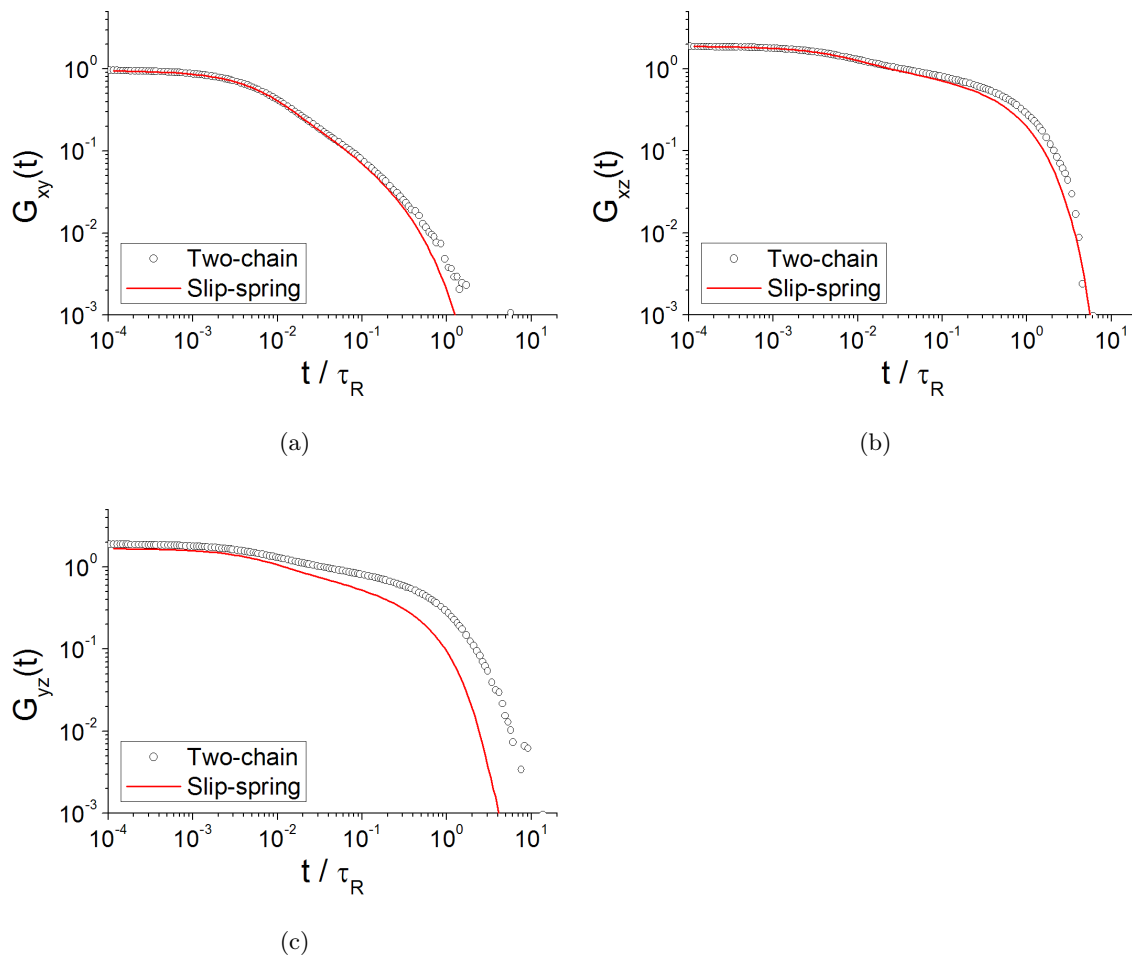


Figure 3.27: Comparison of two-chain model with the slip-spring model simulation for off-diagonal components of the stress relaxation. Parameters are  $N = 16$ ,  $H = 10$ ,  $D = 10$ ,  $h = 10.89$  and  $N_S = 4.20$ .

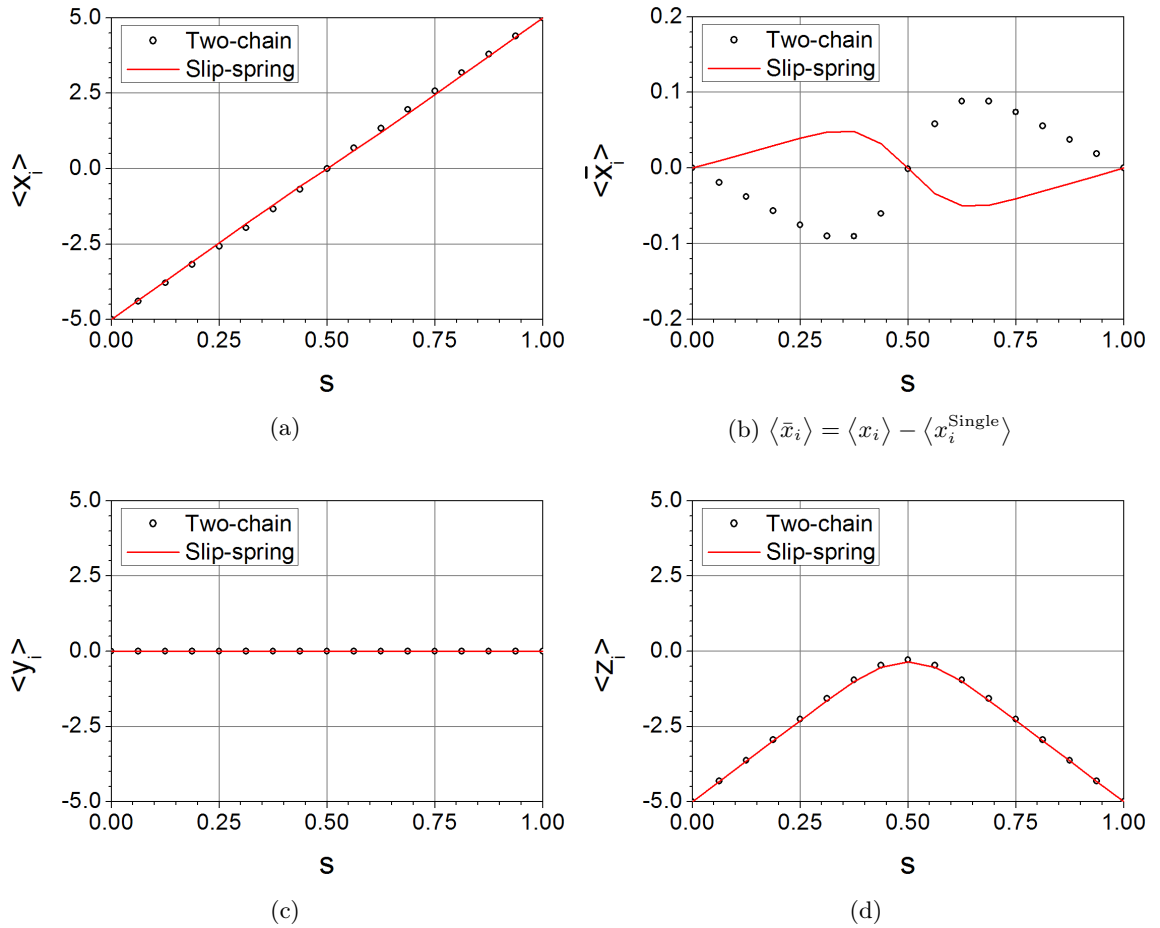


Figure 3.28: Mean position of each bead, where the bead number is expressed as a fraction along the chain,  $s = \frac{i}{N}$ . Plotted in Fig.3.28b is the unentangled x-direction positions subtracted from the entangled model's x-direction positions. Parameters are  $N = 16$ ,  $H = 10$ ,  $D = 10$ ,  $h = 10.89$  and  $N_S = 4.20$ .

in Fig.3.28a, which is made clearer when plotted as

$$\langle \bar{x}_i \rangle = \langle x_i \rangle - \langle x_i^{\text{Single}} \rangle \quad (3.57)$$

where  $\langle x_i^{\text{Single}} \rangle$  is given by Eq.(3.52), such that  $\langle \bar{x}_i \rangle$  is the displacement of the bead from its unentangled position. It is observed that, while the two-chain simulation pushes beads away from the middle bead, the slip-spring pulls beads towards the slip-spring anchoring point. This discrepancy is difficult to address, since it challenges the nature of the slip-spring model, which is based on a purely attractive linear spring. A bulky slip-chain model, introduced in section 4.3, will attempt to address this and is discussed further in section 6.6.

### 3.2.6 Variance of bead positions

The variances of bead positions are plotted in Fig.3.29. In the two-chain model, the variances are influenced by the entanglement and in the slip-spring model by the slip-spring. Fig.3.29d plots  $\text{var}(z_i)$  for a three-arm-star, representing the slip-spring model with no slip mechanism. The presence of the third arm reduces the variance of the middle bead compared to that of a single unentangled chain, which in turn reduces the variance of the neighbouring beads. The same effect is also noticed in the two-chain and slip-spring models. However,  $\text{var}(z_i)$  is higher for the slip-spring model, than the three-arm-star, as was similarly observed when the two-chain model was compared to the four-arm-star model in section 3.1.3. This was attributed to the application and removal of the entanglement, which is supported here by the observation that the slip-spring creates the same effect with the application and removal of the slip-spring as it slips from bead to bead.

In Fig.3.29a it is observed that  $\text{var}(x_i)$  and  $\text{var}(y_i)$  are much more like the single-chain model than  $\text{var}(z_i)$ , because the slip-link slips more easily in these directions, which reduces the effects of the slip-spring on the chain. Furthermore, Fig.3.29b and Fig.3.29c indicate that the slip-spring may be too strong in the x- and y-directions, causing  $\text{var}(x_i)$  and  $\text{var}(y_i)$  to be lower for the

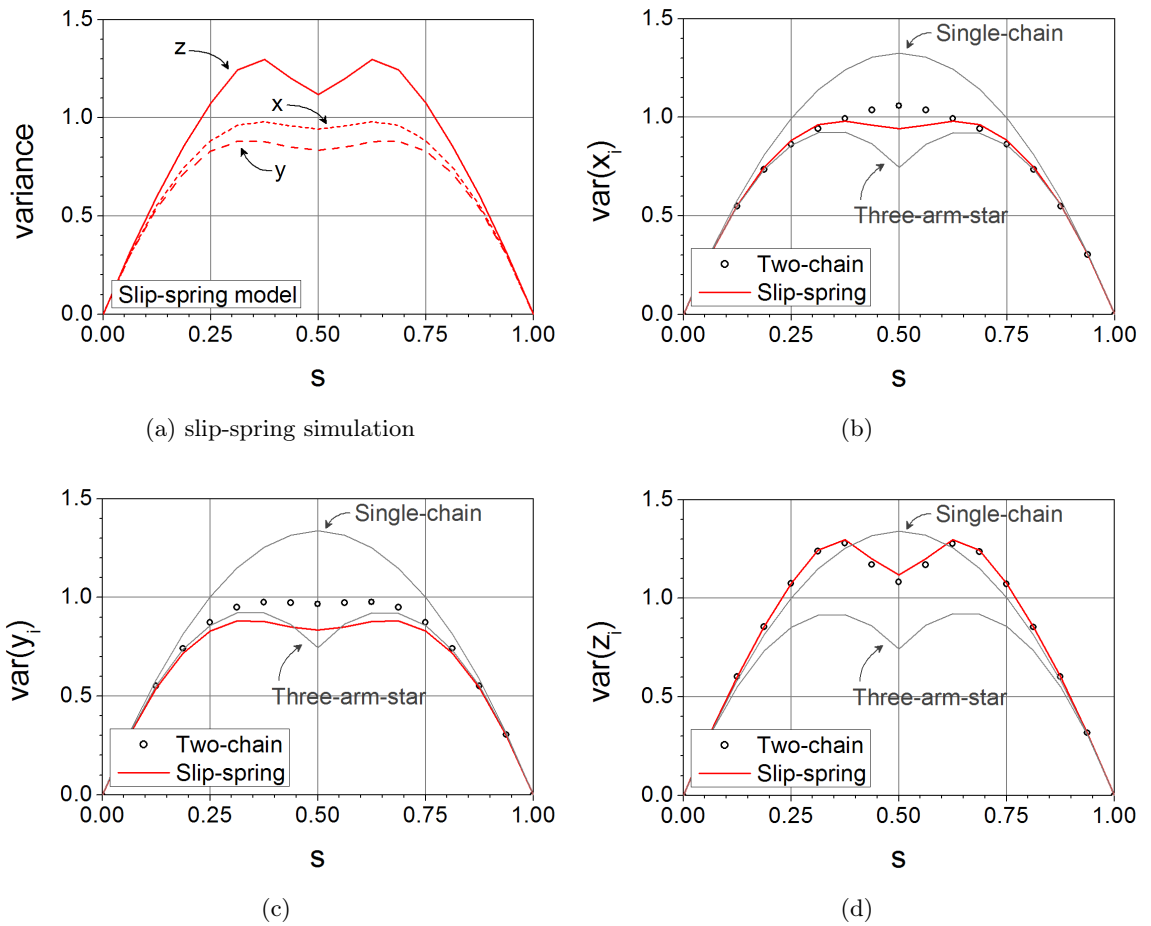


Figure 3.29: Variance from the mean position for each bead, where the bead number is expressed as a fraction along the chain,  $s = \frac{i}{N}$ . Parameters are  $N = 16$ ,  $H = 10$ ,  $D = 10$ ,  $h = 10.89$  and  $N_S = 4.20$ .

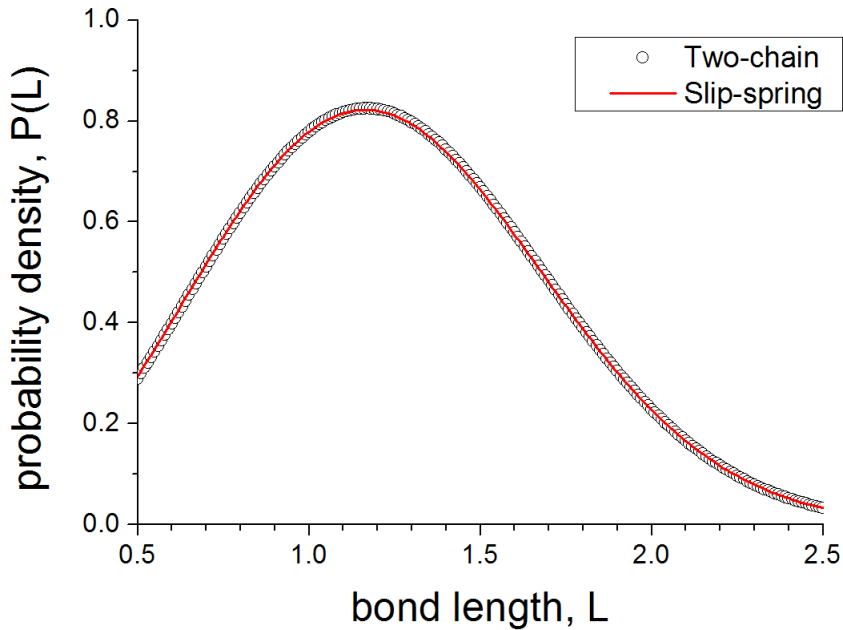


Figure 3.30: Probability density of bond lengths for the two-chain simulation and the slip-spring model. Parameters are  $N = 16$ ,  $H = 10$ ,  $D = 10$ ,  $h = 10.89$  and  $N_S = 4.20$ .

slip-spring model than the two-chain model. It is suggested that the fit would improve in these directions if the slip-spring was weaker and  $N_S$  larger. Indeed the parameter fitting in Fig.3.25 also indicated that a larger value of  $N_S$  is required to fit  $\langle \sigma_{xx} \rangle$  and  $\langle \sigma_{yy} \rangle$ .

### 3.2.7 Mean and variance of bond vectors

Fig.3.30 plots the probability density of bond lengths in the system, and it is observed that the slip-spring model agrees well with the two-chain simulation. However, Fig.3.31 shows that these bond lengths are not uniformly distributed and that the two models differ in the x-direction. In the two-chain simulation, the x-component of bond vectors increase near the middle bead, but in the slip-spring model, bonds decrease in length near the middle bead, as was observed from the bead positions. Despite this discrepancy, the stress relaxation (Fig.3.26a) is not too different between the two models. By analysing the bond vectors with respect to Eq.(2.29), it is clear why this occurs. The stress is dependent on the sum  $\sum_{i=1}^N \langle X_{i,i-1} \rangle^2$ , independent of the order

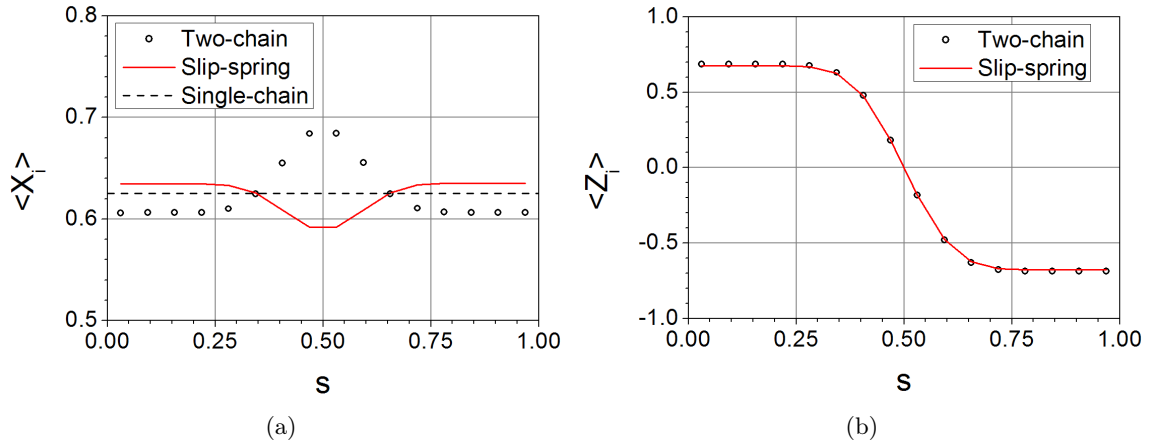


Figure 3.31: Average vector of each bond, where the bond number is expressed as a fraction along the chain,  $s = (i_{\text{bond}} + \frac{1}{2})/N$ . Parameters are  $N = 16$ ,  $H = 10$ ,  $D = 10$ ,  $h = 10.89$  and  $N_S = 4.20$ .

of bonds, so that both models may produce similar  $\langle \sigma_{xx} \rangle$ .

Stress in Eq.(2.29) also involves a sum of the variances of bond vectors, which are plotted in Fig.3.32. The two-chain model has a peak in  $\text{var}(X_i)$ , which is not reproduced by the slip-spring model. It is this difference which is responsible for  $\langle \sigma_{xx} \rangle$  being greater in the two-chain model; the same is observed in the y-direction. However, the variance of the z-component does have a peak around the middle bead in both models. The increase in bond variance can be explained by slip, as was done previously for the bead variance. This is supported by comparing Fig.3.32c to Fig.3.32d, where the probability density of slip-link position has the same width as the increase in bond variance.

### 3.2.8 Mean squared displacement, $g_{1,\text{mid}}(t)$

In Fig.3.33,  $g_{1,\text{mid}}(t)/t^{0.5}$  is examined for the slip-spring model. As described in section 2.1.4, a constant value of this function indicates Rouse motion. It is observed that the middle bead in the slip-spring model moves faster than the same bead in the two-chain simulation at intermediate time. To investigate this further, the individual components are displayed in Fig.3.34. Whilst

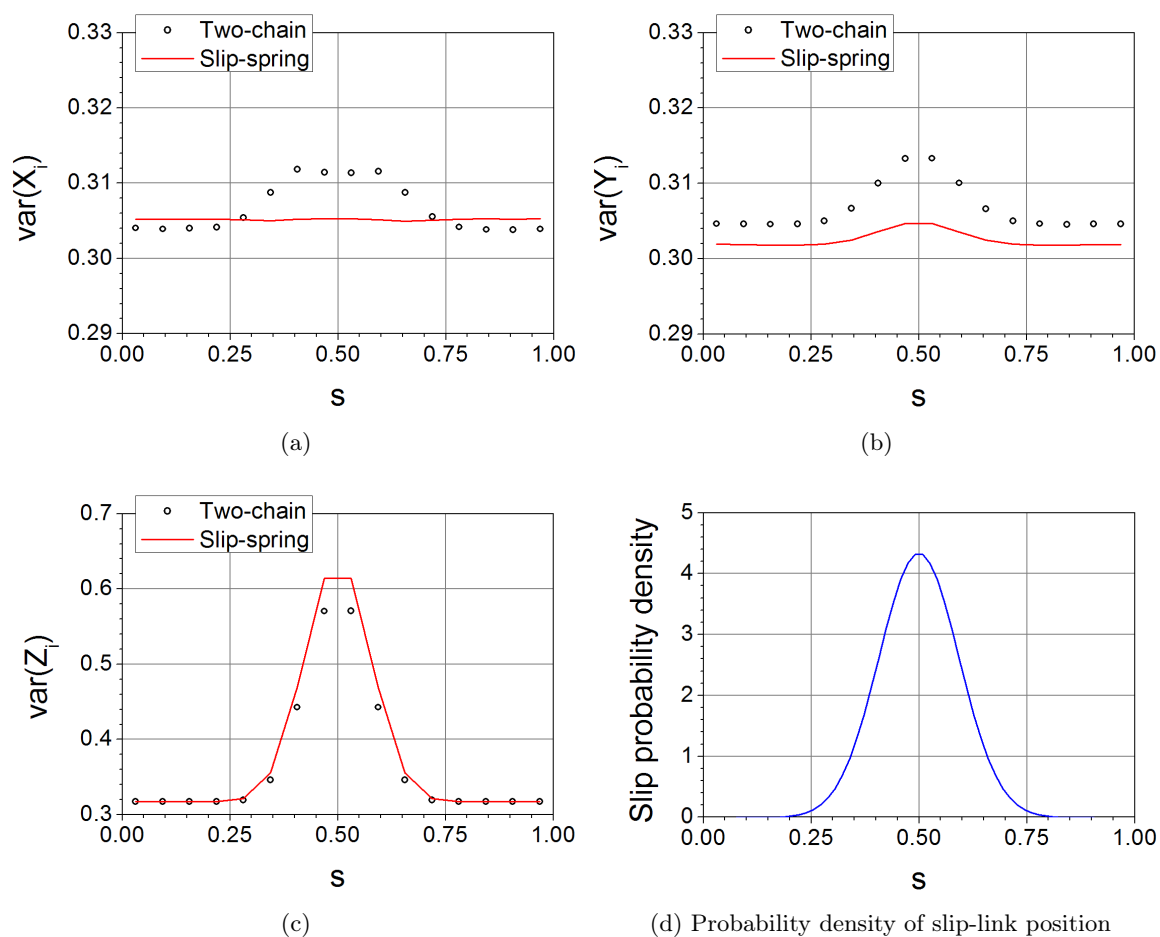


Figure 3.32: Variance from the average vector for each bond, where the bond number is expressed as a fraction along the chain,  $s = (i_{\text{bond}} + \frac{1}{2})/N$ . Parameters are  $N = 16$ ,  $H = 10$ ,  $D = 10$ ,  $h = 10.89$  and  $N_S = 4.20$ .

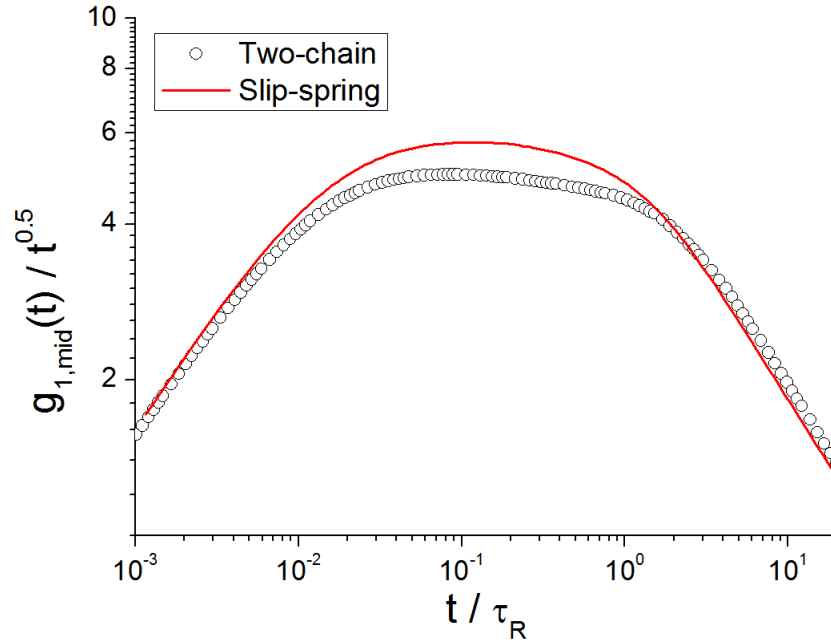


Figure 3.33: Mean squared displacement of the middle bead,  $g_{1,\text{mid}}(t)/t^{0.5}$ . Parameters are  $N = 16$ ,  $H = 10$ ,  $D = 10$ ,  $h = 10.89$  and  $N_S = 4.20$ .

the x- and y-components are not exactly the same for the two models, they are relatively good fits compared to the z-direction, where the middle bead moves significantly faster in the slip-spring model. This might explain why a delay in the stress relaxation,  $G_{zz}(t)$ , was not properly modelled by the slip-spring model in Fig.3.26a. It is possible that a modification to the slip-spring model that slows the middle bead in the z-direction, will also provide a delay in  $G_{zz}(t)$  that will improve both these properties. In section 4.2, such a modification is presented.

### 3.2.9 Summary

Using analytical calculations, a search was performed for the best pair of slip-spring parameters that reproduces the two-chain simulation. However, when the parameters are selected to fit the z-direction stress relaxation function,  $G_{zz}(t)$ , the other two diagonal components,  $G_{xx}(t)$  and  $G_{yy}(t)$ , differ somewhat from those in the two-chain simulation. Equally, if the parameters are adjusted to fit  $G_{xx}(t)$  and  $G_{yy}(t)$ , then  $G_{zz}(t)$  does not fit. It was observed that this was

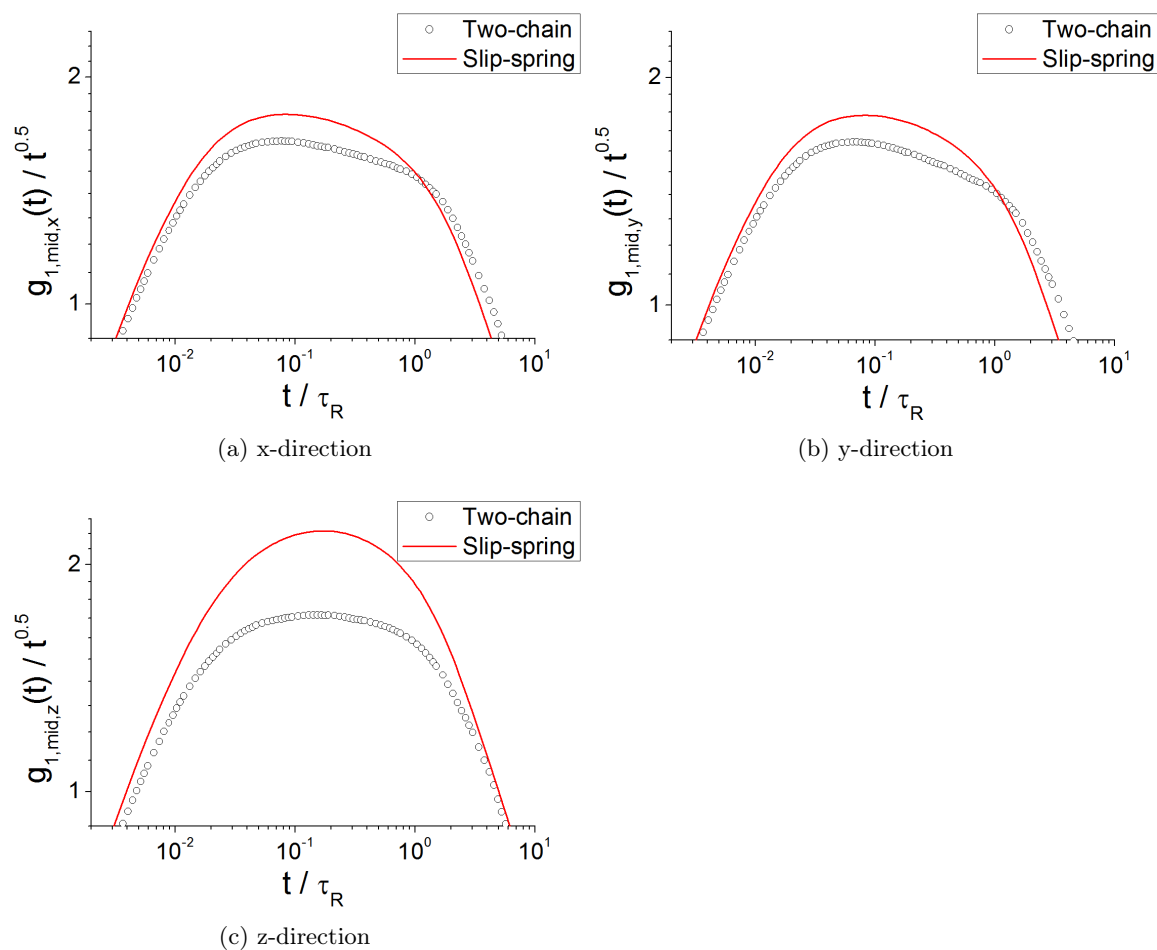


Figure 3.34: Mean squared displacement for individual components. Parameters are  $N = 16$ ,  $H = 10$ ,  $D = 10$ ,  $h = 10.89$  and  $N_S = 4.20$ .

due to lower average bond variance in the x- and y-directions, an issue that will be addressed with a non-isotropic model in section 4.1. The dynamics of  $G_{zz}(t)$  have also demonstrated a discrepancy between the two models; the slip-spring model fails to show the same delay in the stress relaxation that was observed in the two-chain simulation. As well as this, the mean squared displacement dynamics indicated that the middle bead moves in the z-direction faster in the slip-spring model than in the two-chain simulation. The slip-chain model provides a solution to both these discrepancies as will be shown in section 4.2. Finally, it has been observed in the x-component of the bead and bond positions that beads are pulled towards the middle of the system in the slip-spring model, rather than pushed away from the entanglement as in the two-chain model. A possible solution to this problem is presented in section 4.3.

## Chapter 4

# Modifications to the slip-spring model

### 4.1 Non-isotropic slip-spring model

It has been observed that the two-chain entanglement acts differently in each direction. In the x-direction, the lower chain can slide through the entanglement; in the y-direction, the upper chain hooks around the lower chain restricting its movement, forcing a section of the lower chain to follow the movement of the upper chain; and in the z-direction, the entanglement both hooks around the chain and stretches it. Hence, the entanglement applies a different effective force in each direction. It was originally assumed that the slip-spring would be able to reproduce the entanglement's different strengths, since the slip-spring vector is shortest in the x- and y-directions, giving a smaller force in these directions, as required. However, it was seen in the previous chapter that this alone does not simultaneously fit  $G_{\gamma\gamma}(t)$  for  $\gamma = x, y, z$ . Since it was demonstrated in Fig.3.25 that different values of  $N_S$  allow different components of the stress relaxation to fit the two-chain model results, a suggested solution is to make the slip-spring spring-constant non-isotropic.

Previously the potential energy of the slip-spring was given by

$$U^S = \frac{1}{2}kR_{A,j}^2 \quad (4.1)$$

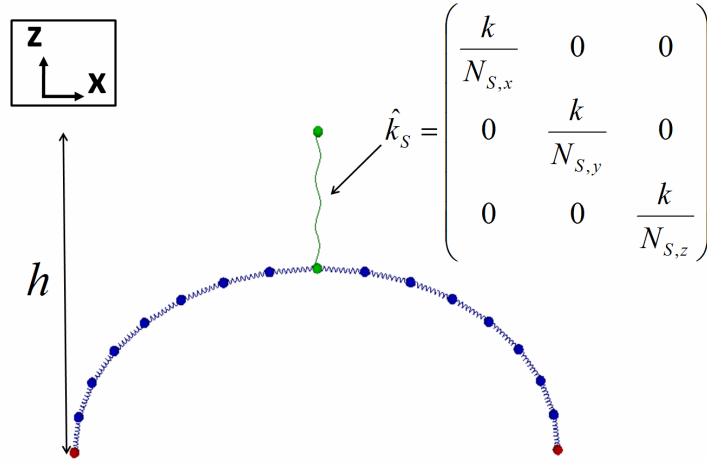


Figure 4.1: Diagram of the non-isotropic slip-spring model with the new slip-spring spring constant  $\hat{k}_S$

where  $\mathbf{R}_{A,j} = \mathbf{r}_A - \mathbf{r}_j$ . With the non-isotropic slip-spring this becomes

$$\begin{aligned} U^S &= \frac{1}{2} \mathbf{R}_{A,j} \hat{k}_S \mathbf{R}_{A,j} \\ &= \frac{1}{2} (X_{A,j} k_{S,xx} X_{A,j} + X_{A,j} k_{S,xy} Y_{A,j} + \dots + Z_{A,j} k_{S,zz} Z_{A,j}) \end{aligned} \quad (4.2)$$

where  $\mathbf{R}_{A,j} = (X_{A,j}, Y_{A,j}, Z_{A,j})$  and  $\hat{k}_S$  is a tensor spring-constant. Since, the system is symmetric in the x- and y-directions, the transformations  $X \rightarrow -X$  and  $Y \rightarrow -Y$  should have no effect on the energy, but in Eq.(4.2) terms like  $X_{A,j} k_{S,xy} Y_{A,j}$ ,  $X_{A,j} k_{S,xz} Z_{A,j}$  and  $Y_{A,j} k_{S,xz} Z_{A,j}$  change sign with this transformation. Thus, the off-diagonal components of the spring-constant tensor must be zero, and the new spring-constant tensor is written as

$$\hat{k}_S = \begin{pmatrix} \frac{k}{N_{S,x}} & 0 & 0 \\ 0 & \frac{k}{N_{S,y}} & 0 \\ 0 & 0 & \frac{k}{N_{S,z}} \end{pmatrix} \quad (4.3)$$

where the slip-spring strength parameter,  $N_S$ , becomes a set of three values

$$\{N_S\} = N_{S,x}, N_{S,y}, N_{S,z} \quad (4.4)$$

This new model with its four parameters is illustrated in Fig.4.1. The energy of this system is

$$\begin{aligned} U &= \frac{1}{2} \left( k \sum_{i=1}^N (\mathbf{r}_i - \mathbf{r}_{i-1})^2 + (\mathbf{r}_j - \mathbf{r}_A)^T \hat{k}_S (\mathbf{r}_j - \mathbf{r}_A) \right) \\ &= \frac{k}{2} \left( \sum_{i=1}^N (\mathbf{r}_i - \mathbf{r}_{i-1})^2 + \frac{(x_j - x_A)^2}{N_{S,x}} + \frac{(y_j - y_A)^2}{N_{S,y}} + \frac{(z_j - z_A)^2}{N_{S,z}} \right) \end{aligned} \quad (4.5)$$

and has the equation of motion

$$\xi d\mathbf{r}_i = k (\mathbf{r}_{i+1} - 2\mathbf{r}_i + \mathbf{r}_{i-1}) dt + \sqrt{2k_B T \xi} d\mathbf{W}_i(t) + \delta_{ij} \hat{k}_S (\mathbf{r}_A - \mathbf{r}_j) dt \quad (4.6)$$

#### 4.1.1 Analytical calculations

Because the energy of the system has changed, the partition function of the slip-spring object (Eq.(3.37)) is now

$$\begin{aligned} Z_S(\mathbf{r}_A, \mathbf{r}_j, \{N_S\}) &= \exp \left( -\frac{1}{2} (\mathbf{r}_j - \mathbf{r}_A)^T \hat{k}_S (\mathbf{r}_j - \mathbf{r}_A) \right) \\ &= \exp \left( -\frac{1}{2} \left( \frac{k(x_j - x_A)^2}{N_{S,x}} + \frac{k(y_j - y_A)^2}{N_{S,y}} + \frac{k(z_j - z_A)^2}{N_{S,z}} \right) \right) \end{aligned} \quad (4.7)$$

This modifies the partition function of the whole slip-spring system (Eq.(3.39)), which is now

$$\begin{aligned} Q_j(\mathbf{r}_A, \{N_S\}) &= \int Z_S(\mathbf{r}_A, \mathbf{r}_j, \{N_S\}) Z(\mathbf{r}_B, \mathbf{r}_j, j) Z(\mathbf{r}_C, \mathbf{r}_j, N-j) d^3\mathbf{r}_j \\ &= \int d^3\mathbf{r}_j \left( \frac{1}{j(N-j)} \right)^{\frac{3}{2}} \left( \frac{2\pi k_B T}{k} \right)^{\frac{3}{2}(N-2)} \\ &\quad \exp \left( -\frac{1}{2k_B T} \left( (\mathbf{r}_j - \mathbf{r}_A)^T \hat{k}_S (\mathbf{r}_j - \mathbf{r}_A) + \frac{k(\mathbf{r}_j - \mathbf{r}_B)^2}{j} + \frac{k(\mathbf{r}_j - \mathbf{r}_C)^2}{N-j} \right) \right) \end{aligned} \quad (4.8)$$

where each component of  $\mathbf{r}_j$  provides a factor

$$\begin{aligned} & \int dx_j \exp \left( -\frac{1}{2k_B T} \left( \frac{k(x_j - x_A)^2}{N_{S,x}} + \frac{k(x_j - x_B)^2}{j} + \frac{k(x_j - x_C)^2}{N-j} \right) \right) \\ &= \sqrt{\frac{2\pi}{k} \left( \frac{1}{j} + \frac{1}{N-j} + \frac{1}{N_{S,x}} \right)^{-1}} \\ & \exp \left( -\frac{1}{2k_B T} \left( \frac{k(x_j - x_A)^2}{N_{S,x}} + \frac{k(x_j - x_B)^2}{j} + \frac{k(x_j - x_C)^2}{N-j} \right) \right) \end{aligned} \quad (4.9)$$

to produce

$$\begin{aligned} Q_j(\mathbf{r}_A, \{N_S\}) &= \left( \frac{1}{j(N-j)} \right)^{\frac{3}{2}} \left( \frac{2\pi k_B T}{k} \right)^{\frac{3}{2}(N-1)} \\ & \frac{1}{\sqrt{\left( \frac{1}{j} + \frac{1}{N-j} + \frac{1}{N_{S,x}} \right)}} \exp \left( -\frac{\left( \frac{k(x_B - x_C)^2}{j(N-1)} + \frac{k(x_A - x_B)^2}{N_{S,x}j} + \frac{k(x_A - x_C)^2}{N_{S,x}(N-j)} \right)}{2k_B T \left( \frac{1}{j} + \frac{1}{N-j} + \frac{1}{N_{S,x}} \right)} \right) \\ & \frac{1}{\sqrt{\left( \frac{1}{j} + \frac{1}{N-j} + \frac{1}{N_{S,y}} \right)}} \exp \left( -\frac{\left( \frac{k(y_B - y_C)^2}{j(N-1)} + \frac{k(y_A - y_B)^2}{N_{S,y}j} + \frac{k(y_A - y_C)^2}{N_{S,y}(N-j)} \right)}{2k_B T \left( \frac{1}{j} + \frac{1}{N-j} + \frac{1}{N_{S,y}} \right)} \right) \\ & \frac{1}{\sqrt{\left( \frac{1}{j} + \frac{1}{N-j} + \frac{1}{N_{S,z}} \right)}} \exp \left( -\frac{\left( \frac{k(z_B - z_C)^2}{j(N-1)} + \frac{k(z_A - z_B)^2}{N_{S,z}j} + \frac{k(z_A - z_C)^2}{N_{S,z}(N-j)} \right)}{2k_B T \left( \frac{1}{j} + \frac{1}{N-j} + \frac{1}{N_{S,z}} \right)} \right) \end{aligned} \quad (4.10)$$

The changes to the partition function also result in a new slip-link position probability distribution (Eq.3.49) given by

$$P(j, \mathbf{r}_A, \{N_S\}) = \frac{Q_j(\mathbf{r}_A, \{N_S\})}{\sum_{j'=1}^{N-1} Q_{j'}(\mathbf{r}_A, \{N_S\})} \quad (4.11)$$

As was done previously for the slip-spring model this partition function is used to calculate the average position of the slip-link while attached to bead  $j$

$$\langle x_j \rangle = \frac{\frac{x_A}{N_{S,x}} + \frac{x_B}{j} + \frac{x_C}{N-j}}{\frac{1}{N_{S,x}} + \frac{1}{j} + \frac{1}{N-j}} \quad (4.12)$$

$$\langle y_j \rangle = \frac{\frac{y_A}{N_{S,y}} + \frac{y_B}{j} + \frac{y_C}{N-j}}{\frac{1}{N_{S,y}} + \frac{1}{j} + \frac{1}{N-j}} \quad (4.13)$$

$$\langle z_j \rangle = \frac{\frac{z_A}{N_{S,z}} + \frac{z_B}{j} + \frac{z_C}{N-j}}{\frac{1}{N_{S,z}} + \frac{1}{j} + \frac{1}{N-j}} \quad (4.14)$$

It is found that the average position is now dependent upon its own component of  $\{N_S\}$ . The same is found for Eq.(3.44) and Eq.(3.48), which are now

$$\begin{aligned} \langle \sigma_{j,\gamma\gamma} \rangle &= \frac{k_B T}{V} (N-2) + \frac{k_B T}{V} \frac{\frac{1}{j} + \frac{1}{N-j}}{\frac{1}{N_{S,\gamma}} + \frac{1}{j} + \frac{1}{N-j}} \\ &+ \frac{k}{V} \frac{\left( r_B^\gamma - \langle r_j^\gamma \rangle \right)^2}{j} + \frac{k}{V} \frac{\left( r_C^\gamma - \langle r_j^\gamma \rangle \right)^2}{N-j} \end{aligned} \quad (4.15)$$

and

$$\begin{aligned} \langle \sigma_{j,\gamma\gamma}^2 \rangle &= \frac{(k_B T)^2}{V^2} \left( N(N-2) + 2(N-2) \frac{\frac{1}{j} + \frac{1}{N-j}}{\frac{1}{N_{S,\gamma}} + \frac{1}{j} + \frac{1}{N-j}} + 3 \left( \frac{\frac{1}{j} + \frac{1}{N-j}}{\frac{1}{N_{S,\gamma}} + \frac{1}{j} + \frac{1}{N-j}} \right)^2 \right) \\ &+ 2 \frac{1}{V^2} k_B T k (N-2) \left( \frac{\left( r_B^\gamma - \langle r_j^\gamma \rangle \right)^2}{j} + \frac{\left( r_C^\gamma - \langle r_j^\gamma \rangle \right)^2}{N-j} \right) \\ &+ 2 \frac{1}{V^2} k_B T \frac{k}{\frac{1}{N_{S,\gamma}} + \frac{1}{j} + \frac{1}{N-j}} \left( \frac{\left( r_B^\gamma - r_C^\gamma \right)^2}{j(N-j)} + 3 \left( \frac{\langle r_j^\gamma \rangle - r_B^\gamma}{j} + \frac{\langle r_j^\gamma \rangle - r_C^\gamma}{N-j} \right)^2 \right) \\ &+ \frac{k^2}{V^2} \left( \frac{\left( r_B^\gamma - \langle r_j^\gamma \rangle \right)^2}{j} + \frac{\left( r_C^\gamma - \langle r_j^\gamma \rangle \right)^2}{N-j} \right)^2 \end{aligned} \quad (4.16)$$

We note here that, although stress moments  $\langle \sigma_{\gamma\gamma} \rangle$  and  $\langle \sigma_{\gamma\gamma}^2 \rangle$  with fixed  $j$  depend only on the corresponding  $N_{S,\gamma}$ , the slip couples all components through Eq.(4.11). Therefore,  $\langle \sigma_{xx} \rangle$ , for example, will depend on  $N_{S,y}$  and  $N_{S,z}$  as well as  $N_{S,x}$ .

### 4.1.2 Parameter finding

With these analytical solutions for the diagonal components of the stress tensor, it is once again possible to find the best parameters for the slip-spring model. However, this model has four parameters and while a graph was the best method to investigate parameter space for two parameters, a system with four parameters is not as simple to visualise. Instead, a minimisation technique is used to find the best point in parameter space. The technique used in this study was Nelder–Mead downhill simplex minimisation [34]. The height of the slip-spring,  $h$ , and the non-isotropic strength of the slip-spring,  $\{N_S\}$ , were adjusted to minimise the function

$$\sum_{\gamma=x,y,z} \left( \langle \sigma_{\gamma\gamma}^{\text{TC}} \rangle - \langle \sigma_{\gamma\gamma}^{\text{SS}} \rangle \right)^2 + \sum_{\gamma=x,y,z} \left( \sqrt{\langle (\sigma_{\gamma\gamma}^{\text{TC}})^2 \rangle} - \sqrt{\langle (\sigma_{\gamma\gamma}^{\text{SS}})^2 \rangle} \right)^2 \quad (4.17)$$

where  $\sigma^{\text{TC}}$  is the stress tensor for the two-chain simulation and  $\sigma^{\text{SS}}$  is the stress tensor for the slip-spring model.

Using this method, a two chain simulation with parameters  $N = 16$ ,  $H = 10$  and  $D = 10$  was fit to a non-isotropic slip-spring model, producing the parameter set  $h = 10.89$ ,  $N_{S,x} = 8.48$ ,  $N_{S,y} = 9.85$ ,  $N_{S,z} = 4.20$ . Previously, the parameters of the original slip-spring model were  $h = 10.89$  and  $N_S = N_{S,\gamma} = 4.20$ . The parameters have remained the same in the z-direction, but have changed in the x- and y-directions.  $N_{S,x}$  and  $N_{S,y}$  have significantly increased in value, weakening the slip-spring in those directions, as expected.

### 4.1.3 Parameters and dependence on entanglement strength

This minimisation technique was also used to obtain slip-spring parameters for a range of two-chain models with different system heights,  $H$ . The system height represents the strength of the entanglement as discussed in section 1.1. Fig.4.2a demonstrates that when the system is stretched in the z-direction, the slip-spring height minus a constant,  $h - 1.1$ , is also stretched affinely, such that  $H \rightarrow \lambda H$  when  $(h - 1.1) \rightarrow \lambda(h - 1.1)$ , where  $\lambda$  is the deformation coefficient. A constant must be added to  $h$  because the rejection routine causes a separation between the two chains

even when  $H = 0$ . The graphs for  $N_{S,\gamma}$  suggest that these three parameters remain constant during a deformation of system height for an intermediate level of stretch. This is promising for the model because it implies that the parameters do not have to be modified when the system is deformed. It is found that  $N_{S,z} \approx 4$ , which is significant because this corresponds to the effective spring strength of two chains of length 8 as found in the four-arm-star approximation of the two-chain simulation, when  $N = 16$ . However, it is found that  $N_{S,x} \approx N_{S,y} \approx 9$ , which does not have a simple explanation, apart from that it is due to the chain being to slide through the entanglement more easily in these directions.

For small and negative values of  $H$ , the two chains are not strongly entangled. With enough separation and  $H < 0$ , the two chains should not interact at all. When this occurs, it is expected that all components of  $\{N_S\}$  become infinite, corresponding to the slip-spring having no effect on the chain. In Fig.4.2 it is found that the change in behaviour occurs earlier than this. Furthermore, the point where this occurs depends on direction, validating the need for a different  $N_S$  per direction. The two-chain model is considered to explain this behaviour. As  $H$  decreases, the hooking between the two chains is reduced and beads have much more freedom to move in the x- and y-directions; Fig.1.1a demonstrates this situation. This results in  $N_{S,x}$  and  $N_{S,y}$  approaching infinity earlier than  $N_{S,z}$ , which remains strong, because the presence of the other chain still causes repulsion between the two entangled chains. With further separation the slip-spring will also become weaker in the z-direction, eventually becoming infinitely weak when the two chains are no longer interacting.

For  $H \rightarrow \infty$  it was predicted that the slip-link would be permanently on the middle bead, since  $h$  had become large, and  $N_{S,\gamma}$  should remain constant. Yet, it is observed in Fig.4.2 that at  $H > 20$  the values of  $N_{S,x}$  and  $N_{S,y}$  increase. This could be due to the rejection method generating artifacts as  $H$  becomes too large, which causes the number of rejections to become extreme. This would then cause the fitting method to produce inaccurate parameter values, because the two-chain simulation it is fitting to is inappropriate.

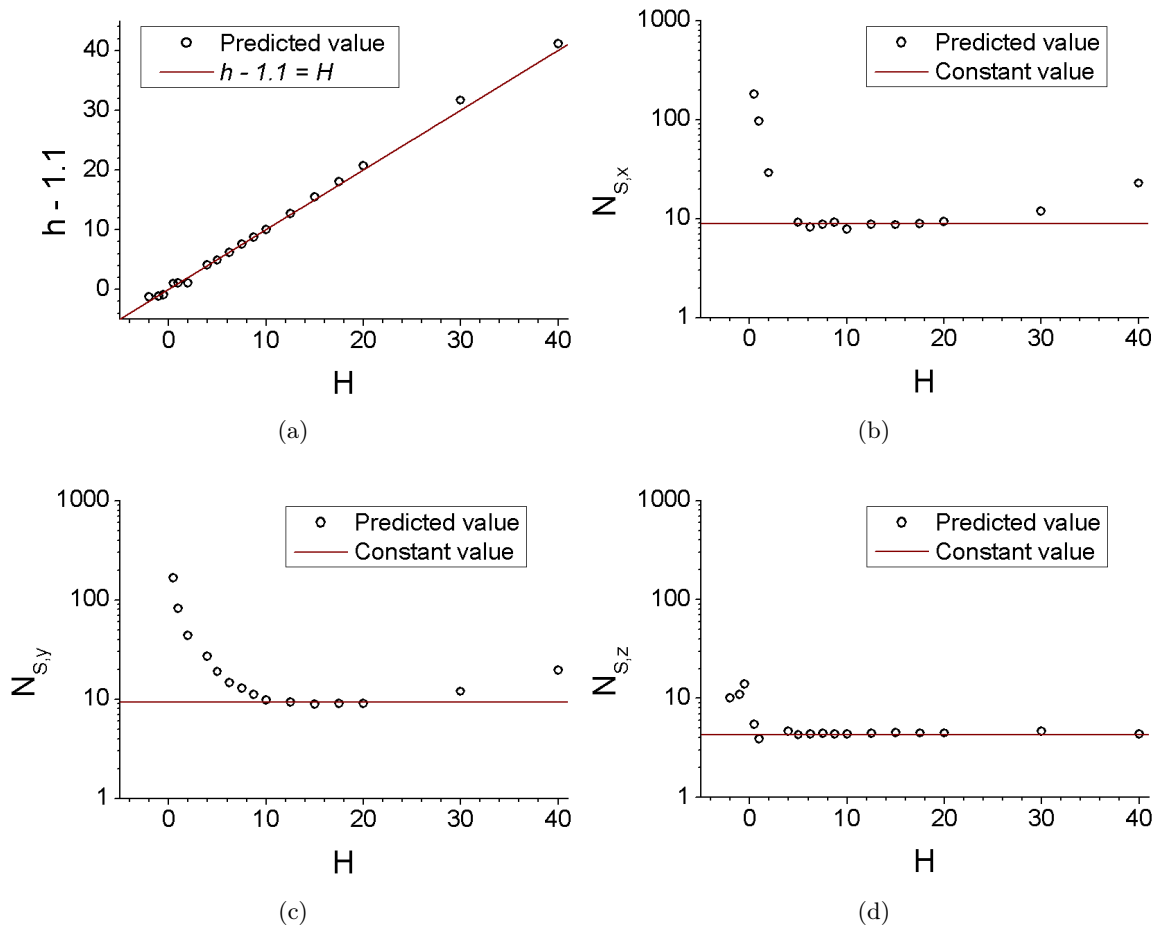


Figure 4.2: Slip-spring parameters as a function of two-chain simulation height. The system has parameters  $N = 16$ ,  $D = 10$ . Noise on the graphs is due to statistical errors in the two-chain simulation data target values provided to the minimisation method.

#### 4.1.4 Stress relaxation functions

As expected from the analytical calculations, stress relaxation function graphs for the diagonal components in Fig.4.3 have good agreement between the two-chain simulation and the non-isotropic slip-spring model. The non-isotropic model values for  $G_{xx}(t)$  and  $G_{yy}(t)$  agree with the two-chain simulation at  $t = 0$  and  $t = \infty$ , where they previously did not for the original slip-spring model; the dynamics of  $G_{xx}(t)$  and  $G_{yy}(t)$  are also in agreement. For  $G_{zz}(t)$  there is a good fit for  $G_{zz}(0)$  and  $G_{zz}(\infty)$ , as there was before in the original isotropic slip-spring model, but the model still relaxes faster than the two-chain simulation.

#### 4.1.5 Variance of bead and bond vectors

In Fig.4.4 it is observed that the non-isotropic model has increased variance of bead positions in the x- and y-directions, since the slip-spring strength has been made weaker in these two directions. This has made the variance closer to that of the two-chain simulation, but it is still not a perfect match. In both directions the variance is slightly too high and in the x-direction the distribution of the variance is different for the central four beads.

In Fig.4.5 the variance of bonds in the x- and y-directions is plotted. These graphs show that, with increased  $N_S$  in the x- and y-directions, the non-isotropic model, rather than increasing the bond variance at the centre of the chain, has increased the variance of all bonds. This made the value of  $\langle \sigma_{xx} \rangle$  equal by changing  $\sum_{i=1}^N \text{var}(X_{i,i-1})$  in Eq.(2.29), but did not do so by fitting individual bonds to the two-chain simulation. To understand why this occurred, consider a single unentangled Rouse chain. The energy of a single chain is given by the sum of its bonds,

$$\begin{aligned} U^{\text{Single}}(\{\mathbf{r}_i\}) &= \frac{1}{2}k(\mathbf{r}_0 - \mathbf{r}_1)^2 + \frac{1}{2}k(\mathbf{r}_1 - \mathbf{r}_2)^2 + \dots + \frac{1}{2}k(\mathbf{r}_{n-1} - \mathbf{r}_n)^2 \\ \Rightarrow U^{\text{Single}}(\{\mathbf{R}_{ij}\}) &= \frac{1}{2}kR_{0,1}^2 + \frac{1}{2}kR_{1,2}^2 + \dots + \frac{1}{2}kR_{n-1,n}^2 \end{aligned} \quad (4.18)$$

where  $\mathbf{R}_{ij} = \mathbf{r}_i - \mathbf{r}_j$ . Hence, the probability density of bead positions can be expressed in terms

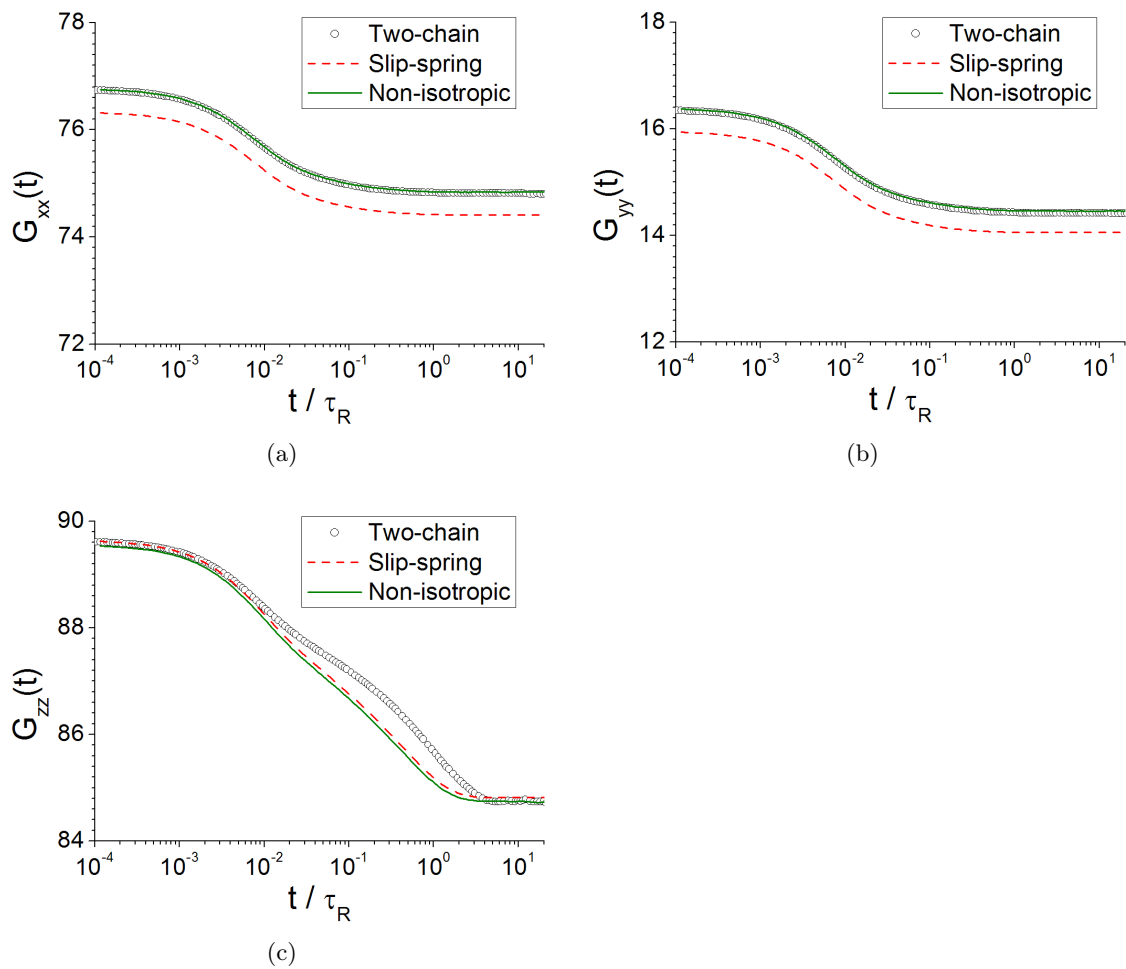


Figure 4.3: Stress relaxation functions of the diagonal components of the stress tensor. Parameters are  $N = 16$ ,  $H = 10$ ,  $D = 10$ . In the slip-spring model  $h = 10.89$  and  $N_S = 4.20$ . In the non-isotropic slip-spring model  $h = 10.89$ ,  $N_{S,x} = 8.48$ ,  $N_{S,y} = 9.85$ ,  $N_{S,z} = 4.20$ .

of individual bonds,

$$\begin{aligned} P^{\text{Single}}(\{\mathbf{R}_{ij}\}) &= \frac{1}{\mathcal{N}} \exp\left(\frac{-U^{\text{Single}}(\{\mathbf{R}_{ij}\})}{k_B T}\right) \\ &= \frac{1}{\mathcal{N}} \exp\left(\frac{k}{2k_B T} R_{0,1}^2\right) \exp\left(\frac{k}{2k_B T} R_{1,2}^2\right) \dots \exp\left(\frac{k}{2k_B T} R_{n-1,n}^2\right) \end{aligned} \quad (4.19)$$

which is a product of the probability density of each bond

$$P(\mathbf{R}_{ij}) = \frac{1}{\mathcal{N}_{ij}} \exp\left(\frac{k}{2k_B T} R_{ij}^2\right) \quad (4.20)$$

where  $\mathcal{N}$  and  $\mathcal{N}_{ij}$  are normalisation are such that

$$\int P(\mathbf{R}_{ij}) d^3\mathbf{R}_{ij} = 1 \quad (4.21)$$

$$\mathcal{N} = \prod_{ij} \mathcal{N}_{ij} \quad (4.22)$$

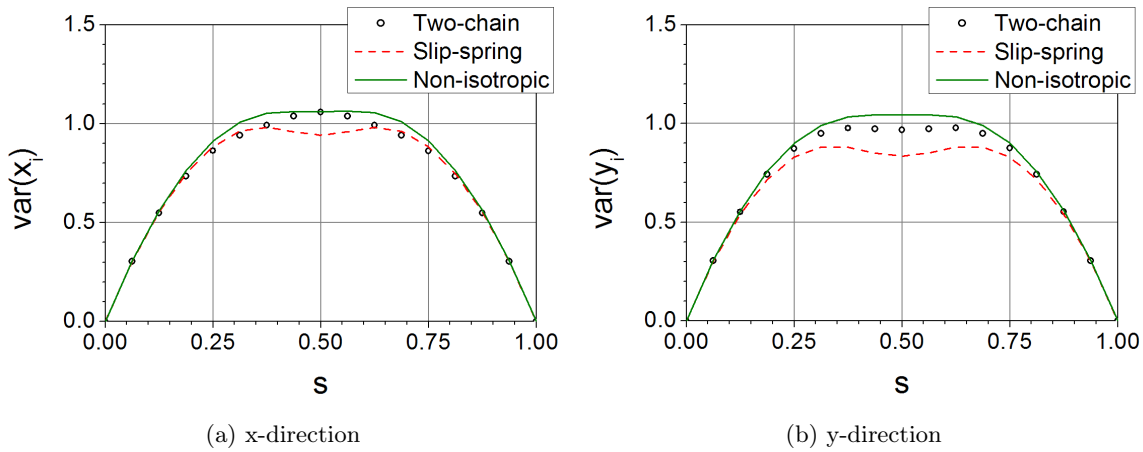


Figure 4.4: Variance of position for each bead, where the bead number is expressed as a fraction along the chain,  $s = \frac{i}{N}$ . Parameters are  $N = 16$ ,  $H = 10$ ,  $D = 10$ . In the slip-spring model  $h = 10.89$  and  $N_S = 4.20$ . In the non-isotropic slip-spring model  $h = 10.89$ ,  $N_{S,x} = 8.48$ ,  $N_{S,y} = 9.85$ ,  $N_{S,z} = 4.20$ .

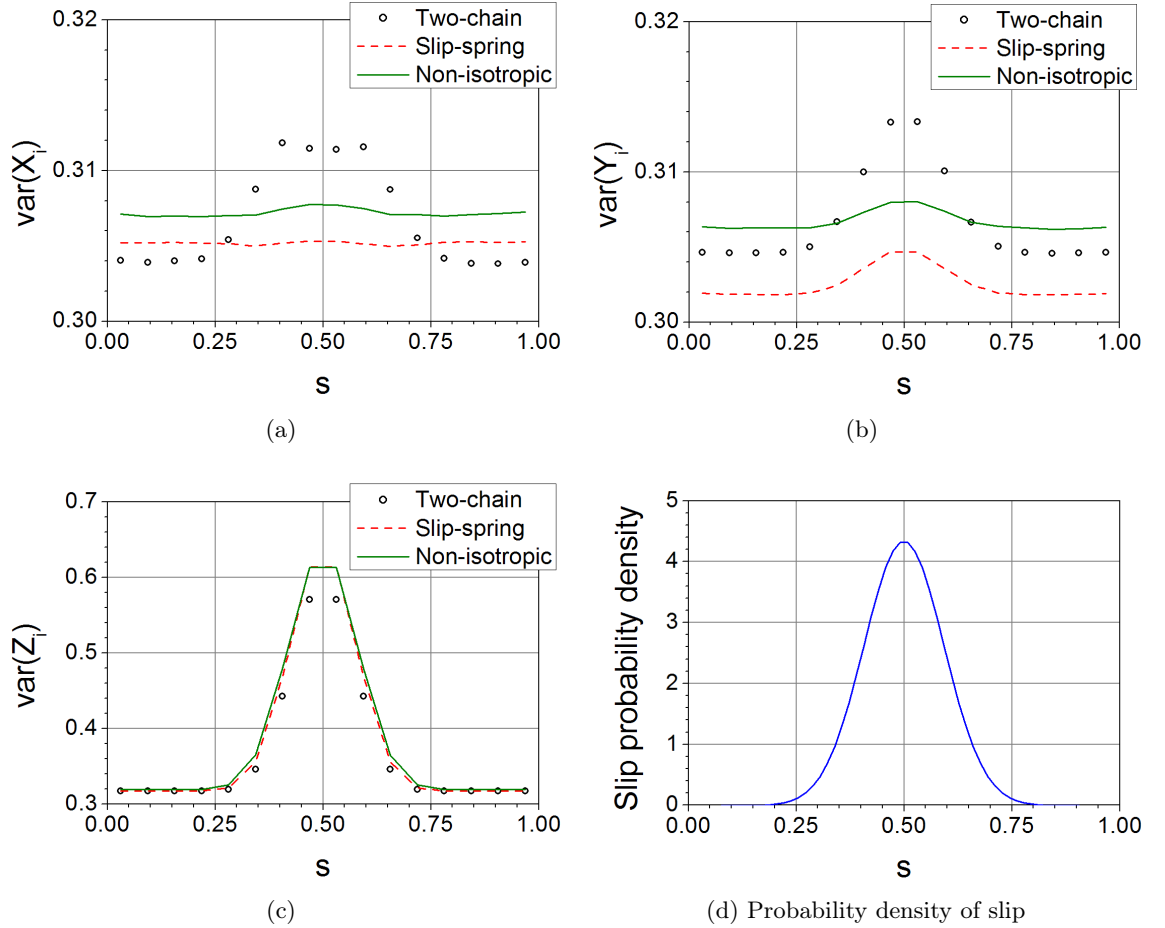


Figure 4.5: Variance from the average vector for each bond, where the bond number is expressed as a fraction along the chain,  $s = (i_{\text{bond}} + \frac{1}{2})/N$ . In the non-isotropic model  $N_{S,x}$  and  $N_{S,y}$  are larger than  $N_S$  in the slip-spring model. Parameters are  $N = 16$ ,  $H = 10$ ,  $D = 10$ . In the slip-spring model  $h = 10.89$  and  $N_S = 4.20$ . In the non-isotropic slip-spring model  $h = 10.89$ ,  $N_{S,x} = 8.48$ ,  $N_{S,y} = 9.85$ ,  $N_{S,z} = 4.20$ .

These probability densities are independent from each other, which means the variance of bonds are independent from each other and thus equal in an unentangled chain. Despite the presence of an additional force on bead  $j$ , the probability densities of each bond within the lower chain are still equal. The value of this variance can be calculated from  $\langle \sigma_{\gamma\gamma} \rangle$ . In the y-direction, where the average stretch term is zero, the relationship between stress and variance is known from Eq.(2.29) to be

$$\langle \sigma_{yy} \rangle = \frac{k}{V} \sum_{i=1}^n \text{var} (Y_{i,i-1}) \quad (4.23)$$

where  $Y_{ij} = y_i - y_j$ . Because the average length of the bonds is equal in the y-direction,  $|Y^{\text{Single}}| = |Y_{i,i-1}|$  and

$$\langle \sigma_{yy}^{\text{Single}} \rangle = \frac{k}{V} N \text{var} (Y^{\text{Single}}) \quad (4.24)$$

The average stress for the unentangled chain is also given by Eq.(2.16),

$$\langle \sigma_{yy}^{\text{Single}} \rangle = \frac{k_B T}{V} (N - 1) \quad (4.25)$$

Thus, the combination of Eq.(4.24) and Eq.(4.25) creates an equation for the variance of bonds in terms of the number of bonds in the chain,  $N$ ,

$$\text{var} (Y^{\text{Single}}) = \frac{k_B T}{k} \frac{(N - 1)}{N} \quad (4.26)$$

where  $k = \frac{3k_B T}{b^2}$ .

Using the stress for a slip-spring model with no slip, Eq.(4.15), with Eq.(4.24), an equation for the variance of each bond in a slip-spring model with no slip is constructed,

$$\text{var} (Y^{\text{noslip}}) = \frac{b^2}{3N} \left( N - 2 + \frac{\frac{1}{j} + \frac{1}{N-j}}{\frac{1}{N_{s,y}} + \frac{1}{j} + \frac{1}{N-j}} \right) \quad (4.27)$$

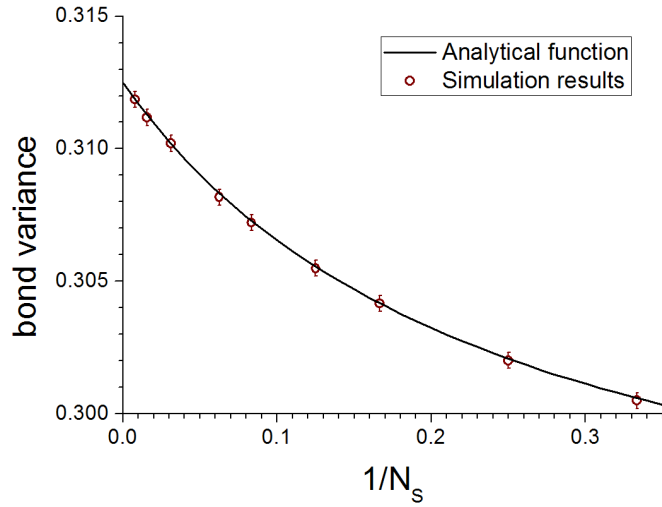


Figure 4.6: Variance of bond vectors in a single direction, for a range of slip-spring strengths in a slip-spring model with no slip mechanism. The variance is equal for all bonds in all directions. The analytical function is given by (4.27). Parameters are  $N = 16$ ,  $j = 8$ .

where  $j$  is the bead index to which the slip-link is permanently fixed. In Fig.4.6 this function is confirmed by comparing it to simulation data for the same model. Hence, changing the strength of the third arm (slip-spring) affects the variance of all chain bonds equally, no matter where the arms are connected. Because of this, the slip-spring model adds a variance to all bonds proportional to  $N_S$ , independent of the bead that the slip-link is on. But a second effect is also applied to individual bonds by the slip, as observed in Fig.4.5, causing peaks in variance around the central beads, especially in  $\text{var}(Z_i)$ , which has been demonstrated in section 3.2.6 to be due to the slip applying and removing a deformation. It is still observed that the entanglement in the two-chain model caused higher variance peaks than the slip-spring model, even with the non-isotropic model. It is likely that the two-chain simulation has a higher peak variance because the chain does not just slide along the chain as the slip-link does, but the two chains can also separate and break contact. This mechanism of two chain separation provides another method of force removal that would result in additional variance. Unable to replicate this, the slip-spring model increases the variance of every bond using Eq.(4.27), by increasing  $N_{S,x}$  and  $N_{S,y}$ , such that  $\sum_{i=1}^N \text{var}(Y_{i,i-1})$  is the same for both the slip-spring and the two-chain simulation. This

is why the two models differ. Without changing the fundamental way that the model works, it would appear that this effect can not be exactly reproduced by the slip-spring model.

#### 4.1.6 Summary

The non-isotropic slip-spring model replaces the scalar spring constant of the slip-spring with a tensor spring-constant. This makes the spring strength parameter,  $N_S$ , a set of parameters,  $\{N_S\} = N_{S,x}, N_{S,y}, N_{S,z}$ . With this modification, analytical calculations and a minimisation technique were used to find the best parameters to fit the model to values of  $\langle \sigma_{\gamma\gamma} \rangle$  and  $\langle \sigma_{\gamma\gamma}^2 \rangle$  obtained from a two-chain simulation. This indicated increased values of  $N_{S,x}$  and  $N_{S,y}$  were required. With the parameters now adjusted to fit all the static values of  $G_{\gamma\gamma}(t)$ , the slip-spring stress relaxation functions,  $G_{xx}(t)$  and  $G_{yy}(t)$  were great fits to the two-chain model. However, the variance of bonds in this model are still different to the two-chain simulation. The two-chain simulation has a mechanism whereby the two chains can separate, which is not reproduced in the slip-spring model. This effect results in a higher variance on the central bonds and can not be reproduced by the slip-spring model. The non-isotropic model compensates for this by increasing the variance of all bonds uniformly. While not a perfect solution, this fulfills the aim of a model, which is to simplify the original two-chain situation, but still reproduce the important properties such as stress.

## 4.2 Slip-chain model

Comparing the slip-spring model to the two-chain model has indicated that beads in the slip-spring model move too fast in the  $z$ -direction, the direction in which the system is stretched by the entanglement. The non-isotropic model was unable to solve this problem by changing the parameters of the slip-spring model. It is therefore necessary to add a new physical mechanism to the model, one which can slow the motion of the beads in the  $z$ -direction. A possible option is to change the slip-spring into a slip-chain (Fig.4.7). Rather than having a single bond connecting

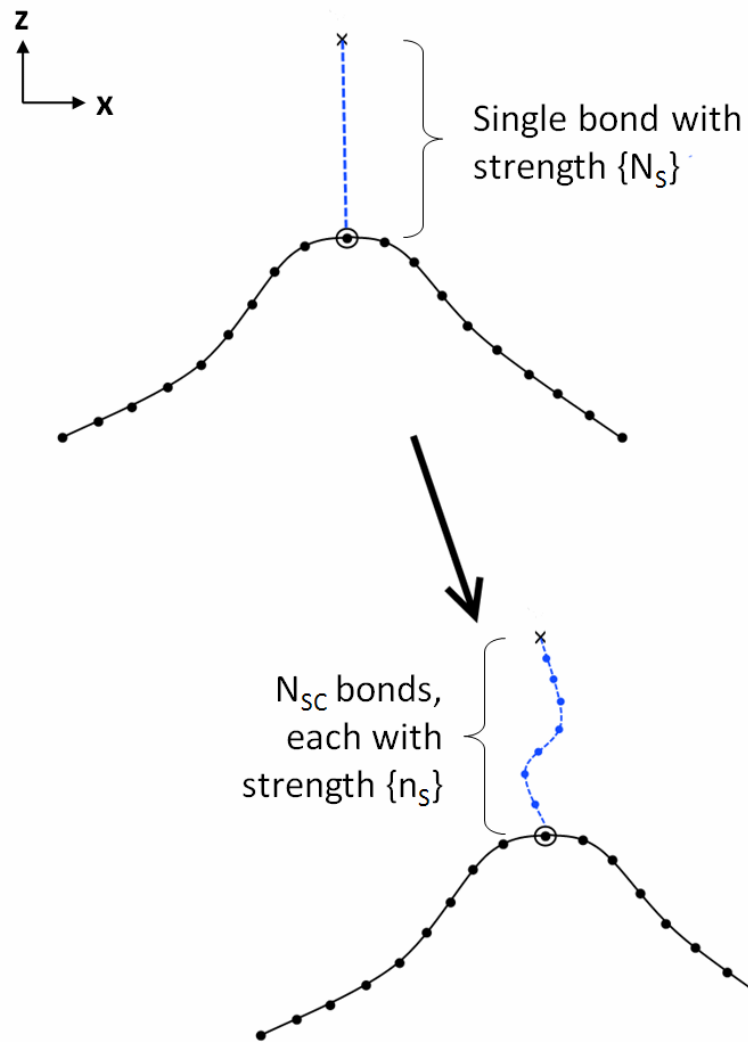


Figure 4.7: The slip-chain model replaces the spring from the slip-spring model, with a Rouse chain composed of  $N_{SC}$  bonds. Each bond in the slip-chain has the strength  $\{n_S\}$ , such that  $N_{S,\gamma} = N_{SC} n_{S,\gamma}$ .

the slip-link to its anchor without any extra friction, this new model has a Rouse chain connecting the slip-link to the anchor, which adds friction to the motion of the slip-link. The beads within this slip-chain have equal friction to the beads in the polymer chain, and the total strength of the slip-chain is equal to that of the previous slip-spring. Hence,

$$N_{S,\gamma} = N_{SC} n_{S,\gamma} \quad ; \quad \gamma = x, y, z \quad (4.28)$$

and

$$\hat{k}_{SC} = \begin{pmatrix} \frac{k}{n_{S,x}} & 0 & 0 \\ 0 & \frac{k}{n_{S,y}} & 0 \\ 0 & 0 & \frac{k}{n_{S,z}} \end{pmatrix} \quad ; \quad k = \frac{3k_B T}{b^2} \quad (4.29)$$

where  $N_{SC}$  is the number of slip-chain bonds and  $n_S$  is the strength of each individual slip-chain bond.

The equation of motion for the system is now in two parts, one describing the motion of the beads within the polymer chain

$$\xi d\mathbf{r}_i = k (\mathbf{r}_{i+1} - 2\mathbf{r}_i + \mathbf{r}_{i-1}) dt + \sqrt{2k_B T \xi} d\mathbf{W}_i(t) + \delta_{ij} \hat{k}_{SC} (\mathbf{s}_{N_{SC}-1} - \mathbf{r}_j) dt \quad (4.30)$$

and one describing the motion of the beads within the slip-chain, which have position vectors  $\mathbf{s}_m$ ,

$$\xi d\mathbf{s}_m = \hat{k}_{SC} (\mathbf{s}_{m+1} - 2\mathbf{s}_m + \mathbf{s}_{m-1}) dt + \sqrt{2k_B T \xi} d\mathbf{W}_m(t) \quad (4.31)$$

for  $1 < m < N_{SC}$ . The anchoring point of the slip-chain is labelled as  $m = 0$ , such that  $\mathbf{s}_0 = \mathbf{r}_A$ , and the slip-link is  $\mathbf{s}_{N_{SC}} = \mathbf{r}_j$ . The energy of the slip-chain model is given by

$$U = \sum_{i=1}^N \frac{3k_B T}{2b^2} (\mathbf{r}_i - \mathbf{r}_{i-1})^2 + \sum_{m=1}^{N_{SC}} \frac{1}{2} (\mathbf{s}_m - \mathbf{s}_{m-1})^T \hat{k}_{SC} (\mathbf{s}_m - \mathbf{s}_{m-1}) \quad (4.32)$$

Because the energy is now a sum of slip-chain bonds, the partition function for the non-isotropic

slip-spring Eq.(4.7) becomes a partition function for a Rouse chain Eq.(3.36),

$$Z_{SC}(\mathbf{r}_A, \mathbf{r}_j, \{N_S\}, N_{SC}) = \left(\frac{1}{N_{sc}}\right)^{\frac{3}{2}} \left( \left(\frac{2\pi k_B T}{k}\right)^3 \frac{N_{S,x} N_{S,y} N_{S,z}}{N_{SC}^3} \right)^{\frac{1}{2}(N_{sc}-1)} \exp\left(-\frac{1}{2k_B T} \left( \frac{k(x_j - x_A)^2}{N_{S,x}} + \frac{k(y_j - y_A)^2}{N_{S,y}} + \frac{k(z_j - z_A)^2}{N_{S,z}} \right)\right) \quad (4.33)$$

Thus, the partition function for the entire slip-chain model is

$$\begin{aligned} Q_j(\mathbf{r}_A, N_S, N_{SC}) &= \int Z_{sc} Z_A Z_B d^3 \mathbf{r}_j \\ &= \left(\frac{1}{N_{SC} j (N-j)}\right)^{\frac{3}{2}} \left(\frac{2\pi k_B T}{k}\right)^{\frac{3}{2}(N-1)} \left( \left(\frac{2\pi k_B T}{k}\right)^3 \frac{N_{S,x} N_{S,y} N_{S,z}}{N_{SC}^3} \right)^{\frac{1}{2}(N_{sc}-1)} \\ &\quad \frac{1}{\sqrt{\left(\frac{1}{j} + \frac{1}{N-j} + \frac{1}{N_{S,x}}\right)}} \exp\left(-\frac{\left(\frac{k(x_B - x_C)^2}{j \cdot (N-1)} + \frac{k(x_A - x_B)^2}{N_{S,x} \cdot j} + \frac{k(x_A - x_C)^2}{N_{S,x} \cdot (N-j)}\right)}{2k_B T \left(\frac{1}{j} + \frac{1}{N-j} + \frac{1}{N_{S,x}}\right)}\right) \\ &\quad \frac{1}{\sqrt{\left(\frac{1}{j} + \frac{1}{N-j} + \frac{1}{N_{S,y}}\right)}} \exp\left(-\frac{\left(\frac{k(y_B - y_C)^2}{j \cdot (N-1)} + \frac{k(y_A - y_B)^2}{N_{S,y} \cdot j} + \frac{k(y_A - y_C)^2}{N_{S,y} \cdot (N-j)}\right)}{2k_B T \left(\frac{1}{j} + \frac{1}{N-j} + \frac{1}{N_{S,y}}\right)}\right) \\ &\quad \frac{1}{\sqrt{\left(\frac{1}{j} + \frac{1}{N-j} + \frac{1}{N_{S,z}}\right)}} \exp\left(-\frac{\left(\frac{k(z_B - z_C)^2}{j \cdot (N-1)} + \frac{k(z_A - z_B)^2}{N_{S,z} \cdot j} + \frac{k(z_A - z_C)^2}{N_{S,z} \cdot (N-j)}\right)}{2k_B T \left(\frac{1}{j} + \frac{1}{N-j} + \frac{1}{N_{S,z}}\right)}\right) \end{aligned} \quad (4.34)$$

The partition function is involved in the probability distribution of the slip-link,

$$P(j, \mathbf{r}_A, \{N_S\}, N_{SC}) = \frac{Q_j(\mathbf{r}_A, \{N_S\}, N_{SC})}{\sum_{j'=0}^N Q_{j'}(\mathbf{r}_A, \{N_S\}, N_{SC})} \quad (4.35)$$

but factors involving  $N_{SC}$  are independent of  $j$  and subsequently cancel out, so the probability distribution does not change. This means that the model has not changed the static values of  $G_{\gamma\gamma}(0)$  and  $G_{\gamma\gamma}(\infty)$ , whilst providing a new parameter to control the dynamics.

All simulations		Slip-chain	
$N$	16	$h$	10.89
$H$	10	$N_{S,x}$	8.48
$D$	10	$N_{S,y}$	9.85
		$N_{S,z}$	4.20

Figure 4.8: Parameters for the simulations in this chapter.

### 4.2.1 Mean squared displacement, $g_{1,\text{mid}}(t)$

As described previously, the slip-spring model allowed the slip-spring to move too fast in the z-direction. In Fig.4.9  $g_{1,\text{mid}}(t)/t^{0.5}$  is examined for a range of  $N_{SC}$  values (when  $N_{SC} = 1$  the slip-chain model is identical to the non-isotropic slip-spring model). In Fig.4.9a it is observed that movement of the middle bead decreases at intermediate time as  $N_{SC}$  increases, and a value of  $N_{SC} = N = 16$  has the best fit of the slip-chain model to the two-chain simulation. The other three graphs in Fig.4.9 display  $g_{1,\text{mid},\gamma}(t)/t^{0.5}$  for  $\gamma = x, y, z$ . All components show signs of the middle bead being slowed with increasing values of  $N_{SC}$ . In the z-direction this reduction in speed is greatest, as required. Once again,  $N_{SC} = N = 16$  is found to be the best parameter for all components. It is reasonable to find that reproducing the effects of the upper chain from the two-chain simulation, requires a slip-chain with a similar number of bonds as the chain.

### 4.2.2 Stress relaxation functions

Fig.4.10 considers  $G_{zz}(t)$  for a range of  $N_{SC}$  values, and it is observed that  $N_{SC}$  can be used to increase the longest relaxation time. This longest relaxation time was explained in section 3.1.6, where it was shown analytically that  $G_{zz}(t)$  has an additional relaxation not present in  $G_{xx}(t)$  or  $G_{yy}(t)$ . Eq.(3.23) and Eq.(3.19) indicate that the additional stress relaxation in  $G_{zz}(t)$  can be separated from the stress relaxation present in all components. To examine this additional relaxation time, we define the function  $H_{\gamma\gamma}(t)$  such that

$$(G_{\gamma\gamma}(t) - G_{\gamma\gamma}(\infty)) = (G_{yy}(t) - G_{yy}(\infty)) + (H_{\gamma\gamma}(t) - H_{\gamma\gamma}(\infty)) \quad (4.36)$$

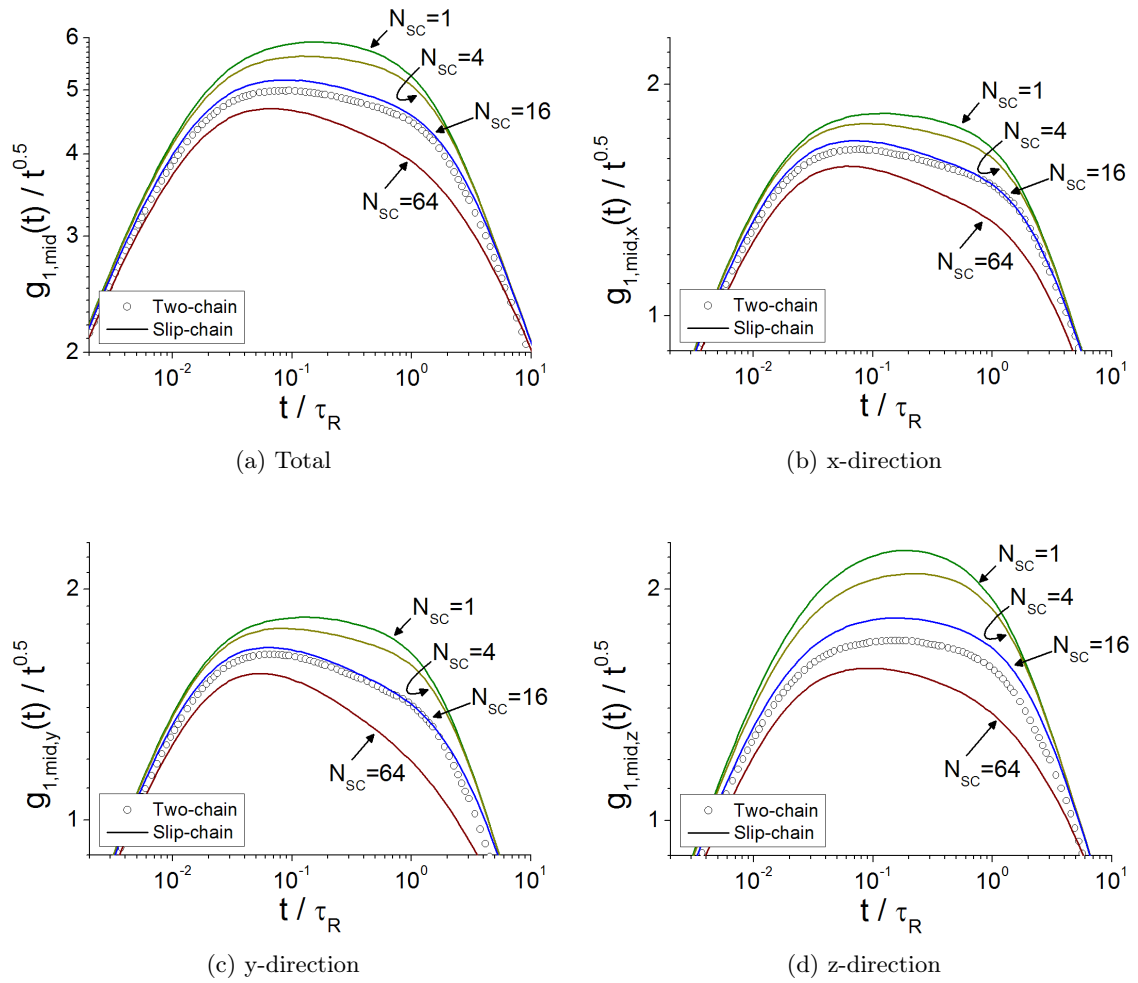


Figure 4.9:  $g_{1,\text{mid}}(t)/t^{0.5}$ , mean squared displacement of middle bead divided by  $t^{0.5}$ . Parameters are given in the table Fig.4.8.

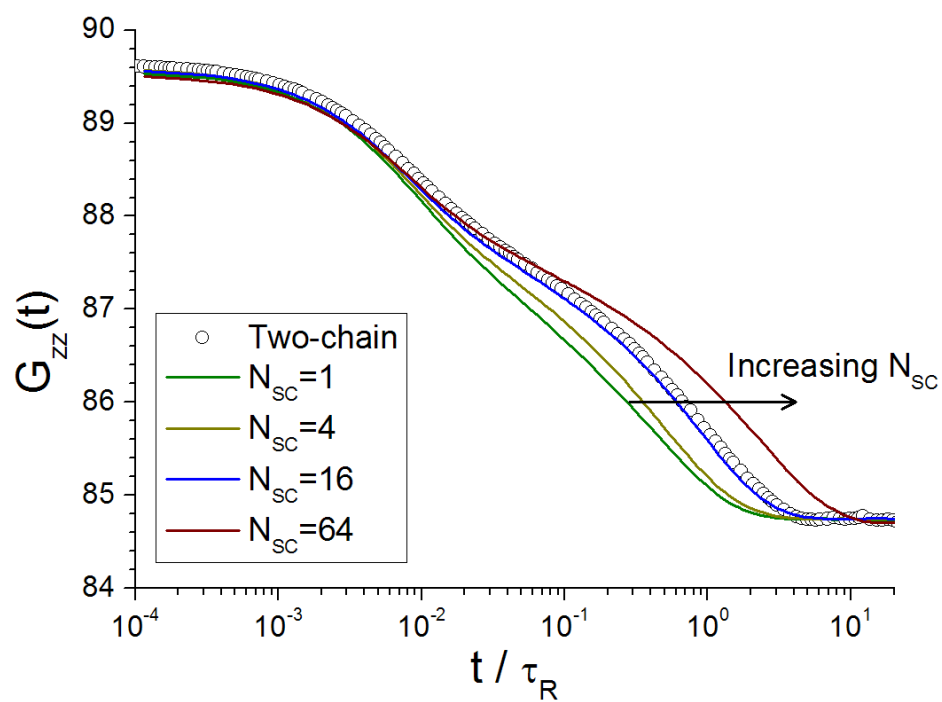


Figure 4.10:  $G_{zz}(t)$  for the slip-chain model, for multiple  $N_{SC}$  values. Parameters are given in the table Fig.4.8.

where  $G_{yy}(t) - G_{yy}(0)$  represents the relaxation that is common to all  $\gamma$ . In Fig.4.11,  $G_{yy}(t) - G_{yy}(\infty)$  and  $H_{zz}(t) - H_{zz}(\infty)$  are compared, displaying that only  $H_{zz}(t)$  depends on  $N_{SC}$ . It is known that the relaxation time of a Rouse chain is dependent on the number of bonds within the chain,  $\tau_R = \frac{N^2 b^2 \xi}{3\pi^2 k_B T}$ , so it is not unreasonable to discover that the relaxation time of the slip-chain model is dependent upon  $N_{SC}$  in this longest relaxation. Fig.4.11 confirms that  $N_{SC} = N = 16$  provides the best reproduction of the relaxation time.

Fig.3.27 showed that the off-diagonal components  $G_{xz}(t)$  and  $G_{yz}(t)$  in the slip-spring model do not have the same relaxation time as their counterparts in the two-chain simulation. These properties are plot for the slip-chain model in Fig.4.12, where it is observed that  $N_{SC} \approx N = 16$  fits the properties better than the slip-spring model. There are still slight differences observed, but these are minor.

### 4.2.3 Stress cross-correlation functions

So far the slip-chain model has been developed to improve the dynamics of the lower chain as an individual entity. One might assume the two-chain simulation can be thought of as the sum of two slip-chain models, as illustrated by Fig.4.13. Whilst this is true for the energy, it is not true for the stress correlations, because the stress correlation function for the entire model involves cross-correlation, Eq.(3.13). A paper by Ramirez et. al. [35] demonstrated that the total stress can still be considered as two parts as long as both parts include the cross-correlation function,

$$\begin{aligned} G_{\alpha\beta}^T(t) &= (G_{\alpha\beta}^A(t) + G_{\alpha\beta}^X(t)) + (G_{\alpha\beta}^X(t) + G_{\alpha\beta}^B(t)) \\ &= G_{\alpha\beta}^{TA}(t) + G_{\alpha\beta}^{TB}(t) \end{aligned} \quad (4.37)$$

Therefore, the total stress correlation function can be split into the lower half,  $G_{\alpha\beta}^{TA}(t)$ , and the upper half,  $G_{\alpha\beta}^{TB}(t)$ . However, the slip-spring model does not have two chains to cross-correlate

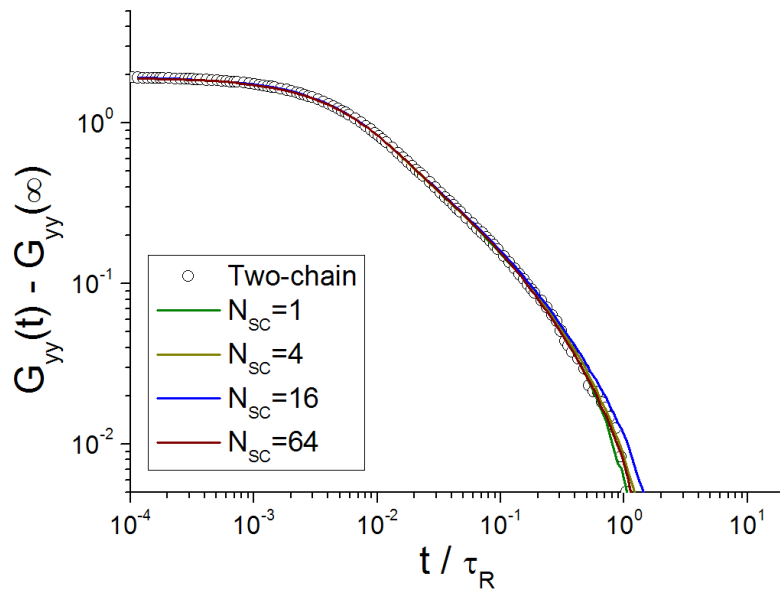
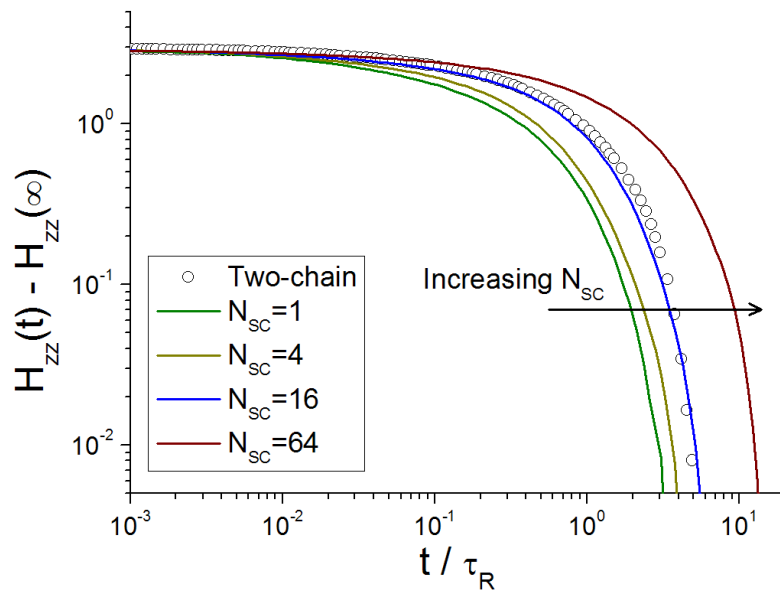
(a)  $(G_{yy}(t) - G_{yy}(\infty)) = (G_{zz}(t) - G_{zz}(\infty)) - (H_{zz}(t) - H_{zz}(\infty))$ (b)  $H_{zz}(t) - H_{zz}(\infty)$ 

Figure 4.11: The  $zz$ -component stress relaxation is expressed as the  $yy$ -component plus an additional relaxation function, Eq.(4.36). Parameters are given in the table Fig.4.8.

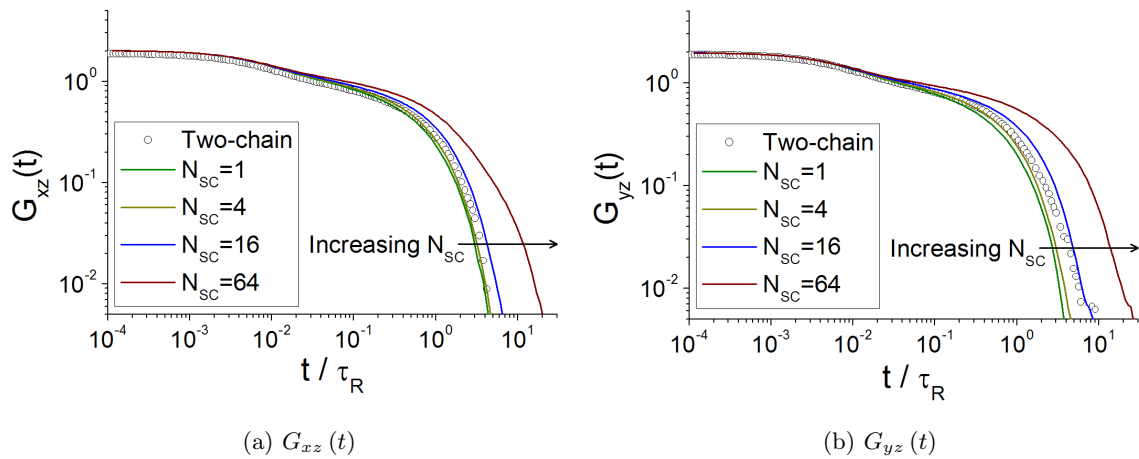


Figure 4.12: Relaxation of the off-diagonal components of the stress tensor. Parameters are given in the table Fig.4.8.

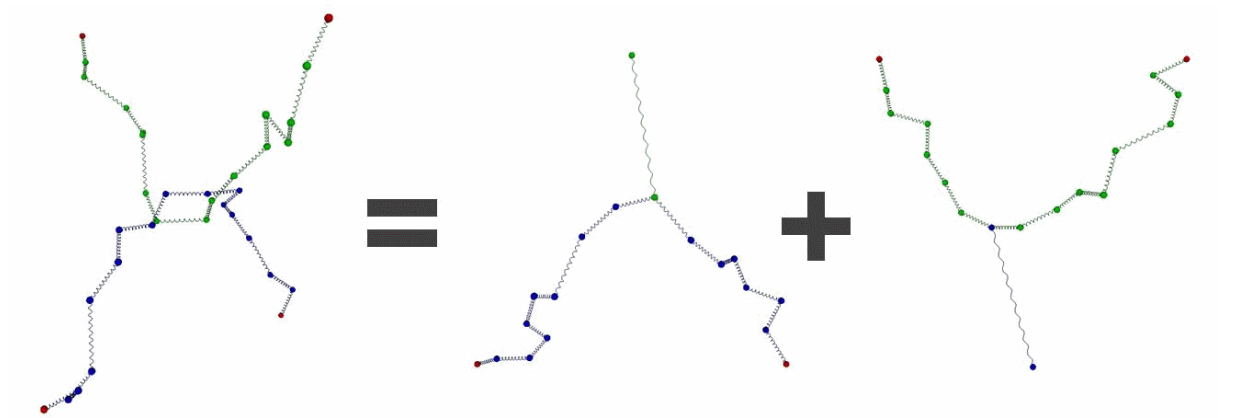


Figure 4.13: The two chains of the two-chain simulation can be modelled by the sum of two slip-spring models

in order to calculate

$$G_{\alpha\beta}^X(t) = \langle \sigma_{\alpha\beta}^A(t) \sigma_{\alpha\beta}^B(0) \rangle \quad (4.38)$$

where  $\sigma^A(t)$  is the stress contribution of the lower chain and  $\sigma^B(t)$  is the stress of the upper chain. Instead the slip-chain object must provide  $\sigma_{\alpha\beta}^B(t)$ . This poses a problem because the slip-spring object is distinctly different from the upper chain by design. One major factor is that the upper chain in the two-chain model contributes stress from bead fluctuations (Eq.(3.45)), but the stress of the slip-spring object (Eq.(3.46)) lacks these fluctuations because it has no beads to fluctuate. With the introduction of the slip-chain model, we have introduced new slip-chain beads that fluctuate in space, which makes the average stress of the slip-chain

$$\begin{aligned} \langle \sigma_{j,\gamma\gamma}^{SC} \rangle &= \frac{k_B T}{V} (N_{SC} - 1) + \frac{k_B T}{V} \frac{1}{N_{S,\gamma}} \left( \frac{1}{N_{S,\gamma}} + \frac{1}{j} + \frac{1}{N-j} \right)^{-1} \\ &\quad + \frac{k}{V N_{S,\gamma}} \left( r_A^\gamma - \langle r_j^\gamma \rangle \right)^2 \end{aligned} \quad (4.39)$$

which is more similar to that of the polymer chain. Hence, it is possible to control the stress in the virtual slip-chain object by discrete increments, with the parameter  $N_{SC}$ . In Fig.4.14,  $N_{SC} = 13$  is shown to provide the closest match between the slip-chain's  $\langle \sigma_{zz}^{SC} \rangle$  and the two-chain's  $\langle \sigma_{zz}^B \rangle$ . Note that the value is not  $N$ , as required to best match the delay in relaxation already compared. This is due to differences between the slip-chain object and the upper chain that it replaced. For example, the slip-chain is connected to the lower chain by a slip-link at the end bead, whereas the upper chain is entangled at a varying position around the central beads. Using cross-correlations to calculate  $G_{zz}^{TA}(t)$ , plotted in Fig.4.15, it is confirmed that  $N_{SC} = 16$  is significantly worse than  $N_{SC} = 13$ .

In Fig.4.16 it is observed that, while setting the parameter  $N_{SC} = 13$  has made  $G_{zz}^X(\infty)$  comparable between the models,  $G_{xx}^X(\infty)$  and  $G_{yy}^X(\infty)$  have not been fit well. This is because of the differences between the slip-chain and the upper chain. For example, in the y-direction the

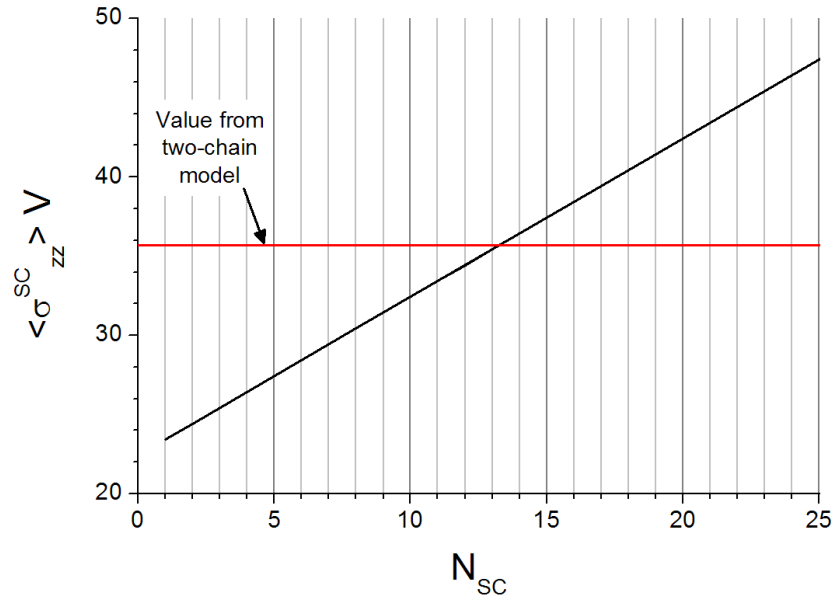


Figure 4.14: Average stress of the slip-chain object,  $\langle \sigma_{zz}^{SC} \rangle$ , as a function of  $N_{SC}$ . The horizontal dashed line indicates the average stress of the upper chain from the two-chain simulation,  $\langle \sigma_{zz}^B \rangle$ .  $N_{SC}$  must be an integer and  $N_{SC} = 13$  shows the best match between the two-chain simulation and the slip-chain object. Parameters are given in the table Fig.4.8.

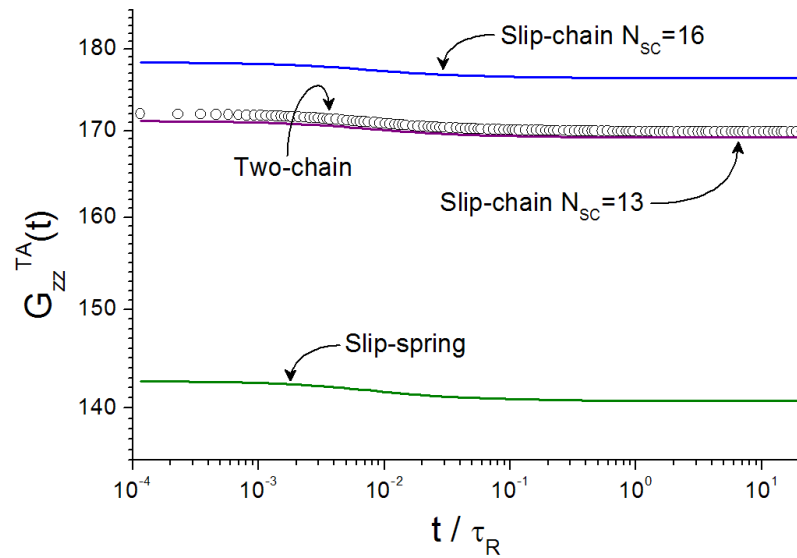
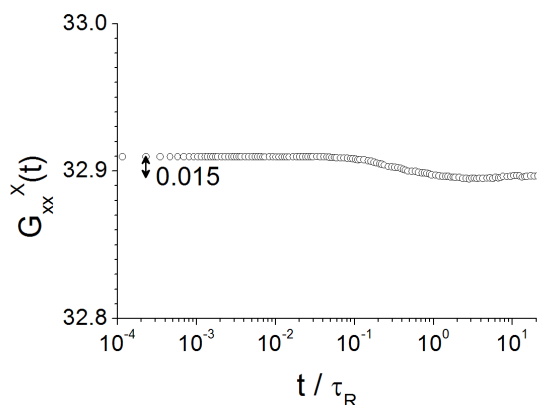
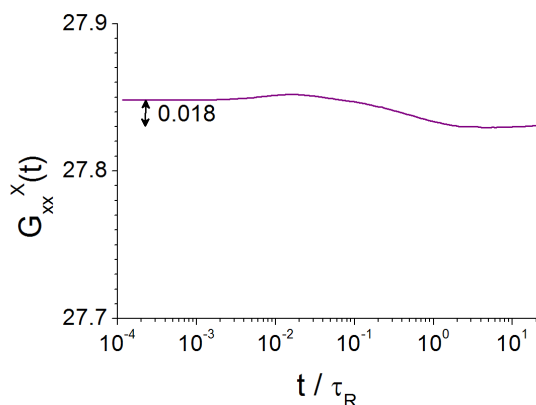


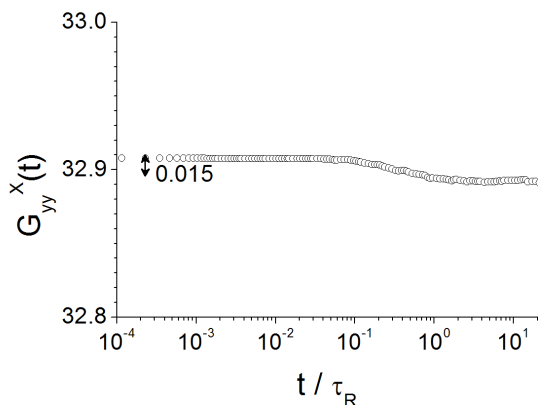
Figure 4.15:  $G_{zz}^{TA}(t)$  for different values of  $N_{SC}$ . Parameters are given in the table Fig.4.8.



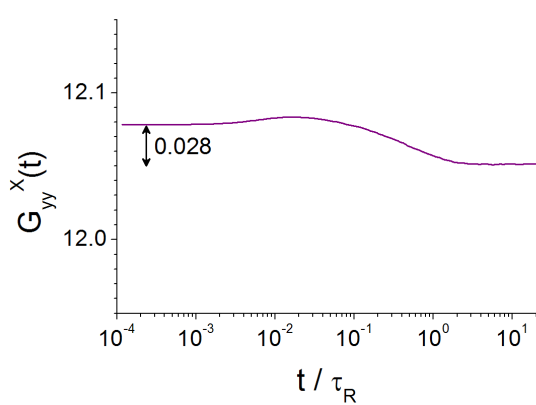
(a) Two-chain



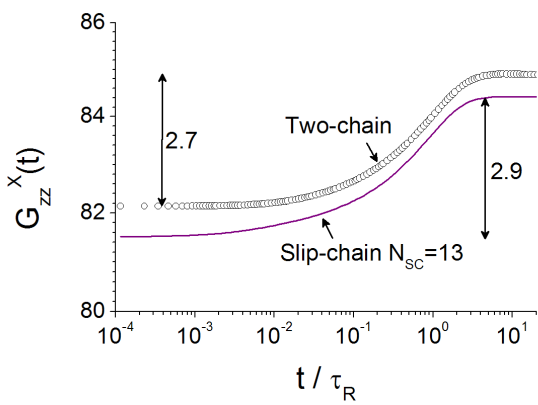
(b) Slip-chain  $N_{SC} = 13$



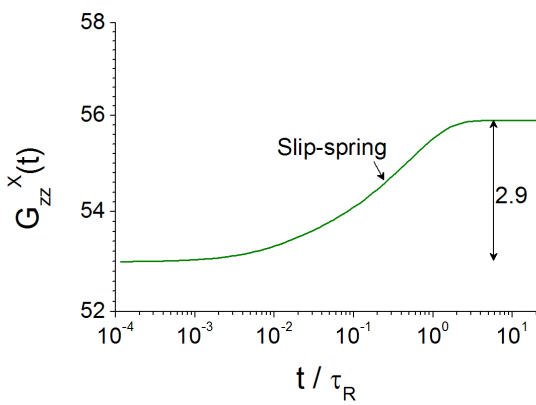
(c) Two-chain



(d) Slip-chain  $N_{SC} = 13$



(e) Two-chain and slip-chain  $N_{SC} = 13$



(f) Slip-spring  $N_{SC} = 1$

Figure 4.16: Cross-correlation functions between upper and lower chains in the two-chain simulation; and lower chain with the slip-chain object in the slip-chain model. Parameters are given in the table Fig.4.8.

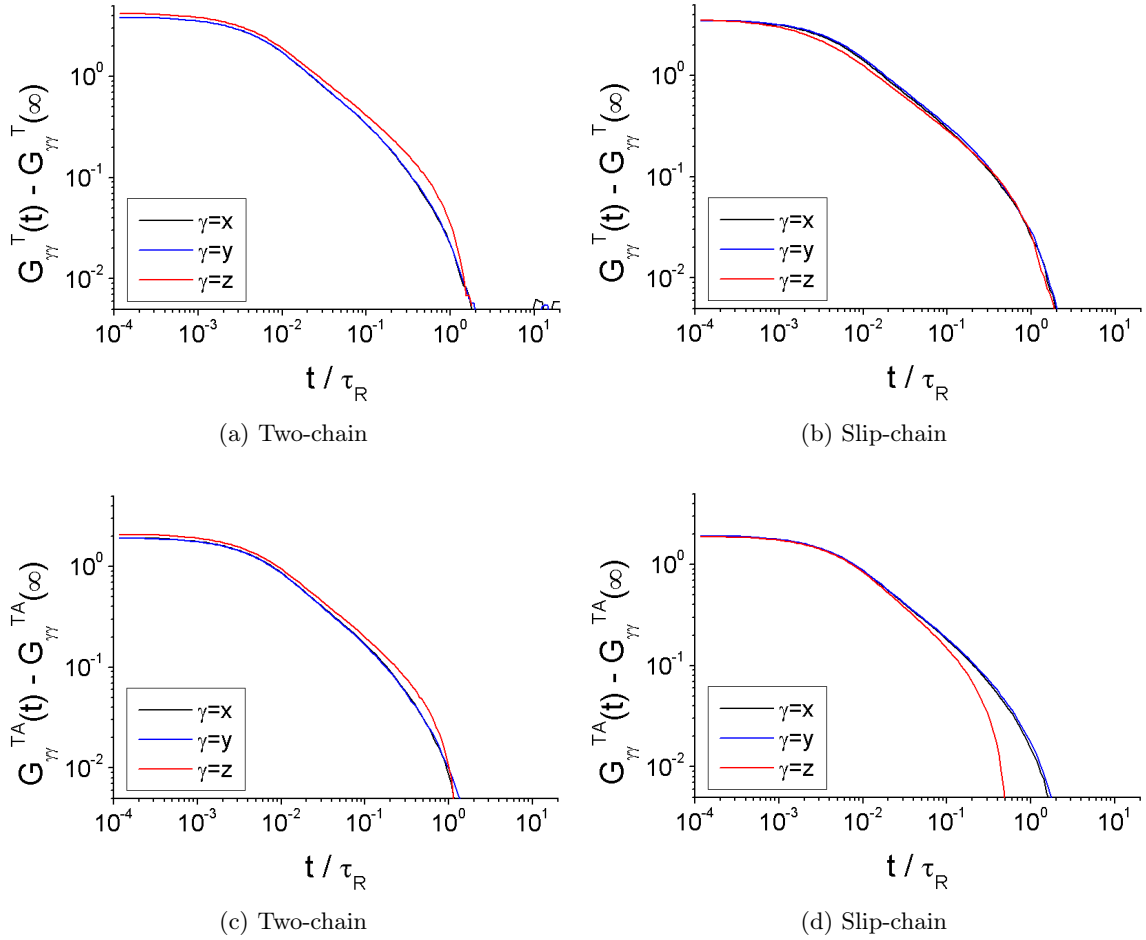


Figure 4.17: Total stress auto-correlation functions,  $G_{\gamma\gamma}^T(t) = G_{\gamma\gamma}^{TA}(t) + G_{\gamma\gamma}^{TB}(t)$ , plotted as the function  $G_{\gamma\gamma}(t) - G_{\gamma\gamma}(\infty)$ . Parameters are given in the table Fig.4.8.

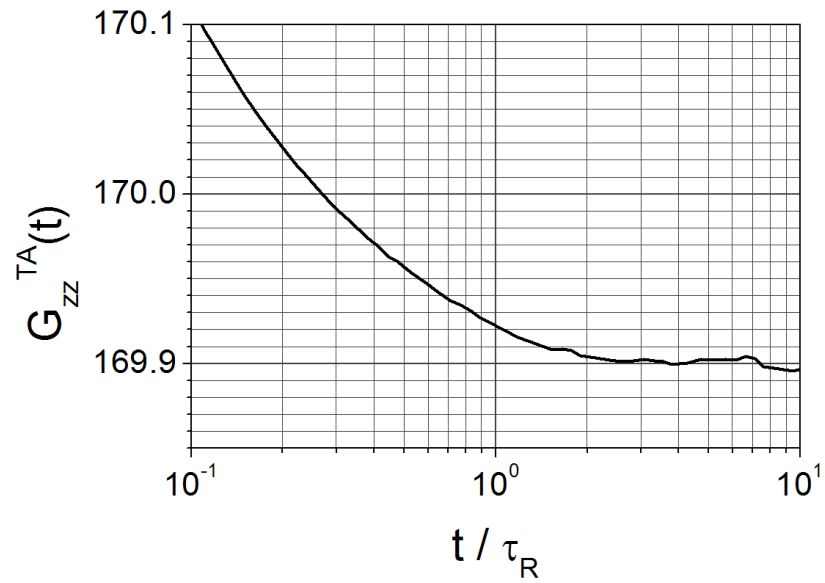
two-chain model has symmetry between the lower and upper chain, such that  $G_{xx}^X(t) = G_{yy}^X(t)$ , whilst the slip-chain object has zero average stretch in the horizontal directions. The amplitude of  $G_{zz}^X(t)$  also demonstrates a discrepancy between the two models due to the configurational differences between the slip-chain and the upper chain. Comparing Fig.4.16e to Fig.4.16f it is found that the slip-chain's cross-correlation amplitude is not dependent on  $N_{SC}$ , but is slightly larger than the amplitude of the function observed for the two-chain model. However, despite these discrepancies, the slip-chain model is a significant improvement over the slip-spring model.

The total stress auto-correlation function is the observable measured experimentally, rather

than the cross-correlation. In section 3.1.6 it was demonstrated that the relaxation of the cross-correlation cancels out with the slowest relaxation of  $G_{zz}(t)$ . Therefore,  $G_{\gamma\gamma}^T(t) - G_{\gamma\gamma}^T(\infty)$  in Fig.4.17a and Fig.4.17b is equal for all three components,  $\gamma = x, y, z$ . In Fig.4.17c for the two-chain model the relaxation time of  $G_{\gamma\gamma}^{TA}(t)$ , as defined in Eq.(4.37), is shown to be equal for all  $\gamma$ . However, Fig.4.17d displays that this is not the case for  $\gamma = z$  in the slip-chain model, which appears to relax faster than any other component. In Fig.4.18 the final point of relaxation for  $G_{zz}^{TA}(t)$  is displayed and it is found that the slip-spring simulation undershoots, unlike the two-chain simulation. An undershoot indicates that the chain encountered a point where it became more relaxed than it is when the system has minimal potential energy. Such a situation is able to occur because the minimum level of stress in the lower chain does not correspond to the lowest energy state of the entire system, but instead the stress of the lower chain is lowest when it is least stretched in the z-direction. A further investigation of a three-arm-star model, equivalent to having the slip-link fixed upon only one bead, observed no sign of an undershoot, which indicates that the undershoot is caused by the slip mechanism. However, it is unknown how the slip-link is causing this effect and why this undershoot is not also demonstrated by the two-chain model, where the dynamics of the entanglement should be analogous to the dynamics of the slip-link.

#### 4.2.4 Summary

The slip-chain model was designed to address the additional stress relaxation time observed in  $G_{zz}(t)$ , which was not correctly reproduced by the slip-spring model. The slip-chain replaced the single spring in the slip-spring model with a Rouse chain. Such a simulation would take longer to run, but adjusting the number of bonds in the slip-chain allows the delay in stress relaxation to be controlled. This additional parameter also allowed the cross-correlation between chain stress and slip-spring stress to be a better fit in the zz-direction, but all of the cross-correlation functions were not matched exactly. The total stress,  $G_{zz}^{TA}(t)$ , is a fit better with the slip-chain model, than with the previous slip-spring model. The best reproduction of the two-chain entanglement simulation in this study so far is found when fitting the parameter  $N_{SC}$ , so that  $\langle \sigma_{zz}^{SC} \rangle \approx \langle \sigma_{zz} \rangle$ .



(a) Two-chain

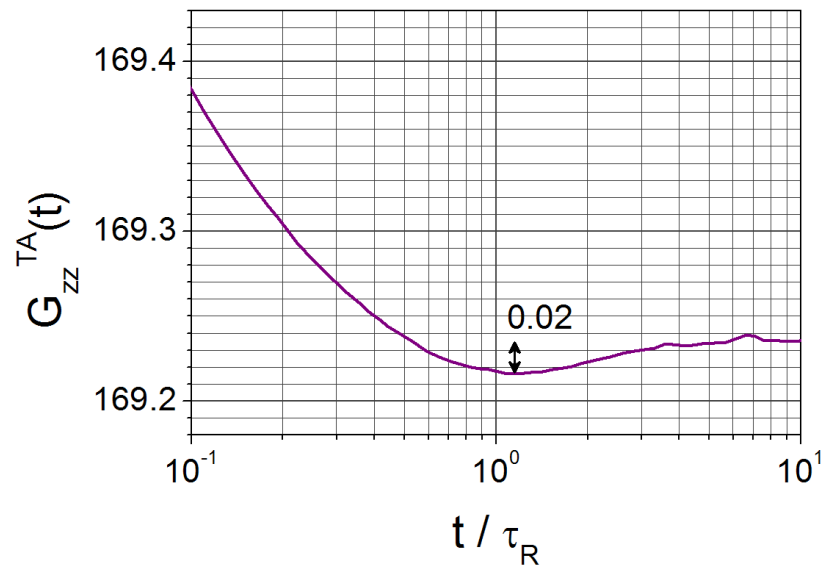
(b) Slip-chain  $N_{SC} = 13$ 

Figure 4.18: Total stress auto-correlation function of the lower section,  $G_{zz}^{TA}(t) = G_{zz}^A(t) + G_{zz}^X(t)$ . Parameters are given in the table Fig.4.8.

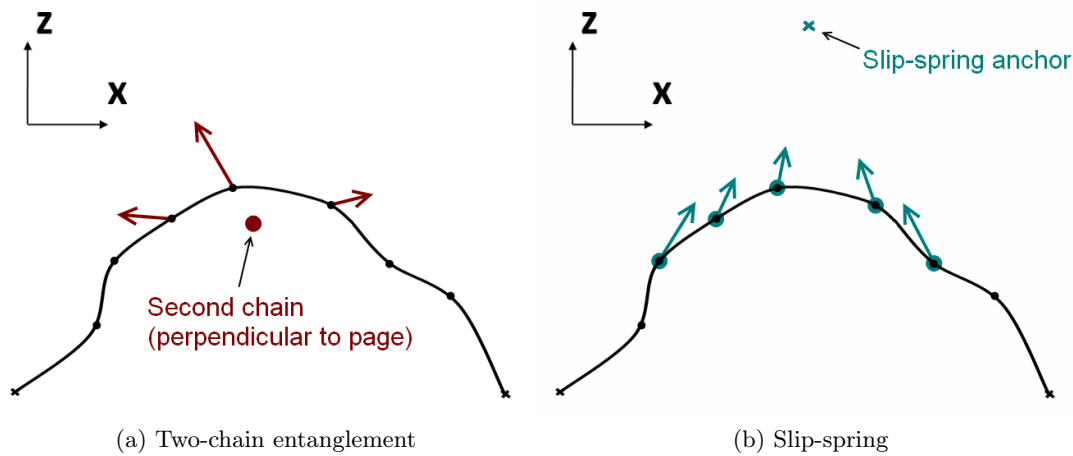


Figure 4.19: Diagram of entanglement forces within the two-chain simulation and the slip-spring modelling of the forces.

### 4.3 Bulky-slip-chain model

In Fig.3.28b it was observed that the slip-spring model fails to reproduce the bead positions in the x-direction. The slip-spring applies a force to every bead pulling it towards an anchoring point above the chain, while the entanglement modelled in the two-chain simulation repels the beads from the entanglement position, as illustrated in Fig.4.19. This ultimately means that beads in both models experience an equivalent force in the z-direction, but in the x-direction the slip-spring is frequently acting in the wrong direction. A solution is to consider the entanglement as consisting of two forces. First, a force that attracts a bead towards the centre of the second chain's anchors. Second, a repulsive force that repels the other beads away from the entanglement. The bulky-slip-chain model mimics this by using the slip-chain to provide the entanglement's pull, and applying a new repulsive force between the two beads adjacent to the slip-link, as demonstrated in Fig.4.20.

This section is a proof-of-concept study of the bulky-slip-chain model, with a force only applied in the x-direction. The potential of this repulsive force is chosen to be

$$U_b = -k_b b (x_{j+1} - x_{j-1}) \quad (4.40)$$

with a spring-constant  $k_b$ , such that the bulky forces are

$$\begin{aligned}\mathbf{F}_{b,j-1} &= \left( -\frac{\partial U_b}{\partial x_{j-1}}, -\frac{\partial U_b}{\partial y_{j-1}}, -\frac{\partial U_b}{\partial z_{j-1}} \right) \\ &= (-k_b b, 0, 0)\end{aligned}\quad (4.41)$$

$$\begin{aligned}\mathbf{F}_{b,j+1} &= \left( -\frac{\partial U_b}{\partial x_{j+1}}, -\frac{\partial U_b}{\partial y_{j+1}}, -\frac{\partial U_b}{\partial z_{j+1}} \right) \\ &= (k_b b, 0, 0)\end{aligned}\quad (4.42)$$

where  $\mathbf{r} = (x, y, z)$ . The equation of motion for this new model is therefore

$$\begin{aligned}\xi d\mathbf{r}_i &= k(\mathbf{r}_{i+1} - 2\mathbf{r}_i + \mathbf{r}_{i-1}) dt + \sqrt{2k_B T \xi} d\mathbf{W}_i(t) \\ &\quad + \delta_{i,j} \hat{k}_{SC} (\mathbf{s}_{NSC-1} - \mathbf{r}_j) dt \\ &\quad - \delta_{i,j-1} k_b b dt \quad + \delta_{i,j+1} k_b b dt\end{aligned}\quad (4.43)$$

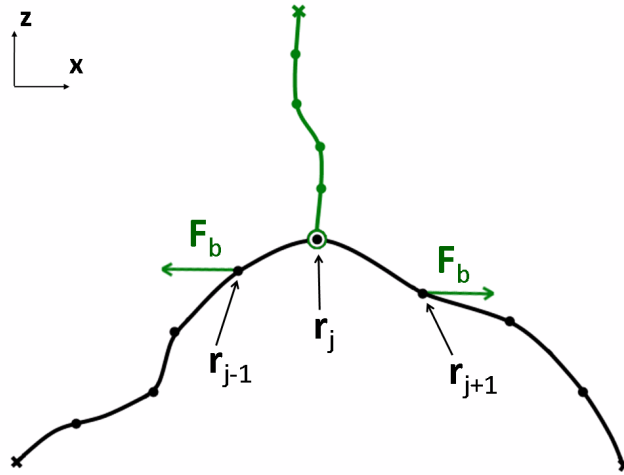


Figure 4.20: Diagram of the bulky-slip-chain model

		Equation of motion			
		<i>Brownian Dynamics</i>	<i>Molecular Dynamics</i>	<i>Monte-Carlo</i>	
Potential	<i>Bonded potential</i>	<i>Entanglement method</i>			
		Linear springs	Rejection Algorithm	a	
	Lennard-Jones Repulsion	e			
	FENE + LJ springs	Rejection Algorithm			c
Lennard-Jones Repulsion			b	d	

Figure 4.21: Two-chain simulations used within this study.

a) *BD: Linear bonds + rejection*b) *MD: FENE + LJ bonds + LJ repulsion*c) *MC: FENE + LJ bonds + rejection*d) *MC: FENE + LJ bonds + LJ repulsion*e) *BD: Linear bonds + LJ repulsion*

### 4.3.1 Modified two-chain simulation

In section 3.1.7 different versions of the two-chain simulation were compared. It was demonstrated that the two-chain simulation with rejection had some differences from the more realistic simulation with repulsion between chains, but most of these effects could be corrected for by a slight shift in parameters. However, one of the discrepancies that could not be corrected for was an increased bead position variance in the x-direction (Fig.3.18). Since, the bulky-slip-chain model is attempting to perfect the reproduction of the x-direction properties of the entanglement, it is worth comparing it with an improved two-chain simulation that uses repulsion to prevent the chains from crossing.

The diagram in Fig.4.21 depicts the simulations used in this study so far, along with their equation of motion and force potentials. The two-chain simulation that has been used for the majority of this study is simulation (a), and the new two-chain simulation we introduce now is

(e). This new simulation is identical to the current two-chain simulation, except that a repulsive Lennard-Jones force is applied between the opposite chains - within each chain the forces are unchanged. The equation of motion for this model is given by

$$\xi \mathbf{r}_i = \mathbf{F}_i^{\text{B}} dt + \mathbf{F}_i^{\text{NB}} dt + \mathbf{F}_i^{\text{R}} dt \quad (4.44)$$

with the forces from the previous two-chain model

$$\mathbf{F}_i^{\text{B}} dt = -k(\mathbf{r}_{i+1} - 2\mathbf{r}_i + \mathbf{r}_{i-1}) dt \quad (4.45)$$

$$\mathbf{F}_i^{\text{R}} dt = \sqrt{2k_B T \xi} d\mathbf{W}_i(t) \quad (4.46)$$

and introduces the non-bonded Lennard-Jones force

$$\mathbf{F}_i^{\text{NB}} dt = \sum_{j=0}^N \mathbf{F}^{\text{LJ}}(\mathbf{u}_j - \mathbf{r}_i) \quad (4.47)$$

$$\mathbf{F}^{\text{LJ}}(\mathbf{R}) = \frac{24\epsilon}{\sigma^2} \mathbf{R} \left( \left( \frac{\sigma}{R} \right)^8 - 2 \left( \frac{\sigma}{R} \right)^{14} \right) \quad (4.48)$$

where  $\mathbf{u}$  represents beads in the opposite chain, labelled  $\mathbf{u}_0, \dots, \mathbf{u}_N$ .

Adding the repulsion between chains has slightly modified most of the properties. Mainly because the beads are stretched further in the z-direction and repelled further in the x-direction (see section 3.1.7). This has not changed the ability of the slip-spring model to reproduce most of the properties of the two-chain simulation, but merely requires the model parameters to be fit to the new simulation values. However, an important difference between the two-chain simulations is demonstrated in  $\text{var}(x_i)$ , where the old rejection simulation has a fairly rounded shape, but the repulsion simulation observes a sharp peak for the centre beads, as can be seen later in Fig.4.24a and Fig.4.24b. Much like the variances observed in the z-direction, this increase in variance is caused by the application and removal of a force to beads. Previously this effect was not as strong in the x-direction because the other chain is not felt unless a rejection takes place,

All simulations		Slip-chain / Bulky-slip-chain	
$N$	16	$h$	12.62
$H$	10	$N_{S,x}$	2
$D$	10	$N_{S,y}$	26
		$N_{S,z}$	5.12
		$N_{SC}$	13

Figure 4.22: Parameters for the simulations in this chapter. The slip-chain model is equivalent to a bulky-slip-chain model with  $k_b = 0$ .

but with the repulsive two-chain simulation, the effect of the other chain is felt more often.

### 4.3.2 Mean bead positions

Displayed on Fig.4.23 is the new bulky-slip-chain model, for a range of  $k_b$  values, compared with the new repulsive two-chain model (Fig.4.21e). It is observed that the bulky force creates the repulsion away from the entanglement as required, such that  $\langle \bar{x}_i \rangle$  is opposite to the previous slip-chain model. Larger values of  $k_b$  increase the amplitude of  $\langle \bar{x}_i \rangle$  and it is discovered that  $k_b = 2.0$  will provide the best match to the repulsive two-chain simulation. The parameter  $N_{S,x}$  can be used to provide the correct width of this plot, and  $N_{S,x} = 1.0$  is used in Fig.4.23 to provide the width displayed. However, we note that this makes the slip-spring significantly stronger than before.

### 4.3.3 Variance of bead positions

The variances of bead positions in the slip-chain model are a fairly good match to the values in the rejection two-chain simulation (Fig.4.21a), as demonstrated in Fig.4.24a. However, it was noted that there appears to be a narrowing peak around the middle bead, that was not captured by the slip-chain model. With the new repulsive two-chain model (Fig.4.21e) the narrowing around the middle bead forms a more distinct peak, as observed in Fig.4.24b. Since the repulsive two-chain simulation is more realistic than the rejection simulation, it is important that the bulky-slip-chain model reproduces the peak observed in the repulsive simulation, rather than the shape of

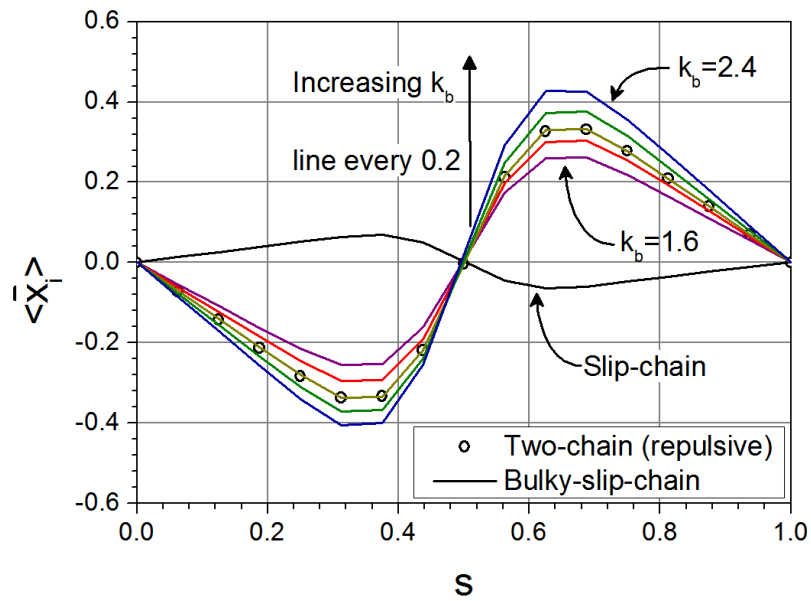


Figure 4.23:  $\langle \bar{x}_i \rangle = \langle x_i \rangle - \langle x_i^{\text{Single}} \rangle$ , the average bead position in the x-direction relative to the unentangled case. The bead number,  $i$ , is expressed as a fraction along the chain,  $s = \frac{i}{N}$ . Parameters are given in the table Fig.4.22.

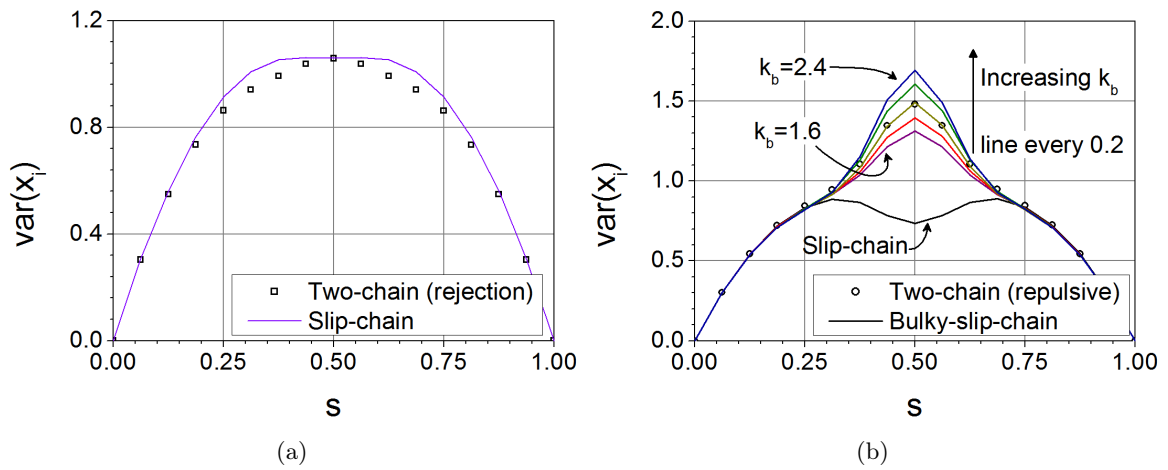


Figure 4.24: Bead position variance in the x-direction. The bead number is expressed as a fraction along the chain,  $s = \frac{i}{N}$ . Parameters are given in the table Fig.4.22.

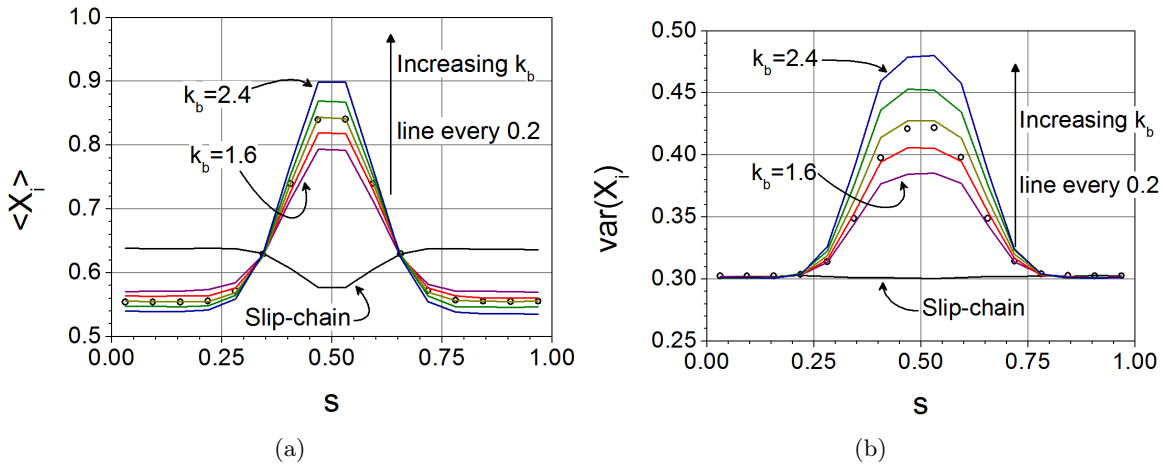


Figure 4.25: Mean and variance of bond vectors in the x-direction. The bond number is expressed as a fraction along the chain,  $s = (i_{\text{bond}} + \frac{1}{2}) / N$ . Parameters are given in the table Fig.4.22. The two-chain simulation is shown as symbols, and the slip-chain and bulky-slip-chain simulations as lines.

the rejection simulation, which it does for  $k_b = 2.0$ . It is also observed that increasing  $k_b$  has the effect of increasing the variance of the central beads, which agrees with the idea that this peak is caused by the application and removal of the repulsive force as the slip-link samples different beads. This is the same mechanism that has been observed for  $\text{var}(z_i)$  previously and discussed in section 3.2.6.

### 4.3.4 Mean and variance of bond vectors

The mean bond vectors, plotted in Fig.4.25a, show that, analogous to the mean bead positions, without the repulsive bulky force the slip-chain model compressed bonds in the centre of the chain rather than stretching them. With the repulsive force, the bulky-slip-chain model stretches the central bonds, which matches the two-chain simulation.

In the x-direction bond variance, the slip-chain model demonstrates a worrying discrepancy (Fig.4.25b), where the slip-chain produces a nearly insignificant peak in variance around the central bonds, whilst the central bonds of the two-chain simulation demonstrated a distinct peak. The repulsive two-chain simulation makes this peak larger, but it is observed that the

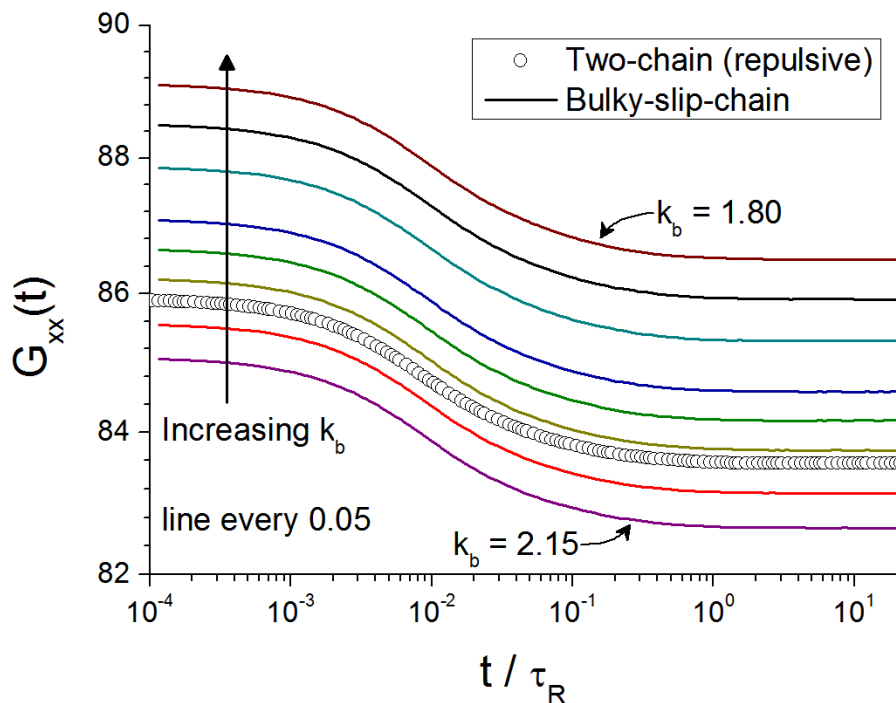
bulky-slip-chain model can create the peak required and is able to control the amplitude with  $k_b$ , where  $k_b \approx 2.0$  provides the best results for comparison to the two-chain simulation, which is the same value that has been found for all properties considered so far. However, it is observed that the best value is slightly below 2.0 and the shape of the bulky-slip-chain line is slightly wider than that of the two-chain simulation.

### 4.3.5 Stress relaxation functions

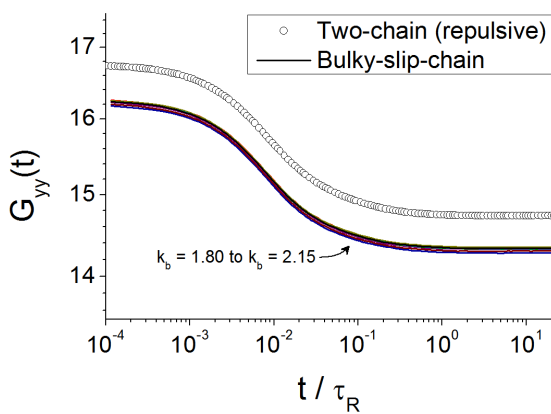
$G_{xx}(t)$  is strongly affected by  $k_b$ , more than by  $N_{S,x}$ . It is observed in Fig.4.26a that  $k_b = 2.07$  provides the best match for  $G_{xx}(t)$ , which is close to the parameter value required to match the properties fitted already, but not exact due to the difference in width for  $\text{var}(X_i)$  observed above. Since the energy is dependent on  $k_b$ , the probability distribution of the slip-link and therefore  $G_{yy}(t)$  and  $G_{zz}(t)$  also indicate a slight dependence on  $k_b$ . However, this dependence is so weak that it cannot be observed in Fig.4.26b and Fig.4.26c.

$G_{zz}(t)$  is still a good fit to the new repulsive two-chain simulation with the correct values of  $h$  and  $N_{S,z}$ . However, whilst  $G_{yy}(t)$  could be fit to the rejection two-chain simulation results, the repulsion two-chain model has a higher average stress that cannot be matched by adjusting  $N_{S,y}$ . Fig.4.27 demonstrates why this occurs. Previously, the non-isotropic slip-spring model corrected for a lack of a peak bond variance, by increasing the variance of all bonds uniformly (Fig.4.5b), but the repulsive two-chain simulation has a much larger peak variance than the rejection simulation and cannot be corrected by reducing  $N_{S,y}$  in this way. It is possible that a bulky repulsive force suitably applied in the y-direction would provide the variance required, in the same way it did for  $\text{var}(X_i)$ . However, the bulky potential,  $U(X_{ij})$ , defined in Eq.(4.40) is dependent on the sign of  $X_{ij}$ , which makes it only applicable for a large stretch between the chain anchors,  $D = x_N - x_0$ , such that the direction in which the force should act is known. In the y-direction there is no stretch,  $y_0 = y_N$ , which means that a bulky potential

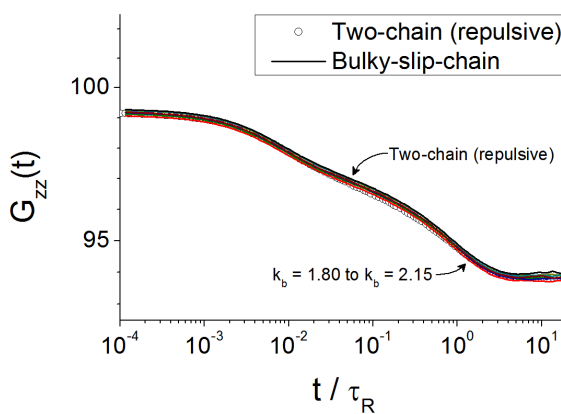
$$U_b = -k_b b ((x_{j+1} - x_{j-1}) + (y_{j+1} - y_{j-1})) \quad (4.49)$$



(a)



(b)



(c)

Figure 4.26: Stress auto-correlation functions. In (b) and (c) all  $k_b$  values collapse onto the same line. Parameters are given in the table Fig.4.22.

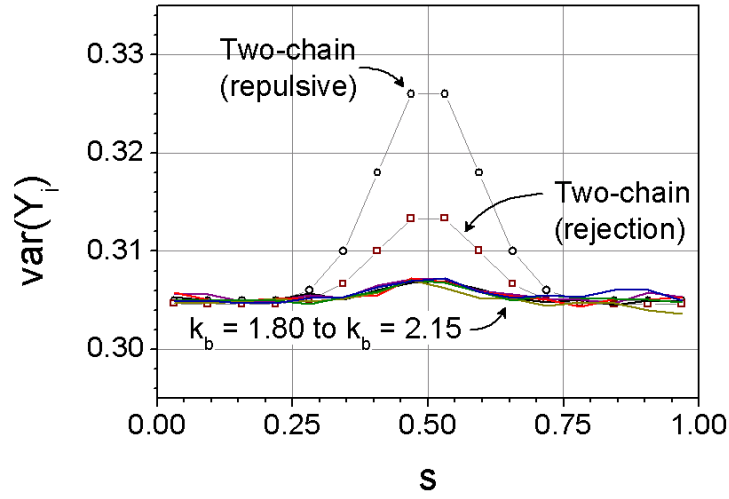


Figure 4.27: Variance of bond vectors in the y-direction. The bond number is expressed as a fraction along the chain,  $s = (i_{\text{bond}} + \frac{1}{2})/N$ . Parameters are given in the table Fig.4.22. The two-chain simulations are shown as symbols, and the slip-chain and bulky-slip-chain simulations as lines.

would not be appropriate, since  $Y_{ij} < 0$  has a lower energy than  $Y_{ij} > 0$ , which violates the symmetry of the system. A future study of this model shall search for a more sophisticated potential that may be applied to all Cartesian components.

### 4.3.6 Summary

The bulky-slip-chain model is a proof-of-concept model for correcting the x-direction properties of the slip-spring model. The original slip-spring model attracted beads towards the entanglement point, whilst the two-chain model repelled them in the x-direction. Using a simple constant force repelling the two beads adjacent to the slip-link, the bulky-slip-chain model has been able to reproduce the x-direction mean bead positions and bond vectors of the two-chain model, as well as improve upon the variance of beads and bonds. In this bulky-slip-chain model,  $G_{xx}(t)$  and  $G_{zz}(t)$  match the two-chain model, but  $G_{yy}(t)$  does not, because there is a lack of y-direction variance of bonds. It is possible that, with a more advanced potential, the bulky force may be applied to all directions. This could allow  $\text{var}(Y_i)$  and  $G_{yy}(t)$  to be fit correctly, as was done in

the x-direction, but the current potential used is not appropriate to be used in the y-direction.

## Chapter 5

# Maximum likelihood estimation

During this study, parameters of the slip-spring models have been fit to the two-chain simulation through comparison of specific properties. However, in doing so we have implemented a bias towards the properties that are most interesting to this study. This is most clear in section 3.2.3, where the parameters chosen are clearly dependent on preference. Since chapter 3 was most interested in properties in the z-direction, the parameters were chosen so that  $G_{zz}(t)$  was best fit, rather than  $G_{xx}(t)$  and  $G_{yy}(t)$ . Maximum likelihood estimation (MLE) is a statistical tool that can be used for obtaining model parameters, given observations of a common set of variables. In this study, the full set of observables shared by all models are the instantaneous positions of all beads in the lower chain  $\{\mathbf{r}_i\} = (\mathbf{r}_1, \dots, \mathbf{r}_{n-1})$ .

### 5.1 Estimation of parameters

The probability of observing the  $n_k$  independent observations,  $\{\mathbf{r}_i\}_1, \{\mathbf{r}_i\}_2, \dots, \{\mathbf{r}_i\}_{n_k}$ , given a slip-spring model with parameters  $\theta$  is

$$P(\{\mathbf{r}_i\}_1, \{\mathbf{r}_i\}_2, \dots, \{\mathbf{r}_i\}_{n_k} | \theta) = \prod_{k=1}^{n_k} P(\{\mathbf{r}_i\}_k | \theta) \quad (5.1)$$

$P(\{\mathbf{r}_i\}|\theta)$  is the probability distribution of bead positions  $\{\mathbf{r}_i\}$ , from a single observation, given the model parameters  $\theta$ . This can be obtained from the Boltzmann distribution, such that

$$P(\{\mathbf{r}_i\}|\theta) = \frac{1}{Q(\theta)} \exp\left(-\frac{U(\{\mathbf{r}_i\}, \theta)}{k_B T}\right) \quad (5.2)$$

where  $U(\{\mathbf{r}_i\}, \theta)$  is the energy of the system for the observation  $\{\mathbf{r}_i\}$  and model parameters.  $Q(\theta)$  is the partition function found from the condition

$$\int P(\{\mathbf{r}_i\}|\theta) d^3\mathbf{r}_1 \dots d^3\mathbf{r}_{N-1} = 1 \quad (5.3)$$

The advantage that the slip-spring models have over some other polymer models, is that  $U(\{\mathbf{r}_i\}_k, \theta)$  is known exactly.

The aim of MLE is to find the most probable set of parameters  $\theta$  given the observations. Hence,

$$\theta = \arg \max_{\theta} \left( P(\{\mathbf{r}_i\}_1, \{\mathbf{r}_i\}_2, \dots, \{\mathbf{r}_i\}_{n_k} | \theta) \right) \quad (5.4)$$

But, the actual probability values are of no consequence, so the logarithm of Eq.(5.1) divided by the number of observations may be used to get the likelihood function

$$\begin{aligned} L(\{\mathbf{r}_i\}_1, \{\mathbf{r}_i\}_2, \dots, \{\mathbf{r}_i\}_{n_k}, \theta) &= \frac{1}{n_k} \sum_{k=1}^{n_k} \ln(P(\{\mathbf{r}_i\}_k | \theta)) \\ &= -\ln(Q(\theta)) - \frac{1}{n_k} \sum_{k=1}^{n_k} \frac{U(\{\mathbf{r}_i\}_k, \theta)}{k_B T} \end{aligned} \quad (5.5)$$

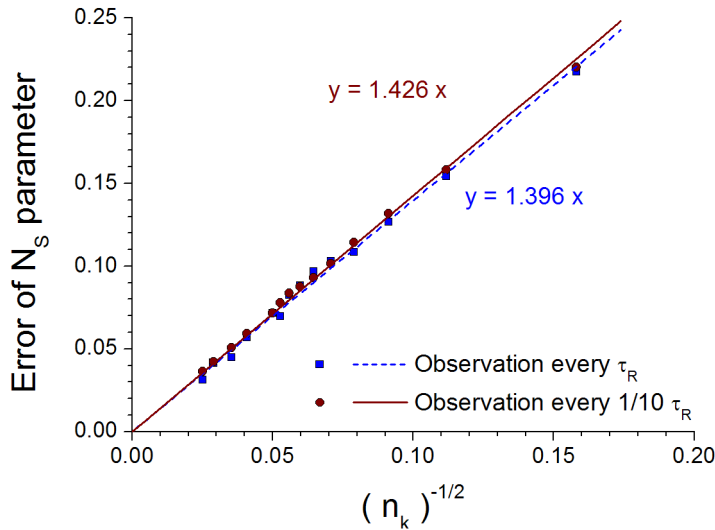
This function is sometimes easier to calculate. Using this, the best parameters for the model are given by

$$\theta = \arg \max_{\theta} \left( L(\{\mathbf{r}_i\}_1, \{\mathbf{r}_i\}_2, \dots, \{\mathbf{r}_i\}_{n_k}, \theta) \right) \quad (5.6)$$

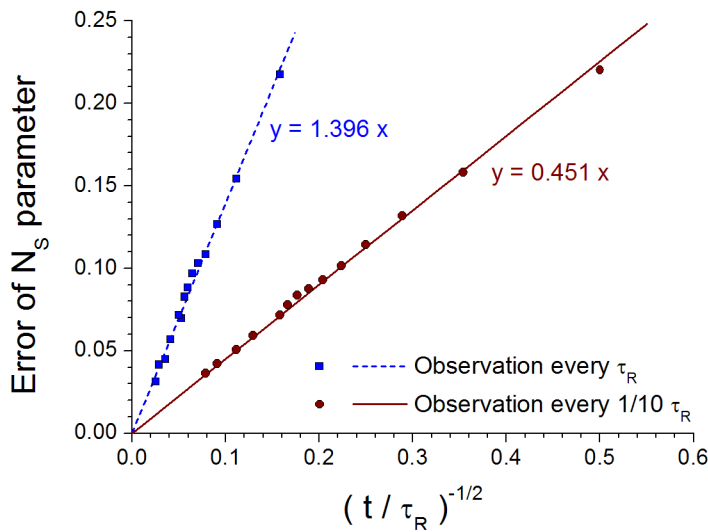
## 5.2 Collection of observations, $\{\mathbf{r}_i\}_1, \{\mathbf{r}_i\}_2, \dots, \{\mathbf{r}_i\}_{n_k}$

When collecting observations of bead positions, one must consider the frequency of observations. When taken too frequently, observations show a dependence upon each other, which reduces the effectiveness of each new observation, because information from the last observation is repeated. Observations that are taken every  $\tau_R$  are almost independent of each other, but have the disadvantage of requiring a longer simulation time to obtain the same number of observations. It is important to balance both the frequency of observation and the number of observations that are possible to be taken during the time allotted for the simulation, in order to use processor time effectively. The time taken to gather observations is significantly longer than the time taken to calculate MLE with the observations after the simulation; a simulation of the two-chain model will take days to obtain the observations, whilst the parameter fitting afterwards will be on the scale of tens of minutes. Hence, it is of interest to optimise the frequency of observations.

A short investigation was undertaken, the results of which are plotted in Fig.5.1. In this investigation a measure of the error in the MLE calculation was constructed. The MLE calculation was run for a reasonably small number of observations,  $n_k = 40, 80, \dots, 1600$ , but repeated 100 times or more, and the standard deviations of the estimated values for the parameter  $N_S$  were taken as the error for each value of  $n_k$ . This was done for data collected every  $\tau_R$  and every  $\frac{1}{10}\tau_R$ , which is plotted in Fig.5.1a as a function of  $\frac{1}{\sqrt{n_k}}$ . It is observed that the results for observations every  $\tau_R$  approaches zero slightly faster than the data collected every  $\frac{1}{10}\tau_R$ , which is an indication that the observations made in the second case are not completely independent. In Fig.5.1b the error is plotted against  $\frac{1}{\sqrt{t}}$ , where  $t$  is the final simulation time. In this plot it is observed that data collected every  $\frac{1}{10}\tau_R$  approaches zero faster than data collected every  $\tau_R$ , because 10 times as many observations are made in the same period of time, despite each one being slightly less effective. However, this is only a sample of two observation frequencies and it is anticipated that this trend will not continue. If observations are taken too frequently, the



(a) Error in the  $N_S$  parameter against  $\frac{1}{\sqrt{n_k}}$ , where  $n_k$  is the number of observations used in the MLE calculation.



(b) Error in the  $N_S$  parameter against  $\frac{1}{\sqrt{t/\tau_R}}$ , where  $t$  is the final simulation time.

Figure 5.1: Reduction of error in MLE with increasing numbers of observations and simulation time.

effectiveness of each observation will eventually become so much worse that the error will converge slower as the frequency of observations is increased. In this study, observations are taken every  $\frac{1}{10}\tau_R$ , with  $n_k = 200\,000$  observations obtained from multiple simulations. It is useful to note that, because the observations are independent, separate simulations can be used to obtain the observations, allowing the time taken to scale with the number of computers available.

### 5.3 MLE for the slip-spring models

The likelihood function is now applied to the slip-spring model, where  $P(\{\mathbf{r}_i\}, \mathbf{r}_A, N_S)$  is given by Eq.(3.50). In Fig.5.2, the likelihood function (Eq.(5.5)) is plotted as a contour map over the two parameters  $h$  and  $N_S$ , where the slip-spring has anchor point  $\mathbf{r}_A = (0, 0, h)$  and spring constant  $k_S = k/N_S$ . It is observed that there is a steep drop in likelihood when the slip-spring becomes too strong and a similar drop when the slip-spring anchoring point is too close to the chain. Between these drops there is a ridge of high likelihood. Further investigation, in Fig.5.3, plots the most likely value of  $N_S$  as a function of  $h$ , as well as the likelihood value associated with these parameters. This indicates that small values of  $N_S$  are very unlikely. This is a reasonable conclusion to reach, since basic observation of the two-chain model does not indicate a static point in the simulation box through which both chains slide. Instead the entanglement point fluctuates through space. This is in direct contrast with the slip-link models of Hua-Schieber and Doi-Takimoto discussed in section 1.3.3. In these models the slip-links are fixed in space, which is equivalent to  $N_S \rightarrow 0$ .

In Fig.5.4 the analytical fitting of the slip-spring parameters, seen previously in Fig.3.25, is compared to the MLE ridge seen in Fig.5.3. The MLE results closely follow those of  $G_{zz}(t)$ , which is not unexpected since to obtain  $\langle z_{N/2} \rangle$ , the slip-spring must provide sufficient force in the z-direction. It is observed that the point where the MLE results intercept the best parameters line for  $G_{zz}(t)$  occurs at the same point where the  $G_{zz}(t)$  best parameters line intercepts the  $(G_{zz}(0) - G_{zz}(\infty))$  parameters line; this point is  $h = 10.89$ . However, the MLE ridge is not flat

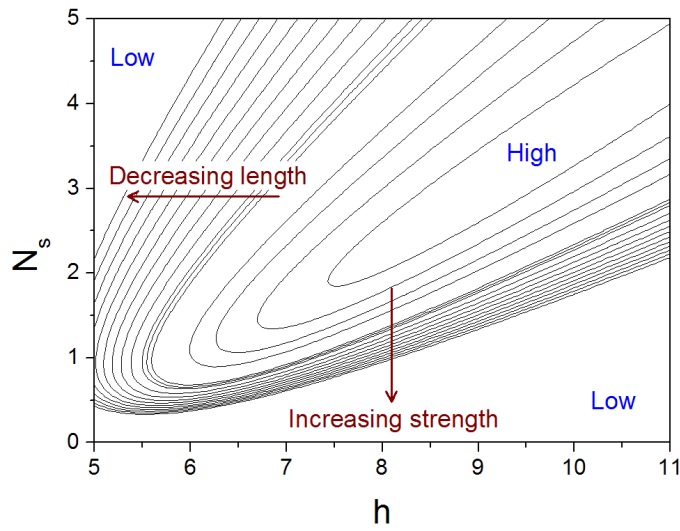


Figure 5.2: Contour map of likelihood values for the slip-spring model. Two-chain model parameters are  $N = 16$ ,  $D = 10$  and  $H = 10$ .

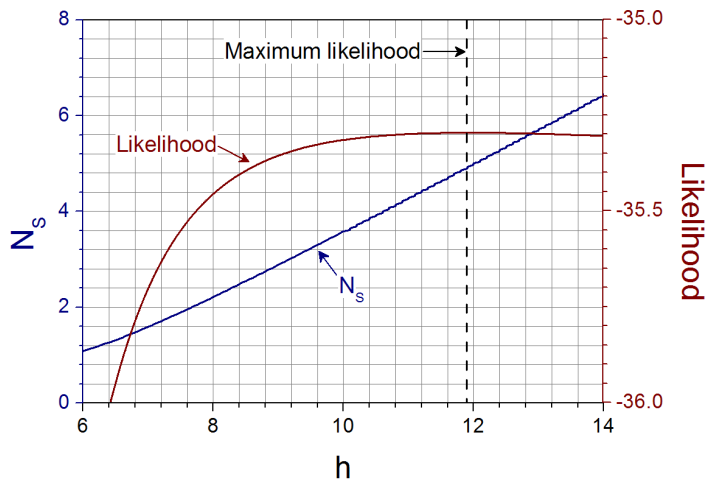


Figure 5.3: Most likely values of  $N_S$  as a function of  $h$ , for the slip-spring model. Plotted on the right axis is the likelihood value for these parameters. The maximum likelihood value occurs at  $h = 11.9$ , as indicated by the dashed line. Two-chain model parameters are  $N = 16$ ,  $D = 10$  and  $H = 10$ .

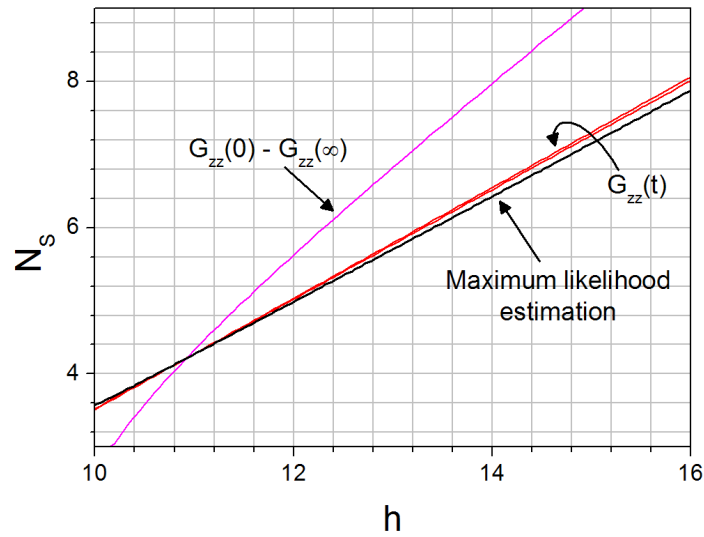


Figure 5.4: Analytical fitting of slip-spring parameters from Fig.3.25 combined with the MLE ridge from Fig.5.3. Lines for  $G_{xx}(t)$  and  $G_{yy}(t)$  do not cross the other lines within the displayed parameter space and are omitted. Two-chain model parameters are  $N = 16$ ,  $D = 10$  and  $H = 10$ .

and the maximum value identified by MLE is  $h = 11.9$ . The reason for this can be explained using Fig.3.25, where it is observed that  $G_{xx}(t)$  and  $G_{yy}(t)$  would be best matched with a larger value of  $h \approx 24$ . MLE has identified the parameters best for the model, which favours  $G_{zz}(t)$ , but has not completely ignored  $G_{xx}(t)$  and  $G_{yy}(t)$ . Hence, the value found is slightly larger than is best for  $G_{zz}(t)$ .

The MLE parameter fitting was also applied to the non-isotropic model, the results for which can be found in Fig.5.5. It is observed that the values for  $h$  and  $N_{S,z}$  are in agreement with the analytical fitting, whilst  $N_{S,x}$  and  $N_{S,y}$  are not. The difference in  $N_{S,x}$  values is likely due to the issues highlighted in Fig.3.28b, where the bead positions are known to be wrong, despite giving the correct stress value. This caused a conflict with MLE, resulting in a different value from the analytical fitting to  $G_{xx}(t)$ . The difference found in  $N_{S,y}$  is relatively small. Fig.4.4b shows that in the y-direction the analytical fitting provided a bead position variance that was too large. Hence, when fitting  $N_{S,y}$  the MLE method selected a smaller value, resulting in a better fit of  $\text{var}(y_i)$ , but worse  $G_{yy}(t)$ . Once again, this fits the model to what is actually happening with

Slip-spring model	Best fit of stress moments	MLE value
$h$	10.89	11.93
$N_S$	4.20	4.95
Non-isotropic model	Best fit of stress moments	MLE value
$h$	10.89	10.91
$N_{S,x}$	8.48	4.32
$N_{S,y}$	9.85	7.32
$N_{S,z}$	4.20	4.20

Figure 5.5: MLE parameters for the slip-spring model and the non-isotropic slip-spring model. The best fit of stress moments,  $G_{\gamma\gamma}(0)$  and  $G_{\gamma\gamma}(\infty)$  are found by comparing simulation results of the two-chain model against analytical calculations of the slip-spring model. The two-chain model parameters are  $N = 16$ ,  $D = 10$  and  $H = 10$ .

the beads, rather than fitting the property of most interest.

## 5.4 MLE for a multiple entanglement slip-spring model

MLE can also be applied to the multiple entanglement slip-spring model, for which we now present the partition function. To construct this partition function, a number of equations from section 3.2.2 are required. The partition function of a single Rouse chain constructed from  $n$  beads with fixed ends at  $\mathbf{r}_A$  and  $\mathbf{r}_B$  is known from Eq.(3.36) as

$$Z(\mathbf{r}_A, \mathbf{r}_B, n) = \left(\frac{1}{n}\right)^{\frac{3}{2}} \left(\frac{2k_B T \pi}{k}\right)^{\frac{3}{2}(n-1)} \exp\left(-\frac{k}{2k_B T} \frac{(\mathbf{r}_A - \mathbf{r}_B)^2}{n}\right) \quad (5.7)$$

The partition function for a slip-spring with spring-constant  $k_S$  is similarly given by Eq.(3.37) as

$$Z_S(\mathbf{r}_A, \mathbf{r}_B, k_S) = \exp\left(-\frac{k_S}{2k_B T} (\mathbf{r}_A - \mathbf{r}_B)^2\right) \quad (5.8)$$

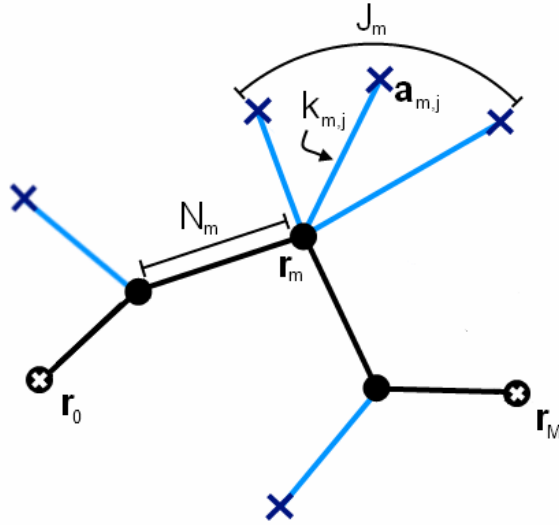


Figure 5.6: Diagram of the multiple slip-spring model

It is known from Eq.(5.9) that the combination of two of these chains, where the connecting bead is no longer fixed, is

$$Z_1(\mathbf{r}_A, \mathbf{r}_C, n_A, n_C) = \int Z(\mathbf{r}_A, \mathbf{r}, n_A) Z(\mathbf{r}, \mathbf{r}_C, n_C) d^3\mathbf{r} \quad (5.9)$$

$$Z_2(\mathbf{r}_A, \mathbf{r}_C, n_A, k_S) = \int Z(\mathbf{r}_A, \mathbf{r}, n_A) Z_S(\mathbf{r}, \mathbf{r}_C, k_S) d^3\mathbf{r} \quad (5.10)$$

Using the above equations, the partition function of the multiple entanglement slip-spring model does not need to consider the individual  $N$  bonds and  $N+1$  beads. Instead the system can be broken down into  $M$  Rouse chains between  $M-1$  slip-link positions, as depicted in Fig.5.6. In this section, the beads with slip-links attached are labelled  $\mathbf{r}_1$  to  $\mathbf{r}_{M-1}$ , and the fixed beads at the end of the chain are  $\mathbf{r}_0$  and  $\mathbf{r}_M$ . The number of beads within a section of chain  $\mathbf{r}_{m-1}$  to  $\mathbf{r}_m$  is labelled as  $N_m$ , where  $m = 1, \dots, M$ . In order to permit slip-links to occupy the same bead, the number of slip-springs attached to bead  $m$  is labelled as  $J_m$ , and the total number of slip-springs in the system is

$$N_{\text{Slip-Springs}} = \sum_{m=1}^{M-1} J_m \quad (5.11)$$

The anchoring points of these slip-springs are labelled as  $\mathbf{a}_{m,j}$ , where  $j = 1, \dots, J_m$  is the index of each slip-spring attached to slip-link  $m$ . The spring-constants of each of these beads are labelled as

$$k_{m,j} = \frac{k}{N_{S,m,j}} \quad (5.12)$$

where  $k$  is the spring constant for a bond in the Rouse chain, and the spring strength  $N_S$  is allowed to be different for each slip-spring.

The partition function of each Rouse chain is given by  $Z(\mathbf{r}_{m-1}, \mathbf{r}_m, N_m)$  and each slip-spring as  $Z_S(\mathbf{r}_m, \mathbf{a}_{m,j}, k_{m,j})$ . To obtain the partition function for the entire system without the slip mechanism,  $Q^{\text{fixed}}$ , these chains are connected by Eq.(5.9) and Eq.(5.10). Hence,

$$\begin{aligned} Q^{\text{fixed}}(\mathbf{r}_0, \mathbf{r}_M, M, \{J_m\}, \{N_m\}, \{a_{m,j}\}, \{k_{m,j}\}) \\ = \int \left( \prod_{m=1}^M Z(\mathbf{r}_{m-1}, \mathbf{r}_m, N_m) \prod_{m=1}^{M-1} \prod_{j=1}^{J_m} Z_S(\mathbf{r}_m, \mathbf{a}_{m,j}, k_{m,j}) \right) d^3\mathbf{r}_1 \dots d^3\mathbf{r}_{M-1} \end{aligned} \quad (5.13)$$

This equation may be integrated in matrix notation using

$$\begin{aligned} Q^{\text{fixed}} &= \lambda \exp(-\alpha C) \int \exp(-\alpha (A_{ij}\mathbf{r}_i\mathbf{r}_j - \mathbf{B}_i\mathbf{r}_i)) d^3\mathbf{r}_1 \dots d^3\mathbf{r}_{M-1} \\ &= \lambda \exp(-\alpha C) \left( \frac{1}{\det A} \left( \frac{\pi}{\alpha} \right)^{M-1} \right)^{\frac{3}{2}} \exp\left( \frac{\alpha}{4} \mathbf{B}^T A^{-1} \mathbf{B} \right) \end{aligned} \quad (5.14)$$

(as demonstrated in appendix B), where  $\lambda$  is given by the product of the prefactors from  $Z(\mathbf{r}_{m-1}, \mathbf{r}_m, N_m)$  in Eq.(5.13), such that

$$\begin{aligned} \lambda &= \prod_{m=1}^M \left( \left( \frac{1}{N_m} \right)^{\frac{3}{2}} \left( \frac{2k_B T \pi}{k} \right)^{\frac{3}{2}(N_m-1)} \right) \\ &= \left( \prod_{m=1}^{M-1} \frac{1}{N_m} \right)^{\frac{3}{2}} \left( \frac{2k_B T \pi}{k} \right)^{\frac{3}{2}(N-M)} \end{aligned} \quad (5.15)$$

( $Z_S(\mathbf{r}_m, \mathbf{a}_{m,j}, k_{m,j})$  has no prefactors). The components  $\alpha$ ,  $A$ ,  $\mathbf{B}$ ,  $C$  are given by the expansion of the terms inside the exponential:  $\alpha$  is a scalar constant,

$$\alpha = \frac{1}{2k_B T} \quad (5.16)$$

$A$  is a symmetric  $(M-1) \times (M-1)$  tri-diagonal matrix of scalars, where

$$\begin{aligned} A_{i,i} &= \frac{k}{N_i} + \frac{k}{N_{i+1}} + \sum_{j=1}^{J_i} k_{i,j} \\ A_{i,i+1} &= -\frac{k}{N_{i+1}} \end{aligned} \quad (5.17)$$

$\mathbf{B}$  is a  $1 \times (M-1)$  matrix of position vectors,

$$\mathbf{B} = \begin{pmatrix} 2k \frac{\mathbf{r}_0}{N_1} + 2 \sum_{j=1}^{J_1} k_{1,j} \mathbf{a}_{1,j} \\ 2 \sum_{j=1}^{J_2} k_{2,j} \mathbf{a}_{2,j} \\ 2 \sum_{j=1}^{J_3} k_{3,j} \mathbf{a}_{3,j} \\ \vdots \\ 2k \frac{\mathbf{r}_M}{N_M} + 2 \sum_{j=1}^{J_{M-1}} k_{M-1,j} \mathbf{a}_{M-1,j} \end{pmatrix} \quad (5.18)$$

and  $C$  is a scalar,

$$C = \frac{k r_0^2}{N_1} + \frac{k r_M^2}{N_M} + \sum_{m=1}^{M-1} \sum_{j=1}^J k_{m,j} a_{m,j}^2 \quad (5.19)$$

This partition function can be used with the MLE routine and Eq.(5.5) to estimate the set of parameters  $\{k_{m,j}\}$  and  $\{\mathbf{a}_{m,j}\}$  for a multiple slip-spring model with no slip mechanism, using observations from a single chain within a MD polymer melt simulation.

In order to test the MLE fitting, it has been used to reproduce the parameters of a slip-spring model with fixed slip-link indices (Fig.5.7a). There was a single spring-constant used for all the slip-springs in this test, which was known by the MLE routine. Only the anchor positions had to be fitted (which required 24-dimensional minimisation for the 8 slip-links used) and there were no

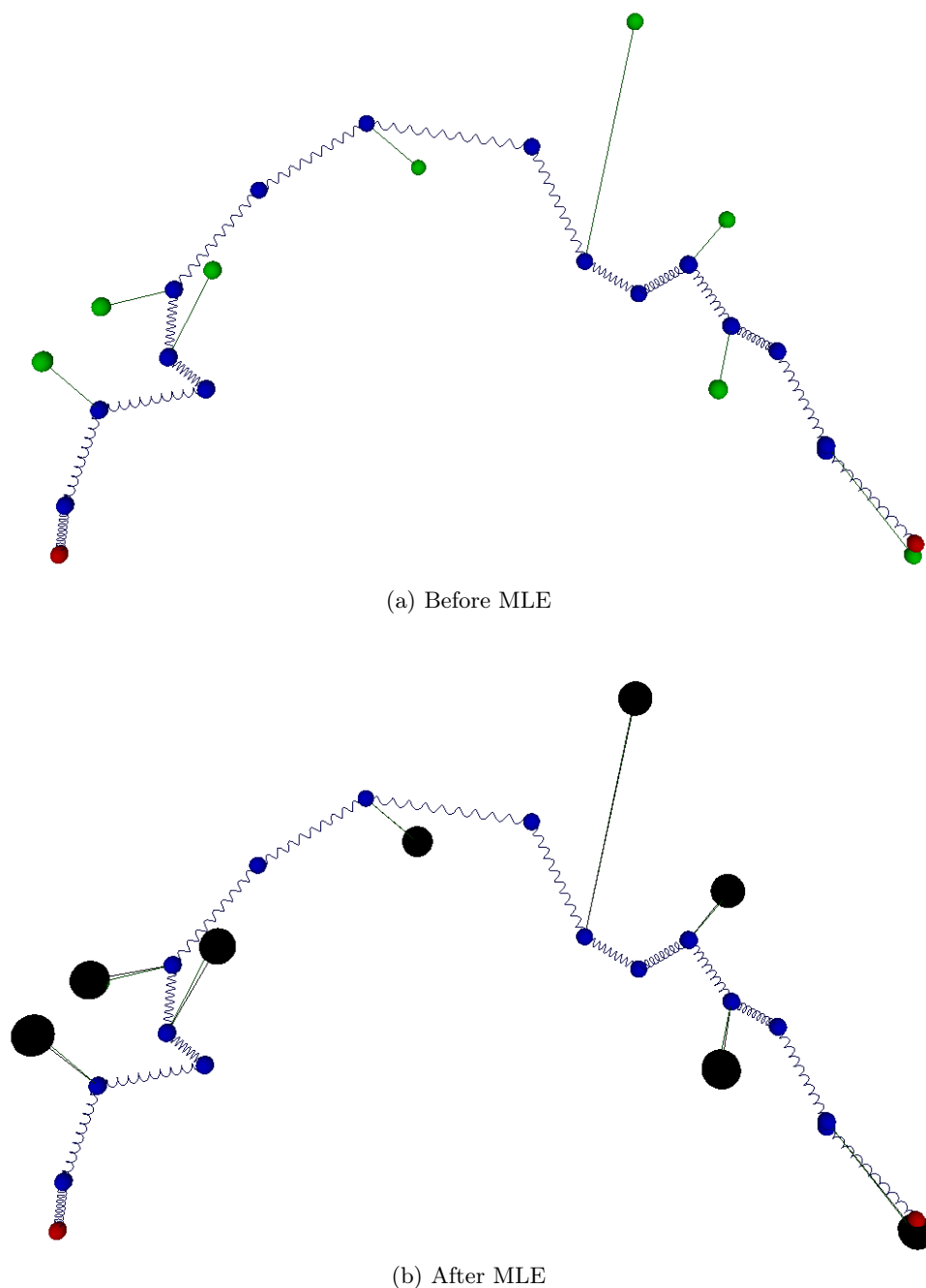


Figure 5.7: A slip-spring model with 8 entanglements was used to generate a collection of observations for the MLE function. The MLE function was then tasked with fitting a collection of anchor positions (minimisation in 24-dimensional space). Regular-sized green spheres are slip-spring anchors, while large black spheres are MLE estimated positions. The chain in the screen shots is a snapshot of the bead positions at a single time step.

approximate positions supplied to the fitting, so the method began with all anchor points at the origin. It is observed in Fig.5.7b that, after MLE fitting, the estimated anchor points (large black spheres) overlap with the real anchoring points from Fig.5.7a. The slip-springs connecting the anchor points to the chain are also included on this image for both real and estimated anchoring points, but due to the accuracy of the parameter estimation, these are very close or overlapping.

This is a model without the slip mechanism, such that  $M$ ,  $\{N_m\}$  and  $\{J_m\}$  are constants. In order to implement the slip mechanism, a summation over all possible slip-link positions is required, similar to Eq.(3.49) for the single entanglement model. In this case it would involve a sum of  $N^{N_{\text{Slip-Spring}}}$  partition functions (one for each combination of slip-link positions), which would be a monumental task even for today's computational abilities. The current challenge of applying the MLE function to the multiple entanglement slip-spring model, is to simplify the calculation of the partition function.

## 5.5 Summary

Using MLE, it is possible to find parameters for any model with known probability distribution, as has been done for the slip-spring models. The MLE fitting uses the actual position of the beads to find the best parameters, without a bias towards desired properties. This resulted in some disagreement between analytical fitting and MLE fitting for the slip-spring models. Since MLE fitting obtains the best parameters for the model, any disagreement with analytical fitting is due to flaws in the model. This is not a bad thing and is useful for identifying such flaws. For example, when comparing the non-isotropic slip-spring model parameter estimates, it was observed that  $h$ ,  $N_{S,z}$  were estimated accurately, whilst  $N_{S,x}$  disagreed significantly from analytical fitting of  $G_{xx}(t)$ . This highlighted the largest flaw in the model, which is known to be the distribution of beads in the x-direction. Previous parameter fitting was able to make  $G_{xx}(t)$  equal to that of the two-chain simulation, but did so only by ignoring the motion of the beads, which obscured the flaw in the model. Hence, MLE fitting can be used, not only as a useful tool

for finding parameters, but also as a tool for highlighting areas of the model that require further improvement.

## Chapter 6

# Discussion and future directions

### 6.1 Dependence on system stretch

It has been demonstrated that the slip-spring model represents a single entanglement in great detail and was found to be an accurate model for stress relaxation, as was calculated from fluctuations using fluctuation-dissipation theorem. Deformation and dependence on system stretch has not been thoroughly investigated, although a limited study was done using the non-isotropic slip-spring model in section 4.1.3; through parameter finding to fit  $\langle \sigma_{\gamma\gamma} \rangle$  and  $\langle \sigma_{\gamma\gamma}^2 \rangle$  it was demonstrated that the anchor position should deform affinely as the system height,  $H$ , is increased. Also, for a moderately strong entanglement, it was found that the spring strength of

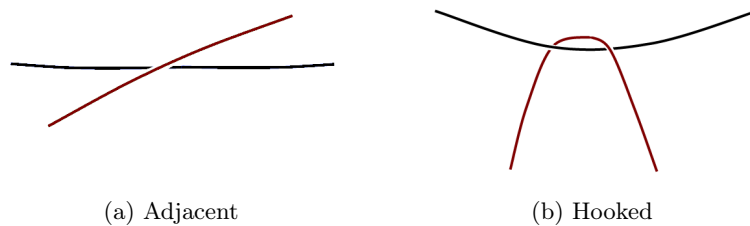


Figure 6.1: Diagrams of a weak entanglement (adjacent) and of a strong entanglement (hooked), as originally discussed in section 1.1. The difference between them is the curvature of the chains, controlled in the two-chain model by the system stretch,  $H$ .

the slip-spring can be kept constant during this deformation. However, it was found that if the entanglement becomes weak, the spring-strength must change non-isotropically.

When the entanglement becomes weaker, the spring strengths also become weaker, eventually becoming infinitely weak for unentangled chains. However, it was noticed that the entanglement strength in the x- and y-directions become weak much sooner, than in the z-direction. This is because the system becomes akin to two adjacent chains as depicted in Fig.6.1a as opposed to the hooked case as shown in Fig.6.1b. When two chains are adjacent to each other, there is still a topological constraint between the chains, which requires a slip-spring force away from the other chain (z-direction), but there is little constraint perpendicular to this (x- and y-directions), which requires the slip-spring to be much weaker in these directions. The original isotropic slip-spring model would not have been able to reproduce these weak entanglement effects accurately; it is only the non-isotropic slip-spring model that is able to model this effect correctly.

## 6.2 Slip-spring model for the case of $N_S \rightarrow 0$ , where slip-links are fixed in space

A recent paper by Schieber and Horio [36] stated that “*the plateau modulus for the elastic slip-link model [slip-spring model] was unchanged in the rigid limit. The presence of elasticity in the slip-links would lead only to a change in the shape of the relaxation modulus, but not its height*”. This contradicts the concept of the slip-spring model and suggests that the slip-links should be fixed in space, which in our model corresponds to  $N_S \rightarrow 0$ . Our study used maximum likelihood estimation to predict the best pair of parameters for the slip-spring model (section 5.3) and observed that  $N_S \rightarrow 0$  is extremely unlikely. Such a finding is corroborated by consideration of the two-chain simulation, since no fixed point in space - through which both chains must always pass - is observed; instead the point of the entanglement has its own motion as two chains fluctuate.

A slip-spring model deformed affinely, should find that the slip-spring anchors are deformed

affinely as confirmed in section 4.1.3, but the slip-links attached to the end of the slip-springs are deformed sub-affinely [22]. (I.e. the z-position of the slip-link does not undergo the transformation  $z \rightarrow \lambda z$  when the deformation  $H \rightarrow \lambda H$  is applied to the system.) As such the height of the plateau modulus should be dependent on the strength of the slip-springs. If the model was defined with the slip-spring anchors at the average position of the slip-link, then an affine deformation of slip-links may be observed, but this is not how the slip-spring model should be applied; the slip-springs should pull the chain away from its unentangled mean path as described in section 1.3.4 and depicted in Fig.1.12.

### 6.3 Dual-slip-chain model

The slip-chain model delayed the relaxation of  $\sigma_{zz}(t)$ , but also allowed the cross-correlation of stress,  $G_{zz}^X(t)$ , to be better described. However, the cross-correlation function is calculated between the lower chain and the slip-spring virtual object, which is not ideal. It is only because the slip-chain modification provides a mechanism to add extra stress into the slip-spring object, that  $G_{\gamma\gamma}^X(t)$  can be adjusted to fit the two-chain model. Yet, this mechanism cannot fit all stress components simultaneously and, unlike the non-isotropic spring-constant, the number of beads in the slip-chain cannot be different in each direction.

A modification can be suggested for future work that improves upon the slip-chain model even further and should allow all  $G_{\gamma\gamma}^X(t)$  to be fit. This improvement would introduce a second slip-chain to the model, where both slip-chains share the same slip-link, but have different anchoring points. The anchoring positions of this model would be defined as

$$\begin{aligned} \mathbf{r}_{A1} &= \left( \frac{1}{2}h_x, \quad \frac{1}{2}h_y, \quad h_z \right) \\ \mathbf{r}_{A2} &= \left( -\frac{1}{2}h_x, \quad -\frac{1}{2}h_y, \quad h_z \right) \end{aligned} \tag{6.1}$$

to add stretch in the x- and y-directions, allowing the stretch term of  $\langle \sigma_{\gamma\gamma}^{\text{Slip-chain}} \rangle$  to be adjusted, in order to fit all the cross-correlation components, where  $\langle \sigma_{\gamma\gamma}^{\text{Slip-chain}} \rangle$  is calculated from

Eq.(4.39). Further improvement could also be added to such a model by allowing beads to be exchanged between the two slip-chains in a slip style mechanism such that

$$N_{SC} = N_{SC,1}(t) + N_{SC,2}(t) \quad (6.2)$$

This would make the dual-slip-chain model more similar to the two-chain model than any other slip-spring model considered so far. However, one must be conscious when suggesting additional modifications to a model to make sure that it does not become too complex. A common criticism of the tube model is that too many modifications to the model have made it cumbersome to use.

## 6.4 Computational costs of model modifications and the slip-chain model

In the slip-chain modification (section 4.2) extra beads are added to the slip-spring to slow the middle bead motion, allowing the relaxation of  $\sigma_{zz}(t)$  to be delayed to fit to the two-chain model. However, one must stress that such a solution comes at a cost. The slip-chain increased the number of beads in the simulation by  $N_{SC} \sim N$ . This means that there are approximately twice as many beads to move in each simulation step and results in the computation of each time step taking twice as long (excluding time taken for calculating observed properties). The non-isotropic slip-spring model does not result in a significant increase in computational costs, but has its own challenges involved in parameter fitting for the multiple entanglement case.

## 6.5 Expansion to the case of melts

The aim of this study was to investigate a single entanglement in the simplest model of a polymer network, in order to identify how well the slip-spring model reproduces the static and dynamic properties. When studying the simplest case, flaws in the model were identified and addressed, with the aim of eventually applying the knowledge gained to the full multiple slip-spring model of

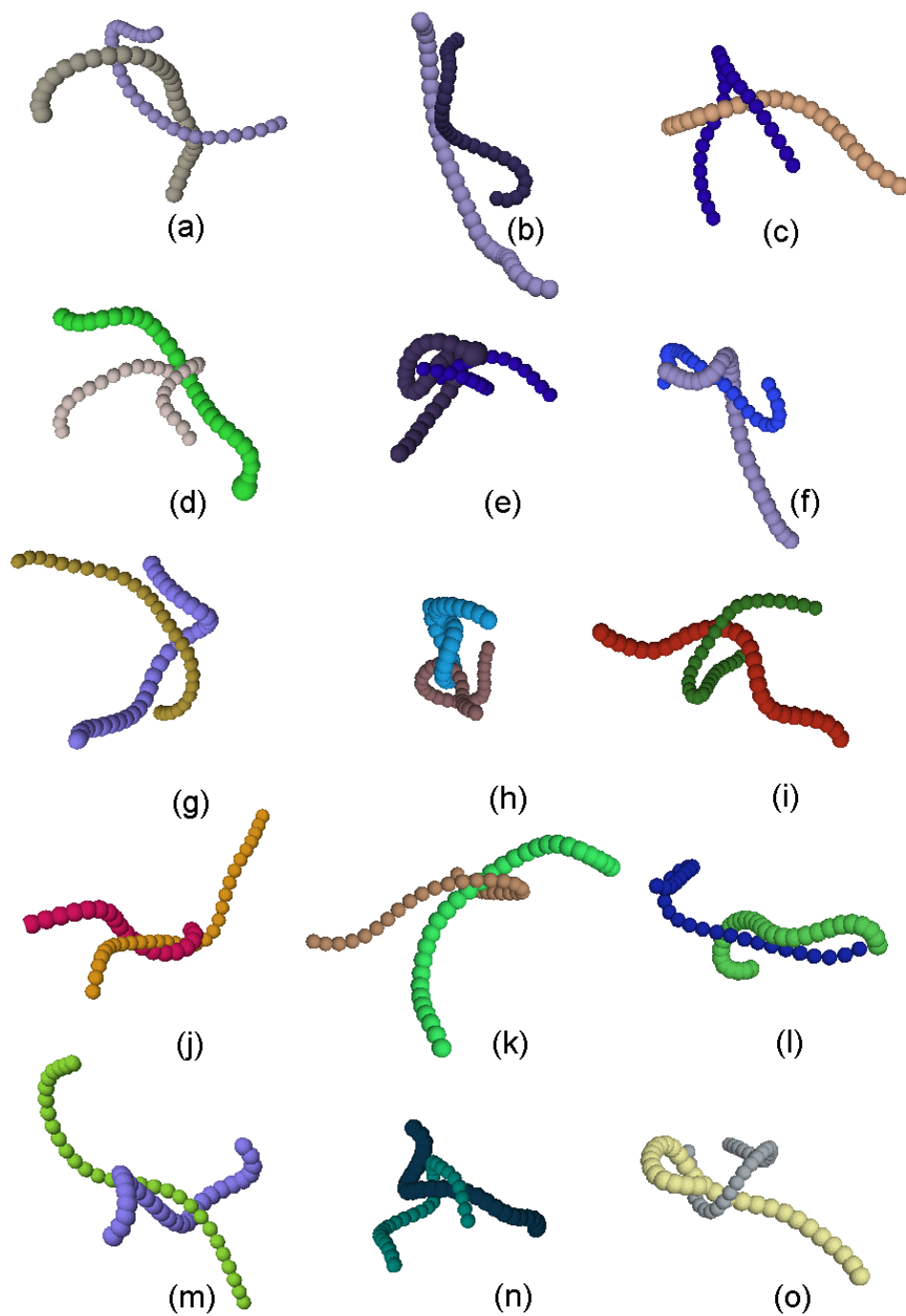


Figure 6.2: Sample of entanglements observed in a polymer melt MD simulation [3]

a polymer melt. A recent study by Likhtman, Ponnuragan and Cao [3] has developed a technique of identifying entanglements in MD simulations by persistent contacts and the linking number between two chains. As such, it is now possible to get a clear picture of the entanglements within a polymer melt, which may be used to justify the model of the simplest entanglement used. A sample of these images are collated in Fig.6.2. In these images the chains are mean paths - the beads' positions averaged over a period of time, which smooths the chain without completely averaging out the temporary entanglements. Fig.6.2 is of interest to this study, because it allows the types of entanglement to be identified: sub-figure (a) is a clear example of the style of entanglement studied with the two-chain model, whilst in (h) the chains are completely looped around each other, and in (j) the two chains are twisted around each other. Importantly, the two-chain model style of entanglement dominates. Hence, the modifications developed in comparison to the two-chain model, should be beneficial to the multiple entanglement slip-spring model.

When applying the modifications, the slip-chain model adds the extra parameter for the number of bonds in each slip-chain, which may be fit in the multiple entanglement model based upon the average number of chain bonds between slip-links. The non-isotropic model also adds new parameters, namely the scalar spring strength became a set of strengths:  $\{N_S\} = N_{S,x}, N_{S,y}, N_{S,z}$ . These are more difficult to fit in the multiple entanglement slip-spring model, because each entanglement has a different orientation. Maximum likelihood estimation may be used to fit  $\{N_S\}$  for each entanglement, as described in section 5.4. The non-isotropic model may also be implemented by defining a spring-constant dependent on the current orientation of the chain bonds adjacent to the slip-link. This would require only three spring strengths to be defined for the entire chain and applied to each entanglement relative to the current orientation, such that  $N_{S,x}$  is always applied in the direction that the chain is stretched by the outermost bonds and  $N_{S,z}$  is always applied in the primary direction that the entanglement distorts the chain. Further research is required on applying the non-isotropic slip-spring model to entanglements with variable orientation.

## 6.6 Entanglements within a solvent and the bulky-slip-chain model

The bulky-slip-chain model (section 4.3) repels the beads adjacent to the slip-link, in order to reproduce a repulsion observed in the two-chain model. However, it can be argued that this repulsion might not be required if the chain was surrounded by a solvent or polymer melt. Within such a system, it is possible that the interaction with the surrounding solvent would apply a pressure opposing the repulsion of the chain beads away from the entanglement point in all directions. In order to test whether or not this is the case, one should run a two-chain simulation with an explicit solvent. If the net effect is that beads are attracted towards the slip-link, then the non-isotropic slip-spring model is likely to be capable of reproducing the average bead positions.

## Chapter 7

# Conclusions

A simple model of a single polymer entanglement in a network has been considered (Fig.7.1), similar to the case studied analytically by Graessley and Pearson [2]. By investigating this simple case, this study examined the ability of the slip-spring model to reproduce the static and dynamic properties of an entanglement, which will potentially lead to a better understanding of the multiple entanglement case and suggested possible improvements to the model. In this study, the following properties were considered:

- **Stress auto-correlation function (statics):** The original slip-spring model is able to reproduce  $G_{\gamma\gamma}(0)$  and  $G_{\gamma\gamma}(\infty)$  of the entanglement, where  $\gamma = x, y, z$ , but not simultaneously with one common set of parameters. To address this, the slip-spring spring-constant was replaced by a tensor, creating the *non-isotropic slip-spring model*.
- **Stress auto-correlation function and mean squared displacement of the middle bead (dynamics):** The slip-spring model reproduced the dynamics of  $G_{xx}(t)$  and  $G_{yy}(t)$  accurately, but  $G_{zz}(t)$  was observed to relax faster for the slip-spring model than the two-chain simulation (the orientation of the entanglement is given by Fig.7.1). Furthermore,  $g_{1,\text{mid}}(t)$  indicated that the middle bead in the slip-spring model moved too fast in the z-direction at intermediate time. Therefore, the *slip-chain model* added extra beads along

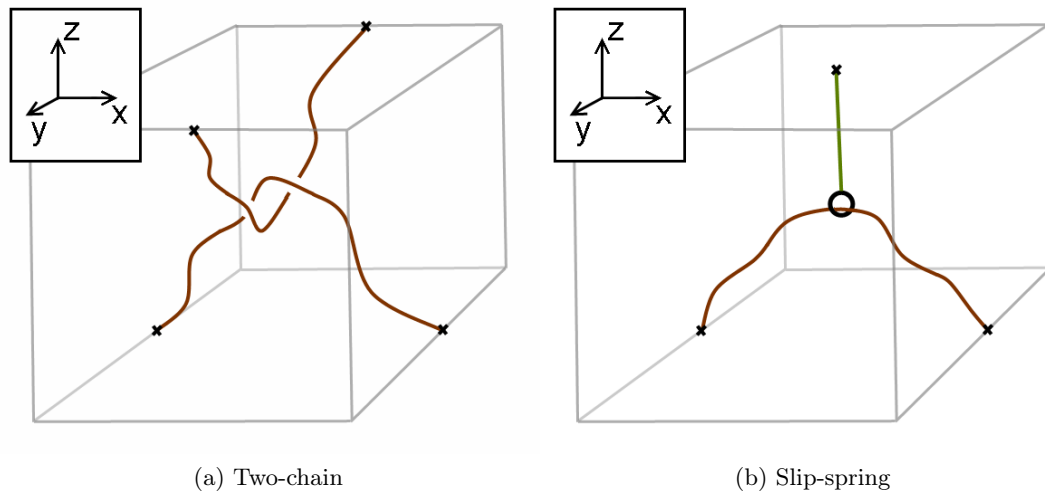


Figure 7.1: Main models used within this study

the slip-spring object to slow the bead motion, which improved the fit of  $g_{1,\text{mid}}(t)$  and delayed the relaxation of  $G_{zz}(t)$ .

- Stress cross-correlation function:** The slip-spring model is poor at reproducing cross-correlations, since the virtual slip-spring object is significantly different from the polymer chain that it replaced. The slip-chain model provided a parameter suited for approximately addressing the discrepancy, allowing a better fit of  $G_{zz}^X(t)$ , but not  $G_{xx}^X(t)$  and  $G_{yy}^X(t)$ .
- Average bead positions:** The slip-spring model reproduces the average bead positions in the  $z$ -direction accurately. This is not a trivial task, since the mean path of the chain is sensitive to the way the entanglement slides along the chain, producing a curved shape. With the best parameter set for  $G_{zz}(t)$ , the slip mechanism of the slip-spring model samples the chain with the same distribution as the two-chain model's entanglement, allowing an accurate reproduction of the  $z$ -direction average bead positions.
- Variance of beads and bond vectors:** It was demonstrated that the  $z$ -direction variance increases for those beads and bonds due to the entanglement. This is because the repeated

application and removal of an entanglement to a section of chain causes the variance of that section to increase. Since the slip mechanism is equivalent to the entanglement sliding along the chain, the slip-spring model was able to reproduce the same effect. However, the x- and y-direction variance of bond vectors do not have a peak in variance around the middle bonds created by the slip-spring, despite this effect being observed in the two-chain simulation. It is suspected that this is due to an increased repulsion by the entanglement model that is not fully reproduced by the slip-spring. The *bulky-slip-chain model* was able to address this discrepancy.

The slip-spring model does a reasonable job of reproducing the statics and dynamics of an entanglement, but nevertheless this can be improved upon by implementing the non-isotropic, slip-chain and bulky modifications. However, these modifications increase the complexity and the number of unknown parameters in the model. Thus, a tool like maximum likelihood estimation (MLE) is helpful for finding the model parameters. Furthermore, MLE is recommended for any model with known bead probability distribution, since it fits the model parameters based on observed bead motion from a multi-chain simulation, rather than fitting a desired property and is therefore free of bias.

## Appendix A

# Stress correlation functions for a simple four-arm-star model

To explain the relation between the cross-correlation and auto-correlations of a two-chain model in Fig.3.13, a simple four-arm-star model is considered, where each arm is a single linear spring, with spring constant,  $k = \frac{3k_B T}{b^2}$ . The end of each arm is fixed in space and joined at a central bead,  $\mathbf{r} = (x, y, z)$ , as illustrated in Fig.A.1. The equation of motion for the central bead is

$$\begin{aligned}
 d\mathbf{r} &= \frac{k}{\xi} ((\mathbf{A}_1 - \mathbf{r}) + (\mathbf{A}_2 - \mathbf{r}) + (\mathbf{B}_1 - \mathbf{r}) + (\mathbf{B}_2 - \mathbf{r})) dt + \sqrt{\frac{2k_B T}{\xi}} d\mathbf{W}(t) \\
 &= \frac{k}{\xi} \left( \left( \begin{pmatrix} \frac{D}{2} \\ 0 \\ -\frac{H}{2} \end{pmatrix} \right) + \left( \begin{pmatrix} -\frac{D}{2} \\ 0 \\ -\frac{H}{2} \end{pmatrix} \right) + \left( \begin{pmatrix} 0 \\ \frac{D}{2} \\ \frac{H}{2} \end{pmatrix} \right) + \left( \begin{pmatrix} 0 \\ -\frac{D}{2} \\ \frac{H}{2} \end{pmatrix} \right) - 4\mathbf{r} \right) dt + \sqrt{\frac{2k_B T}{\xi}} d\mathbf{W}(t) \\
 &= -\frac{4k}{\xi} \mathbf{r} dt + \sqrt{\frac{2k_B T}{\xi}} d\mathbf{W}(t)
 \end{aligned} \tag{A.1}$$

This is an Ornstein-Uhlenbeck process,

$$d\mathbf{r} = -\frac{1}{\tau} \mathbf{r} dt + \sqrt{2d_c} d\mathbf{W}(t) \tag{A.2}$$

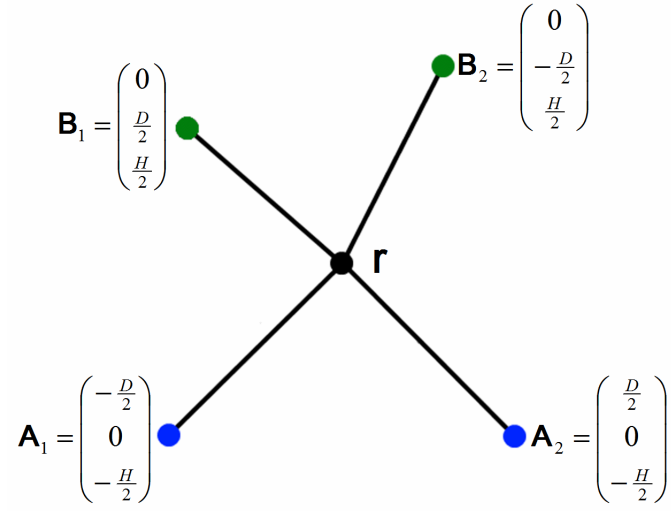


Figure A.1: Diagram of the single bead four-arm-star model

To map the model onto this process, the diffusion constant  $d_c = \frac{k_B T}{\xi}$  and the characteristic time  $\tau = \frac{\xi}{4k}$ . Because the model is an Ornstein-Uhlenbeck process the first two moments at a time,  $t$ , after a deformation are known to be

$$\langle \mathbf{r}(t) \rangle = \langle \mathbf{r} \rangle e^{-\frac{t}{\tau}} \quad (\text{A.3})$$

$$\langle \mathbf{r}(t) \cdot \mathbf{r}(s) \rangle = \text{var}(\mathbf{r}) e^{-\frac{t+s}{\tau}} + d_c \tau \left( e^{-\frac{s-t}{\tau}} - e^{-\frac{s+t}{\tau}} \right) \quad (\text{A.4})$$

$$\langle r^2(t) \rangle = d_c \tau + (\text{var}(\mathbf{r}) - d_c \tau) e^{-\frac{2t}{\tau}} \quad (\text{A.5})$$

In the four-arm-star model the average position of the central bead is known to be the centre of the model, which defined such that  $\langle \mathbf{r} \rangle = 0$ . The variance of the central bead position at

equilibrium can therefore be calculated from Eq.(A.4),

$$\begin{aligned}\text{var}(\mathbf{r}) &= \langle r^2 \rangle - \langle \mathbf{r} \rangle^2 \\ &= \lim_{t \rightarrow \infty} \langle r^2(t) \rangle \\ &= d_c \tau\end{aligned}\tag{A.6}$$

With these equations it is possible to find the stress correlation functions,

$$G_{\gamma\gamma}^A(t) = \frac{V}{k_B T} \langle \sigma_{\gamma\gamma}^A(t) \sigma_{\gamma\gamma}^A(0) \rangle\tag{A.7}$$

$$G_{\gamma\gamma}^B(t) = \frac{V}{k_B T} \langle \sigma_{\gamma\gamma}^B(t) \sigma_{\gamma\gamma}^B(0) \rangle\tag{A.8}$$

$$G_{\gamma\gamma}^X(t) = \frac{V}{k_B T} \langle \sigma_{\gamma\gamma}^A(t) \sigma_{\gamma\gamma}^B(0) \rangle\tag{A.9}$$

$$G_{\gamma\gamma}^T(t) = \frac{V}{k_B T} \langle \sigma_{\gamma\gamma}^T(t) \sigma_{\gamma\gamma}^T(0) \rangle\tag{A.10}$$

where  $\sigma^A$  is the stress contribution from the bonds connecting  $\mathbf{A}_1$  to  $\mathbf{r}$  and  $\mathbf{r}$  to  $\mathbf{A}_2$

$$\sigma_{\gamma\gamma}^A(t) = \frac{k}{V} (r^\gamma(t) - A_1^\gamma)^2 + \frac{k}{V} (r^\gamma(t) - A_2^\gamma)^2\tag{A.11}$$

$\sigma^B$  the stress contribution from the upper bonds connecting  $\mathbf{B}_1$ ,  $\mathbf{r}$  and  $\mathbf{B}_2$

$$\sigma_{\gamma\gamma}^B(t) = \frac{k}{V} (r^\gamma(t) - B_1^\gamma)^2 + \frac{k}{V} (r^\gamma(t) - B_2^\gamma)^2\tag{A.12}$$

and

$$\sigma^T = \sigma^A + \sigma^B\tag{A.13}$$

is the total stress in the system.

**The xx-component,  $\gamma = x$**

Substituting Eq.(A.11) into Eq.(A.7) one obtains

$$\begin{aligned}
\frac{k_B T V}{k^2} G_{xx}^A(t) &= \frac{V^2}{k^2} \langle \sigma_{xx}^A(t) \sigma_{xx}^A(0) \rangle \\
&= \left\langle \left( \left( x(t) - \frac{D}{2} \right)^2 + \left( x(t) + \frac{D}{2} \right)^2 \right) \left( \left( x(0) - \frac{D}{2} \right)^2 + \left( x(0) + \frac{D}{2} \right)^2 \right) \right\rangle \\
&= 4 \langle x^2(t) x^2(0) \rangle + 2D^2 \langle x^2 \rangle + \frac{1}{4} D^4
\end{aligned} \tag{A.14}$$

where Eq.(A.6) gives

$$\langle x^2 \rangle = d_c \tau = \frac{1}{4} \frac{k_B T}{k} \tag{A.15}$$

and using Wick's theorem the first term of Eq.(A.14) is expanded to obtain

$$\langle x^2(t) x^2(0) \rangle = 2 \langle x(t) x(0) \rangle^2 + \langle x^2 \rangle^2 \tag{A.16}$$

where we know from Eq.(A.4) that

$$\begin{aligned}
\langle x(t) x(0) \rangle &= d_c \tau e^{-\frac{t}{\tau}} + d_c \tau \left( e^{-\frac{t}{\tau}} - e^{-\frac{t}{\tau}} \right) \\
&= d_c \tau e^{-\frac{t}{\tau}} \\
&= \frac{1}{4} \frac{k_B T}{k} e^{-\frac{t}{\tau}}
\end{aligned} \tag{A.17}$$

Hence,

$$G_{xx}^A(t) = \frac{1}{2} \frac{k_B T}{V} e^{-\frac{2t}{\tau}} + \frac{1}{4} \frac{k_B T}{V} + \frac{1}{2} \frac{k}{V} D^2 + \frac{1}{4} \frac{k^2}{k_B T V} D^4 \tag{A.18}$$

Similarly we can find

$$G_{xx}^B(t) = \frac{1}{2} \frac{k_B T}{V} e^{-\frac{2t}{\tau}} + \frac{1}{4} \frac{k_B T}{V} \tag{A.19}$$

Using Eq.(A.11) and Eq.(A.12) in Eq.(A.9), the cross correlation is

$$\begin{aligned}
\frac{k_B T V}{k^2} G_{xx}^X(t) &= \frac{V^2}{k^2} \langle \sigma_{xx}^A(t) \sigma_{xx}^B(0) \rangle \\
&= \left\langle \left( \left( x(t) - \frac{D}{2} \right)^2 + \left( x(t) + \frac{D}{2} \right)^2 \right) (2x^2(0)) \right\rangle \\
&= 4 \langle x^2(t) x^2(0) \rangle + D^2 \langle x^2 \rangle \\
&= 8 \langle x(t) x(0) \rangle^2 + 4 \langle x^2 \rangle^2 + D^2 \langle x^2 \rangle \\
G_{xx}^X(t) &= \frac{1}{2} \frac{k_B T}{V} e^{-\frac{2t}{\tau}} + \frac{1}{4} \frac{k_B T}{V} + \frac{1}{4} \frac{k}{V} D^2
\end{aligned} \tag{A.20}$$

Using the above correlation functions the correlation function for the entire system is

$$\begin{aligned}
G_{xx}^T(t) &= G_{xx}^A(t) + 2G_{xx}^X + G_{xx}^B(t) \\
&= 2 \frac{k_B T}{V} e^{-\frac{2t}{\tau}} + \frac{k_B T}{V} + \frac{k}{V} D^2 + \frac{1}{4} \frac{k^2}{k_B T V} D^4
\end{aligned} \tag{A.21}$$

The longest relaxation time of these correlation functions,  $\tau'_{xx}$ , is given by the term  $e^{-\frac{t}{\tau'_{xx}}}$ , such that

$$\tau'_{xx} = \frac{\tau}{2} \tag{A.22}$$

**The yy-component,  $\gamma = y$**

By symmetry the yy-component will relax in exactly the same way as the xx-component, except there will be a rotation about the z-axis such that  $G_{yy}^A(t) = G_{xx}^B(t)$  and  $G_{yy}^B(t) = G_{xx}^A(t)$ .

**The zz-component,  $\gamma = z$** 

First we write the auto-correlation for the lower chain, using Eq.(A.11) and Eq.(A.7), as before,

$$\begin{aligned}
\frac{k_B T V}{k^2} G_{zz}^A(t) &= \frac{V^2}{k^2} \langle \sigma_{zz}^A(t) \sigma_{zz}^A(0) \rangle \\
&= \left\langle \left( 2 \left( z(t) - \frac{H}{2} \right)^2 \right) \left( 2 \left( z(0) - \frac{H}{2} \right)^2 \right) \right\rangle \\
&= 4 \langle z^2(t) z^2(0) \rangle - 4H \langle z^2(t) z(0) \rangle - 4H \langle z(t) z^2(0) \rangle \\
&\quad + 4H^2 \langle z(t) z(0) \rangle + 2H^2 \langle z^2 \rangle - 2H^3 \langle z \rangle + \frac{1}{4} H^4
\end{aligned} \tag{A.23}$$

Compared to Eq.(A.14) there is a subtle change in that both chains are now anchored at the same position  $A_{1,z} = A_{2,z} = -\frac{H}{2}$ . As a consequence, we now have third moment terms  $\langle z^2(t) z(0) \rangle$ , which are known to be zero by symmetry. Hence,

$$\frac{k_B T V}{k^2} G_{zz}^A(t) = 4 \langle z^2(t) z^2(0) \rangle + 4H^2 \langle z(t) z(0) \rangle + 2H^2 \langle z^2 \rangle + \frac{1}{4} H^4 \tag{A.24}$$

This is equivalent to Eq.(A.14) apart from the new second term,  $4H^2 \langle z(t) z(0) \rangle$ . Using Eq.(A.17) this term may be written as

$$4H^2 \langle z(t) z(0) \rangle = H^2 \frac{k_B T}{k} e^{-\frac{t}{\tau}} \tag{A.25}$$

to get the auto-correlation function

$$G_{zz}^A(t) = \frac{1}{2} \frac{k_B T}{V} e^{-\frac{2t}{\tau}} + \frac{k}{V} H^2 e^{-\frac{t}{\tau}} + \frac{1}{4} \frac{k_B T}{V} + \frac{1}{2} \frac{k}{V} H^2 + \frac{1}{4} \frac{k^2}{k_B T V} H^4 \tag{A.26}$$

This new term gives the new longest relaxation time,  $\tau'_{A,zz} = \tau$ , which means that the stress relaxes twice as slow in the z-axis than in the x- and y-axes. The auto-correlation function of the upper chain can be seen to be equal to the auto-correlation function of the lower chain by symmetry,  $G_{zz}^B(t) = G_{zz}^A(t)$ . However, the cross-correlation shows something interesting. Using

Eq.(A.11), Eq.(A.12) and Eq.(A.9) the function is

$$\begin{aligned}
\frac{k_B T V}{k^2} G_{zz}^X(t) &= \frac{V^2}{k} \langle \sigma_{zz}^A(t) \sigma_{zz}^B(0) \rangle \\
&= \left\langle \left( 2 \left( z(t) - \frac{H}{2} \right)^2 \right) \left( 2 \left( z(0) + \frac{H}{2} \right)^2 \right) \right\rangle \\
&= 4 \langle z^2(t) z^2(0) \rangle - 4H^2 \langle z(t) z(0) \rangle + 2H^2 \langle z^2 \rangle + \frac{1}{4} H^4 \quad (\text{A.27})
\end{aligned}$$

which is identical to Eq.(A.24), except the sign on the second term has changed. Hence,

$$G_{zz}^X(t) = \frac{1}{2} \frac{k_B T}{V} e^{-\frac{2t}{\tau}} - \frac{k}{V} H^2 e^{-\frac{t}{\tau}} + \frac{1}{4} \frac{k_B T}{V} + \frac{1}{2} \frac{k}{V} H^2 + \frac{1}{4} \frac{k^2}{k_B T V} H^4 \quad (\text{A.28})$$

When the total stress auto-correlation is calculated

$$\begin{aligned}
G_{zz}^T(t) &= 2G_{zz}^A(t) + 2G_{zz}^X(t) \\
&= 2 \frac{k_B T}{V} e^{-\frac{2t}{\tau}} + \frac{k_B T}{V} + 2 \frac{k}{V} H^2 + \frac{k^2}{k_B T V} H^4 \quad (\text{A.29})
\end{aligned}$$

the longest relaxation time found in the auto- and cross-correlations has been exactly cancelled out. Hence the relaxation time of the total stress in all directions is  $\frac{\tau}{2}$ , faster than the auto- and cross-correlations in the z-direction which has a relaxation time of  $\tau$ . This is analogous to the effect observed in Fig.3.13 for the more complicated two-chain model.

## Appendix B

# List of Gaussian integrals

### Gaussian integrals of the form $\int \exp(-ax^2) dx$

For a scalar  $x$ :

$$\int_{-\infty}^{\infty} \exp(-ax^2) dx = \left(\frac{\pi}{a}\right)^{\frac{1}{2}} \quad (\text{B.1})$$

For a vector,  $\mathbf{r}$ , of dimension  $d$ :

$$\int \exp(-a\mathbf{r}^2) d^d\mathbf{r} = \left(\frac{\pi}{a}\right)^{\frac{d}{2}} \quad (\text{B.2})$$

Generalised for integrating by  $n$  vectors,  $d^d\mathbf{r}_1 \dots d^d\mathbf{r}_n$ , using matrix notation:

$$\int \exp(-A_{ij}\mathbf{r}^i\mathbf{r}^j) d^d\mathbf{r}_1 \dots d^d\mathbf{r}_n = \left(\frac{\pi^n}{\det A}\right)^{\frac{d}{2}} \quad (\text{B.3})$$

where  $A$  is a  $n \times n$  matrix of scalars.

### Gaussian integrals of the form $\int \exp(-\alpha [ax^2 - bx]) \, dx$

For a scalar  $x$ :

$$\int_{-\infty}^{\infty} \exp(-\alpha [ax^2 - bx]) \, dx = \left(\frac{\pi}{\alpha a}\right)^{\frac{1}{2}} \exp\left(\frac{\alpha b^2}{4a}\right) \quad (\text{B.4})$$

For vectors,  $\mathbf{r}$  and  $\mathbf{b}$ , of dimension  $d$ :

$$\int \exp(-\alpha [ar^2 - \mathbf{b} \cdot \mathbf{r}]) \, d^d \mathbf{r} = \left(\frac{\pi}{\alpha a}\right)^{\frac{d}{2}} \exp\left(\frac{\alpha b^2}{4a}\right) \quad (\text{B.5})$$

Matrix notation for integrating by  $d^d \mathbf{r}_1 \dots d^d \mathbf{r}_{n-1}$ :

$$\begin{aligned} & \int \exp(-\alpha (A_{ij} \mathbf{r}_i \mathbf{r}_j - \mathbf{B}_i \mathbf{r}_i + C)) \, d^d \mathbf{r}_1 \dots d^d \mathbf{r}_n \\ &= \left(\frac{1}{\det A} \left(\frac{\pi}{\alpha}\right)^n\right)^{\frac{d}{2}} \exp\left(\frac{\alpha}{4} \mathbf{B}^T A^{-1} \mathbf{B} - \alpha C\right) \end{aligned} \quad (\text{B.6})$$

where  $A$  is a  $n \times n$  matrix of scalars,  $\mathbf{B}$  is a  $n \times 1$  vector of vectors with dimension  $d$ , and  $C$  a constant. In the above we use Einstein notation, such that when an index variable appears more than once in the same term a summation over all possible values is implied. Therefore

$$B_i x_i = \sum_{i=1}^n B_i x_i \quad (\text{B.7})$$

and

$$A_{ij} x_i x_j = \sum_{i=1}^n \sum_{j=1}^n A_{ij} x_i x_j \quad (\text{B.8})$$

### Example: Partition function of a Rouse chain with fixed ends

Eq.(B.6) can be used to obtain Eq.(3.36), the partition function for a Rouse chain with fixed end beads,  $\mathbf{r}_0$  and  $\mathbf{r}_n$ . The integral has the form

$$Q = \int \exp\left(-\frac{3}{2b^2} \sum_{i=1}^n (\mathbf{r}_i - \mathbf{r}_{i-1})^2\right) \, d^d \mathbf{r}_1 \dots d^d \mathbf{r}_{n-1}$$

After expanding the terms within the exponential it can be seen that  $\alpha$ ,  $A$ ,  $\mathbf{B}$  and  $C$  are

$$\alpha = \frac{3}{2b^2}$$

$$A = \begin{pmatrix} 2 & -1 & & 0 \\ -1 & 2 & -1 & \ddots \\ & \ddots & \ddots & -1 \\ 0 & & -1 & 2 \end{pmatrix}; \quad \det A = n$$

$$\mathbf{B} = \begin{pmatrix} \mathbf{r}_0 \\ 0 \\ \vdots \\ 0 \\ \mathbf{r}_n \end{pmatrix}$$

$$C = r_0^2 + r_n^2$$

Hence

$$\begin{aligned} Q &= \int \exp\left(-\frac{3}{2b^2} \sum_{i=1}^n (r_i - r_{i-1})^2\right) d^d \mathbf{r}_1 \dots d^d \mathbf{r}_{n-1} \\ &= \left(\frac{1}{n} \left(\frac{2\pi b^2}{3}\right)^{n-1}\right)^{\frac{d}{2}} \exp\left(-\frac{3}{2b^2} \frac{(\mathbf{r}_n - \mathbf{r}_0)^2}{n}\right) \end{aligned}$$

**Gaussian integrals of the form  $\int x \exp(-\alpha [ax^2 - bx]) dx$**

For a scalar  $x$ :

$$\int_{-\infty}^{\infty} x \exp(-\alpha [ax^2 - bx]) dx = \frac{b}{2a} \left(\frac{\pi}{\alpha a}\right)^{\frac{1}{2}} \exp\left(\frac{\alpha b^2}{4a}\right) \quad (\text{B.9})$$

For vectors,  $\mathbf{r}$  and  $\mathbf{b}$ , of dimension  $d$ :

$$\int \mathbf{r} \exp(-\alpha [ar^2 - \mathbf{b} \cdot \mathbf{r}]) \, d^d \mathbf{r} = \frac{\mathbf{b}}{2a} \left(\frac{\pi}{\alpha a}\right)^{\frac{d}{2}} \exp\left(\frac{\alpha b^2}{4a}\right) \quad (\text{B.10})$$

### Gaussian integrals of the form $\int x^2 \exp(-ax^2) \, dx$

For a scalar  $x$ :

$$\int_{-\infty}^{\infty} x^2 \exp(-ax^2) \, dx = \frac{1}{2a} \left(\frac{\pi}{a}\right)^{\frac{1}{2}} \quad (\text{B.11})$$

For a vector,  $\mathbf{r}$ , of dimension  $d$ :

$$\int \mathbf{r}^2 \exp(-ar^2) \, d^d \mathbf{r} = \frac{d}{2a} \left(\frac{\pi}{a}\right)^{\frac{d}{2}} \quad (\text{B.12})$$

For the special case of a single component  $r^\gamma$  squared and multiplied by a Gaussian involving the vector  $\mathbf{r}$ :

$$\int (r^\gamma)^2 \exp(-ar^2) \, d^d \mathbf{r} = \frac{1}{2a} \left(\frac{\pi}{a}\right)^{\frac{d}{2}} \quad (\text{B.13})$$

These integrals and those below do not have an appropriate equation for Gaussians of the form  $\exp(-ax^2 + bx)$ , but this can be overcome by using a change of variables that allows the Gaussian to be written as  $\exp(-a\tilde{x}^2 + C)$ . This change of variables is

$$\tilde{x} = x - \frac{b}{2a} \quad (\text{B.14})$$

$$C = -\frac{b^2}{4a} \quad (\text{B.15})$$

such that

$$\begin{aligned} ax^2 - bx &= a \left(x - \frac{b}{2a}\right)^2 - \frac{b^2}{4a} \\ &= a\tilde{x}^2 + C \end{aligned} \quad (\text{B.16})$$

Since  $\frac{d\tilde{x}}{dx} = 1$ , the differential for  $\tilde{x}$  is simply

$$d\tilde{x} = dx \quad (\text{B.17})$$

With this change of variables it is possible to use Eq.(B.1) to obtain Eq.(B.4).

## Gaussian integrals of the general form $\int x^p \exp(-ax^2) dx$

For a scalar  $x$ :

$$\int_{-\infty}^{\infty} x^p \exp(-ax^2) dx = \begin{cases} \frac{(2q-1)!!}{(2a)^q} \left(\frac{\pi}{a}\right)^{\frac{1}{2}} & ; \quad p = 2q \\ 0 & ; \quad p = 2q + 1 \end{cases} \quad (\text{B.18})$$

where  $p, q$  are integers and  $!!$  is the double factorial defined as

$$(2q-1)!! = \prod_{i=1}^q (2i-1) \quad (\text{B.19})$$

For the special case of  $(r^\gamma)^p$  multiplied by a Gaussian involving the vector  $\mathbf{r}$ :

$$\int (r^\gamma)^p e(-ar^2) d^d\mathbf{r} = \begin{cases} \frac{(2q-1)!!}{(2a)^q} \left(\frac{\pi}{a}\right)^{\frac{d}{2}} & ; \quad p = 2q \\ 0 & ; \quad p = 2q + 1 \end{cases} \quad (\text{B.20})$$

## Gaussian integral over $n$ elements, multiplied by $2w$ elements

For the situation where the Gaussian  $\exp(-\alpha A_{ij}x^i x^j)$  is multiplied by  $2w$  individual elements,  $x_k$ , indexed  $k_1, k_2, \dots, k_{2w}$ , and integrated over all  $x_i$  the following integral is useful:

$$\begin{aligned} & \int x_{k_1} x_{k_2} \dots x_{k_{2w}} \exp(-A_{ij}x_i x_j) dx_1 \dots dx_n \\ &= \left( \frac{1}{\det A} \left( \frac{\pi}{\alpha} \right)^n \right)^{\frac{1}{2}} \frac{1}{2^w w! \alpha} \sum_{\psi \in S_{2w}} (A^{-1})_{k_{\psi(1)}k_{\psi(2)}} (A^{-1})_{k_{\psi(3)}k_{\psi(4)}} \dots (A^{-1})_{k_{\psi(2w-1)}k_{\psi(2w)}} \end{aligned} \quad (\text{B.21})$$

where  $\psi$  is a permutation of  $\{1, \dots, 2w\}$  and  $\sum_{\psi \in S_{2w}}$  is the summation over all pair combinations of  $\{1, \dots, 2w\}$ , producing  $w$  copies of  $A^{-1}$  [37]. This result is analogous to Wick's theorem, in which, for  $w = 2$ ,

$$\sum_{\psi \in S_{2w}} \langle x_{\psi(1)}x_{\psi(2)} \rangle \langle x_{\psi(3)}x_{\psi(4)} \rangle = \langle x_1x_2 \rangle \langle x_3x_4 \rangle + \langle x_1x_3 \rangle \langle x_2x_4 \rangle + \langle x_1x_4 \rangle \langle x_2x_3 \rangle$$

### Example: Calculating $\langle \Delta x_a \Delta x_b \rangle$ for a multiple slip-spring chain model for $M - 1$ entanglements

Consider a slip-spring model with  $M - 1$  slip-springs with strength  $N_S$  and slip-link positions  $\mathbf{r}_i$ . There are  $M$  chain segments in this system with  $N_i$  beads in each segment, as illustrated in Fig.B.1. In this model slip-links are fixed to beads and do not slip, such that the Cartesian components are decoupled and may be considered individually. The deviation from the average bead position in the x-direction is given by  $\Delta x_i = x_i - \bar{x}_i$ , such that the energy of the system may be written as

$$U = \frac{k}{2} A_{ij} \Delta x_i \Delta x_j + k_B T C$$

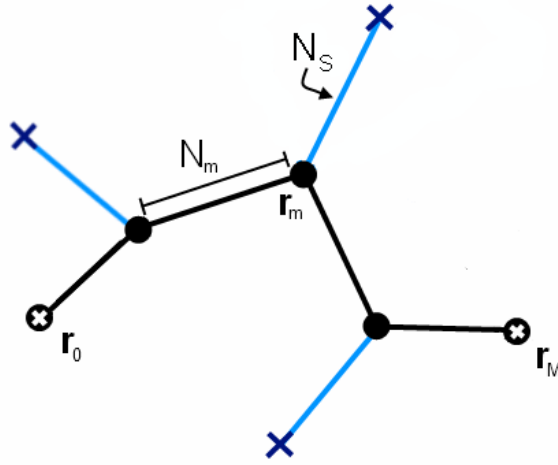


Figure B.1: Diagram of the slip-spring model

where

$$k = \frac{3k_B T}{b^2}$$

$A$  is a symmetric  $(M - 1) \times (M - 1)$  tri-diagonal matrix of scalars,

$$A_{i,i} = \frac{1}{N_i} + \frac{1}{N_{i+1}} + \frac{1}{N_S}$$

$$A_{i,i+1} = -\frac{1}{N_{i+1}}$$

and  $C$  is a constant. Therefore,  $\langle \Delta x_a \Delta x_b \rangle$  may be written as

$$\langle \Delta x_a \Delta x_b \rangle = \frac{\int \Delta x_a \Delta x_b \exp(-\alpha A_{ij} \Delta x_i \Delta x_j + C) d\Delta x_1 d\Delta x_2 \dots d\Delta x_{M-1}}{\int \exp(-\alpha A_{ij} \Delta x_i \Delta x_j + C) d\Delta x_1 d\Delta x_2 \dots d\Delta x_{M-1}} = \frac{I_1}{I_2}$$

where

$$\alpha = \frac{k}{2k_B T} = \frac{3}{2b^2}$$

$I_1$  is integrated first, using Eq.(B.21), where  $\Delta x_{k_1} = \Delta x_a$ ,  $\Delta x_{k_2} = \Delta x_b$  and  $w = 1$ , such that

$$\sum_{\psi \in \mathcal{S}_{2N}} (A^{-1})_{k_{\psi(1)} k_{\psi(2)}} = A_{ab}^{-1}$$

Thus,

$$\begin{aligned} I_1 &= \int \Delta x_a \Delta x_b \exp(-\alpha A_{ij} \Delta x_i \Delta x_j + C) d\Delta x_1 d\Delta x_2 \dots d\Delta x_{M-1} \\ &= \left( \frac{1}{\det A} \left( \frac{\pi}{\alpha} \right)^{M-1} \right)^{\frac{1}{2}} \exp(C) \frac{1}{2\alpha} A_{ab}^{-1} \end{aligned}$$

$I_2$  may be similarly integrated using Eq.(B.6),

$$\begin{aligned} I_2 &= \int \exp(-\alpha A_{ij} \Delta x_i \Delta x_j + C) d\Delta x_1 d\Delta x_2 \dots d\Delta x_{M-1} \\ &= \left( \frac{1}{\det A} \left( \frac{\pi}{\alpha} \right)^{M-1} \right)^{\frac{1}{2}} \exp(C) \end{aligned}$$

Substituting back into  $\langle \Delta x_a \Delta x_b \rangle = \frac{I_1}{I_2}$  it is found that

$$\langle \Delta x_a \Delta x_b \rangle = \frac{1}{2\alpha} A_{ab}^{-1} = \frac{1}{3} b^2 A_{ab}^{-1}$$

Hence,

$$\langle \Delta r_a^\alpha \Delta r_b^\beta \rangle = \frac{1}{3} b^2 A_{ab}^{-1} \delta_{\alpha\beta}$$

# Bibliography

- [1] P.G. de Gennes. *Reptation of a polymer chain in the presence of fixed obstacles* J. Chem. Phys. **55**, 572 - 579 (1971)
- [2] W.W. Graessley, D.S. Pearson. *Stress-strain behavior in polymer networks containing non-localized junctions* J. Chem. Phys. **66**, 3363-3370 (1977)
- [3] A.E. Likhtman, M. Ponmurugan, J. Cao. *Microscopic definition of polymer entanglements* (In preparation)
- [4] A. Likhtman 'Viscoelasticity and molecular rheology' in *Comprehensive Polymer Science* (2nd ed.) Elsevier (2012)
- [5] M.P. Allen, D.J. Tildesley. *Computer Simulation of Liquids* Oxford University Press (1989)
- [6] K. Kremer, G. S. Grest. *Dynamics of entangled linear polymer melts - a molecular-dynamics simulation* J. Chem. Phys. **92**, 5057-5086 (1990)
- [7] P.E. Rouse. J. Chem. Phys. **21**, 1272 (1953)
- [8] M. Doi, S.F. Edwards. *Dynamics of Concentrated Polymer Systems Part 1 - Brownian Motion in the Equilibrium State* J. Chem. Soc., Faraday Trans. 2 **74** 1789 (1978)
- [9] A.E. Likhtman, T.C.B. McLeich. *Quantitative Theory for Linear Dynamics of Linear Entangled Polymers* Macromolecules **35**, 6332-6343 (2002)

- 
- [10] S.F. Edwards. Proc. Phys. Soc. **91**, 513 (1967); J. Phys. A **1**, 15 (1968)
- [11] M. Doi. *Explanation for the 3.4 power law of viscosity of polymeric liquids on the basis of the tube model* J. Poly. Sci. C Lett. **19**, 265-273 (1981)
- [12] P.G. DeGennes. J. Phys (Paris) **36**, 1199 (1975)
- [13] M. Doi, S.F. Edwards. *Dynamics of Concentrated Polymer Systems Part 2 - Molecular Motion under Flow* J. Chem. Soc., Faraday Trans. 2 **74** 1802 (1978)
- [14] C.C. Hua, J.D. Schieber. *Segment connectivity, chain-length breathing, segmental stretch, and constraint release in reptation models. I. Theory and single-step strain predictions* J. Chem. Phys. **109**, 10018 (1998)
- [15] Y. Masubuchi, H. Watanabe, et.al. *Comparison among Slip-Link Simulations of Bidisperse Linear Polymer Melts* Macromolecules **41**, 8275-8280 (2008)
- [16] M. Doi, J. Takimoto. *Molecular modelling of entanglement* Phil. Trans. R. Soc. Lond. A **361**, 641-652 (2003)
- [17] Y. Masubuchi, et al. *Brownian simulations of a network of reptating primitive chains* J. Chem. Phys **115**, 4387 (2001)
- [18] D.M. Nair, J.D. Schieber. *Linear Viscoelastic Predictions of a Consistently Unconstrained Brownian Slip-Link Model* Macromolecules **39**, 3386-3397 (2006)
- [19] J.D. Schieber. *Fluctuations in entanglements of polymer liquids* J.Chem. Phys. **118**, 5162-5166 (2003)
- [20] R.N. Khaliullin, J.D. Schieber. *Self-Consistent Modelling of Constraint Release in a Single-Chain Mean-Field Slip-Link Model* J. Chem. Phys. **42**, 7504-7517 (2009)

- [21] A.E. Likhtman. *Single-Chain Slip-Link Model of Entangled Polymers: Simultaneous Description of Neutron Spin-Echo, Rheology, and Diffusion* Macromolecules **38**, 6128-6139 (2005)
- [22] M. Rubinstein, S. Panyukov. *Elasticity of Polymer Networks* Macromolecules **35**, 6670-6686 (2002)
- [23] J. Ramirez, S.K. Sukumaran, A.E. Likhtman. Macromol. Symp. **252**, 119-129 (2007)
- [24] M. Müller, K. Daoulas. *Single-chain dynamics in a homogeneous melt and a lamellar microphase: A comparison between Smart Monte Carlo dynamics, slithering-snake dynamics, and slip-link dynamics* J. Chem. Phys. **129**, 164906 (2008)
- [25] P.J. Flory, J.Rehner. *Statistical Mechanics of Cross-Linked Polymer Networks (I. Rubberlike Elasticity)* J. Chem. Phys. **11**, 512 (1943)
- [26] D. Chandler, *Introduction to Modern Statistical Mechanics (pp.234-269)* OUP USA (1987)
- [27] R. Zwanzig, *Time-correlation functions and transport coefficients in statistical mechanics* Annu. Rev. Phys. Chem. **16**, 67-102 (1965)
- [28] M. Doi, S.F. Edwards. *The Theory of Polymer Dynamics* Oxford Science Publications (1986)
- [29] J. Ramirez, S.K. Sukumaran, B. Vorselaars, A.E. Likhtman. *Efficient on the fly calculation of time correlation functions in computer simulations* J. Chem. Phys. **133**, 154103 (2010)
- [30] L.Wasserman. *All of statistics: a concise course in statistical inference* Springer (2004)
- [31] S. J. Plimpton, Fast Parallel Algorithms for Short-Range Molecular Dynamics, J Comp Phys, 117, 1-19 (1995)
- [32] <http://lammmps.sandia.gov/>
- [33] A.E. Likhtman. *Whither tube theory: From believing to measuring* Journal of Non-Newtonian Fluid Mechanics **157**, 158-161 (2009)

- 
- [34] J.A. Nelder, R. Mead. *A simplex method for function minimization* Computer Journal **7**, 308–313 (1965)
- [35] J. Ramirez, S.K. Sukumaran, A.E. Likhtman. *Significance of cross correlations in the stress relaxation of polymer melts* J. Chem. Phys. **126**, 244904 (2007)
- [36] J.D. Schieber, K. Horio. *Fluctuation in entanglement positions via elastic slip-links* J. Chem. Phys. **132**, 074905 (2010)
- [37] M.K. Simon. *Probability Distributions Involving Gaussian Random Variables: A Handbook for Engineers and Scientists (2nd ed.)* Springer (2006)